Evolution of galactic star formation in galaxy clusters and post-starburst galaxies

Marcel Lotz

München 2020

Evolution of galactic star formation in galaxy clusters and post-starburst galaxies

Marcel Lotz

Dissertation
an der Fakultät für Physik
der Ludwig–Maximilians–Universität
München

vorgelegt von
Marcel Lotz
aus Frankfurt am Main

München, den 16. November 2020

Erstgutachter: Prof. Dr. Andreas Burkert
Zweitgutachter: Prof. Dr. Til Birnstiel
Tag der mündlichen Prüfung: 8. Januar 2021

Contents

Zusammenfassung

Während die meisten Galaxien sich allmählich entwickeln, gibt es Galaxien, welche eine wesentlich rasantere Entwicklung durchlaufen, zum Beispiel sternbildende Galaxien, die in Galaxienhaufen hineinfallen oder Post-Sternausbruch Galaxien (PSG). Diese sich rasant entwickelnden Galaxien kennzeichnen sich durch erhebliche Änderungen der Sternentstehungsrate auf kurzen Zeitskalen und ermöglichen entscheidende Einblicke in die Prozesse, welche die Galaxienentwicklung vorantreiben. Zum Entschlüsseln dieser Prozesse wird die interne Galaxienentwicklung, die Bahndynamik in Galaxienhaufen und das Wachstum Schwazer Löcher über zahlreiche Giga-jahre untersucht. Zu diesem Zwecke, nutzten wir die modernen hydrodynamischen *Magneticum Pathfinder* Simulationen. Diese ermöglichen die Betrachtung und Auswertung der Galaxienentwicklung in verschiedenen Umgebungen innerhalb kosmologischer Volumina.

Im ersten Teil dieser Dissertation analysieren wir die Prozesse und Bedingungen, welche zur Unterdrückung der Sternbildung von Galaxien in Galaxienhaufen führen. Der Vergleich der Bahndynamiken zwischen sternbildenden Galaxien und Galaxien, die keine Sterne bilden, also 'erloschene' Galaxien, zeigt, dass erstere wesentlich häufiger radiale Umlaufbahnen innerhalb von Galaxienhaufen haben. Dieser Unterschied zwischen sternbildenden und erloschenen Galaxien zeigt sich auch bei der Betrachtung des Phasenraums: Erstere sind dabei in die Galaxienhaufen hineinzufallen und liegen mehrheitlich außerhalb des Virialradius des Galaxienhaufens, während Zweitere überwiegend innerhalb des Virialradius liegen. Die Analyse einzelner Galaxien zeigt, dass die überwältigende Mehrheit an sternbildenden Galaxien während der ersten Umlaufbahn, innerhalb von 1 Ga nach Durchquerung des Virialradius des Galaxienhaufens, gelöscht werden. Die verbleibenden Galaxien ($< 5\%$), welche eine Sternentstehung länger aufrechterhalten können, haben entweder tangentiale Umlaufbahnen oder eine sehr hohe stellare Masse. Aus alledem wird ersichtlich, dass der erhebliche Staudruck, welcher beim Hineinfallen in einen Galaxienhaufen aufkommt, dass für die Sternentstehung notwendige galaktische Gas ausstößt und dadurch die Sternbildung der Galaxie erlischt.

Der zweite Teil widmet sich der Untersuchung der Ursache des Sternausbruches, und dem nachfolgenden abrupten Abfall der Sternentstehung, der in PSG beobachtet wird. Wir zeigen, dass PSG, ähnlich zu sternbildenden Galaxien, sich durch eine Vielzahl von Galaxienverschmelzungen auszeichnen. Innerhalb der letzten 2.5 Ga erlebten 89% der $z \sim 0$ PSG mindestens eine Galaxienverschmelzungen und 65% durchliefen sogar mindestens eine Verschmelzung zwischen Galaxien ähnlicher Masse. Bemerkenswerterweise haben 23% der

PSG sogar eine Verjüngung erlebt, also waren vor ihrem Sternausbruch erloschen. Durch die Galaxienverschmelzungen, welche unter anderem neues Gas einbringen, wird die Sternentstehung kurzfristig angeregt. Im Anschluss wäschst das zentrale Schwarze Loch innerhalb der PSG rasant und die Energie, die der aktive Galaxienkern in der Umgebung deponiert, senkt die Sternentstehung abrupt. Diese Senkung ist besonders effektiv, weil PSG statistisch weniger kaltes Gas haben. Beim Vergleich mit Beobachtungen gibt es sowohl Übereinstimmungen mit der stellaren Massenfunktion als auch mit der Verteilung von PSG im Phasenraum innerhalb von Galaxienhaufen. Die Untersuchung von PSG in Galaxienhaufen zeigt, ähnlich zu den Ergebnissen aus dem ersten Teil, dass PSG überwiegend zum ersten Mal in Galaxienhaufen hineinfallen. Zusammenfassend, während PSG in Galaxienhaufen durch den Staudruck gelöscht werden, ist der aktive Galaxienkern außerhalb von Galaxienhaufen maßgeblich für die Stilllegung der Sternentstehung verantwortlich.

Abstract

While most galaxies evolve gradually, a subset of galaxies, such as star-forming galaxies falling into galaxy cluster or post-starburst galaxies (PSBs), evolve far more quickly. These transition galaxies are characterised by a short timescale decrease of star formation and offer key insights into how and by what mechanisms galaxies evolve. To resolve the extensive range of relevant physical processes involved in galaxy evolution, we analyse the state-of-the-art cosmological hydrodynamical simulation suite *Magneticum Pathfinder*. We track the orbits, merger history, galactic properties, and black holes of transition galaxies and control samples in different environments over several $\sim$ Gyr.

The first part of this thesis investigates the processes whereby, and the conditions under which, star-forming satellite galaxies are quenched in galaxy cluster. We find a strong dichotomy in both the line-of-sight and radial phase space between star-forming and quiescent galaxies: While the former are generally found beyond the cluster virial radius and are dominated by radial orbits, the latter populate the inner cluster region. More importantly, most star-forming satellite galaxies are quenched during their first passage through the galaxy cluster. In particular, the tracking of individual orbits shows that the star formation of almost all satellite galaxies drops to zero within 1 Gyr after cluster infall. The subset ($< 5\%$) of satellite galaxies that remain star-forming the longest after infall have either tangential orbits or high stellar mass. All this indicates that star-forming satellite galaxies are quenched by ram-pressure stripping.

In the second part, we explore the reasons for the starburst phase and the subsequent rapid shutdown observed in PSBs. We find that $z \sim 0$ PSBs, similar to star-forming control galaxies, show a high abundance of mergers within the last 2.5 Gyr: 89% of PSBs have experienced at least one merger, and 65% have had at least one major merger event. Notably, 23% of PSBs underwent rejuvenation during their starburst. While mergers generally increase the gas supply, leading to star formation, PSB progenitors have statistically less cold gas compared to star-forming galaxies. Following the mergers, strong active galactic nucleus (AGN) feedback is registered, leading to a quick shutdown of star formation. We find agreement with observations for stellar mass functions and line-of-sight phase space distributions of PSBs in galaxy cluster. Finally, similar to star-forming galaxies in the first part, we find that $z \lesssim 0.5$ cluster PSBs are dominated by recent cluster infall, especially at high cluster mass. Thus, we conclude that the majority of PSBs in galaxy clusters are shutdown via ram-pressure stripping, while field PSBs are generally quenched by AGN feedback.

Chapter 1

Introduction

Parts of this chapter have been published in Lotz et al. (2019) and Lotz et al. (2020).

1.1 A brief history of astronomy

As the oldest natural science astronomy dates back millennia: The oldest celestial maps are $20000 - 35000$ years old (Joglekar et al., 2011; Rappenglück, 2010). In other words, Homo Sapiens have been sufficiently concerned with their role in the surrounding spatiotemporal structure to transcribe and thereby preserve their observations for posterity. Initially, astronomers belonged to a spiritual or religious caste and astronomy was deeply interwoven with astrology: The positions and movements of celestial bodies primarily served as a means of understanding and interpreting the divine (Krupp, 2003).

Over time, both the tools and interpretations became more sophisticated. In 467 BC Anaxagoras explained eclipses, suggesting that the Sun was a ball of fire larger than the Peloponnese, and that the Moon was illuminated by reflected sunlight (Russell, 2008). Shortly thereafter, in 400 BC, the Babylonians divided the heavens into twelve equal parts, a division which yielded the twelve zodiac signs and, subsequently, the twelve months of the year, still commonly used around the word to date (Britton, 2010). Around the same time, Democritus postulated that the distinguishable bright band in the night sky might consist of stars (Plutarch, 2006).

In 270 BC, Aristarchus of Samos challenged the established geocentric model of the Universe, which was based on the harmonious movement of celestial bodies. He proposed a heliocentric alternative. However, the geocentric model was firmly established in 140 AD when Ptolemy developed the equant, a mathematical concept describing the observed motions of planets (Goldstein, 1997). For the next one and half millennia, the geocentric view of the Universe remained undisputed.

During this period, European astronomy evolved slowly, while primarily Indian and Arabic astronomers continued to push the boundaries of the known. The fourteen chapters of the *Surya Siddhanta*, which mapped the known constellations and described the rules governing the motions of various celestial bodies was composed and revised (Plofker, 2009;

Montgomery & Kumar, 2015). In the 5th century, the astronomical treatise *Aryabhatiya* described the rotation of the Earth on its axis and introduced algorithms that were necessary for astronomical calculations (Ray et al., 2009; Yadav & Mohan, 2011). Thereafter, in 628 the *Brahma-Sphuta-Siddhanta* was written completely in verse: It provided insights into algebra and more calculations concerning the motion of celestial objects (Colebrooke et al., 1817). After these texts were translated into Arabic in 777, the first of hundreds of Islamic astronomical books was composed, referred to as *Zij* (Kennedy, 1956). This knowledge was only translated into Latin in 1126, thereby introducing Europeans to the comprehensive mathematical and astronomical works of past centuries (Joseph, 2011).

The existing geocentric world view, endorsed by Ptolemy a thousand years earlier, began to be challenged: Declaring that the Ptolemaic system was not physical in 1190, Spanish-Arab astronomer Al-Bitruji (Latin: Alpetragius) proposed an alternative geocentric system, which spread throughout Europe (Bolt et al., 2007). Other active critics of Ptolemy's astronomical model included the Syrian astronomer and geometer Al-Urdi, the Persian polymath Nasir al-Din Tusi, the Iranian polymath and poet Qutb al-Din al-Shirazi, and the Arab astronomer and engineer Ibn al-Shatir (Pearson). Al-Urdi developed the Urdi lemma, a more general form of the Apollonius theorem, which allowed the transposition of reference points for uniform motions needed for observations, which was later employed by Copernicus (Saliba, 2011). Commonly considered one of the greatest scientists of medieval Islam, Nasir al-Din al-Tusi, amongst his many mathematical contributions, developed the Tusi couple, a device which provided a substitute for Ptolemy's equant (Van Brummelen, 2009). In 1281 Qutb al-Din al-Shirazi discussed the possibility of heliocentrism (Niazi, 2014). Born in 1304, Ibn al-Shatir favoured empirical observations over theoretical considerations, leading to the most accurate celestial models of the time, showing many similarities with later works by the Polish astronomer Nicolaus Copernicus (Saliba, 1995).

In 1543, the seminal work *De revolutionibus orbium coelestium* by Copernicus triggered a paradigm shift, known now as the Scientific Revolution (Neuber et al., 2014). The book, printed in Nuremberg, advanced the idea that the Earth travelled around the Sun, a theory that had not been given much thought since Aristarchus of Samos had proposed it some 18 centuries previously. The pursuit of curiosity and the associated broadening of horizons is illustrated by Figure 1.1. The spread of the heliocentric model coincided with developments of more sophisticated tools: In 1608, Hans Lippershey, a German-Dutch spectacle maker, was the first to attempt to patent a refractive telescope (King, 2003). A year later the German astronomer Johannes Kepler published *Astronomia nova*, a detailed study of the motion of Mars, further strengthening the heliocentric model (Voelkel, 2001; Kepler & Donahue, 2004). His works, especially Kepler's laws of planetary motion, have become a cornerstone of modern astronomy. Shortly thereafter, in 1610, the Italian astronomer Galileo Galilei published the first telescope based research, *Sidereus Nuncius*, which included observations of our (mountainous) Moon, Jupiter's moons, sunspots, as well as a hundreds of hitherto undetected stars (Galilei & Blumenberg, 1965; Galilei et al., 2009).

The era of invention, increased observation, and empiricism continued to unfold across Europe. The Dutch scientist Christiaan Huygens, not only improved the telescope and

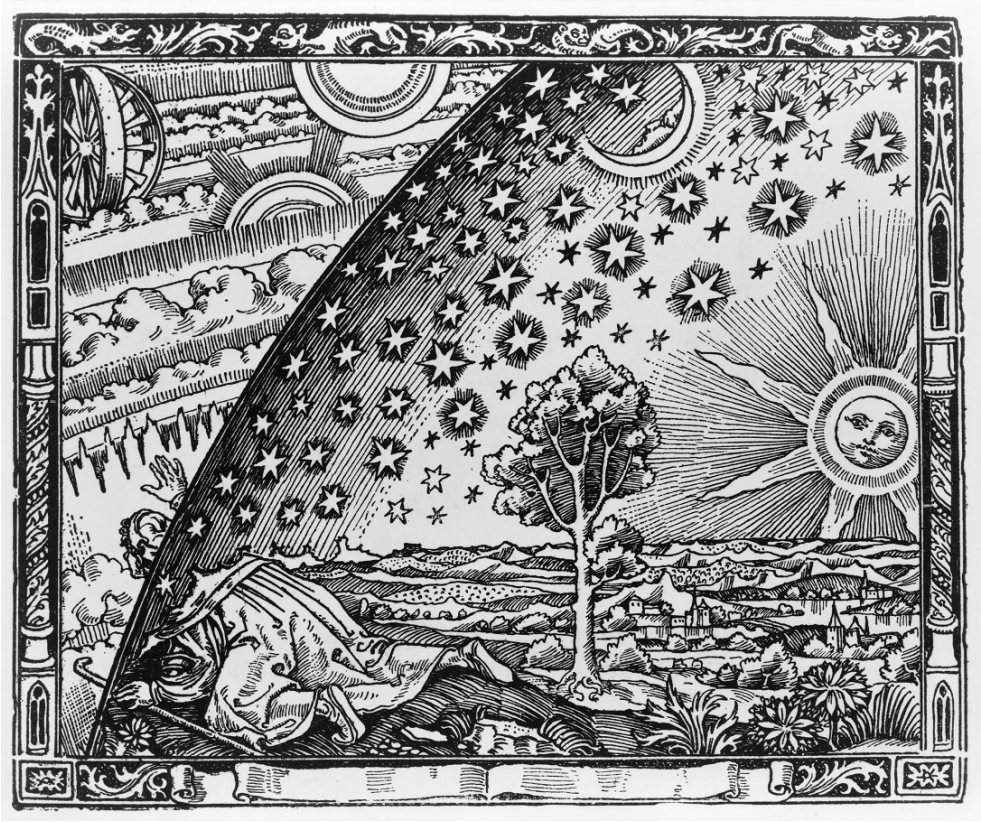

Figure 1.1: Taken from Flammarion (1888), p. 163. Wood engraving by Camille Flammarion, published in 1888, illustrating the pursuit of knowledge, accompanied by the caption: "A missionary of the Middle Ages tells that he had found the point where the sky and the Earth touch..."

invented the pendulum clock, but in 1655 also discovered Titan while identifying a ring around Saturn (Huygens, 1654; Huygens & Clarke, 2014). The English natural philosopher Isaac Newton built the first reflecting telescope in 1668 (Hall & Knight, 1996). In 1687, he published the first edition of *Philosophiae Naturalis Principia Mathematica*, including Newton's laws of motion, Newton's law of universal gravitation and a derivation of Kepler's empirical laws of planetary motion (Newton, 1999). The development of larger telescopes continued: The German-born, later British naturalised, astronomer William Herschel constructed a 40-foot (12m) long telescope between 1785 and 1789 (Cunningham, 2017). He also discovered the hitherto furthest planet, Uranus, conducted deep space surveys, and discovered infrared radiation by using a prism and thermometer while observing sunspots (Aughton, 2013). Around this time, the French astronomer Charles Messier published a catalogue of 110 nebulae and faint star clusters, still commonly used today (Messier, 1781).

As scientific progress continued to accelerate in Europe, novel tools opened up new fields of astronomy: When the German physicist Joseph von Fraunhofer invented the spectroscope and, in 1814, discovered absorption lines in the Sun's spectrum, spectroscopy

was established as an astronomical field (Roth, 1976). Around 1845, the French physicists Jean Foucault and Hippolyte Fizeau used the newly invented photographic process by the French artist Louis Daguerre to photograph the Sun (Lowry & Lowry, 2000; Hughes, 2012). Thus began the systematic photographic surveying of the night sky. In 1868, adding to the existing spectral absorption lines observed by Fraunhofer, Norman Lockyer (also the founder and first editor of the journal *Nature* (Meadows, 1972)) and Pierre Jules Janssen detected a bright yellow line in the spectrum of the Sun, which was subsequently named Helium (Lockyer, 1868; Kochhar, 1991).

In the early 20th century, Henrietta Leavitt discovered that the Cepheid variable star period-luminosity relation enabled reliable distance measurements by providing a so-called 'standard candle' (Leavitt, 1908; Leavitt & Pickering, 1912). Using this relation, Ejnar Hertzsprung measured the distances to 13 Cepheid variable stars via parallax (Hertzsprung, 1913). Thereafter, Hertzsprung and Henry Norris Russell developed the Hertzsprung-Russell diagram (Russell, 1914). It revealed the relation between luminosity or absolute magnitude and colour of a star, i.e. its temperature, or spectral class, yielding extensive insights into stellar evolution. During the same time theoretical work also advanced significantly: The field equations of general relativity were published by Albert Einstein in 1915, however, he only provided their approximate solutions (Einstein, 1915). Karl Schwarzschild was the first to provide exact solutions, while stationed on the Russian front during World War I, using a polar-like coordinate system (Schwarzschild, 1916). His work implied that above a certain mass density, gravitational collapse results in the formation of a singularity, i.e. a black hole.

For many centuries, the expanse of the Milky Way and its relation to the entirety of the Universe had remained unclear. On 26 April, 1920 a great debate was held concerning the scale of the Universe and its relation to our galaxy (Shapley & Curtis, 1921). Harlow Shapley argued that the so-called spiral nebulae (the Milky Way) encompassed the majority of the Universe, believing that distant nebulae were relatively small and proximal (Shapley, 1918). On the other hand, Heber Curtis argued that the spiral nebulae that hosts our Sun is merely a small region embedded within a far greater Universe: The Universe described by Curtis is populated with 'island universes' (galaxies), a term coined by Immanuel Kant (Kant, 1755), separated by vast distances (Curtis, 1917). The debate itself did not resolve the question concerning the scale of the Universe. However, observations of Cepheid variable stars in M31 and M33 (Messier catalogue) by Edwin Hubble, using the period-luminosity relation, provided conclusive evidence (Hubble, 1925): Indeed, Curtis was correct, the Universe is composed of individual galaxies separated by vast distances (Trimble, 1995). Hubble subsequently published his morphological galaxy classification scheme in 1926 (see Section 1.3.1) (Hubble, 1926b,a, 1927). In 1929 Hubble presented observations which demonstrate that the Universe is expanding (see Hubble-Lemaître law in Section 1.2.1 (Hubble, 1929), based on work by Friedmann (1922), Lemaître (1927), and earlier measurements by Slipher (1917).

During this time our understanding of stellar physics also greatly improved: In 1925, Cecilia Payne-Gaposchkin published her doctoral thesis in which she provided the evidence that stars were overwhelmingly comprised of hydrogen, by inference making it the most

abundant element in the Universe (Payne, 1925). This led to a heightened interest in the chemical evolution of the Universe (Wayman, 2002). A few years later, Subrahmanyan Chandrasekhar provided the theoretical groundwork for late stage stellar evolution models and demonstrated that the mass of a white dwarf may not exceed 1.4 times that of the Sun (the Chandrasekhar limit), else it collapses into a neutron star or at higher masses into a black hole (Chandrasekhar, 1931a,b, 1939). This was accompanied by extensive research into stellar (remnant) collapse, leading to the term 'supernova' being coined by Walter Baade and Fritz Zwicky (Baade & Zwicky, 1934). By observing the Coma galaxy cluster, Fritz Zwicky also inferred the existence of dark matter in 1933 (see Section 1.2.2) (Zwicky, 1933, 1937). At the end of the 30s, Hans Bethe explained the energy production mechanism in stars by detailing the nuclear reactions involved in the carbon-nitrogen-oxygen cycle (Bethe, 1939, 1940).

With the onset of World War II, physicists became increasingly devoted to reaping and advancing the destructive potential of physical phenomena. The advancements in rocketry and nuclear physics were extensive (Chun, 2006). During the Cold War, vast resources were directed towards technological advancements, especially during the space race: In 1957, the Soviet Union (Sputnik 1) and the United States (Explorer 1) each launched their first satellites into orbit (Tucker, 2020). In the midst of the space race, Arno Penzias and Robert Wilson accidentally discovered the cosmic microwave background (CMB, see Section 1.2.1, Figure 1.2) (Penzias & Wilson, 1965). In 1977, Voyager 1 and Voyager 2 were launched. Today, both have entered interstellar space and are therefore the two most distant objects (from Earth) constructed by Homo Sapiens (Kohler, 2020). Various probes and satellites followed, mapping the sky with increasing detail and depth, across different wavelengths.

The first exoplanets were discovered orbiting a pulsar in 1992 (Wolszczan & Frail, 1992). As of 15 November, 2020, the *Extra-solar Planets Catalog* counts 4374 confirmed exoplanets in 3234 planetary systems (Schneider et al., 2011). Using supernovae type Ia as 'standard candles', in 1998, two independent projects discovered that our Universe is not only expanding, but is doing so at an accelerated rate (see Section 1.2.2) (Riess et al., 1998). In 2015, the first gravitational waves were detected by *LIGO*, the existence of which were predicted by the theory of general relativity a century earlier (Abbott et al., 2016, 2017).

Our joint human endeavour for meaning (see Figure 1.1), particularly our desire to understand our role within the greater cosmos has yielded an increasingly sophisticated field of research. The original yearning for meaning has brought forth an abundance of knowledge concerning the unfolding of the Universe. The initial 'why', directed at the skies, remains.

1.2 Cosmology

Cosmology is the field of astronomy which is primarily concerned with the study of the origin and evolution of the Universe, ideally from 'beginning' to 'end'. As more tools

become available, our understanding of the structure and the formation of structure in our Universe is evolving continuously. Basing our understanding on empirical observations has thus far proven to be elementary in describing, predicting, and advancing our current knowledge of the natural world (see Section 1.1).

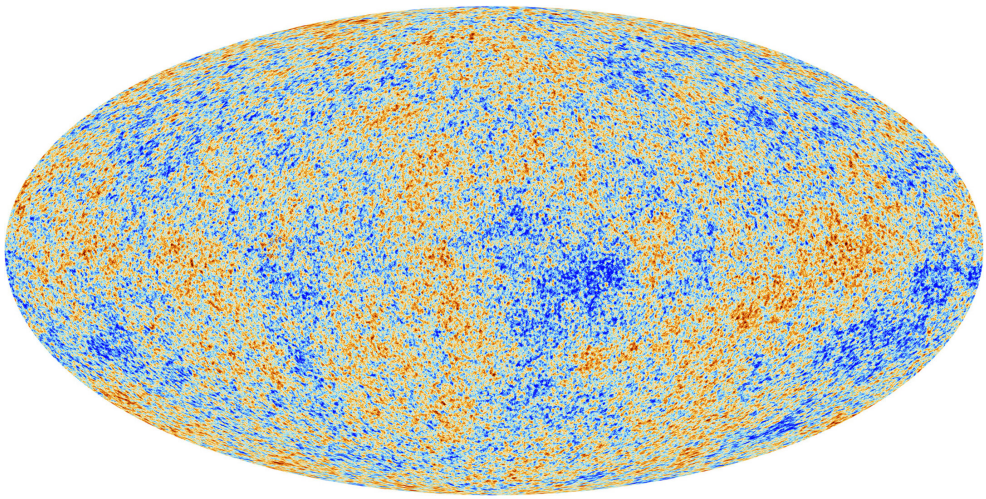

Figure 1.2: Cosmic microwave background (CMB) as seen by the Planck satellite. The CMB has a thermal black body spectrum at a temperature of $2.72548 \pm 0.00057\,\mathrm{K}$ (Fixsen, 2009). The colours represent tiny temperature fluctuations from the average temperature: Red indicates warmer and blue colder regions. Credit: ESA and the Planck Collaboration

1.2.1 The Cosmological Principle and our expanding Universe

When looking outward from our vantage point on Earth, we find that on large scales the Universe appears to be isotropic (Collins & Hawking, 1973). If we combine the observed isotropy with the assumption of the **Copernican Principle**, i.e. nothing about our place in the Universe is unique, **the Cosmological Principle** emerges: It states that the Universe appears isotropic and homogeneous (Peacock, 1999; Clarkson, 2012). Although this cannot be proven, the assumption is strengthened by Cosmic Microwave Background (CMB) observations, which find a high degree of isotropy (Partridge & Wilkinson, 1967; de Bernardis et al., 2000; Planck Collaboration et al., 2014a). Figure 1.2 shows the apparent isotropy from our point of view by displaying the tiny temperature fluctuations within the CMB.

The Cosmological Principle is accompanied by a number of important implications: First, it suggests that more distant objects, i.e. objects with long light travel times, are observed at an earlier stage within a common evolution. In particular, this implies that the change in morphology observed in galaxies (see Section 1.3.1) from high to low redshift is a reflection of a universal galaxy evolution, rather than different evolutionary pathways associated with different regions of the Universe (Abraham & van den Bergh, 2001). Second, the fact that distant galaxies host fewer metals heavier than lithium (Erb

et al., 2006; Zahid et al., 2014), provides restrictions on the origin(s) of heavier metals: Namely, heavier metals were not created in the Big Bang but rather accumulated via nucleosynthesis in stars and their subsequent supernovae (Meyer et al., 1989).

Third, homogeneity and isotropy on scales $\gtrsim 100\,\mathrm{Mpc}$ suggest that the largest identifiable structures in the Universe are in mechanical equilibrium with one another, resting within a larger indistinguishable structure. When considering smaller scales, the Universe appears to be ordered: both higher density filamentary structures, as well as low density voids are distinguishable (Kawaharada et al., 2010).

Lastly, the Cosmological Principle is relevant to general relativity. Its assumptions allow the derivation of the Friedmann equations, i.e. a set of equations based on Einstein's field equations of gravitation governing the expansion of space, as well as specifying the metric (Friedmann, 1922). Thus, a Universe which abides by the Cosmological Principle reduces the possible space-time metrics to the **Friedmann-Lemaître-Robertson-Walker metric** (Friedmann, 1922; Lemaître, 1933; Robertson, 1935; Walker, 1935):

$$ds^2 = (cdt)^2 - a(t)^2 \left[\frac{dr^2}{1 - Kr^2} + r^2(d\theta^2 + \sin^2(\theta d\phi^2) \right] \tag{1.1}$$

with polar coordinates r (reduced-circumference), θ and ϕ, cosmic time t, cosmic scale factor $a(t)$, which marks the relative expansion of the Universe (see below), and curvature parameter K. The metric has three distinct solutions for the curvature parameter, i.e. the topology of the Universe: flat ($K = 0$), open ($K > 0$), and closed ($K < 0$). The curvature is determined by the relationship between the actual density of the Universe and the critical density (Goldsmith, 1997; Dodelson & Knox, 2000). The **critical density** is defined as the amount of mass needed to halt the expansion of a matter-only Universe at some infinitely distant time in the future (Freeman & McNamara, 2006)

$$\rho_c = \frac{3H_0^2}{8\pi G} \tag{1.2}$$

where H_0 is the Hubble constant, i.e. the Hubble parameter at redshift zero (see below), and G is the gravitational constant.

In a **flat**, i.e. euclidean, Universe the actual density is equal to the critical density. However, due to the dark energy component (see Section 1.2.2) the Universe expands forever (Goldsmith, 1997): The non-zero abundance of dark energy only influences the rate of expansion. The positive curvature case characterises a **closed**, spherical Universe, with an actual density greater than the critical density, in which the scale factor increases to a maximum value, followed by a decrease to zero. In contrast, the negative curvature case with actual density smaller than the critical density, describes an **open** hyperbolic topology, in which the Universe expands at an accelerated rate. Using the standard 6 parameter ΛCDM cosmology model (see Section 1.2.2), extensive observations conducted by large collaborations have determined the observable Universe to be flat (Spergel et al., 2003; Komatsu et al., 2011; Planck Collaboration et al., 2016b).

This fundamental theoretic work (Friedmann, 1922; Lemaître, 1933; Robertson, 1935; Walker, 1935) was accompanied by one of the most important cosmological observations,

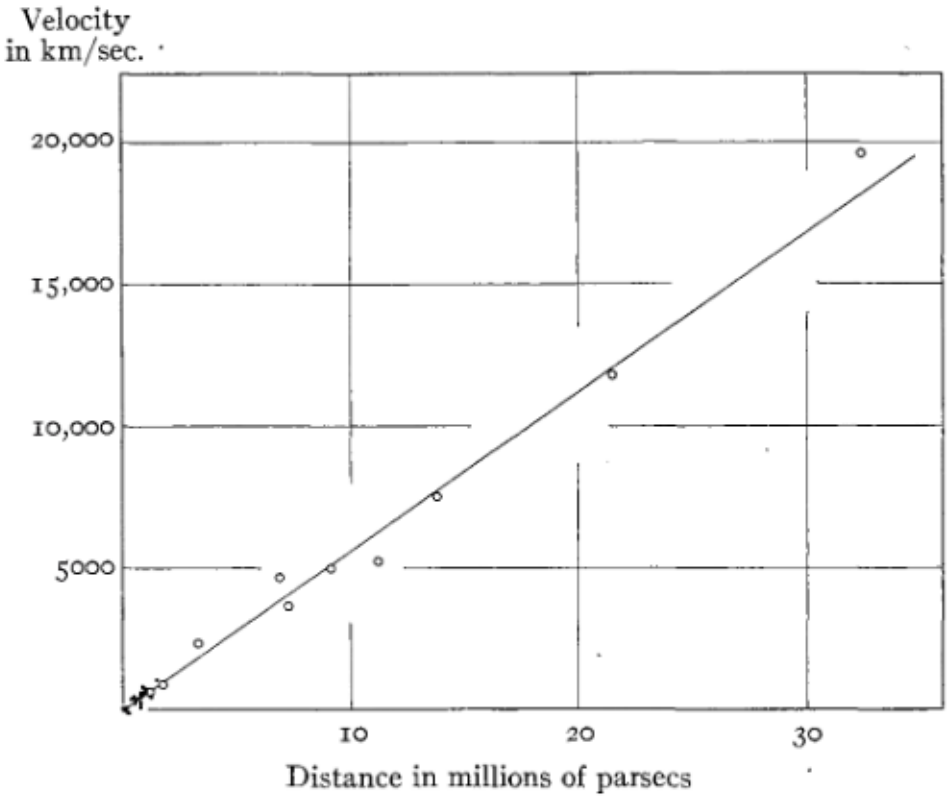

Figure 1.3: Fig. 5 taken from Hubble & Humason (1931) showing the velocity-distance relation for clusters or groups of nebulae. In other words, the recession velocity, driven by the expansion of the Universe, as a function of cosmic distance is shown for an initial sample of galaxies and clusters. This, together with earlier results (Lemaître, 1927), provided the basis for the formulation of the Hubble-Lemaître law.

to date: Our Universe is expanding (Slipher, 1917; Lemaître, 1927; Hubble & Humason, 1931; Hubble, 1936). Due to the expanding space-time metric, distant galaxies appear to be moving away from our point of observation, as shown in Figure 1.3: Specifically, the greater the distance of an astronomical object (in this case galaxies and galaxy clusters), the greater its recession velocity, i.e. the faster it moves away. This implies that at some previous time the metric was less expanded, leading to the idea of a starting point, i.e. the Big Bang (see Section 1.2.3). The effect of the expansion of the Universe (Figure 1.3) is captured by the **Hubble-Lemaître law**, which states that the relationship between distance D and recession velocity v is linear (Slipher, 1917; Friedmann, 1922; Lemaître, 1927; Hubble, 1929; Hubble & Humason, 1931; Hubble, 1936)

$$v = H(t)D \tag{1.3}$$

where the Hubble parameter at present-day, i.e. the **Hubble constant**, is commonly

expressed as

$$H(t_0) = H_0 = h\,100\frac{\mathrm{km}}{\mathrm{s\,Mpc}} \tag{1.4}$$

where h is the dimensionless Hubble parameter (Croton, 2013). Generally, the **Hubble parameter** may be expressed as

$$H(t) = \frac{\dot{a}(t)}{a(t)} \tag{1.5}$$

which, given the Friedmann-Lemaître-Robertson-Walker metric, may be expressed using the cosmology dependent **scale factor**

$$a(t) = \frac{1}{1+z}. \tag{1.6}$$

The scale factor and its derivative are, in turn, functions of **cosmological redshift**

$$z \equiv \frac{\lambda_0 - \lambda_t}{\lambda_t} \tag{1.7}$$

with λ_t being the wavelength of the radiation emitted at time t and the wavelength observed in the present given by λ_0. As such, cosmological redshift is a non-linear time scale ranging from now $z = 0$ to arbitrary high values asymptotically approaching the 'beginning' of time, i.e. in the currently favoured model: the Big Bang.

1.2.2 Dark matter, dark energy and the ΛCDM cosmological model

As mentioned in Section 1.1, early evidence, based on the observed velocity dispersion of stars in the central region of the Milky Way, suggested that the majority of massive objects, then believed to be stars, may be dark, i.e. they showed no signs of electromagnetic radiation (Kelvin, 1904). Several measurements of our galactic neighbourhood (Kapteyn, 1922; Oort, 1932; Babcock, 1939; Roberts, 1966; Gottesman et al., 1966; Rubin & Ford, 1970; Roberts & Whitehurst, 1975), and more distant objects (Zwicky, 1933, 1937; Oort, 1940; Freeman, 1970) consistently appeared to show a lack of matter when compared to the expected mass, which was initially derived either by the mass-luminosity relationship or via the inferred dynamics. This indirectly observed type of matter, which appears to not (or only very weakly) interact with baryonic matter, is referred to as **dark matter**. To date, there is ample indirect evidence for dark matter, including: galaxy rotation curves (Kapteyn, 1922; Babcock, 1939; Roberts, 1966; Rubin & Ford, 1970; Freeman, 1970; Roberts & Whitehurst, 1975), velocity dispersion measurements in bound systems (Battaglia et al., 2005; Cappellari et al., 2006; Wolf et al., 2010), and its effect on structure formation (density profiles, clustering) (Davis et al., 1985; Navarro et al., 1996). Furthermore, different independent mass estimates of galaxy clusters can be calculated (Allen et al., 2011), by either (1) combining the velocity dispersion with the virial theorem (Zwicky, 1933), (2) using the X-ray luminosity of hot cluster gas to derive its density

and subsequently its pressure, which, in turn, can be equated with the gravitational force, allowing the calculation of a mass profile (Randall et al., 2008; Pratt et al., 2009; Arnaud et al., 2010), or (3) gravitational lensing, i.e. measuring the gravitation effect on light from more distant line-of-sight sources (Kaiser & Squires, 1993; Tyson et al., 1998; Postman et al., 2012). In general, observations consistently find that dark matter is a factor ~ 5 times more abundant than baryonic matter (Allen et al., 2011). Specifically, 4.9% and 25.9% of the observed energy density of the Universe consists of baryonic and dark matter, respectively (Planck Collaboration et al., 2016b).

A historic example of dark matter evidence is displayed in Figure 1.4: The **circular velocity profile** of both the Milky Way (filled circles and dashed line) (Rougoor & Oort, 1960; Schmidt, 1965) and M31 (solid line) as a function of galacto-centric distance is shown (Rubin & Ford, 1970). Rather than showing a strong decline, which would be expected by estimates based on the distribution of baryonic matter, the rotational velocity remains fairly flat, i.e. elevated. This implies the presence of non visible matter, i.e. dark matter, which changes the mass distribution, thereby providing rotational support, especially towards increasing galactic radii.

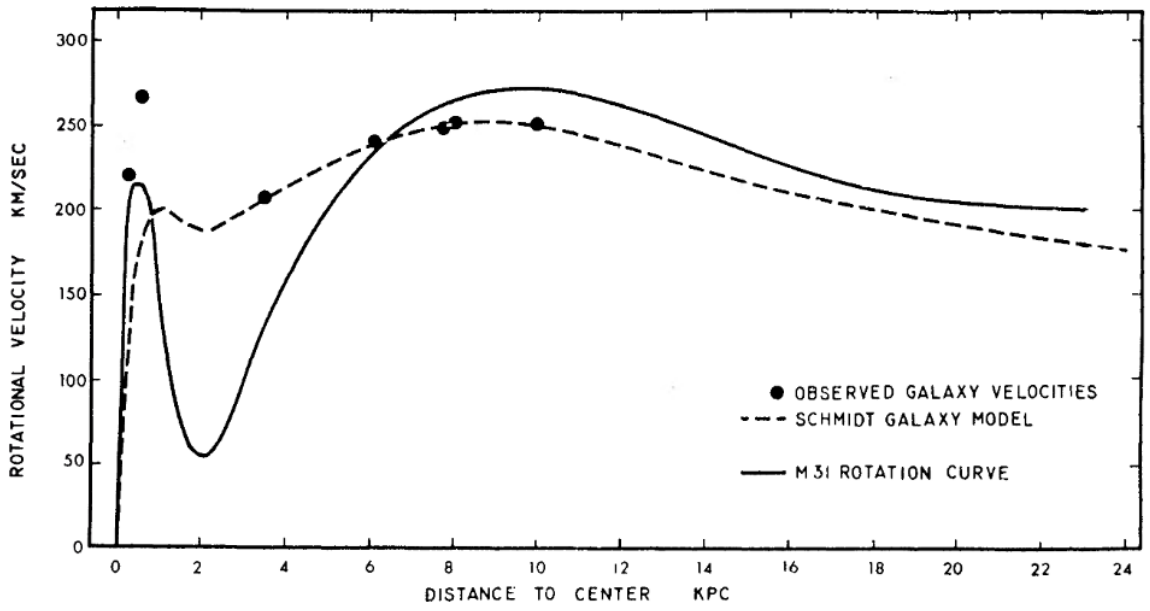

Figure 1.4: Fig. 15 taken from Rubin & Ford (1970). Comparison of rotation curves from M31 and the Milky Way (referred to as Galaxy in the legend), as a function of distance from the centre. Solid line: Rotation curve for M31. Dashed line: Rotation curve from Schmidt model of the Milky Way (Schmidt, 1965). Filled circles: Observed rotational velocities for the Milky Way (Rougoor & Oort, 1960).

All hypotheses, which attempt to explain the discrepancy between directly observable matter and matter inferred via indirect observations, are associated with unsolved problems. As a result, the search for different types of dark matter, as well as different

cosmological models continues (Bull et al., 2016). Understanding what subatomic particles dark matter is composed of, e.g. by ruling out potential candidates, and discovering how dark matter interacts with other types of matter is a critical endeavour within astro- and particle physics (Bergström, 2000; Beringer et al., 2012; Olive & Particle Data Group, 2014). A wide range of potential candidates for dark matter exist, ranging in size from quantum to galactic scales. However, as both particle accelerators and observational techniques become more sophisticated some potential candidates have become increasingly unlikely: Detailed micro-lensing studies of the Magellanic clouds have ruled out massive compact halo objects (MACHOs), i.e. dense baryonic objects such as stellar remnants, in mass ranges $10^{-7} \lesssim M/\mathrm{M}_\odot \lesssim 15$ (Tisserand et al., 2007; Wyrzykowski et al., 2011).

Other potential dark matter candidates include axions, i.e. hypothetical elementary particles which are postulated to resolve the strong CP problem in quantum chromodynamics (Peccei & Quinn, 1977b,a). Furthermore, hypotheses such as modified Newtonian dynamics (MOND) propose that Newton's laws act differently on large scales and as such do not rely on dark matter particles to explain observations (Milgrom, 1983b,a,c). However, MOND does not completely resolve the need for dark matter particles in galaxy clusters, most prominently in the strongly interacting Bullet Cluster (Clowe et al., 2004, 2006). Weakly interacting massive particles (WIMPs), i.e. a broad class of non baryonic hypothetical particles (Baer et al., 2015), belong to the most promising dark matter candidates. Although some (supersymmetric) predictions of WIMPs have become increasingly unlikely due increasing constraints from direct-detection experiments (Aprile et al., 2012), a wide array of candidates still exists. Independent of the specific dark matter particle, we are able to make some general statements concerning its characteristics. In particular, we can consider different types of dark matter based on their relative velocity in the early Universe, allowing the division into the kinematic categories of hot, warm or cold dark matter (Dekel & Ostriker, 1999). The currently favoured model is **cold dark matter** (CDM), which is long-lived, collisionless and kinematically cold: It is the most successful model for explaining both galaxy and galaxy cluster formation (Blumenthal et al., 1984; Davis et al., 1985; Navarro et al., 1996; Spergel & Steinhardt, 2000).

The radial density profile $\rho(r)$, derived from N-body simulations, most commonly used to describe the distribution of cold dark matter halos is the Navarro-Frenk-White (NFW) profile (Navarro et al., 1997):

$$\rho(r) = \frac{\rho_c}{\frac{r}{r_s}\left(1 + \frac{r}{r_s}\right)^2} \tag{1.8}$$

where ρ_c and the scale radius r_s are two a priori free characteristic parameters fitted to each individual halo, which turn out to be correlated (Navarro et al., 1996).

Other density profiles exist which describe the distribution of dark matter halos, each with its own caveats: For example, while the NFW profile diverges for small radii, the (pseudo-)isothermal model (Gunn & Gott, 1972; Binney & Tremaine, 2011) fails to converge to finite values as the radius approaches infinity. Meanwhile, the Einasto profile (Einasto, 1965) requires an additional free parameter and, similarly to the NFW profile,

predicts a density cusp at small radii. In contrast, observations find constant density cores in galaxies (de Blok et al., 2001): This discrepancy between theory and observations is commonly referred to as the **core-cusp problem** (de Blok, 2010). A possible solution is provided by the additional consideration of (baryonic) feedback mechanisms (see Section 1.4.2), which may flatten the overall density profile in the central galactic regions (Governato et al., 2010). While the Burkert profile (Burkert, 1995) is characterised by a flat core, the strong agreement with observations only holds at low and intermediate masses (Salucci & Burkert, 2000). In practice, depending on the mass regime, different profiles are used to characterise the radial density distribution of halos. Radial (luminosity) profiles of galaxies are discussed in Section 1.3.1.

Section 1.2.1 established that the Universe is expanding (e.g. Figure 1.3). However, more recent observational evidence based on supernovae type Ia, which due to their consistent peak luminosity can be used as 'standard candles' to robustly measure distances, indicates that our Universe is not only expanding, but it is doing so at an accelerated rate (Riess et al., 1998). Similarly to the problem posed by the apparent lack of visible matter many decades before, which led to the concept of dark matter, an accelerated expanding Universe also challenged our existing understanding (Turner & White, 1997). Specifically, the observed accelerated expansion of the Universe (Riess et al., 1998) could not be explained without introducing a novel type of energy (Turner & Riess, 2002). This new type of energy was termed **dark energy** (Huterer & Turner, 1999; Perlmutter et al., 1999b): It is commonly described by the cosmological constant (Carroll, 2001). Other solutions for the accelerated expansion of the Universe include scalar fields, i.e. equations of state that are different from matter, radiation, or the cosmological constant (Ratra & Peebles, 1988; Caldwell et al., 1998).

The concept of a **cosmological constant** Λ was introduced by Einstein to complement his previously published field equations (Einstein & der Wissenschaften, 1915): In particular the cosmological constant was added as a means to balance the attractive effects of gravity, allowing the description of the model preferred at the time, a static Universe (Einstein, 1917). After it was shown that the Universe is indeed expanding (Hubble & Humason, 1931), the model of a static Universe was replaced by models assuming a vanishing cosmological constant, such as the Einstein-de Sitter Universe (Einstein & de Sitter, 1932). Setting the cosmological constant to zero remained the consensus for many decades (Weinberg, 1989; Carroll et al., 1992; Peebles & Ratra, 2003), until the Universe was observed to be expanding at an accelerated rate (Turner & White, 1997). Thereafter, the cosmological constant was assumed and measured to have a positive non-zero value (Perlmutter et al., 1998; Riess et al., 1998; Schmidt et al., 1998; Perlmutter et al., 1999a). Indeed, recent results find that energy density of the Universe is dominated (68.9%) by dark energy (Planck Collaboration et al., 2020).

Combining the concepts of dark energy, as expressed by a positive cosmological constant Λ, and cold dark matter (CDM), yields the currently favoured cosmological model: **ΛCDM**. The ΛCDM model is based on six parameters: (1) physical baryon density parameter, (2) physical dark matter density parameter, (3) age of the Universe, (4) scalar spectral index, (5) curvature fluctuation amplitude, and (6) the reionisation optical depth

(Planck Collaboration et al., 2014b). Despite being based on only six parameters, the ΛCDM model has been successful in describing an abundance of cosmological data (Planck Collaboration et al., 2014b): First, it predicts both the existence and the (very weak) degree of anisotropy of the CMB (see Figure 1.2), as well as its polarisation (Kovac et al., 2002). Second, it describes the Type Ia supernovae magnitude-distance relation, i.e. both the acceleration and the rate of acceleration of our Universe (Perlmutter et al., 1999a). Third, the ΛCDM model matches baryon acoustic oscillation measurements. These are particularly important as they are based on simple geometric measurements, which makes them less susceptible to systematic errors compared to most astrophysical data (Planck Collaboration et al., 2016b). Fourthly, it successfully predicts weak gravitational lensing by large scale structure (Bacon et al., 2000; Van Waerbeke et al., 2000).

1.2.3 Chronology of the Universe

Little is known about the very early Universe. Our current understanding of the unfolding Universe is firmly based on the Friedmann-Lemaître-Robertson-Walker metric (Friedmann, 1922; Lemaître, 1933; Robertson, 1935; Walker, 1935). In this cosmological model, the Universe, via its metric, may be traced back to a time of origin in which it was far less extended, i.e. **the Big Bang**. At the Big Bang, the distances between objects, as measured by the metric, are either zero or infinitesimally small (Lemaître, 1927). Only from this point on-wards, as the Universe expands, time becomes a useful construct.

In the first 10^{-43} seconds the radiation temperature exceeded $> 10^{32}$ K (Kolb, 2018). During this period, it is assumed that the fundamental forces, i.e. the strong nuclear force, the weak nuclear force, electromagnetism, and gravitation, were unified (Mukhanov, 2005). The continuous expansion, and thus cooling, of the Universe led to the separation of the individual forces. These hypothesised phase transitions, in which individual forces are separated below critical temperatures, are motivated by the unified description of the electroweak force at high energies (Glashow, 1959; Salam & Ward, 1959; Weinberg, 1967). Following the separation of the unified force into gravitation and the electrostrong force, the electrostrong force further split into the strong nuclear and the electroweak force (De Vega et al., 2012).

Within the first 10^{-32} seconds after the Big Bang, the Friedmann-Lemaître-Robertson-Walker metric underwent an **inflation** on a timescale of $\sim 10^{-33} - 10^{-32}$ seconds, in which the volume of the early Universe increased by a factor of $\geq 10^{78}$ (Guth, 1998). This inflation facilitated the realisation of a homogeneous and isotropic Universe, i.e. the basis of the Cosmological Principle. In other words, inflation caused the primordial quantum fluctuations of the very early Universe to be inflated to macroscopic scales, thereby effectively freezing in primordial density perturbations (Rubakov & Gorbunov, 2011). As a result, perturbations which are no longer in causal contact with each other appear to be in thermal equilibrium (Tegmark et al., 2006; Planck Collaboration et al., 2016b,a).

The conclusion of the inflationary epoch marks a transition, after which our understanding of the early Universe improves: Energy levels (of order GeV and TeV) were reached which are replicable in particle physics experiments, e.g. with the Large Hadron

Collider (Aad et al., 2012; Chatrchyan et al., 2012). At 10^{-12} seconds, all forces had separated and the Universe was filled with a quark-gluon plasma at temperatures $> 10^{12}$ K (Hawley & Holcomb, 2005). As the temperature decreased further, at around $> 10^{10}$ K, i.e. $\sim 10^{-6}$ seconds after the Big Bang, quarks became bound (Heacox, 2015). This marked the beginning of the **hadron epoch**: The first mesons and baryons, and their anti-particles appeared, as well as pairs of hadrons and anti-hadrons. As the temperature continued to fall, the hadron/anti-hadron pairs were no longer formed. During the annihilation of these pairs, the matter/anti-matter asymmetry became evident: Due to the hadron excess of 1 part in $\sim 10^9$ compared to anti-hadrons, the pair annihilation ($x + \bar{x} \rightarrow \gamma + \gamma$) left a remaining legacy of $\sim 10^9$ photons per surviving hadron (Heacox, 2015).

The **lepton epoch** began $\sim$ 1 second after the Big Bang, when leptons dominated the mass of the Universe (for a few seconds) (Yahil & Beaudet, 1976; Chaisson, 1988). Until $\sim$ 10 seconds after the Big Bang, the temperature was still sufficiently high for the formation of new lepton/anti-lepton pairs (Kuznetsov et al., 2014). Thereafter, leptons and anti-leptons were no longer in thermal equilibrium and, as they annihilated each other, the matter asymmetry led to a significantly decreased lepton population. Despite our knowledge of some of the relevant processes, the origin of matter and the reasons for its asymmetry remain a mystery (Canetti et al., 2012).

At the beginning of the lepton epoch, at temperatures $T \sim 2 - 3$ MeV, **neutrinos decoupled** from baryonic matter, leaving them free to travel the Universe (Lesgourgues et al., 2013). Prior to the decoupling, which occurred when the characteristic rate of weak interactions dropped below the rate of expansion of the Universe, photons, (anti-)neutrinos ($\bar{\nu}_e$) ν_e, protons p, neutrons n, electrons e^-, and positrons e^+ were in thermal equilibrium (Valle & Romao, 2015):

$$n + \nu_e \rightleftharpoons p + e^- \tag{1.9}$$

$$p + \bar{\nu}_e \rightleftharpoons n + e^+ \tag{1.10}$$

By evaluating the Boltzmann factors, we know that $n_n/n_p \propto e^{-1/T}$. In other words, thermal equilibrium between neutrinos and baryonic matter implied that the ratio of neutrons to protons decayed exponentially with decreasing temperature. However, due to the decoupling of neutrinos the ratio of neutrons to protons was 'frozen' at $n_n/n_p \sim 1/5$ (Valle & Romao, 2015).

The **Big Bang nucleosynthesis**, which lasted between $\sim$ 10 seconds to 20 minutes after the Big Bang, was characterised by the production of nuclei heavier than the lightest hydrogen isotope (^2H) (Olive et al., 2000). Due to the temporal constraints imposed by the continuous expansion driven cooling of the Universe, the primordial nuclear reactor was only able to synthesise a subset of light isotopes, such as deuterium, helium-3, helium-4, and lithium-7, in quantities comparable to current abundances (Olive et al., 2000). Any unstable isotopes (e.g. tritium and beryllium-7) decayed into stable isotopes, thereby no longer being present at similar abundances today as when they were formed. Notably, the previously 'frozen' neutron to proton ratio provided the necessary neutron abundances for the production of isotopes beyond ^2H, thereby locking neutrons into stable atoms (Valle

& Romao, 2015). This preserved neutrons in sufficient quantities to allow the production of heavier isotopes during later stellar nucleosynthesis, which then produced the necessary elements needed for the formation of life, as we understand it.

During and long after the Big Bang nucleosynthesis (from $\sim 10\,\mathrm{s}$ to $380,000\,\mathrm{years}$ after the Big Bang), the Universe contained a hot dense plasma of nuclei, electrons and photons (Narison, 2015). The so-called **photon epoch** was characterised by an optically opaque Universe, in which elastic Thomson scattering of photons off of free electrons kept photons and matter in thermal equilibrium (Bambi & Dolgov, 2015). The primordial density fluctuations began to grow via gravitational attraction. As baryonic matter and photons were coupled, a strong counteracting pressure force, driven by the heating associated with the uptick in matter-photon interactions, opposed the gravitational attraction (Peebles & Yu, 1970). Consequently, the coupled baryons and photons began to oscillate, while dark matter remained in the inner regions of the over-densities. When matter and photons decoupled, the baryonic matter was left with measurable density imprints referred to as **baryonic acoustic oscillations** (Eisenstein et al., 2005).

The **cosmic microwave background** (CMB), shown in Figure 1.2, is the oldest detectable (photon) radiation, marking the time when photons decoupled due to the recombination of electrons and protons, i.e. when the Universe was cool enough ($0.4\,\mathrm{eV}$) for the formation of electrically neutral atoms (Tanabashi et al., 2018). At **recombination**, the cross section of the elastic scattering of photons with previously charged matter became much smaller, leading to a transition from an opaque to a transparent Universe (Bambi & Dolgov, 2015). Everything that happened in the first $\sim 380,000$ years after the Big Bang, i.e. before recombination made the Universe transparent to photons, is not available to photon based observations (Mukhanov, 2005). Via measurements of the CMB (Spergel et al., 2003), we find that at recombination, i.e. around 13.7 billion years ago, the Universe consisted of 10% neutrinos, 12% atoms, 15% photons, and 63% dark matter (Komatsu et al., 2009). Furthermore, we learn that the thermal black body spectrum of the CMB, as measured at present times, has a temperature of $2.72548 \pm 0.00057\,\mathrm{K}$ (Fixsen, 2009).

After recombination, as the Universe cooled below a few thousand degrees Kelvin via adiabatic expansion, CMB photons were quickly redshifted, resulting in a Universe devoid of visible light (Mo et al., 2010). The so-called **dark ages** lasted for $\sim 180\,\mathrm{Myr}$ until the first stars were formed via the gravitational collapse of dense gas (Haemmerlé et al., 2018). Population III stars, i.e. a hypothetical class of extremely massive, low metallicity stars, began to illuminate the Universe (Tominaga et al., 2007). Population III stars were pivotal for the formation of later larger structures, as they fused light elements via stellar nucleosynthesis, increasing the metallicity in their immediate environment. As a higher metallicity facilitates gas cooling, Population III stars provided the initial chemistry needed to initiate wide-spread and sustained star formation (Sutherland & Dopita, 1993).

As time progressed, gas was further enriched with metals. At around $\sim 400\,\mathrm{Myr}$ after the Big Bang, the epoch of **reionisation** began, marking the beginning of extensive, luminous structure formation. This epoch began with the formation of the first Population III stars, followed by the formation of galaxies (see Section 1.4.1), i.e. gravitationally bound systems hosting stars and other baryonic components (e.g. gas, dust, stellar remnants), as

well as dark matter (Sparke & Gallagher, 2000). This also corresponds to the age of the most distant, i.e. earliest, observed galaxies to date (Oesch et al., 2016). The formation of the first galaxies inevitably led to the formation of the first galaxy groups and proto-clusters, i.e. the progenitors of the largest gravitationally bound structures in the Universe (Kravtsov & Borgani, 2012).

At the onset of reionisation, initially isolated sources of ultraviolet (UV) radiation, such as stars (Strömgren, 1939), slowly reionised the surrounding medium. As structure formed and evolved, more seeds of UV radiation began to blossom across the Universe. Furthermore, the initially small spheres of reionised inter-galactic medium (IGM) increased in size, while more UV photons were emitted. Once the spheres of reionised IGM began to overlap, reionisation accelerated. Ultimately, the IGM became porous and the remaining regions were reionised by the intergalactic UV radiation field (Fan et al., 2006). The epoch of reionisation ended $sim1$ Gyr after the Big Bang when the IGM was fully ionised.

Over the following billions of years, matter continued to collapse, clump and cluster into the **large scale structures** we observe today (Peebles, 1980). Ultimately, this resulted in the large filamentary structure between voids which characterise the present Universe on large scales. Figure 1.5 shows a 70 Mpc slice of the honeycomb structure at present-day, simulated with Box2/hr of the *Magneticum Pathfinder* simulations (see Section 2.2) (Hirschmann et al., 2014; Dolag et al., 2015). The original seeds from which this structure evolved were provided by the distribution of over-densities originating from the initial quantum fluctuations, which were amplified during the inflationary epoch. Section 1.4 expands on the relevant mechanisms for the formation and evolution of galaxies and galaxy clusters.

1.3 Galaxy properties

Galaxies are gravitationally bound systems consisting of dark matter, stars, stellar remnants, and the interstellar medium (e.g. gas, dust, cosmic rays). They share a set of common properties: Almost all galaxies host a central super massive black hole (exceptions may include low mass and ejected black hole galaxies) (Kormendy & Richstone, 1995; Kormendy & Ho, 2013). Furthermore, the baryonic, i.e. visible, component of a galaxy is typically embedded within an extended dark matter halo (see Section 1.2.2), which reaches far beyond the visible edge of a galaxy and is significantly more massive than the baryonic component (Hoekstra et al., 2005; Papastergis et al., 2012). Specific galaxy properties, such as size, mass, morphology (Section 1.3.1), and colour (Section 1.3.2), vary significantly depending on the individual assembly history. Galaxy formation (Section 1.4.1) and subsequent evolution (Sections 1.4.2 and 1.4.3), as well as the impact of the environment (Section 1.4.4), is discussed in Section 1.4. In total, it is estimated that $2 \cdot 10^{12}$ (two trillion) galaxies populate the Universe at redshifts $z < 8$, albeit most are far less massive than the Milky Way (Conselice et al., 2016).

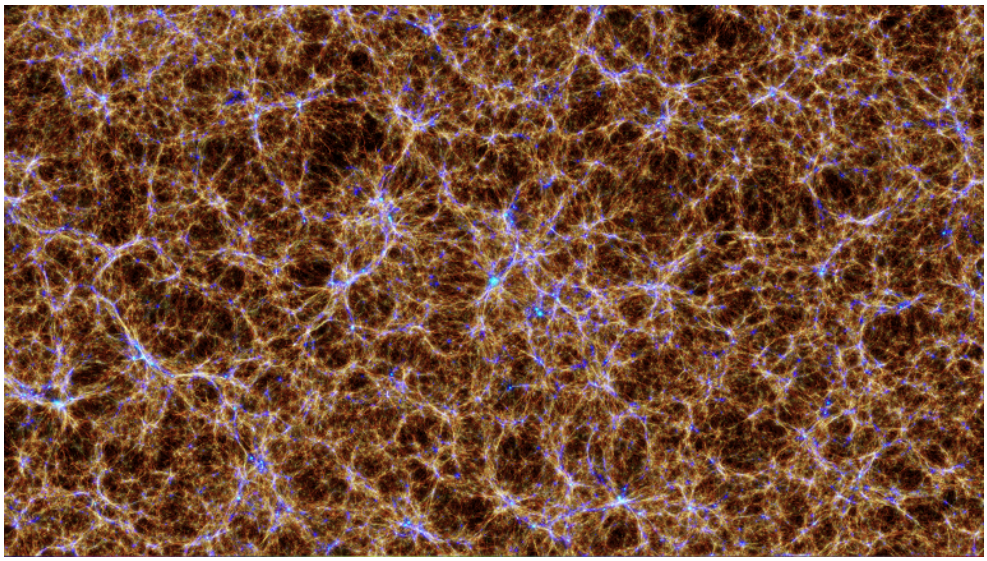

Figure 1.5: Combination of Fig. 2 and Fig. 3 taken from Hirschmann et al. (2014) and Dolag et al. (2015), respectively. A 500 Mpc wide and 70 Mpc thick slice through the baryonic mass distribution of Box2/hr at $z = 0$ in the *Magneticum Pathfinder* simulation visualised with Sanders et al. (2008). The large filamentary structure is commonly referred to as the cosmic web. Clusters are represented by the blue over-densities, the most massive of which is located at the centre of the figure.

1.3.1 Morphology

Historically (see Section 1.1), galaxies were initially classified via their morphology, i.e. their visual appearance, into two distinct types: elliptical and spiral or disc galaxies. This historic **Hubble sequence** classification is shown in Figure 1.6, where the elliptical, also referred to as early-type, and the spiral, also referred to as late-type, galaxies are located on the left and right, respectively (Hubble, 1926b,a, 1927, 1936). In between these two types lies an intermediate type, named a lenticular galaxy (Sandage, 1961). The Hubble classification is largely based on two sets of criteria depending on the galaxy type: For elliptical galaxies the ellipticity, i.e. the degree of flatness, is the determining factor, while the tightness of the galactic spiral arms and whether or not a galactic bar is present determines the specific classification of spiral galaxies. At the time the classification was formulated, as the arrangement in Figure 1.6 suggests, galaxies were believed to evolve from early- to late-type (Hubble, 1936). Today, we know that this does not reflect the evolution of galaxies, rather the opposite evolutionary sequence, i.e. from late- to early-type, is the norm. Nonetheless, the historic classification and its associated naming convention has persisted and has been expanded (de Vaucouleurs, 1959a; Sandage, 1961; Sandage & Tammann, 1981; Buta & Combes, 1996). Additionally, other classification schemes based on spectral properties (Johnson & Morgan, 1953) or kinematics (Emsellem et al., 2011; Krajnović et al., 2011), rather than morphology, have also been established.

The most notable expansion of the Hubble sequence classification scheme was brought

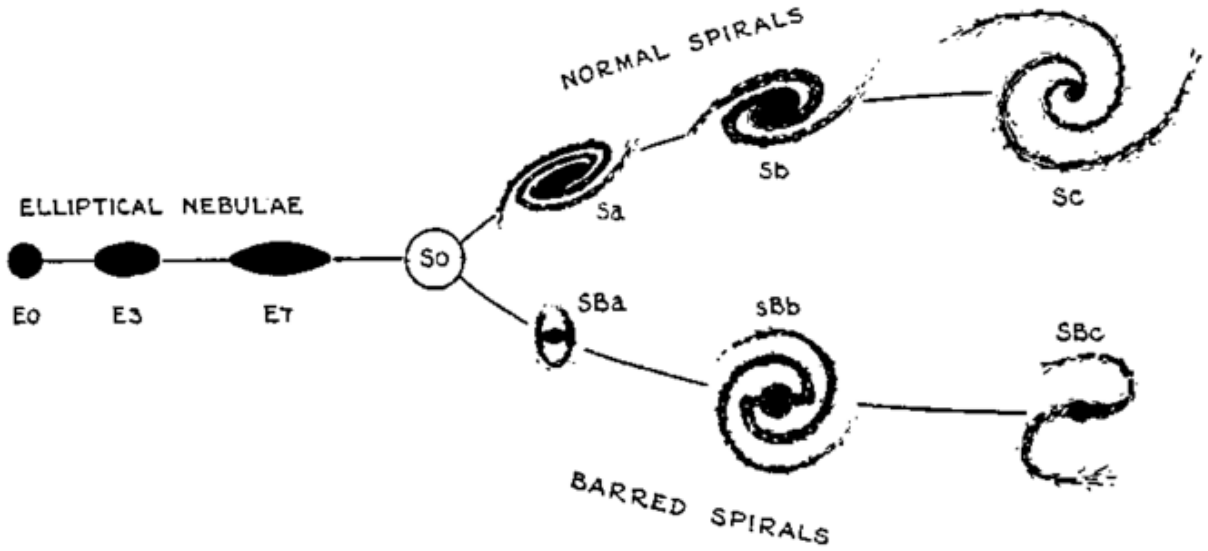

Figure 1.6: Historic Hubble classification taken from Hubble (1936). On the left elliptical (E) galaxies are depicted, historically referred to as elliptical nebulae. The right side shows normal and barred (B) spirals (S), respectively. In between elliptical and spiral galaxies lie lenticular galaxies (S0). Historically, the left are called early type and the right late type galaxies.

forth by de Vaucouleurs (1959a). The **de Vaucouleurs system** introduces continuity between barred and non-barred spirals, distinguishes more continuously between spiral and irregular galaxies, and adds variety to the spiral structure by considering rings (de Vaucouleurs, 1959a). This yields a three-dimensional version of the Hubble sequence, shown in Figure 1.7, based on the galactic stage (spiralness), family (barredness), and variety (ringedness) (de Vaucouleurs, 1959a). Identifying where a galaxy lies within this three-dimensional volume yields its classification along each axis. Generally, the reasons behind the observations (e.g. the evolution between galaxy types, the origins of different luminosity profiles and the build up of different galactic structures) are discussed in Section 1.4, while the static appearance and galactic properties are discussed in the following.

As Figures 1.6 and 1.7 show, **spiral galaxies** are typically subdivided into distinct types. Independent of their type, they all host **spiral arms**, which are typically characterised by an abundance of star formation. As a result, spiral arms are associated with a young, bright stellar population, that increases the visibility of the spiral arms, and thus gives this class of galaxies their name. Furthermore, as indicated in Figures 1.6 and 1.7, spiral galaxies are characterised by a continuum in apparent **galactic bar** strength, varying from weak oval distortions to a strong distinct elongated central bar-shaped population of stars. Indeed, $\sim 25-50\%$ of local spiral galaxies show evidence of a bar structure, with some galaxies hosting multiple bar structures (Sellwood & Wilkinson, 1993; Odewahn, 1996; Elmegreen et al., 2004; Aguerri et al., 2009; Nair & Abraham, 2010; Masters et al.,

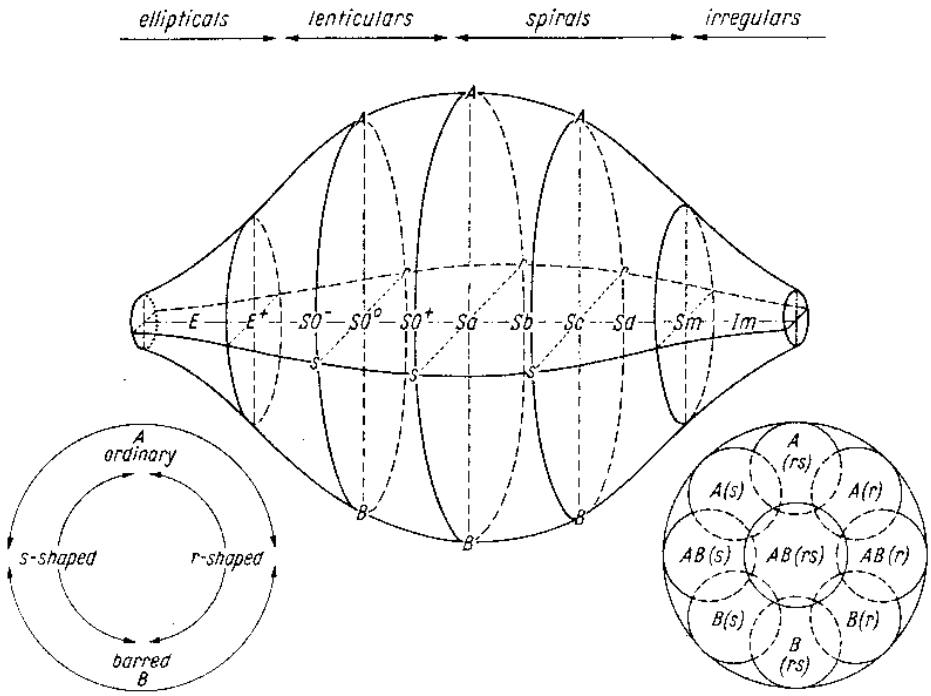

Figure 1.7: Fig. 6 taken from Buta & Combes (1996). Schematic overview of the three-dimensional revised Hubble classification system of de Vaucouleurs (1959a). This method differentiates galaxies based on where they are found within the classification volume. X-axis: Stage, i.e. spiralness ranging from elliptical (E), lenticular (S0), spiral (Sa, Sb, Sc, Sd) to irregular (Sm, Im). Y-axis: Family, i.e. barredness ranging from barred (SB), over mixed (SAB) to non-barred (SA). Z-axis: Variety, i.e. ringedness ranging from ring-like (r), ring/spiral-like (rs), to spiral (s).

2011; Cheung et al., 2013).

The spiral arms lie within a **galactic disc**: Observations suggest that disc galaxies follow a common radial surface brightness profile (Patterson, 1940; de Vaucouleurs, 1956, 1958, 1959b,c; Boroson, 1981; Peng et al., 2002). Specifically, the surface brightness I relates to the galaxy's central brightness I_d and the disc scale length R_d as a function of radius R, as follows (Binney & Tremaine, 2011):

$$I(R) = I_d \, e^{-R/R_d} \tag{1.11}$$

However, observations have also established that most local galaxies break in their exponential profile at $R/R_d \sim 1.5 - 4.5$, with the outer regions being characterised by a steeper profile, while a minority show signs of a shallower profile in the outskirts beyond $R/R_d \sim 4.0 - 6.0$ (Pohlen & Trujillo, 2006). Steeper profiles in the outskirts are associated with later-type, while shallower profiles correlate with early-type galaxies (Pohlen & Trujillo, 2006).

The central region of a spiral galaxy is often associated with an excess of light, compared to the expected exponential disc profile. This inner dense spheroidal region is referred to

as the **bulge**. The bulge is characterised by an old, low metallicity stellar population. Depending on the galaxy in question the bulge shares similarities with scaled down elliptical galaxies or may simply present as a small higher density region within the central region. In 1958, the quantitative decomposition of the luminosity distribution into standard components became possible (de Vaucouleurs, 1958, 1959b): Specifically, surface brightness profiles of spiral galaxies could be resolved into a spheroidal, i.e. bulge, component typically associated with elliptical galaxies (de Vaucouleurs, 1948, 1953) and an exponential disc characteristic of spiral galaxies (Patterson, 1940; de Vaucouleurs, 1956, 1959b,c).

The spheroidal stellar distribution characterising **elliptical galaxies** or bulges may be expressed in terms of the surface brightness I, the galacto-centric distance R, the effective radius R_e, i.e. the radius encompassing half of the total luminosity, and the coefficient I_e, which corresponds to the surface brightness at R_e as follows (de Vaucouleurs, 1948):

$$I(R) = I_e \, e^{-7.669\left[\left(\frac{R}{R_e}\right)^{\frac{1}{4}}-1\right]} \tag{1.12}$$

This luminosity profile, named after de Vaucouleurs, is a special case (with Sérsic index $n = 4$) of the more general Sérsic profile (Sérsic, 1963), which is used to quantify the degree of central concentration of a galaxy. Both elliptical galaxies and the spheroidal component of lenticular galaxies obey the same radius-surface brightness relation (Simien & de Vaucouleurs, 1986). Evaluating the different galactic components (e.g. exponential disc, spheroidal bulge) allows the derivation of more general relations, such as the bulge to disc luminosity ratio (Yoshizawa & Wakamatsu, 1975; Simien & de Vaucouleurs, 1986) or the black hole to bulge mass ratio (Magorrian et al., 1998; Marconi & Hunt, 2003; Häring & Rix, 2004). To date, thousands of individual stars in each galactic region (e.g. bulge, bar, disc, halo) have been spectroscopically surveyed, yielding an increasingly detailed picture of general galactic characteristics and specific assembly histories (Eisenstein et al., 2011).

1.3.2 Colour

The more massive a star is, the shorter its life time and the higher its temperature is, i.e. the bluer it appears (Hertzsprung, 1911, 1909; Russell, 1914; Schaller et al., 1992). As massive stars are short-lived, the colour blue within a galactic region is associated with ongoing star formation. Hence, **spiral galaxies**, which are often characterised by elevated star formation in the spiral arms (Kennicutt, 1989), are typically associated with the colour blue. In contrast, **elliptical galaxies**, which are associated with lesser star formation, host a statistically older stellar population, and are thus typically associated with the colour red (Martig et al., 2009). Generally, the colour of a galaxy strongly depends on its specific assembly history (see Section 1.4).

A recent step in systematically broadening our understanding of the differences between galaxies was provided by the colour separation observed between spiral and elliptical galaxies (Strateva et al., 2001). In combination with additional observations and analysis, this bimodal distribution of galaxy colour yielded the colour-magnitude diagram (Strateva et al., 2001; Bell et al., 2003, 2004; Zehavi et al., 2011). Figure 1.8 shows the colour-mass

diagram (via the mass-luminosity relation (Kuiper, 1938) the magnitude may be converted to mass) based on data from the Sloan Digital Sky Survey (SDSS) (Abazajian et al., 2009), Galaxy Evolution Explorer (GALEX) (Martin et al., 2005), and Galaxy Zoo (Lintott et al., 2008, 2011). The **colour-magnitude or colour-mass diagram** may be divided into the 'red sequence' (top) and the 'blue cloud' (bottom), with the sparsely populated 'green valley' in between, implying that the transition from star-forming to quiescent happens on short timescales, compared to the periods of star formation and quiescence (Wyder et al., 2007; Brammer et al., 2009; Loh et al., 2010). However, more recent results suggest that the distribution of galaxy colour is both more continuous and varied, calling the existence of a singular pathway through the green valley into question (Schawinski et al., 2014; Eales et al., 2018). Section 1.4 discusses the details of how galaxies transition between galaxy types. Specifically, Section 1.4.5 introduces a transitioning population which evolves from the blue cloud to the red sequence on short timescales.

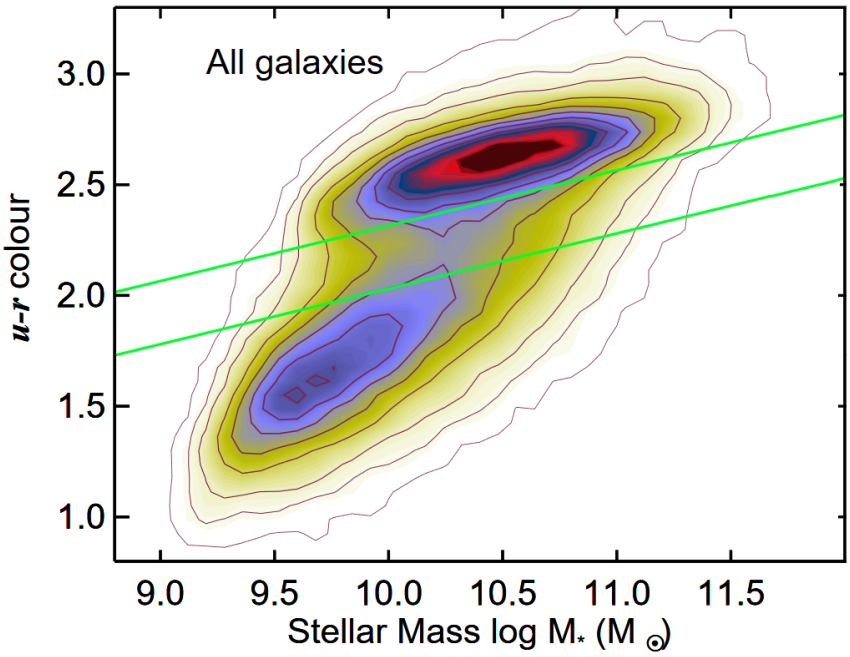

Figure 1.8: Fig. 2 taken from Schawinski et al. (2014). Colour-mass diagram based on Sloan Digital Sky Survey (SDSS) (Abazajian et al., 2009), Galaxy Evolution Explorer (GALEX) (Martin et al., 2005), and Galaxy Zoo (Lintott et al., 2008, 2011) data. The upper high density region is typically referred to as the red sequence, while the lower high density region is referred to as blue cloud, each referencing the associated apparent colour. The transition region between the two solid green lines is referred as the green valley.

1.4 Galaxy evolution

1.4.1 Galaxy formation

At the end of the dark ages, as the Universe is slowly reionised (see Section 1.2.3), the first galaxies are formed. As primordial over-densities grow via gravitational attraction, baryons condense within dark matter halos (see Section 1.2.2). Gas is accreted from (what later becomes known as) the intergalactic medium (IGM) forming the interstellar medium (ISM) and the enveloping circum-galactic medium (CGM) (Dayal & Ferrara, 2018). While some studies favour (early) **galaxy formation models** characterised by rapid wide-spread gravitational collapse within $\sim 10^8$ years (Eggen et al., 1962), others favour a more gradual growth based on proto-galactic fragments such as globular clusters (Searle & Zinn, 1978). Indeed, galaxy formation is based on highly nonlinear density fluctuations and strongly depends on the initial conditions (e.g. redshift, composition, density) (Jeans, 1902; Lifshitz, 1946; Peebles, 1993; Mo et al., 2010; Binney & Tremaine, 2011).

A simplified overview of the current understanding of galaxy formation is shown in Figure 1.9 (Mo et al., 2010). Although all galaxies form via gravitational instabilities within a broader dark matter halo, the individual formation processes quickly diverge thereafter. In the current paradigm, the initial formation of star-forming discs, i.e. at low and intermediate masses, happens via **cold-mode accretion**, meaning that most gas is accreted at temperatures (much) lower than the halo virial temperature ($T \lesssim 10^4\,\mathrm{K}$) (Katz & Gunn, 1991; Birnboim & Dekel, 2003; Kereš et al., 2005; Ocvirk et al., 2008; Dayal & Ferrara, 2018). The previously assumed standard paradigm of **hot-mode accretion**, during which a substantial amount of gas falling into the dark matter halo is shock heated to the halo virial temperature (Dayal & Ferrara, 2018), is now considered to only dominate the growth of high mass systems (Kereš et al., 2005; Ocvirk et al., 2008). Independent of the accretion mode, if gas has any angular momentum it settles into the energetically favourable state of a gaseous disc (Dalcanton et al., 1997). Depending on the specific temperature, i.e. thermal pressure, gas settles into discs of varying scale height (Yoachim & Dalcanton, 2006): The colder the gas the denser it may become, leading to thinner discs, i.e. a smaller disc scale height. Although the vast majority of star formation happens within the thin disc, the disc mass only makes up a few percent of the overall halo mass (Mo et al., 1998). After stars are formed in the thin disc, they experience gradual dynamic heating, e.g. via random interactions or disc perturbations, leading to older stellar populations being associated with larger galactic scale heights (Binney & Tremaine, 2011).

After the formation of a gaseous disc and the associated influx in star formation, the formation process depends on the specific environmental conditions. In other words, the mass, composition, and manner in which matter is accreted strongly influences the subsequent galaxy formation/evolution. As indicated in Figure 1.9, major mergers (see Section 1.4.3) are often associated with the formation of bulge dominated or elliptical galaxies (Bender et al., 1992; Hopkins et al., 2008b; Mo et al., 2010). However, bulges and central discs of massive galaxies may also be formed by **secular evolution** via cold accretion flows along filaments of the cosmic web (Genzel et al., 2008): These streams may introduce (strong)

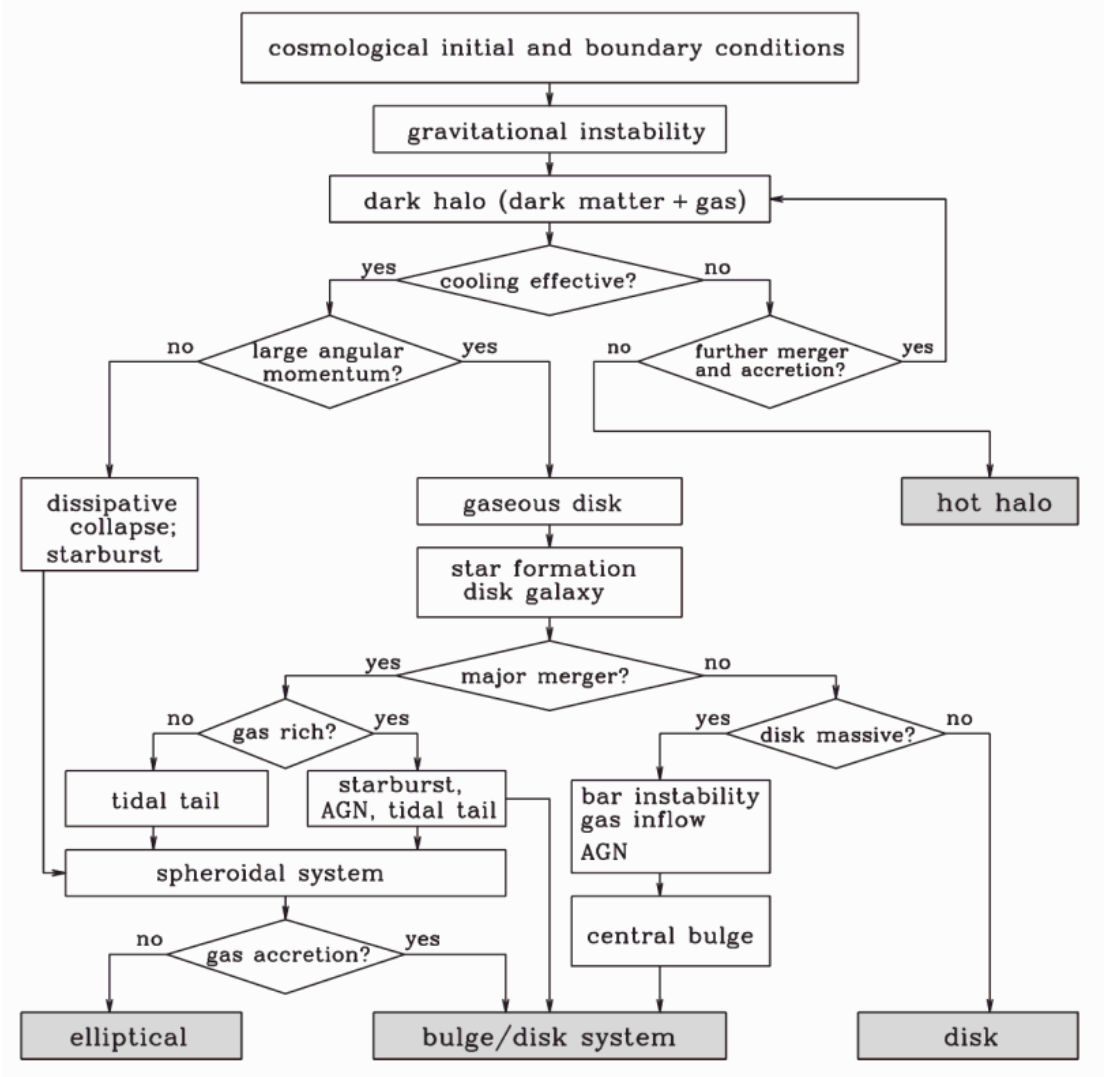

Figure 1.9: Fig. 1.1 taken from Mo et al. (2010). A logic flow chart for galaxy formation. In the standard scenario, the initial and boundary conditions for galaxy formation are set by the cosmological framework. The paths leading to the formation of various types of galaxies are shown along with the relevant physical processes. Note, however, that the processes do not separate as neatly as this figure suggests. For example, cold gas may not have the necessary time to settle into a gaseous disc before a major merger takes place.

turbulence by releasing the gravitational energy associated with (rapid) accretion, thereby impacting the galactic morphology (Dekel et al., 2009). In general, feedback (see Section 1.4.2), mergers (see Section 1.4.3), and the environmental density (see Section 1.4.4) proceed to strongly impact the evolution of galaxies from the onset of their formation.

1.4.2 Star formation and feedback

Fundamentally, regions of cold, dense (molecular) gas are a requirement for star formation: **Cold gas clouds** are only able to gravitationally collapse, i.e. form stars, if their density is sufficiently high to allow the gravitational attraction of the gas cloud to outweigh its thermal pressure. Typically this only occurs in the densest regions in (giant) **molecular clouds** which extend $\sim 10 - 100\,\mathrm{pc}$ and have masses of $\sim 10^5 - 10^6\,\mathrm{M}_\odot$ (Chi & You, 1995). On average, molecular clouds have particle densities of order $\sim 10 - 300\,\mathrm{cm}^{-3}$, with local cores having significantly higher densities, and temperatures of $\sim 10 - 30\,\mathrm{K}$ (Chi & You, 1995). Forming, maintaining, and replenishing these regions is crucial to sustaining galactic star formation.

Any feedback processes, be they thermal and/or kinetic, which impact these regions, either directly and/or indirectly, are relevant to galactic star formation. They can be divided into **positive feedback**, i.e. processes which boost star formation, and **negative feedback**, i.e. processes that quench star formation (Binney & Tremaine, 1987). Prominent sources of positive feedback include turbulence (e.g. introduced by tidal interactions, mergers or shocks) (Larson, 1981; McKee & Tan, 2003; Elmegreen & Scalo, 2004; Mac Low & Klessen, 2004; Ostriker & Shetty, 2011) and chemical enrichment by stars (Matteucci & Greggio, 1986; Nomoto et al., 2013). Star formation decreasing processes, which are primarily related to the stellar mass of an individual galaxy, rather than the surrounding environment (see Section 1.4.4), are referred to as **mass quenching** mechanisms (Peng et al., 2010, 2012): These examples of negative feedback include stellar radiation (Ceverino & Klypin, 2009; Hopkins et al., 2012, 2014), supernovae (Dalla Vecchia & Schaye, 2008; Scannapieco et al., 2008; Dalla Vecchia & Schaye, 2012), and active galactic nuclei (Schawinski et al., 2007; Fabian, 2012; Cicone et al., 2014).

Depending on different properties, such as galactic stellar mass, feedback mechanisms act differently and at varying efficiency: At low stellar masses, i.e. lower galactic halo escape velocities, **supernovae** driven winds are able to accelerate (diffuse) gas to high velocities and expel vast amounts from the galaxy (Larson, 1974; Dekel & Silk, 1986; Norman & Ferrara, 1996; Matzner, 2002; Mac Low & Klessen, 2004; Oppenheimer & Davé, 2008; Krumholz & Matzner, 2009; Murray et al., 2010; Ostriker et al., 2010; Ostriker & Shetty, 2011; Puchwein & Springel, 2013). While expelling large amounts of diffuse (warm/hot) gas has no immediate effect on star formation, it does impact the reservoir of gas available for future star formation. Independent of the galaxy mass, the energetic radiation (UV and X-ray) (Navarro & Steinmetz, 1997; Gnedin, 2000; Benson et al., 2002; Hambrick et al., 2011) and cosmic rays (Jubelgas et al., 2008; Wadepuhl & Springel, 2011) emitted by (massive) stars and SNe is able to suppress star formation by reducing the cold gas component. As galaxy mass increases, **active galactic nuclei** (AGN) feedback, i.e. intense non-stellar emission associated with the accretion onto super massive black holes, becomes increasingly important (Kormendy et al., 2009). In massive galaxies the AGN can deposit vast amounts of energy into the ISM, thereby suppressing star formation (Springel et al., 2005a; Bower et al., 2006; Best et al., 2007; Croton et al., 2006; Lagos et al., 2008; Somerville et al., 2008; Teyssier et al., 2011; Puchwein & Springel, 2013). While the

black hole accretion rate negatively influences the galaxy wide star formation rate, it is especially relevant to central star formation (Hopkins & Quataert, 2010). Although the detailed processes driving the intense nuclear activity are not fully understood (Steinborn et al., 2018), it is well established that mergers (see Section 1.4.3) and interactions with the intra-cluster medium (see Section 1.4.4) are able trigger AGN feedback. As the halo mass increases, the feedback effects associated with **gravitational heating**, i.e. the energy associated with the cosmological accretion of baryons into the dark matter halo (Dekel & Birnboim, 2008), become increasingly important: The gravitational energy released by baryons, which tend to condense at the bottom of the overall halo potential, leads to dynamical heating and decreases the star formation efficiency (Dekel & Birnboim, 2008; Khochfar & Ostriker, 2008; Johansson et al., 2009b).

1.4.3 Mergers

Galaxy mergers, i.e. the inelastic collision of two or more galaxies, are violent and extended ($\sim$ Gyr) events in a galaxy's evolution (Binney & Tremaine, 1987; Boylan-Kolchin et al., 2008). Early N-body models show that galaxy mergers are able to reproduce a wide array of observed morphological features, such as galactic tails and bridges (Toomre & Toomre, 1972; Barnes & Hut, 1986; Barnes & Hernquist, 1992; Hernquist, 1992, 1993). This was corroborated by observations when the connection between irregular galaxies and increased star formation was identified (Sanders et al., 1988; Melnick & Mirabel, 1990): The implication being that the process of merging may induce starbursts (Springel et al., 2005a). Indeed, it appears that, while mergers may temporarily increase star formation (Springel et al., 2005a; Rodríguez Montero et al., 2019; Baron et al., 2020), merger remnants are associated with quenched elliptical morphologies (see Figure 1.9) (Toomre, 1977; Schawinski et al., 2014).

Today it is well established that galaxy mergers can impact the star formation rate (SFR) of galaxies in diverse ways: Mergers have been found to increase (Rodríguez Montero et al., 2019; Baron et al., 2020), not impact (Pearson et al., 2019), and decrease (Wu et al., 2020) the SFR on varying timescales, depending on the details of the specific merger. Direct SFR impacting mechanisms associated with mergers include: introducing turbulence (Ellison et al., 2018), increasing disc instabilities (Lagos et al., 2019), triggering nuclear inflows via tidal interactions (Springel et al., 2005a; Goto et al., 2008), and gravitational heating (Johansson et al., 2009b). Meanwhile, more indirect, potentially merger triggered, mechanisms which impact the SFR include facilitating the central galactic black hole growth (Barai et al., 2014; Schawinski et al., 2014), thus potentially leading to strong AGN feedback (Hopkins et al., 2013), which can facilitate galactic gas removal (Barai et al., 2014), ultimately capable of suppressing star formation on long timescales (Yesuf et al., 2014). Luminous infrared galaxies appear to be characterised by starburst driven activity during the early merger stages, followed by composite starburst-AGN activity during intermediate merger stages, ending with AGN feedback either dominating (Yuan et al., 2010; Hopkins et al., 2013) or emerging (Calabrò et al., 2019) during late merger stages.

Mergers are typically associated with intermediate and lower density environments.

They are rare in higher density environments because galaxies in galaxy clusters have a high velocity dispersion (see Section 1.4.4 for more information on how galaxies in clusters interact) (Menci & Fusco-Femiano, 1996; Gnedin, 2003) and interacting galaxies require sufficiently slow relative velocities to merge (Binney & Tremaine, 1987). Mergers can be divided by considering various characteristics, including the number, gas content, and the relative masses of the involved galaxies. In this thesis, mergers are divided into three types according to the stellar mass fraction of the merging galaxies: Major (1:1 - 1:3), minor (1:3 - 1:10), and mini (1:10 - 1:100) mergers.

1.4.4 Galaxy clusters and environmental quenching

Galaxy clusters are the largest gravitationally bound structures in the observable Universe with total masses $M_{\rm tot} \geq 10^{14} - 10^{15}\,{\rm M}_{\odot}$ (Mohr et al., 1999). Their mass can be divided into three main components: First, the majority ($\sim 88\%$) of the total mass component within r_{200}, i.e. the radius encompassing an over-density 200 times larger than the critical density (see Section 1.2.1), consists of dark matter (see Section 1.2.2). Second, the X-ray emitting hot gas with temperatures $T \sim 10\,{\rm keV} \sim 10^{8}\,{\rm K}$ (Arnaud et al., 2005), i.e. the **intra-cluster medium** (ICM), contributes $\sim 10\%$ of the total mass (Biviano & Salucci, 2006). Third, the hundreds to thousands of galaxies, which are contained by an individual galaxy cluster, only make up $\sim 2\%$ of the total mass (Biviano & Salucci, 2006). Cosmological simulations find that, independent of the original formation environment, galaxies continuously move towards higher density regions (Springel et al., 2005b). This makes the cluster environment an integral part of galaxy evolution, as observations in multiple wavelengths provide insights into a fundamental and often terminal chapter of a galaxy's existence (Dressler, 1984).

Already in 1901, Wolf (1901) noticed that the galaxy population in clusters is different from the population at lower environmental densities, e.g. the field. Later, it was observationally shown (Figure 1.10) that a relation between the environmental density and the morphological galaxy type (see Section 1.3.1), i.e. the **morphology-density relation** for galaxies, exists (Dressler, 1980; Goto et al., 2003; Houghton, 2015): Figure 1.10 shows that spiral or irregular galaxies (S+Irr) are most abundant at low environmental densities, i.e. in the field, while elliptical galaxies (E) are more frequently found in increasingly dense environments, i.e. in groups and especially clusters. Meanwhile, cluster observations suggest that lenticular galaxies (S0) likely belong to an intermediate population of previously star-forming galaxies which have been transformed into passively evolving galaxies (Couch & Sharples, 1987; van Dokkum et al., 1998). As such, Figure 1.10 provides strong evidence for a morphological transformation from spiral to elliptical galaxies, driven by an increasing environmental density.

Galaxy clusters not only influence galactic morphology, but also greatly impact the star formation properties of galaxies in their vicinity (Boselli & Gavazzi, 2014). Due to **environmental quenching**, i.e. mechanisms whereby star formation is reduced by the surrounding environment (Peng et al., 2010, 2012), galaxies in clusters are far more likely to have reduced star formation, compared to field galaxies (Oemler, 1974; Butcher & Oemler,

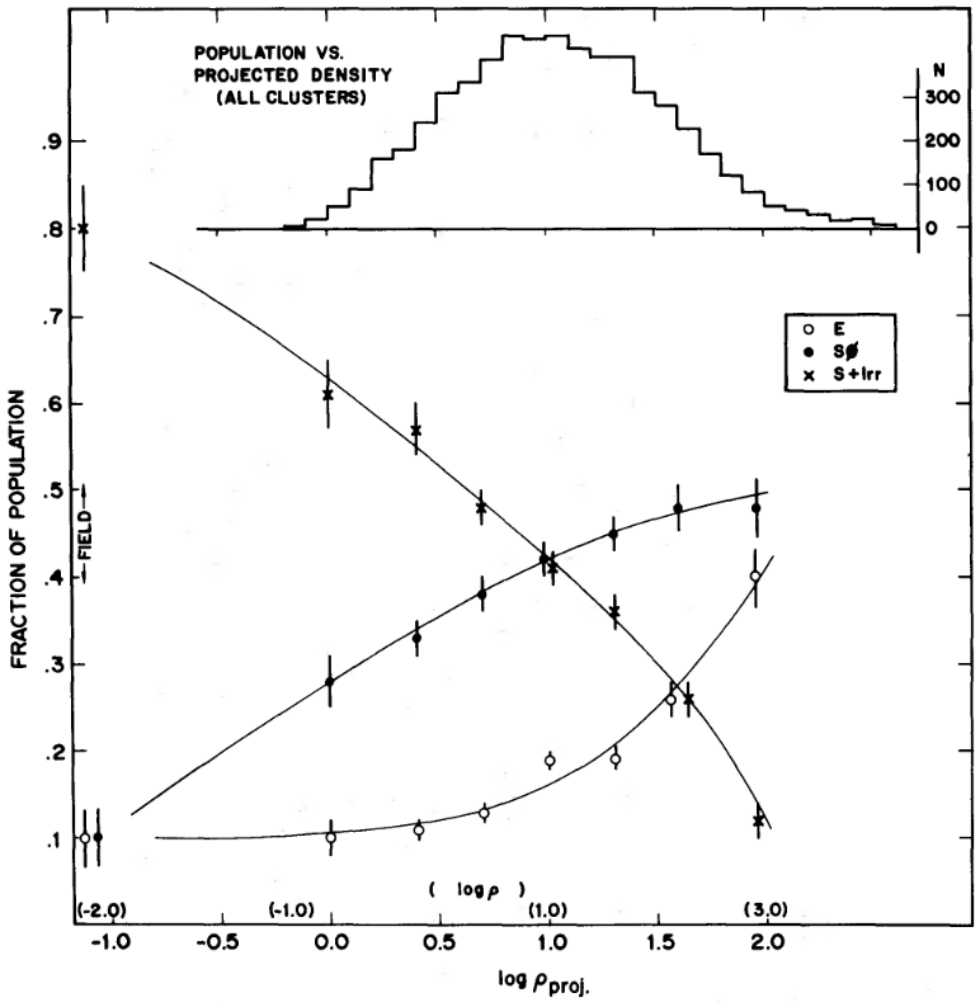

Figure 1.10: Fig. 4 taken from Dressler (1980). The morphology-density relation, i.e. the fraction of elliptical (E), lenticular (S0), and spiral and irregular (S+Irr) galaxies as a function of the logarithm of the projected density, in galaxies Mpc^{-2}. The upper histogram shows the number distribution of the galaxies over the bins of projected density.

1978; Dressler, 1980; Balogh et al., 1997).

One of the aims of current galaxy cluster research is to understand, quantify, and determine the regions in which quenching mechanisms act and how these contribute to galaxy evolution. Observations have established that galaxy cluster environments extend out to $2-3\,\mathrm{R_{vir}}$, much further than previously assumed (Balogh et al., 2000; Solanes et al., 2002; Verdugo et al., 2008; Braglia et al., 2009; Hansen et al., 2009; von der Linden et al., 2010; Wetzel et al., 2012). Computational research suggests that star formation quenching begins $2-3\,\mathrm{Gyr}$ prior to entering the inner cluster region (Zinger et al., 2018). This implies that galaxies are already partially quenched in the outskirts ($2-3\,\mathrm{R_{vir}}$) of the cluster while crossing the shock heated ($10^7 - 10^8\,\mathrm{K}$), X-ray emitting accretion shock region (Sarazin,

1988).

Several quenching mechanisms are under debate. Especially relevant to the outskirts of clusters are strangulation and pre-processing, that are both related to the hot gas halo enveloping a galaxy: **Strangulation** is the disruption of hot halo gas inflow to the inner (star-forming) galactic regions, leading to a cold gas deprivation within the galaxy and hence the quenching of star formation on long time scales (Larson et al., 1980; Weinmann et al., 2006; van den Bosch et al., 2008; Weinmann et al., 2009; von der Linden et al., 2010). Strangulation is typically associated with becoming a satellite of a larger system. During **pre-processing** the hot halo gas is removed prior to cluster infall, typically in groups in the outskirts of galaxy clusters (Bahé et al., 2012). In both these cases, this means that the hot gas halo is removed and/or heated prior to the cold gas within the galaxy (Larson et al., 1980; McCarthy et al., 2008; Bekki, 2009; Bahé et al., 2013). This implies that outside the inner cluster region the star-forming cold gas is not necessarily expelled or significantly heated, but rather the supply in the halo is affected and thus star formation dwindles due to a lack of replenishment via the galactic halo gas (Kawata & Mulchaey, 2008).

A shorter timescale quenching mechanisms acting in the inner cluster regions ($\lesssim 0.5\,\mathrm{R_{vir}}$), is **ram-pressure stripping** (Zinger et al., 2018): It is the process whereby the galactic (cold) gas is removed due to the external gas pressure P_{ram} exerted by the ICM becoming stronger than the galactic gravitational binding energy (Gunn & Gott, 1972).

$$P_{\mathrm{ram}} \approx \rho_{\mathrm{ICM}} \Delta v^2 \tag{1.13}$$

where ρ_{ICM} is the ICM density and Δv^2 is the three-dimensional galaxy velocity with respect to the cluster centre.

Generally, a typical spiral will be able to retain material within its plane if the force per unit area, i.e. the pressure P_{retain}, does not exceed (Gunn & Gott, 1972):

$$P_{\mathrm{retain}} = 2\pi G \sigma_{\mathrm{star}}(r) \sigma_{\mathrm{gas}}(r) \tag{1.14}$$

where $\sigma_{\mathrm{star}}(r)$ is the star surface density at a given radius and $\sigma_{\mathrm{gas}}(r)$ is the gas surface density on the disk at a given radius. Hence, ram-pressure stripping occurs when $P_{\mathrm{ram}} > P_{\mathrm{retain}}$. It also follows that ram-pressure becomes more efficient when a galaxy exposes more of its surface area to P_{ram}.

In addition to gas expulsion, ram-pressure may also compress gas into high-density clouds, leading to an enhancement of star formation (Tonnesen & Bryan, 2009; Vulcani et al., 2018, 2020b; Roberts & Parker, 2020). This compression and expulsion of cold gas in galaxies is best exemplified by jellyfish galaxies (also see Section 1.4.5). **Jellyfish galaxies** are gas rich galaxies that are undergoing gas stripping during infall on highly radial orbits via outside-in ram-pressure stripping, and are characterised by their optically-bright, i.e. star-forming, extended tails of expelled material (Poggianti et al., 2017; Sheen et al., 2017; Jaffé et al., 2018). In other words, while the onset of ram-pressure stripping may be associated with starbursts (Crowl et al., 2005; Vulcani et al., 2018, 2020b; Roberts & Parker, 2020), ram-pressure stripping ultimately leads to the (fast) quenching of galaxies (Quilis

et al., 2000; Vollmer et al., 2001). Interestingly, there is mounting observational evidence suggesting that jellyfish galaxies (George et al., 2019; Radovich et al., 2019; Poggianti et al., 2020), as well as cluster galaxies with recent bursts of star formation (Dressler & Gunn, 1983) host AGN (for details on AGN, see Section 1.4.2), which is corroborated by high resolution simulations (Ricarte et al., 2020). This surprisingly high incidence, compared to the general cluster and field population, suggests that ram-pressure stripping may trigger AGN feedback via nuclear gas inflow (Poggianti et al., 2017, 2020), thereby additionally suppressing star formation after a brief episode of enhancement (George et al., 2019). Following the cessation of star formation, jellyfish galaxies are often characterised as (cluster) post-starburst galaxies (Poggianti et al., 2016), a type of galaxy which is discussed in detail in Section 1.4.5.

Other environmental quenching mechanisms in galaxy clusters include harassment and tidal interactions. While the velocity dispersion of galaxies in galaxy clusters is too high for frequent mergers (Menci & Fusco-Femiano, 1996; Gnedin, 2003), galaxies do interact with each other. Specifically, (multiple) high speed encounters between galaxies, i.e. **galaxy harassment**, influence star formation and are able to drive strong morphological transformations in clusters, building the lenticular and elliptical galaxy population (Moore et al., 1996, 1998). Similarly, **tidal effects**, i.e. gravitational interactions between galaxies and between galaxies and the cluster potential, can lead to both dynamical heating and morphological transformation (Gnedin, 2003). In contrast to the hydrodynamically acting ram-pressure stripping, characterised by interactions with the ICM, harassment and tidal effects are governed by gravitational interactions, likely contributing to the morphological transformation of spiral to lenticular galaxies in clusters (Boselli & Gavazzi, 2006). Low redshift observations of galaxy clusters indicate that the short-timescale star formation quenching channel (e.g. ram-pressure stripping within and galaxy-galaxy interactions outside of the virial radius) contributes two times more than the long timescale one (e.g. strangulation) to the growth of the quiescent cluster population (Paccagnella et al., 2017).

1.4.5 Post-starburst galaxies

Post-starburst (PSB) galaxies, also referred to as E+A or k+a galaxies based on their absorption/emission lines, are characterised by a recent starburst and subsequent short timescale quenching of star-formation (Dressler & Gunn, 1983; Zabludoff et al., 1996; Dressler et al., 1999; Balogh et al., 1999; Caldwell et al., 1999). As such, they offer a unique opportunity to clarify some of the debated details of both the morphological (late- to early-type, see Section 1.3.1) and colour (blue cloud to red sequence, see Section 1.3.2) transition, which are fundamental to understanding galaxy evolution (Poggianti et al., 2009; Pawlik et al., 2016; Almaini et al., 2017; Davis et al., 2019; Wild et al., 2020; Matharu et al., 2020). Furthermore, PSBs are found in all environments and at all redshifts, suggesting the presence of physical processes of universal importance (Belloni et al., 1995; Zabludoff et al., 1996; Dressler et al., 1999; Tran et al., 2003; Wild et al., 2009; Yan et al., 2009; Vergani et al., 2010; Whitaker et al., 2012; Dressler et al., 2013; Wild et al., 2016; Pawlik et al., 2019). Their formation mechanism remains a matter of debate: Typically, PSBs

are assumed to have undergone a recent quenching event rather than gradual depletion, and thus they belong to a transition population between blue disc-like and red early-type galaxies (Davidge, 2008; Wilkinson et al., 2017; Aguerri et al., 2018; Davis et al., 2019).

Different pathways have been proposed to explain the observed strong increase of PSBs with redshift (Wild et al., 2009, 2016; Maltby et al., 2018; Pawlik et al., 2019; Belli et al., 2019) and the varying environmental abundance (Poggianti et al., 1999; Goto, 2005; Wild et al., 2009; Lemaux et al., 2017; Paccagnella et al., 2019) of PSBs. Wild et al. (2016) propose two PSB pathways: First, at $z \gtrsim 2$ PSBs are exclusively massive galaxies which formed the majority of their stars within a rapid assembly period, followed by a complete shutdown in star formation. Second, at $z \lesssim 1$ PSBs are the result of rapid quenching of gas-rich star-forming galaxies, independent of stellar mass. Possible candidates for this rapid quenching at $z \lesssim 1$ include the environment and/or gas-rich major mergers (Wild et al., 2016). More recent work by Maltby et al. (2018) suggests that the $z > 1$ PSB population is the result of a violent event, leading to a compact object, whereas the $z < 1$ population is able to preserve its typically disc-dominated structure, suggesting an environmental mechanism. At redshift $z \sim 0.8$, D'Eugenio et al. (2020) find evidence for a fast pathway associated with a centrally concentrated starburst. Galaxies at redshifts $z < 0.05$ appear to show evidence for three different pathways through the post-starburst phase, mostly occurring in intermediate density environments (Pawlik et al., 2018): First, a strong disruptive event (e.g. a major merger) triggering a starburst and subsequently quenching the galaxy. Second, random star formation in the mass range $9.5 < log(M_*/\mathrm{M}_\odot) < 10.5$ causing weak starbursts and, third, weak starburst in quiescent galaxies, resulting in a gradual climb towards the high mass end of the red sequence (Pawlik et al., 2018).

Despite ongoing arguments, simulations (Wilkinson et al., 2018; Davis et al., 2019) and observations (Schweizer, 1996; Zabludoff et al., 1996; Bekki et al., 2001; Yang et al., 2004; Bekki et al., 2005; Goto, 2005; Yang et al., 2008; Pracy et al., 2009; Wild et al., 2009; Meusinger et al., 2017; Pawlik et al., 2018) of PSBs in the local low density Universe generally show signs of or are consistent with recent galaxy-galaxy interactions and galaxy mergers. This is not surprising, as galaxy mergers can impact the star formation rate of galaxies in diverse ways (see Section 1.4.3). In particular, there is mounting evidence that PSB galaxies, which are associated with recent mergers, also host an AGN (Yuan et al., 2010; Baron et al., 2018; Calabrò et al., 2019; Baron et al., 2020). As established in Section 1.4.2, AGN are capable of depositing vast amounts of energy on short timescales, thereby rapidly shutting down star formation (Springel et al., 2005a). As such, AGN provide a promising explanation for the short timescale cessation of star formation observed in PSBs (Wild et al., 2020). However, the details of the mechanism(s) driving the nuclear activity in the centres of galaxies remains a major unsettled question (Steinborn et al., 2018): This is especially true for PSBs, with some studies suggesting that the AGN does not play a primary role in the initial quenching of the starburst, but rather, that it may be responsible for maintaining the post-starburst phase (Yesuf et al., 2014). It is likely that several mechanisms, dependent on the specific conditions (e.g. mass, redshift, environment), contribute to the short timescale ($< 1\,\mathrm{Gyr}$) quenching of PSBs (Vergani et al., 2010).

Characterising and tracking the change of the properties of (cluster) PSBs is instrumen-

tal in uncovering the relevant evolutionary processes. Quantifying the galactic evolution as a function of the environmental density allows the correlation between internal galactic properties (e.g. star formation, morphology, kinematics) and the specific impact of the immediate environment (see Section 1.4.4). As PSBs belong to a transition population, observations of cluster PSBs find evidence for varying morphological types (see Section 1.3.1) (Poggianti et al., 2009; Wilkinson et al., 2017; Aguerri et al., 2018; Davis et al., 2019). Observations of nearby clusters show that PSBs and star-forming cluster galaxies share many properties (Caldwell et al., 1996; Caldwell & Rose, 1997; Aguerri et al., 2018) and are characterised by similar distributions of environment (Hogg et al., 2006). Long-slit spectra observations of Coma cluster galaxies provide evidence for close kinematic similarities between star-forming and PSB galaxies, i.e. both appear to be rotating systems (Caldwell et al., 1996; Caldwell & Rose, 1997; Pracy et al., 2013). Indeed, (cluster) PSBs are often classified as spiral or lenticular galaxies (Poggianti et al., 2009; Aguerri et al., 2018). The similarity of PSB and disc galaxies is also evidenced by the shared exponential radial light profiles (Caldwell et al., 1996; Caldwell & Rose, 1997). Although cluster PSBs at low redshift appear to be more often associated with late-type morphologies, there is also evidence for low redshift early-type cluster PSB morphologies (Wilkinson et al., 2017). Meanwhile, cluster PSBs at higher redshift ($z \gtrsim 0.4$) are associated with both early-type (Pracy et al., 2010; Matharu et al., 2020) and late-type and irregular PSB morphologies (Belloni et al., 1995; Poggianti et al., 2009). Independent of redshift, cluster PSBs are consistently found along the transition between recently infallen star-forming later types and passively evolving early-type galaxies (Poggianti et al., 2009; Wilkinson et al., 2017).

The primary quenching mechanisms of cluster PSBs at low and intermediate redshift appear to be related to the ICM (Pracy et al., 2010; Paccagnella et al., 2017), as the proportion of PSB galaxies increases with the cluster velocity dispersion, i.e. cluster mass (see Section 1.4.4) (Poggianti et al., 2009; Paccagnella et al., 2019). Further evidence is provided by the fact that many cluster PSBs have been quenched outside-in, i.e. the outskirts reach undetectable levels of star formation prior the inner regions (Gullieuszik et al., 2017; Owers et al., 2019; Matharu et al., 2020; Vulcani et al., 2020a). Furthermore, cluster PSBs lack tidal tails (Pracy et al., 2010) and show no disturbances to their stellar light profiles, suggesting that the responsible quenching mechanism is solely related to the galactic gas component, excluding violent interactions such as mergers, harassment or tidal stripping (Matharu et al., 2020). In summary, the abundance of (rotating) disc-like morphologies, the increasing proportion of cluster PSBs with cluster mass, the outside-in quenching, and the lack of disturbances, all favour a scenario in which interactions with the ICM (e.g. ram-pressure stripping) shut down star formation in cluster PSBs.

Chapter 2

State-of-the-art simulations

Parts of this chapter have been published in Lotz et al. (2019) and Lotz et al. (2020).

2.1 Brief introduction to numerical simulations

We can observe the whole spectrum of galaxy evolution by studying the night sky. However, the collection of individual images, i.e. temporal frames or snapshots, are effectively static, compared to the lifetimes of Homo Sapiens. Furthermore, galaxy evolution (see Section 1.4) need not be linear. Thus, when observing the night sky, we are presented with a variety of correlated, yet individual, impressions of various stages of galaxy evolution. To test and expand our existing knowledge, numerical simulations provide an increasingly useful tool.

In brief, the method is typically characterised by the following steps: First, the current understanding of a given system (e.g. a chunk of the observable Universe or a galaxy) is codified into initial conditions. In cosmological simulations, these initial conditions are typically associated with the earliest observations, e.g. the density distribution derived from the baryonic acoustic oscillations imprinted in the cosmic microwave background (see Figure 1.2 and Section 1.2.3) (Springel et al., 2018). Second, the assumed temporal evolution is expressed by (idealised) formulae or approximations in the form of numerical models. The resulting simulations are then executed and subsequently compared with surveys at varying redshifts, e.g. the Sloan Digital Sky Survey (SDSS), Classifying Objects by Medium-Band Observations in 17 Filters (COMBO-17) survey or the Cosmic Evolution Survey (COSMOS) (York et al., 2000; Bell et al., 2004; Scoville et al., 2007). Additionally, cosmological simulations are constrained by global, redshift evolving, quantities such as the overall star formation rate of the Universe or the stellar mass density (Madau et al., 1996, 1998; Lilly et al., 1996; Dickinson et al., 2003). By evaluating the differences, a continuous refinement of our understanding is possible, leading to the improvement of models and, thus, providing an increasingly detailed picture of relevant processes. The work and conclusions presented in this thesis are based on these principles and are applied by using the *Magneticum Pathfinder* simulations (see Section 2.2).

With time and increasing technological progress, the complexity of numerical simula-

tions has increased significantly: Figure 2.1 shows the exponential growth of the number of resolution elements of different simulations as a function of time. To date, many different numerical approaches exist, each with its own specific strengths and weaknesses, tailored to different flavours (e.g. scale, environment, age) of the same question (Franco et al., 1994; Bodenheimer et al., 2006): How does the Universe (or parts of it) evolve?

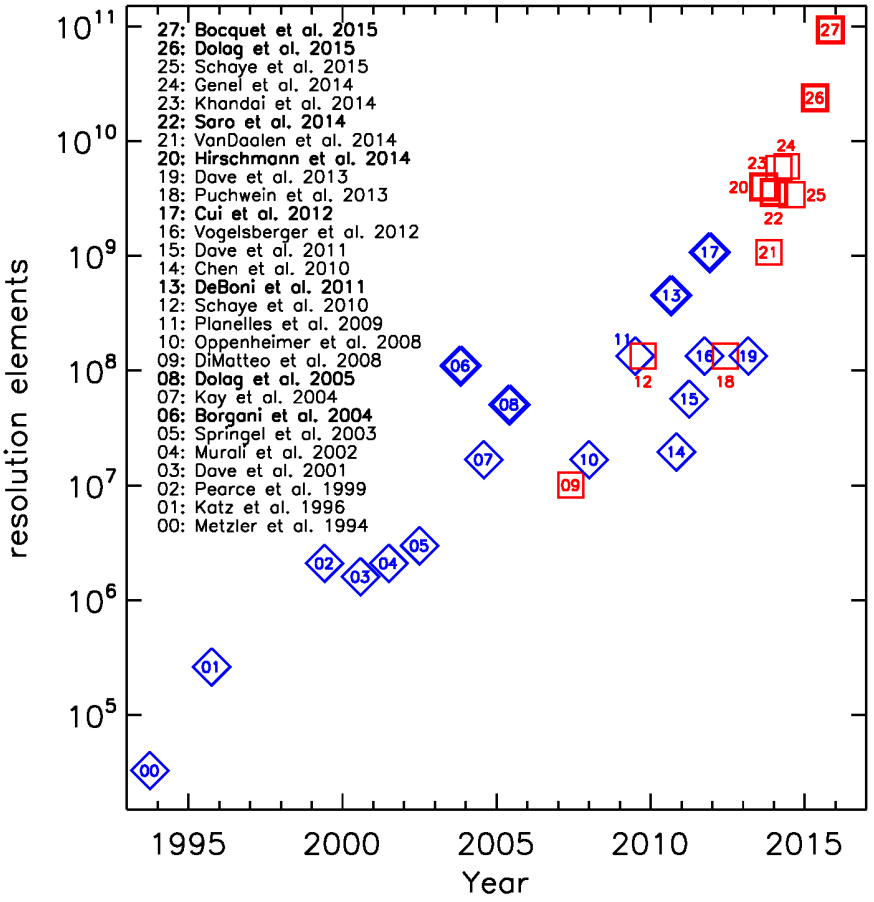

Figure 2.1: Exponential growth of the number of resolution elements of different simulations as a function of time. The red squares show simulations which have implemented active galactic nucleus feedback (AGN, see Section 1.4.2). The blue diamonds show simulations which have no implementation of AGN feedback. Courtesy of Klaus Dolag.

2.1.1 Treatment of the gravitational force

In order to calculate the gravitation force within self gravitating systems (e.g. N-body, SPH), the **softening length** is introduced: It is used to modify the gravitational force on orders smaller than the softening length ϵ. This is done to reduce the impact of large force

fluctuations as the distance between particles becomes smaller than ϵ (Dehnen, 2001). In other words, to avoid the divergence of the gravitational force on small scales, which is associated with the numerical treatment, i.e. the discretisation, the gravitational force is always calculated with a minimum separation. In practice, the Plummer distribution is used (Plummer, 1911) to modify the gravitational force $F(\boldsymbol{r})$ as follows

$$F(\boldsymbol{r}) = -G\frac{m_a m_b \boldsymbol{r}}{(r^2+\epsilon^2)^{3/2}} \tag{2.1}$$

where $\boldsymbol{r}$ marks the distance between the particle pair with masses m_a and m_b, G is the gravitational constant, and ϵ is the softening length (Price & Monaghan, 2007). The softening lengths of the *Magneticum Pathfinder* simulations, at different resolutions, are displayed in Table 2.1.

In practice, calculating the gravitational force between all particles, i.e. evaluating the direct sum, is too computationally expensive, as the computational effort scales quadratically $\mathcal{O}(N^2)$ with the number of particles N. Hence, codes typically approximate the calculation by one of the following methods:

- The **tree** approach groups particles into a hierarchical tree structure. The direct sum is typically only evaluated for close particles, while more distant particles are grouped together into 'pseudo-particles' within a tree structure, allowing an approximate calculation at a reduced computational cost, $\mathcal{O}(N \log N)$ (Barnes & Hut, 1986; Springel et al., 2001).

- The **particle mesh (PM)** approach converts the particle density distribution into a grid/mesh of density values and then applies the (discrete) Poisson equation (in Fourier space) (Dale, 2015).

- A variant of the PM approach is the **particle-particle-particle mesh ($\mathrm{P^3M}$)** method: To reduce the interpolation errors associated with the decreased spatial resolution due to the conversion onto a mesh, $\mathrm{P^3M}$ calculates the direct sum for particles below a characteristic separation (Hockney & Eastwood, 1988).

- The **Tree PM** approach is used by simulations, such as *Magneticum Pathfinder* (see Section 2.2), which are based on the code `GADGET-3` (Springel et al., 2001; Springel, 2005). Similarly, to $\mathrm{P^3M}$, the effect of distant gravitational forces is evaluated via a PM. Meanwhile, at shorter distances a tree approach is used.

2.1.2 Varying hydrodynamic approaches

Fundamentally, there are two distinct types and one intermediate type of numerical methods used in (cosmological) simulations. The three classes, i.e. grid, particle and moving mesh codes, all attempt to model the gaseous baryonic component of simulations (Bodenheimer et al., 2006; Dale, 2015). While calculating gravitational forces is relatively straightforward (see Section 2.1.1), hydrodynamics are required to describe the behaviour

of the fluid, i.e. gaseous, component of the Universe. The numerical approaches differ in the manner in which they approach the calculation of the behaviour of the gaseous component (Agertz et al., 2007): The **Eulerian** approach evaluates the fluid motion in reference to specific determined locations. In this frame of reference, the fluid flow between discrete regions is quantified, e.g. a grid is used and the flow is determined at each boundary (Landau & Lifshitz, 2013). In contrast, the **Lagrangian** approach follows a given discrete fluid element, e.g. a gas particle, as it moves through space and time (Souli & Benson, 2013).

Grid codes divide fluids into a grid, e.g. with fixed volume elements (Cen et al., 1990; LeVeque et al., 2002). In simplified terms, grid based codes compute the forces within each grid cell and then transfer the fluid across adjacent cells accordingly. While some codes maintain a constant grid, others adaptively refine the grid as necessary as a function of the desired resolution, which evolves with the system (Kravtsov et al., 1997; Teyssier, 2002). Figure 2.2 (left) shows a schematic representation of an **adaptive mesh refinement (AMR)** code with three levels of refinement. An example of such an implementation is provided by the cosmological simulation HorizonAGN (Dubois et al., 2016; Kaviraj et al., 2017) (see Figure 2.3), which is based on the AMR code `RAMSES` (Teyssier, 2002).

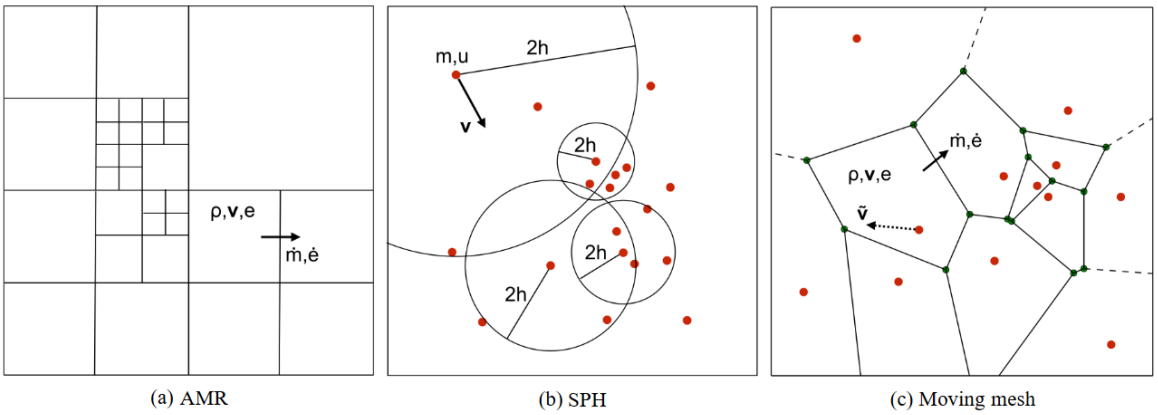

(a) AMR (b) SPH (c) Moving mesh

Figure 2.2: Fig. 1 taken from Dale (2015). Simple illustration of the ideas behind the major types of astrophysical hydrodynamic codes. The left panel shows an adaptive mesh refinement (AMR) representation of a fluid with only three levels of refinement. The gas in each cell has a density ρ, velocity v and internal energy e. Cells exchange mass, momentum and energy with their neighbours. The middle panel shows how a smoothed particle hydrodynamics (SPH) code represents a fluid, with red dots being individual particles carrying a mass m and specific internal energy u. Each particle has a velocity v and feels forces from other particles. Denser regions of gas are represented by higher concentrations of particles. The size of a particle is defined by the radius $2h$ which encloses a constant number of neighbours (here, only 4 for clarity). The right panel depicts a moving mesh code. The fluid mass is again represented by particles, shown as red dots, and the fluid volume is partitioned around these by a Voronoi tessellation (Crelle et al., 1908). Cells exchange matter, momentum and energy, but the particles move with the fluid flow.

In contrast to grid codes, **particle codes** discretise a fluid into individual mass elements, i.e. particles (Dale, 2015). The fluid is evolved by calculating the forces acting on each particle via an approximated sum over all particles (Price, 2012). Subsequently, the overall distribution is adjusted. First formulated by Gingold & Monaghan (1977) and Lucy (1977), **smoothed particle hydrodynamics (SPH)** is the most common particle code method implemented in astrophysics (Dale, 2015). Both the EAGLE (Schaye et al., 2015) and *Magneticum Pathfinder* simulations (see Figures 2.3 and 2.4) are based on variants of the N-body tree particle mesh SPH code `GADGET-3`, which is based on `GADGET-2` (Springel, 2005). The FIRE simulations are based on `GIZMO` (Hopkins et al., 2014) which incorporates a heavily modified version of `GADGET-3` (Springel, 2005). The SPH approach is discussed in greater detail in Section 2.2.1.

The third, most recent, approach is known as **moving mesh codes**, a hybrid of grid and particle codes (Springel, 2010a; Duffell & MacFadyen, 2011; Gaburov & Nitadori, 2011). Similarly to grid codes, moving mesh codes use a finite-volume method, however, the individual cells are partitioned using, e.g. Voronoi tessellation based on the particle distribution (Crelle et al., 1908; Hopkins, 2015). Consequently, the cells move and deform continuously as they follow the particle distribution (see comparison of left and right panel in Figure 2.2). For example, the Illustris(TNG) simulations (see Figure 2.3) (Vogelsberger et al., 2014; Nelson et al., 2018; Pillepich et al., 2018) are based on the moving mesh code `AREPO` (Springel, 2010a).

Overview of different simulations

Investigating galaxy evolution, especially in a cosmological context, is the aim of several independent studies. Figure 2.3 shows an overview of different *Magneticum Pathfinder* boxes (red square), as well as other cosmological (black circle) and isolated (blue triangle) state-of-the-art simulations. The simulations are displayed according to the simulation resolution given as the number of stellar particles in a Milky Way like galaxy ($M_{MW,*} = 5 \cdot 10^{10} M_\odot$ (McMillan, 2017)) as a function of the most massive halo within the simulation. The lower bound of the open horizontal lines marks the mass of halos which are resolved with at least 1000 stellar particles, while the upper bound is determined by the most massive halo in a given simulation. This depiction allows a facilitated comparison of different particle resolutions between simulations and shows the halo mass range in which the sub-grid physics is resolved. In other words, provided one is only interested in global galactic properties (e.g. galactic star formation rate), rather than details on galaxy scales or below (e.g. morphology), this resolution is beyond sufficient. The closed horizontal lines show the halo mass range of isolated or zoom-in simulations.

Figure 2.3 aptly illustrates that numerical simulations are always faced with a balancing act: One can either increase the number of resolution elements within a given system or one can increase the number of systems, which, due to hierarchical growth (Navarro et al., 1997), leads to more massive systems. In short, quality versus quantity. Ideally, one would want to populate the top right region in Figure 2.3. However, intermediate simulations already have computational costs of $\sim 10^7$ CPU hours. As such, trade-offs need to be made

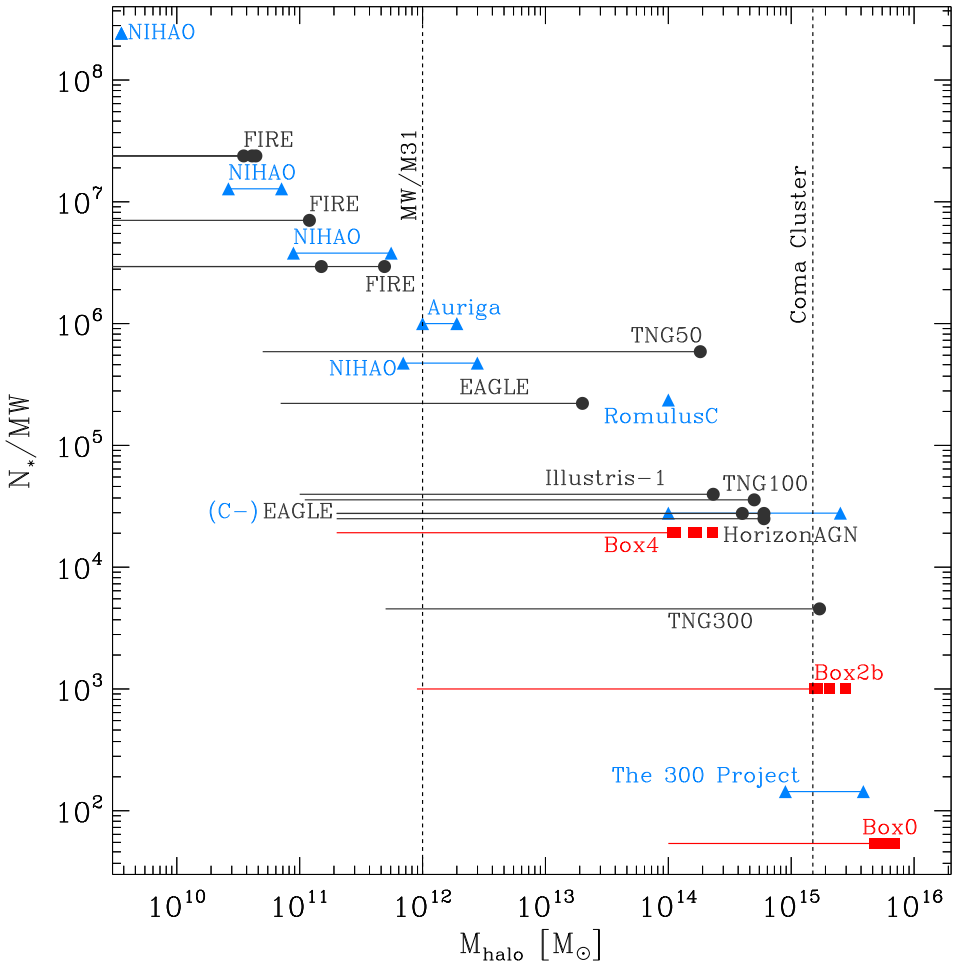

Figure 2.3: Simulation resolution in terms of stellar particles per Milky Way halo ($M_{MW,*} = 5 \cdot 10^{10} M_\odot$ (McMillan, 2017)) as a function of the most massive halo in different state-of-the-art simulations. The lower bound of the open horizontal lines marks the mass of halos which are resolved with at least 1000 stellar particles, while the upper bound is determined by the most massive halo in a given simulation. The closed horizontal lines show the halo mass range of isolated simulations. Red squares indicate different boxes from the *Magneticum Pathfinder* simulations. Black circles depict other cosmological simulations (FIRE (Hopkins et al., 2014; Chan et al., 2018), EAGLE (Schaye et al., 2015), Illustris (Vogelsberger et al., 2014), IllustrisTNG (Nelson et al., 2018; Pillepich et al., 2018), and HorizonAGN (Dubois et al., 2016; Kaviraj et al., 2017)). Blue triangles show high resolution isolated (zoom-in) projects (NIHAO (Wang et al., 2015), Auriga (Grand et al., 2017), RomulusC (Tremmel et al., 2019), C-EAGLE (Barnes et al., 2017), and The 300 Project (Arthur et al., 2019)). The dashed vertical lines indicate the halo mass of the Milky Way (MW) (McMillan, 2017) and Andromeda (M31) (Peñarrubia et al., 2014), as well as the mass of the Coma cluster (Kubo et al., 2007).

and each simulation is oriented towards specific problem sets.

2.2 *Magneticum Pathfinder* simulations

2.2.1 Smoothed particle hydrodynamics

As the *Magneticum Pathfinder* simulations are based on the N-body tree particle mesh SPH code `GADGET-3`, a more detailed discussion of SPH is in order. Generally, SPH aims to provide an answer to the general problem of how to compute the density based on an arbitrary distribution of point mass particles (Price, 2012). In other words, SPH attempts to solve the Poisson equation for gravity

$$\nabla^2\phi = 4\pi G\rho \tag{2.2}$$

where ϕ is the scalar gravitational potential, G is the gravitational constant, and ρ is the mass density at each point.

Figure 2.2 (middle) shows a schematic illustration of how the SPH approach works: SPH particles are not merely treated as point particles, rather their mass is smoothed over a spherical volume, with most mass concentrated close to the centre (Springel, 2010b). The characteristic radius over which this smoothing occurs is referred to as the **smoothing length** h: The smoothing length is continuously computed via iteration and is typically calculated to encompass, on average, a given number of neighbouring particles (four in Figure 2.2) (Monaghan, 2002; Springel & Hernquist, 2002; Price & Monaghan, 2007; Dale, 2015).

The density ρ at any given point $\boldsymbol{r}$ is calculated based on the weighted summation over neighbouring particles m_b as follows (Price, 2012)

$$\rho(\boldsymbol{r}) = \sum_{b=1}^{N_{\mathrm{neigh}}} m_b W(\boldsymbol{r} - \boldsymbol{r}_b, h) \tag{2.3}$$

where W is the weight function referred to as the **smoothing kernel**, which is computed using the smoothing length h. The choice of the smoothing kernel, which has units of inverse volume, determines the density estimate and, in order to conserve the total mass, must fulfil the following condition (Bodenheimer et al., 2006):

$$\int_V W(\boldsymbol{r'} - \boldsymbol{r}_b, h)\mathrm{d}V' = 1. \tag{2.4}$$

In addition, a smoothing kernel should be positive, decrease monotonically, have smooth derivatives, be symmetric, and have a central distribution which is not easily affected by small perturbations of the position of close neighbours (Price, 2012). Several functions exist that fulfil these criteria (Gingold & Monaghan, 1982; Monaghan & Lattanzio, 1985; Monaghan, 1992; Steinmetz & Mueller, 1993; Springel, 2005; Bodenheimer et al., 2006).

The *Magneticum Pathfinder* simulations use a sixth-order Wendland kernel (Dehnen & Aly, 2012), which considers 295 neighbours (Hirschmann et al., 2014).

Calculating the density as accurately and efficiently as possible is critical because the equations of motion may be derived entirely based on the density estimate (Price, 2012). This may be shown by rewriting the Lagrangian $L = T - V$, where T and V are the kinetic and (thermal) potential energy (Demtröder, 2017). In the case of a system of point masses with velocities $\boldsymbol{v} = d\boldsymbol{r}/dt$ and internal energy per unit mass $u(\rho, s)$, which may be expressed in terms of the density ρ and entropy s, the Lagrangian may be written as (Price, 2012):

$$L = \sum_b m_b \left[\frac{1}{2} v_b^2 - u_b(\rho_b, s, b) \right] \tag{2.5}$$

A number of benefits and limitations are associated with the SPH approach: SPH is numerically stable, has a simple implementation of sink particles (Dale, 2015), provides a continuous adaptive resolution, has truncation errors which are independent of the fluid velocity, couples trivially to N-body gravity schemes, exactly solves the particle continuity equation, and the equations of motion can be derived from the particle Lagrangian (Springel & Hernquist, 2002; Hopkins, 2015). However, by construction, the SPH equations of motion are inviscid (Cullen & Dehnen, 2010). To accurately describe the fluid behaviour an artificial viscosity needs to be introduced, e.g. to better model the rapid expansion and compression needed for the treatment of shocks (Hopkins, 2015). On a related note, SPH also introduces artificial pressure forces (see 'softening length' above) in regions with steep density gradients (Agertz et al., 2007), suppressing certain fluid mixing instabilities, such as the Rayleigh-Taylor or Kelvin-Helmholtz instability (Morris, 1996; Dilts, 1999; Ritchie & Thomas, 2001; Marri & White, 2003; Okamoto et al., 2003; Agertz et al., 2007). Generally, SPH is associated with the inexact treatment of sub-sonic turbulence (Kitsionas et al., 2009; Price & Federrath, 2010; Bauer & Springel, 2012; Sijacki et al., 2012).

For a more extensive review of SPH, including its benefits and limitations, refer to Price (2012).

2.2.2 Details of the *Magneticum Pathfinder* simulations

Magneticum Pathfinder is a set of large scale SPH simulations that employ a mesh-free Lagrangian method aimed at following structure formation on cosmological scales. An overview of the involved scales, from Gpc to kpc, is shown in Figure 2.4. The astrophysical processes modelled within the *Magneticum Pathfinder* simulations include, but are not limited to: cooling, star formation and winds (Springel & Hernquist, 2003), metals, stellar populations and chemical enrichment from AGB stars (Tornatore et al., 2003, 2006; Dolag et al., 2017), black holes and AGN feedback (Springel et al., 2005a; Hirschmann et al., 2014; Steinborn et al., 2015), anisotropic treatment (Arth et al., 2014) of thermal conduction (Dolag et al., 2004), low viscosity scheme to track turbulence (Dolag et al., 2005; Beck et al., 2016), higher order SPH kernels (Dehnen & Aly, 2012) and magnetic fields (passive)

(Dolag & Stasyszyn, 2009). For a more in-depth appreciation of the precise (baryonic) physical processes refer to Teklu et al. (2015).

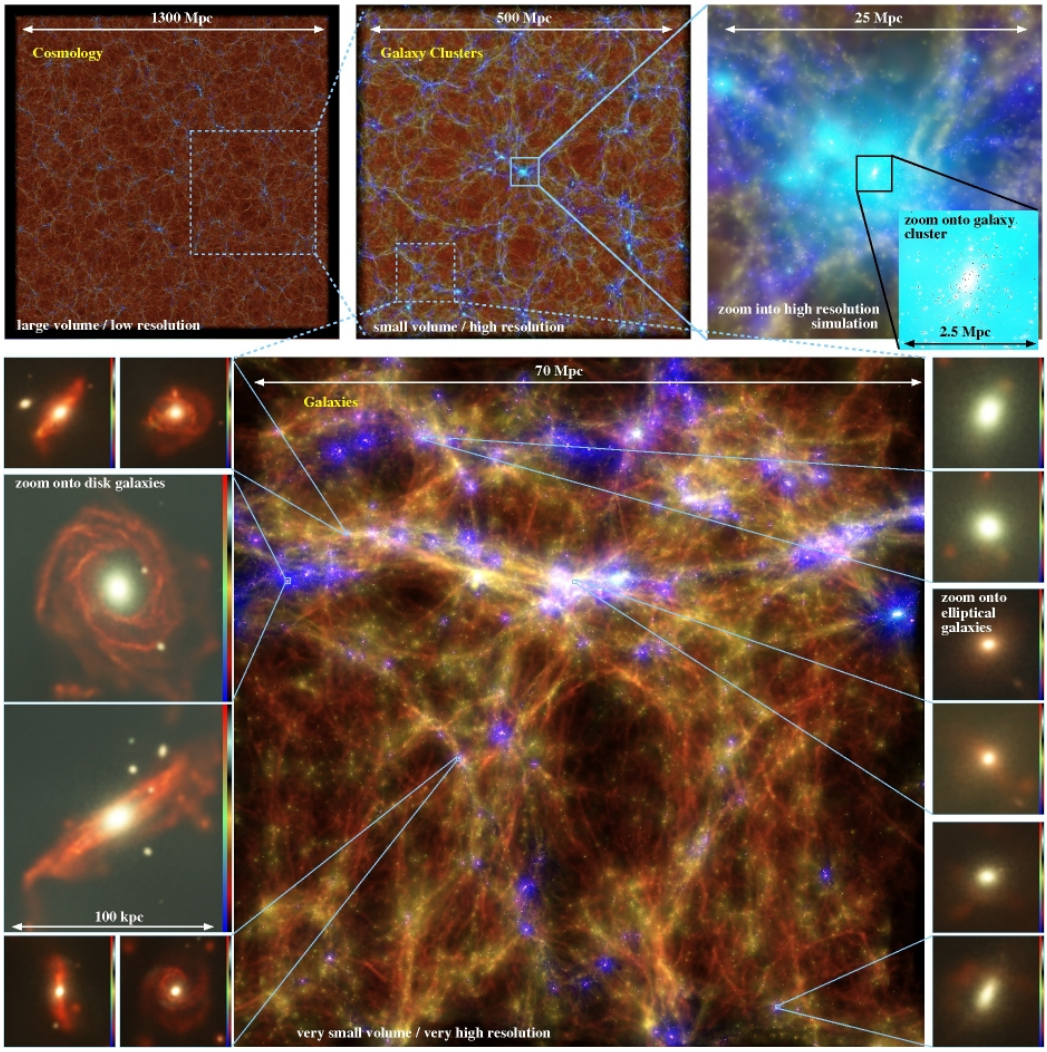

Figure 2.4: Combination of Fig. 1 and Fig. 2 taken from Teklu et al. (2015) and Hirschmann et al. (2014), respectively. Different boxes of *Magneticum Pathfinder* as an overview, zooming from the largest cosmological scales (top left), over intermediate scales (top centre), to galaxy cluster scales (top right). Main panel: Complete Box4/uhr at redshift $z = 0.5$. The left and right panels show examples of spiral and spheroidal galaxies, respectively. The top row is colour-coded according to stellar and gas density and the main panel is colour-coded according to the stellar age (left colour bars) and gas temperature (right colour bars). For more information see `http://www.magneticum.org`

In *Magneticum Pathfinder*, an updated version of the `SUBFIND` halo finder is used, which, in addition to dark matter, also evaluates the baryonic component (Springel et al., 2001; Dolag et al., 2009). Large structures, i.e. extended halos, are first identified via

a **friends-of-friends (FoF)** algorithm. For the FoF algorithm a linking length of 0.16 times the mean dark matter particle separation is used (Dolag et al., 2009). Each stellar and gas particle is associated with the nearest dark matter particle and ascribed to the corresponding FoF group, provided one exists, i.e. has at least 32 dark matter particles (Dolag et al., 2009). Thereafter, `SUBFIND` selects candidates for local substructures, i.e. **subhalos**, within the halo by identifying local over-densities (Dolag et al., 2009). The candidates are confirmed as substructure if a sufficiently large number of particles are gravitationally bound within the subhalo (Springel et al., 2001; Dolag et al., 2009).

As illustrated in Figure 2.4 and indicated in Table 2.1, the simulations range from Box0 (2688 Mpc/h) to Box5 (18 Mpc/h) with multiple levels of resolution ranging from gas particle masses with a medium resolution (mr) of $m_{\mathrm{gas,mr}} = 2.6 \cdot 10^9\, M_\odot/\mathrm{h}$ to extra high (xhr) resolutions of $m_{\mathrm{gas,xhr}} = 3.9 \cdot 10^5\, M_\odot/\mathrm{h}$, where h is the dimensionless Hubble parameter (see Equation 1.4). Relevant to the work presented in the following chapters are Box2/hr ($352\,(\mathrm{Mpc/h})^3$) and Box2b/hr ($640\,(\mathrm{Mpc/h})^3$). As the highlighted rows in Table 2.1 show, Box2/hr is comprised of $2 \cdot 1584^3$ particles, while Box2b/hr is comprised of $2 \cdot 2880^3$ particles. Both boxes are resolved at 'high resolution' (hr): Dark matter (dm) and gas particles have masses of $m_{\mathrm{dm}} = 6.9 \cdot 10^8\, h^{-1}\mathrm{M}_\odot$ and $m_{\mathrm{gas}} = 1.4 \cdot 10^8\, h^{-1}\mathrm{M}_\odot$, respectively. Stellar particles are formed from gas particles and have $\sim 1/4$ of the mass of their parent gas particle, depending on the specific mass evolution of the parent gas particle. At this resolution level, the softening (see Section 2.1.1) of the dark matter, gas and stellar particles is $\epsilon_{\mathrm{dm}} = \epsilon_{\mathrm{gas}} = 3.75\, h^{-1}\mathrm{kpc}$ and $\epsilon_{\mathrm{stars}} = 2\, h^{-1}\mathrm{kpc}$. Of these two boxes, Box2b is significantly larger, providing a far greater statistical sample of galaxies and galaxy clusters. However, due to storage constraints, fewer temporal snapshots of the larger Box2b are saved, compared to Box2/hr. Hence, Box2 has a higher temporal resolution, i.e. a greater number of snapshots are stored (Springel et al., 2001; Dolag et al., 2009). In practice, this means that Box2 is more suitable for evaluating the temporal evolution of objects, while Box2b enables large (static) statistical evaluations.

Both Box2 and Box2b have been used in the past to study various galaxy cluster properties: the intra-cluster light (ICL) - brightest cluster galaxy (BCG) connection in comparison to observations (Remus et al., 2017a), the effect of baryons on large scale structure (Bocquet et al., 2016; Castro et al., 2018), the intra-cluster-medium (ICM) and inter-galactic medium (IGM) (Dolag et al., 2015, 2017; Biffi et al., 2018) and active galactic nuclei (AGN) (Hirschmann et al., 2014; Biffi et al., 2018; Steinborn et al., 2018). Additionally, the *Magneticum Pathfinder* simulations have shown good agreement with a variety of observations, particularly regarding AGN properties (Steinborn et al., 2015, 2016), (dynamical) properties of galaxies (Remus et al., 2015; Teklu et al., 2015; Remus et al., 2017b; Forbes & Remus, 2018; van de Sande et al., 2019; Schulze et al., 2020; Harris et al., 2020) and galaxy cluster environments (Planck Collaboration et al., 2013; McDonald et al., 2014; Tanimura et al., 2020).

In order to differentiate between star-forming and quiescent galaxies within the simu-

Box	Size [Mpc/h]	Resolution level	N_{part}	$m_{\rm dm}$ [$\mathrm{M}_\odot/h$]	$m_{\rm gas}$ [$\mathrm{M}_\odot/h$]	$\epsilon_{\rm dm,gas}$ [kpc/h]	$\epsilon_{\rm stars}$ [kpc/h]
0	2688	mr	$2 \cdot 4536^3$	$1.3 \cdot 10^{10}$	$2.6 \cdot 10^9$	10	5
1	896	mr	$2 \cdot 1526^3$	$1.3 \cdot 10^{10}$	$2.6 \cdot 10^9$	10	5
2	352	mr	$2 \cdot 594^3$	$1.3 \cdot 10^{10}$	$2.6 \cdot 10^9$	10	5
		hr	$2 \cdot 1584^3$	$6.9 \cdot 10^8$	$1.4 \cdot 10^8$	3.75	2
2b	640	hr	$2 \cdot 2880^3$	$6.9 \cdot 10^8$	$1.4 \cdot 10^8$	3.75	2
3	128	mr	$2 \cdot 216^3$	$1.3 \cdot 10^{10}$	$2.6 \cdot 10^9$	10	5
		hr	$2 \cdot 576^3$	$6.9 \cdot 10^8$	$1.4 \cdot 10^8$	3.75	2
4	48	mr	$2 \cdot 81^3$	$1.3 \cdot 10^{10}$	$2.6 \cdot 10^9$	10	5
		hr	$2 \cdot 216^3$	$6.9 \cdot 10^8$	$1.4 \cdot 10^8$	3.75	2
		uhr	$2 \cdot 576^3$	$3.6 \cdot 10^7$	$7.3 \cdot 10^6$	1.4	0.7
5	18	hr	$2 \cdot 81^3$	$6.9 \cdot 10^8$	$1.4 \cdot 10^8$	3.75	2
		uhr	$2 \cdot 216^3$	$3.6 \cdot 10^7$	$7.3 \cdot 10^6$	1.4	0.7
		xhr	$2 \cdot 576^3$	$1.9 \cdot 10^6$	$3.9 \cdot 10^5$	0.45	0.25

Table 2.1: Overview of the *Magneticum Pathfinder* suite of simulations. The work presented in the following chapters is based on the highlighted rows. From left to right: (1) Box number, (2) Box size, (3) Resolution level, where mr, hr, uhr, xhr are abbreviations for medium, high, ultra high, and extra high resolution, (4) Number of particles, (5) Mass of a dark matter (dm) particle, (6), Mass of a gas particle, (7) Softening (see Section 2.2.1) for dark matter and gas particles, (8) Softening for stellar particles. Stellar particles are formed from gas particles and receive $\sim 1/4$ of the gas particle mass. For more information see `http://www.magneticum.org`

lation, we consider the specific star formation rate (SSFR)

$$\mathrm{SSFR} = \frac{\mathrm{SFR}}{M_*} \tag{2.6}$$

where the galactic star formation rate (SFR) is given in units of solar masses per year and M_* is the stellar mass of the galaxy in solar masses. We follow the criterion introduced by Franx et al. (2008) and define star-forming galaxies as

$$\mathrm{SSFR} \cdot t_{\rm H} \geq 0.3 \tag{2.7}$$

where $t_{\rm H}$ is the redshift evolving Hubble time

$$t_{\rm H} = 1/H(t) \tag{2.8}$$

where $H(t)$ is the Hubble parameter (see Equation 1.5) calculated at a given redshift. Conversely, quiescent galaxies are defined as (Franx et al., 2008):

$$\mathrm{SSFR} \cdot t_{\rm H} < 0.3 \tag{2.9}$$

Importantly, this **blueness criterion** presented in Equation 2.7 is time dependent, rather than merely being applicable to low redshifts. Hence, this definition encompasses the changing star formation history on a cosmological scale and is well suited to evaluate and compare galaxies at different redshifts. With this criterion, the Milky Way, for example, would have $\mathrm{SSFR} \cdot t_\mathrm{H} \sim 0.4$ at $z = 0$ and, hence, be considered star-forming (Licquia & Newman, 2015).

Throughout this thesis we use different scaling radii, velocities and masses. To avoid confusion, we clarify the different definitions used: When solely presenting results from *Magneticum Pathfinder* we scale according to the virial radius r_vir and virial mass M_vir as outputted by `SUBFIND`, which calculates the virial radius and the mass therein via a top-hat spherical collapse model (Eke et al., 1996). When comparing to observations, we reproduce the prescription the observations use. In practice there are two relevant observational scaling definitions: First, we use $R_\mathrm{200,crit}$, i.e. the radius encompassing an over-density 200 times larger than the critical density, and the mass $M_\mathrm{200,crit}$ (see Section 1.2.1). Second, we use $R_\mathrm{200,mean}$ and $M_\mathrm{200,mean}$, which are defined analogous to the above but using the mean background matter density rather than the critical density. Depending on the specific radius r the mass M therein may be calculated, thereby enabling the calculation of the associated characteristic (virial) velocity v via the virial theorem: $v = \sqrt{GM/r}$. To avoid confusion between 2D and 3D radii, we use R to indicate the former and r to indicate the latter.

In this thesis the WMAP-7 cosmological parameters are adopted (Komatsu et al., 2011): $h = 0.704$, $\Omega_M = 0.272$, $\Omega_\Lambda = 0.728$ and $\Omega_b = 0.0451$. When comparing to observations the h value is adjusted accordingly.

Chapter 3

Gone after one orbit: How cluster environments quench galaxies

This chapter has been published in Lotz et al. (2019).

Abstract

The effect of galactic orbits on a galaxy's internal evolution within a galaxy cluster environment has been the focus of heated debate in recent years. To understand this connection, we use both the $(0.5\,\mathrm{Gpc})^3$ and the Gpc^3 boxes from the cosmological hydrodynamical simulation set *Magneticum Pathfinder*. We investigate the velocity-anisotropy, phase space, and the orbital evolution of up to $\sim 5 \cdot 10^5$ resolved satellite galaxies within our sample of 6776 clusters with $M_{\mathrm{vir}} > 10^{14}\,\mathrm{M}_\odot$ at low redshift, which we also trace back in time. In agreement with observations, we find that star-forming satellite galaxies inside galaxy clusters are characterised by more radially dominated orbits, independent of cluster mass. Furthermore, the vast majority of star-forming satellite galaxies stop forming stars during their first passage. We find a strong dichotomy both in line-of-sight and radial phase space between star-forming and quiescent galaxies, in line with observations. The tracking of individual orbits shows that the star-formation of almost all satellite galaxies drops to zero within 1 Gyr after infall. Satellite galaxies that are able to remain star-forming longer are characterised by tangential orbits and high stellar mass. All this indicates that in galaxy clusters the dominant quenching mechanism is ram-pressure stripping.

3.1 Data sample

Galaxies are divided into star-forming and quiescent galaxies according to the 'blueness criterion' presented in Equation 2.7. Generally, relevant details of the Magneticum simulation are discussed in Section 2.2.2. For both Box2 and Box2b and all redshifts satellite galaxies in this chapter are selected to have a minimum stellar mass of $M_* = 3.5 \cdot 10^9\, h^{-1}\mathrm{M}_\odot$, corresponding to a minimum of ~ 100 stellar particles for a given galaxy. We choose this threshold since it implies that the galaxy has had enough gas to successfully produce a minimum stellar component.

Throughout this chapter we use different scaling radii, velocities and masses. To avoid confusion, we clarify the different definitions used: When solely presenting results from *Magneticum Pathfinder* we scale according to the virial radius r_{vir}, virial velocity v_{vir}, and virial mass M_{vir}. The virial radius is calculated via a top-hat spherical collapse model (Eke et al., 1996). When comparing to observations, we reproduce the prescription the observations use. In practice there are two relevant scaling definitions: First, we use $R_{200,\mathrm{crit}}$, i.e. the radius encompassing an over-density 200 times larger than the critical density, $v_{200,\mathrm{crit}}$, and $M_{200,\mathrm{crit}}$. Second, we use $R_{200,\mathrm{mean}}$, $v_{200,\mathrm{mean}}$, and $M_{200,\mathrm{mean}}$, which are defined analogous to above but using the mean background matter density rather than the critical density. To avoid confusion between 2D and 3D radii, we use R to indicate the former and r to indicate the latter.

3.1.1 Observational comparison with CLASH

The CLASH survey observes 25 massive galaxy clusters with the Hubble Space Telescope's panchromatic imaging equipment (Wide-field Camera 3, WFC3, and the Advanced Camera for Surveys, ACS) (Postman et al., 2012; Mercurio et al., 2014). One of four primary science goals of CLASH is the study of internal structure and galaxy evolution within and behind the clusters. Thus, it provides an interesting data set to compare with the Magneticum simulation. The CLASH cluster under consideration (MACS J1206.2-0847) is located at a redshift of $z = 0.44$. The cluster hosts 590 identified members obtained at the ESO VLT (Rosati et al., 2014) and has a mass of $M_{200} = (1.4 \pm 0.2) \cdot 10^{15}\,\mathrm{M}_\odot$ with a concentration of $c_{200} = 6 \pm 1$ (Biviano et al., 2013). The data was obtained by the VLT/VIMOS large program, which aims at constraining the cluster mass profile over the radial range of 0-2.5 virial radii.

Studies regarding the velocity-anisotropy include Biviano & Poggianti (2009); Munari et al. (2014); Annunziatella et al. (2016); Biviano et al. (2016). However, they did not investigate the difference between star-forming and quiescent galaxies at the level of detail as demonstrated by Biviano et al. (2013), especially regarding the confidence regions of the populations. The cluster MACSJ1206.2 − 0847 is to date the only CLASH cluster for which the velocity-anisotropy was calculated for both passive and star-forming galaxies. The velocity-anisotropy profiles calculated in Biviano et al. (2016) from the GCLASS survey at $z \sim 1$ have such large confidence regions that a wide range of profiles are encompassed by said regions.

3.2 Velocity-anisotropy Profiles

The goal of parametrising and comparing objects through the use of the velocity-anisotropy β is to gain an understanding of the relative importance of different degrees of freedom, i.e. comparing the preference for tangentially versus radially dominated orbits. The premise being that if a population is dominated by tangential or radial movement the dispersion in the respective degree of freedom will be larger. The velocity-anisotropy is defined as follows (Binney & Tremaine, 1987):

$$\beta \equiv 1 - \frac{\sigma_t^2}{\sigma_r^2}, \tag{3.1}$$

$$\text{with } \sigma_t^2 = \frac{\sigma_\theta^2 + \sigma_\phi^2}{2}. \tag{3.2}$$

where σ_r, σ_t, σ_θ and σ_ϕ parametrise the velocity dispersions in the radial, tangential, θ and ϕ direction respectively. The degree of (an)isotropy is studied providing information on whether the galaxies are moving on radial ($\beta > 0$), tangential ($\beta < 0$) or isotropic ($\beta = 0$) orbits.

The velocity-anisotropy parameter β is binned into equal distance radial differential bins. It is calculated for the total, the star-forming, and the quiescent satellite galaxy population separately. The error associated with the calculation of β is derived via bootstrapping and error bars correspond to the 1σ confidence interval.

3.2.1 CLASH comparison

The velocity-anisotropy, when obtained via observations, is calculated through the inversion of the Jeans equation. This is motivated by the fact that velocities and, thus, dispersions can only be observed along the line-of-sight (LOS). For the $\beta(r)$ and LOS comparison between Magneticum and the CLASH cluster MACSJ1206.2 − 0847, simulated clusters are selected above a mass threshold of $M_{200,\text{crit}} > 5 \cdot 10^{14} \text{M}_\odot$. In order to provide a large statistical sample, both Box2 and Box2b were taken into account. We use only clusters at a redshift of $z = 0.44$, resulting in 15 clusters for Box2 and 71 for Box2b. The velocity-anisotropy comparison is done by considering a sphere around Magneticum clusters, whereas the LOS phase space comparison in Section 3.3 considers a cylinder of height 89.4Mpc, corresponding to the velocity range of cluster members (Biviano et al., 2013). To increase the statistical sample of the LOS phase space analysis, we considered the projection along three independent spatial axes.

Figure 3.1 shows the radial β-profiles for the stacked Magneticum clusters and the CLASH cluster MACS J1206.2-0847. The top panel depicts the total population both from Magneticum (solid line) and Biviano et al. (2013) (dashed line). The bottom panel displays the quiescent (red) and star-forming (blue) populations for Magneticum (solid lines) and the CLASH cluster (dashed lines), with the shaded region representing the 1σ confidence zone of the observations. The vast majority of points lie within each other's 1σ

error regions and bars, respectively. In addition, the global behaviour of the observations is reproduced by the Magneticum profiles for both the star-forming and quiescent populations. Considering that the observations are based on a single cluster with 590 members, while Magneticum utilises 86 clusters to derive its statistics at $z = 0.44$, the results are in good agreement.

As can be clearly seen in Figure 3.1 from both simulations and observations, the anisotropy profile increases with increasing radius. This indicates that the outskirts are more radially dominated than the inner regions of the clusters. Iannuzzi & Dolag (2012) show that of all the galaxies entering a galaxy cluster at a certain time, those that will survive until redshift zero are those characterised by the most tangential orbits at infall. This indicates that longer galaxy cluster membership increases the likelihood of circular obits. Given that smaller radii are associated with a higher probability of long-term cluster membership, the anisotropy profile decreases towards smaller radii.

Intuitively one might assume that the accretion of radially in-falling galaxies leads to more radially dominated orbits of the total population with time, rather than the identified tendency towards isotropy. However, the in-falling population makes up less and less of the total population as time proceeds. In addition, the most radially dominated in-falling galaxies are likely to experience strong tidal stripping by the BCG, thus falling below our resolution limit and consequently no longer contributing to the $\beta(r)$ profiles (Annunziatella et al., 2016).

Figure 3.1 also clearly shows a difference between the star-forming and quiescent population. The star-forming population is more radially dominated than its quiescent counterpart. This suggests that the star-forming population is more infall dominated, as will be further shown in Section 3.3.2. Subsequently, it is likely that the star-forming galaxies belong to a younger population of a given cluster, since they are more removed from isotropy ($\beta = 0$).

Figure 3.1 also shows that the total population (black solid line) is dominated by the quiescent population (red solid line). This is accentuated by the fact that the black and red lines are exceedingly similar. Only a small sample of galaxies are star-forming, with the bulk of clusters being made up of quiescent galaxies, with regard to our star-formation criterion.

The main source of error of the observational calculations are the uncertainties associated with the line-of-sight dispersion. The observational confidence zones depicted in Figure 3.1 are calculated through modifications of the beta profile. These modifications are then inverted to yield a wide grid of predicted line-of-sight velocity dispersion profiles (van der Marel, 1994). This reversed method is employed because error propagation through the Jeans inversion is infeasible (Biviano et al., 2013).

Although the observational method to evaluate $\beta(r)$ is sophisticated, issues remain. For one, the entire calculation of the velocity-anisotropy profiles hinges on the fiducial mass profile. The NFW profile, which was assumed and fitted, can be the source of large errors. Depending on the true nature of the mass profile, the NFW fit by Umetsu et al. (2012) does not necessarily fit well along the entire profile. This is especially significant at large and small radii, where the deviations from the NFW profile are likely to be largest. The

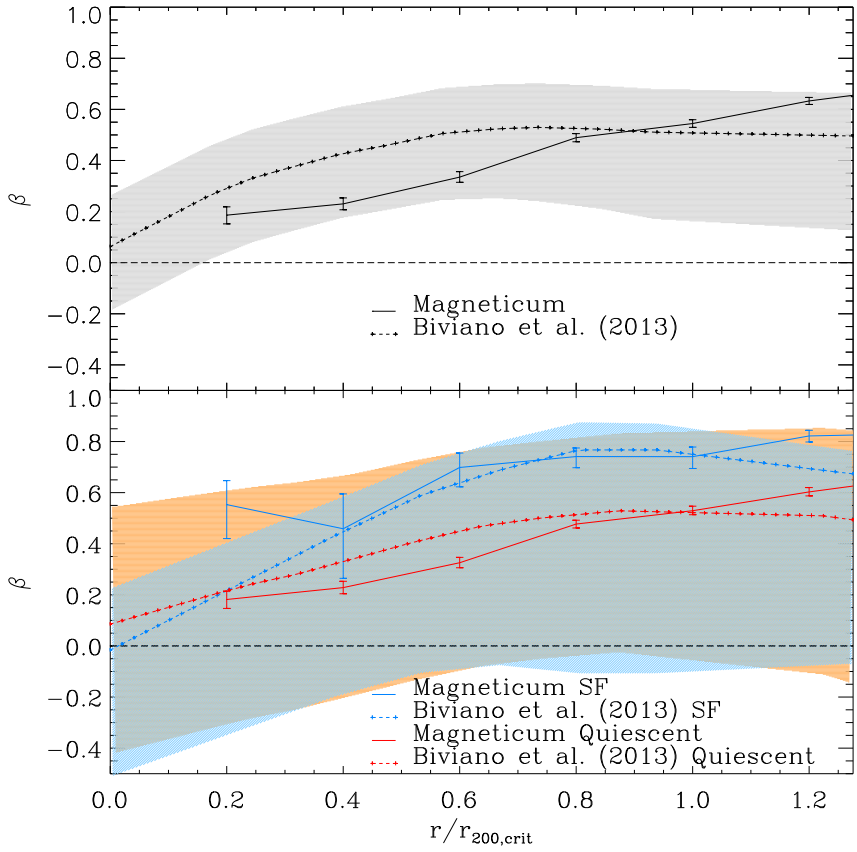

Figure 3.1: Box2 and Box2b differential 3D radial profiles of velocity-anisotropy parameter at $z = 0.44$ of clusters with mass threshold $M_{200,\mathrm{crit}} > 5 \cdot 10^{14}\,\mathrm{M}_{\odot}$. Solid lines describe the selected clusters from the Magneticum simulation, while the dashed lines describe the CLASH observations extracted from Biviano et al. (2013). Top panel: total galaxy population profile. Bottom panel: star-forming (blue) and quiescent (red) population profiles. Shaded regions correspond to the 1σ confidence zone of the respective observations. The horizontal dashed line indicates an isotropic velocity distribution. Values greater than $\beta = 0$ correspond to more radial orbits, while negative values represent tangentially dominated orbits.

error on quantities like the concentration $c_{200} = 6 \pm 1$ of the observed cluster are large and, hence, the fitted NFW profile could easily not accurately describe the actual mass profile (Biviano et al., 2013).

Additionally, interlopers have a potentially major impact on the observationally based calculations of the anisotropy profile. Given solely the line-of-sight velocity, it is virtually impossible to conclusively attribute a galaxy to an individual radial bin of a cluster. Subsequently, the calculation of the observed anisotropy profile will always be subject to inaccuracies. For example, the galaxies in the CLASH cluster (MACS J1206.2-0847) compared to in Figure 3.1 are not distributed spatially isotropically (Umetsu et al., 2012). This

impedes the identification of interlopers further, making their effect less predictable. In contrast, the Magneticum profiles depicted in Figure 3.1 are the result of the construction of an exact sphere, which evaluates each radial shell. As expected by construction, when using the Clean membership identification algorithm (Mamon et al., 2013), which has been used for several observational data-sets already (e.g. Biviano et al. (2013, 2017); Cava et al. (2017)), we found a negligible impact by interlopers on our results.

In addition, ambiguity in the definition of the star-formation criterion gives rise to different categorisations of galaxies. The observers utilise colour-colour diagrams to identify star-forming and quiescent galaxies (Mercurio et al., 2014). In contrast, the criterion applied in the data reduction of the simulation considers the specific star-formation rate in dependence of redshift. This, however, does not account for recently formed stars, which impact the classification on the colour-colour diagram. As such, our star-formation criterion might underestimate the amount of star-forming galaxies compared to observations. As a result, quenching timescales are likely underestimated, too.

While observations of the CLASH cluster and the results from the Magneticum simulations are in very good agreement, there exist both simulations and observations that report opposite trends for quiescent and star-forming satellite populations: Both the Millennium Simulation (Iannuzzi & Dolag, 2012) and observations of the galaxy cluster Abell 85 (Aguerri et al., 2017) find that the quiescent population is characterised by more radially dominated orbits relative to the star-forming population. However, the Millennium Simulation is a DM-only simulation. When searching for clusters with radially dominated orbits for quiescent satellites within the Magneticum simulation, we find a small number of clusters. Specifically, only 28 of the 495 most massive clusters ($h^{-1}M_{200,crit} > 10^{14}\,\mathrm{M}_\odot$), i.e. 5.7 per cent in Box2, were identified as having a more radially dominated quiescent population than was the case for the star-forming population. However, the vast majority of these clusters have extremely low (star-forming) galaxy numbers. We conclude that clusters matching the behaviour reported by Iannuzzi & Dolag (2012) and observed by Aguerri et al. (2017) are rare in the Magneticum simulation, albeit they do exist.

3.2.2 Quenching fractions

To investigate the difference between star-forming and quiescent satellite galaxies further, we explore the impact of stellar mass and host halo mass on the fraction of quenched satellite galaxies. The quenched fraction is defined as the number of quenched satellite galaxies over the total number of satellite galaxies. Figure 3.2 shows the quenched fraction of satellite galaxies split into four different stellar mass intervals in the range of $\log(M_*/\mathrm{M}_\odot) = [9.7, 11.3]$ in dependence of their host halo mass at $z = 0.066$. It compares the Box2 results (solid lines) to observations by Wetzel et al. (2012) (dashed lines) at $z = 0.045$.

Wetzel et al. (2012) use galaxy group/cluster catalogues from the Sloan Digital Sky Survey Data Release 7 (SDSS DR7) with an overall median redshift of $z = 0.045$. Wetzel et al. (2012) consider $\sim$ 19000, 2200, 160 groups with $M_{200,\mathrm{mean}} > 10^{12}, 10^{13}, 10^{14}\,\mathrm{M}_\odot$, respectively, up to the most massive group at $10^{15}\,\mathrm{M}_\odot$ hosting 269 satellites. The employed

catalogue allows the examination of satellites with good statistics in the stellar mass range $M_* = 5 \cdot 10^9 - 2 \cdot 10^{11}\,\mathrm{M}_\odot$.

By considering the stellar mass evolution at fixed halo mass and and the halo mass evolution at fixed stellar mass Figure 3.2 offers a number of insights into environmental quenching dependencies: First, the Magneticum simulation matches the observed increase in the fraction of quenched satellite galaxies with host halo mass, accurately describing the environmental impact on quenching. Second, it also reproduces an increase in quenched fraction with increasing stellar mass, accurately describing the impact of galactic feedback mechanisms on star-formation. Third, a difference in the fraction of quenched satellite galaxies in the stellar mass range of $\log(M_*/\mathrm{M}_\odot) = [10.5, 10.9]$ exists between Magneticum and the observations by Wetzel et al. (2012). Although there exists the discrepancy in the intermediate to high stellar mass range, overall the behaviour is in agreement.

The gap between the two stellar mass ranges $\log(M_*/\mathrm{M}_\odot) = [10.1, 10.5]$ (green) and $\log(M_*/\mathrm{M}_\odot) = [10.5, 10.9]$ (orange) suggests that the quenching of satellite galaxies in the Magneticum simulations is characterised by a strong stellar mass bimodality. Further it suggests that if the stellar mass is below $\log(M_*/\mathrm{M}_\odot) \sim 10.5$ satellite galaxies have a far lower probability of being quenched, while the opposite is true above this stellar mass threshold. The bimodality is strongest at lower host halo masses, implying that the quenching is not a result of the environment, but rather a self-regulatory behaviour, i.e. AGN feedback kicking in at a specific stellar mass as dictated by the implemented feedback model.

In contrast to the Magneticum results, the observations find a flattening in the stellar mass range of $\log(M_*/\mathrm{M}_\odot) = [9.7, 10.5]$ at high host halo masses. The flattening of the observations is likely driven by the incompleteness of the SDSS in the high halo mass regime. As the SDSS median redshift is $z = 0.045$, high host halo mass objects are rare (Wetzel et al., 2012). Consequently, the Magneticum results provide a far more complete sample, especially in the high host halo mass regime compared to the observations.

Figure 3.2 also displays the increasing impact of environmental quenching on lower stellar mass satellite galaxies. Below $\log(M_*/\mathrm{M}_\odot) \sim 10.5$ the quenched fraction of Magneticum results increases strongly with host halo mass, implying a strong environmental dependence. In the higher stellar mass range, $\log(M_*/\mathrm{M}_\odot) \gtrsim 10.5$, only a small host halo mass dependence is found. This is likely due to high stellar mass halos being quenched by feedback processes triggered by the strong mass growth, while low stellar mass satellites are more vulnerable to environmental quenching, lacking strong galactic feedback mechanisms inhibiting star-formation. A similar stellar mass dependence is found in the observations by Wetzel et al. (2012), however, the critical stellar mass threshold is $\log(M_*/\mathrm{M}_\odot) \sim 10.9$.

As described in Section 3.2.1, we expect Magneticum to overestimate the amount of quenched satellite galaxies due to the blueness criterion evaluating the SSFR rather than the colour of satellite galaxies. In contrast, Wetzel et al. (2012) find that an average of 10 per cent of galaxies have been misassigned and state that the primary resultant bias is an underestimation of the quenched fraction for satellites. Therefore, a part of the discrepancy in Figure 3.2 is likely the result of an overestimation on part of the simulation and an underestimation on part of the observations.

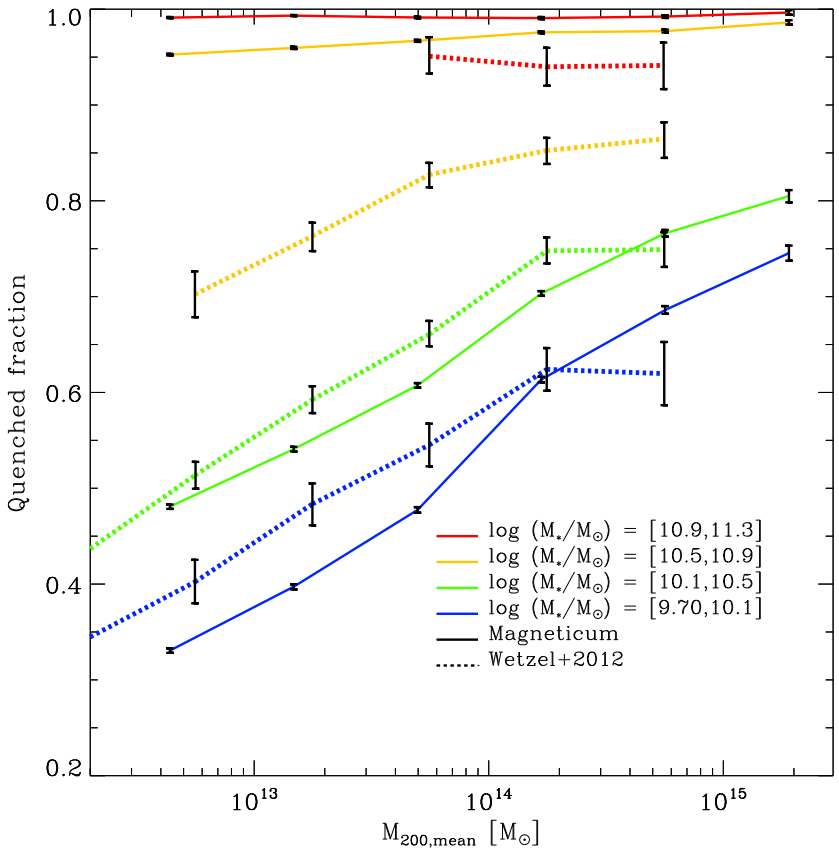

Figure 3.2: Box2 quenched satellite galaxy fractions in dependence of host halo mass, split into four stellar mass bins at $z \sim 0$. Solid lines show the different stellar mass bins from the Magneticum simulation, while the dashed lines show the observations extracted from Wetzel et al. (2012). The Magneticum errors are calculated via bootstrapping.

3.2.3 Mass and temporal evolution

While we, so far, have focused on a comparison to observations, we now use the full predictive power of our simulations to study the velocity-anisotropy for clusters of different mass ranges through redshift. In Figure 3.3 we evaluate the combined results from both Box2 and Box2b. At the lowest redshift considered, $z = 0.25$, we calculate the velocity-anisotropy profiles of $\sim 5 \cdot 10^5$ resolved satellite galaxies within our sample of 6776 clusters with $M_{\rm vir} > 10^{14}\,{\rm M}_\odot$.

Figure 3.3 shows two major similarities independent of mass and redshift. First, the general behaviour of the profiles, albeit displaying differences, is fairly similar in all panels. Specifically, this entails that the star-forming population consistently lies on more radial orbits than its quiescent counterpart. Second, all profiles agree in their broad shape and trend towards isotropy ($\beta = 0$) at smaller radii.

The outskirts are consistently radially dominated since at large radii the likelihood of galaxies being accreted, rather than already belonging to the cluster, is significantly

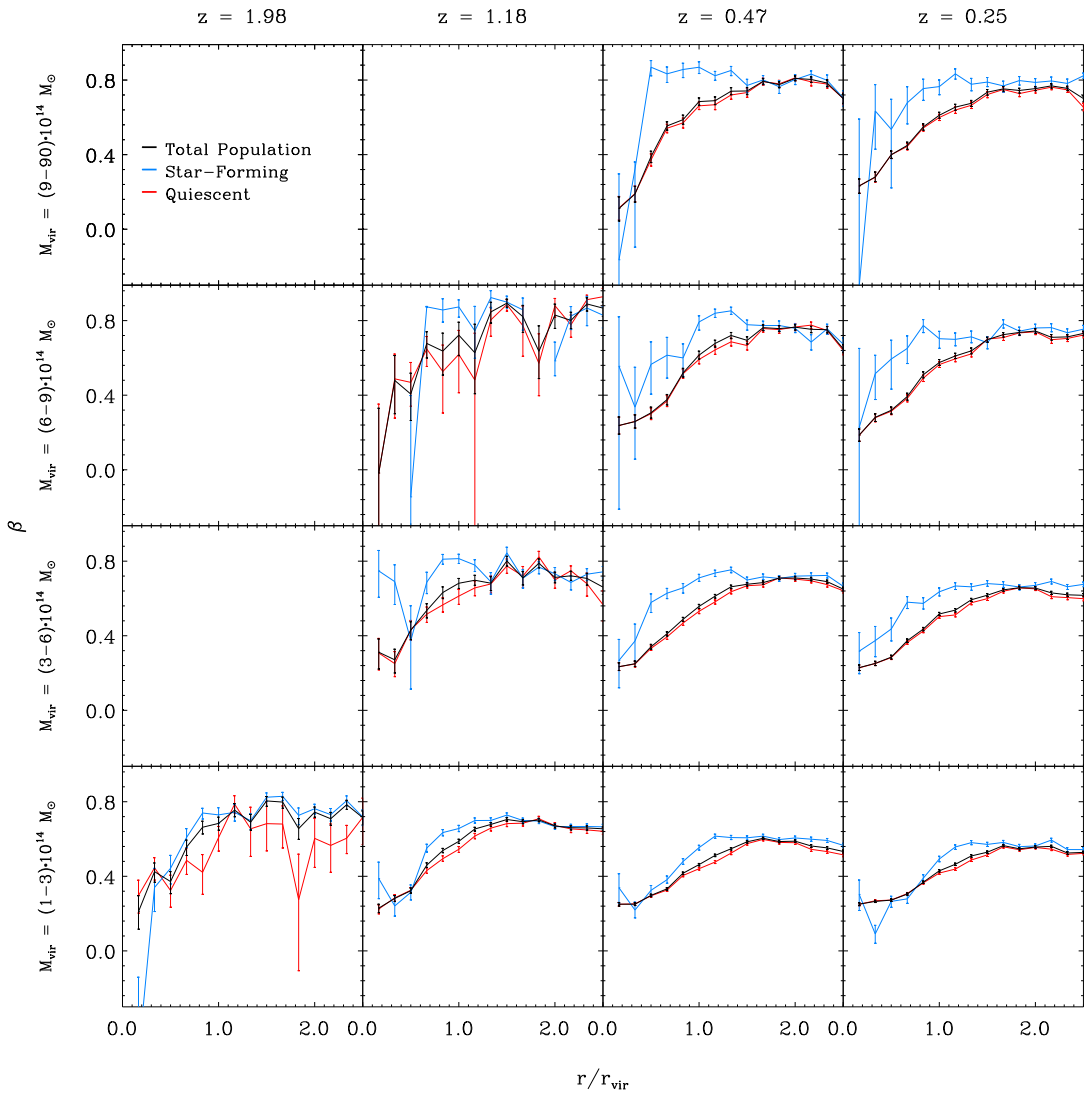

Figure 3.3: Combined Box2 and Box2b differential 3D radial profiles of velocity-anisotropy parameter in dependence of redshift and virial cluster mass. Columns from left to right have the following redshifts: $z = 1.98$, $z = 1.18$, $z = 0.47$ and $z = 0.25$. Rows from top to bottom have the following cluster masses: $M_{\mathrm{vir}} = 9 - 90 \cdot 10^{14}\,\mathrm{M}_{\odot}$, $M_{\mathrm{vir}} = 6 - 9 \cdot 10^{14}\,\mathrm{M}_{\odot}$, $M_{\mathrm{vir}} = 3 - 6 \cdot 10^{14}\,\mathrm{M}_{\odot}$ and $M_{\mathrm{vir}} = 1 - 3 \cdot 10^{14}\,\mathrm{M}_{\odot}$. The blue lines correspond to the star-forming population, while the red lines correspond to the quiescent population. The total galaxy population is indicated by the black line. The empty panels are the result of a lack of clusters in the given redshift and cluster mass range.

higher. In addition, this appears to remain to hold true for the star-forming population at smaller radii too, i.e. the star-forming population is typically more infall dominated than the quiescent population.

Despite close similarities between panels in Figure 3.3, mass and redshift dependent

trends can also be seen. Profiles clearly tend towards being more radially dominated with increasing cluster mass, as mass accretion is expected to occur progressively along small filaments, extending radially outside massive clusters (Iannuzzi & Dolag, 2012). This results in a stronger signal towards radial accretion in the high mass end. In this picture, high mass clusters display more direct infall, i.e. radially dominated orbits, than low mass clusters.

Figure 3.3 shows that the difference between the star-forming (blue) and quiescent (red) profiles becomes more pronounced with cluster mass. In the highest cluster mass bin ($M_{\rm vir} = 9 - 90 \cdot 10^{14}\,{\rm M}_{\odot}$) the star-forming anisotropy profile experiences a strong decline at $r/r_{\rm vir} < 0.5$. This is likely a result of the radially dominated star-forming galaxies being quenched more efficiently through ram-pressure stripping than the subset of more tangentially dominated star-forming galaxies. Hence, we see a selection mechanism, which preferentially quenches radially dominated orbits. This results in only the most circular star-forming galaxies existing at small radii, since the more radially dominated subset no longer exists, i.e. was quenched. Although this is most strongly exhibited in high mass clusters, most star-forming profiles exhibit a stronger decrease at smaller radii $r/r_{\rm vir} < 0.5 - 1$ than the quiescent population. However, the remaining innermost $r/r_{\rm vir} < 0.5$ star-forming population is significantly smaller than the population at $r/r_{\rm vir} \sim 1$, calling for a higher number statistics investigation.

The only apparent redshift-dependent trend is that with decreasing redshift, less satellite galaxies are star-forming. This is visible from the fact that the red and black profiles are closer together at lower redshifts, i.e. the fraction of star-forming galaxies decreases. At high redshift ($z \sim 2$), the majority of galaxies are star-forming. This is not the case at any other redshift surveyed in Figure 3.3. This implies that at high redshift more star-forming galaxies are accreted onto clusters, only to be quenched and become part of the low-redshift quiescent population.

We find that Figure 3.3 is in good agreement with available observations. Specifically, the qualitative behaviour of the results from Biviano et al. (2016) [1] are well reproduced when considering the $z \sim 1$ column and the lower mass bins in Figure 3.3. Our results are also in agreement with Wetzel (2011), who finds that satellite orbits are more radial and plunge deeper into their host haloes at higher host halo masses.

3.3 Phase Space

3.3.1 Line-of-sight phase space

Figure 3.4 shows the line-of-sight (LOS) phase space diagrams for the quiescent (left) and star-forming (right) population at $z = 0.44$. The densities in each plot are scaled to the

[1] The 10 stacked observational clusters in Biviano et al. (2016) have a mass of $M_{200} = 4.5 \pm 1.2 \cdot 10^{14}\,{\rm M}_{\odot}$, which corresponds to a virial mass in the Magneticum simulation of $M_{\rm vir} \sim 3.8 \pm 1.0 \cdot 10^{14}\,{\rm M}_{\odot}$, considering that $M_{\rm vir}$ masses in Magneticum are typically a factor ~ 1.2 smaller at the considered redshift than the M_{200} masses.

respective maximum density of the given population under consideration. In both figures only satellite galaxies are included, i.e. brightest-cluster-galaxies (BCGs) are excluded. The enveloping dashed black lines in Figure 3.4 are introduced to provide a relationship between the velocity and the radius via $|v_{\rm LOS}/v_{200,\rm crit}| \sim |(R/R_{200,\rm crit})^{-1/2}|$. The basis of this relation is the $v \propto r^{-1/2}$ relation, which is derived from the virial theorem. The outer enveloping dashed black lines are motivated by the strongest outlier of the (Biviano et al., 2013) data. We exclude galaxies with properties that are not represented in the observations, as they are likely interlopers, i.e. galaxies that only lie within the cluster due to the LOS projection. We choose the following relation for the filtration: $|v_{\rm LOS}/v_{200,\rm crit}| \sim 2.2|(R/R_{200,\rm crit})^{-1/2}|$, i.e. all galaxies larger than said relation are excluded. The inner enveloping black line depicts the simple virial proportionality. Thus, it provides a theoretical description of the extent of the clusters.

The comparison between the two panels in Figure 3.4 demonstrates the complementary behaviour of the star-forming and quiescent galaxy populations and their individual preference for distinct regions in phase space. This preference, reflected in the phase space number density, is in agreement with the observed CLASH cluster galaxies (Biviano et al., 2013). Typically, quiescent galaxies are located at radii $R < 1\,\mathrm{R}_{200,\rm crit}$, while star-forming galaxies have a significantly increased likelihood of being found in the outskirts of the cluster ($R > 1.5\,\mathrm{R}_{200,\rm crit}$).

At first glance, the left panel of Figure 3.4 seems to display a slight dichotomy in the Magneticum quiescent population. On the one hand we regard the overwhelming majority of the quiescent population at radii $R < 1\,\mathrm{R}_{200,\rm crit}$. On the other hand a second smaller population exists at $R \gtrsim 2.3\,\mathrm{R}_{200,\rm crit}$. However, if we consider the radial histogram (red), we are presented with a constant quiescent number density throughout both the intermediate region ($R \sim (1.2-2.3)\,\mathrm{R}_{200,\rm crit}$) and the second smaller population ($R \gtrsim 2.3\,\mathrm{R}_{200,\rm crit}$). The apparent dichotomy and the constant radial histogram are likely the result of a mixture of two effects. First, accretion in the outskirts, which is discussed more extensively in Section 3.3.2, drives the consistency in the radial histogram. Second, the phase space density increases in the outskirts since the radial histogram remains constant, while the phase space volume decreases, as $|v_{\rm LOS}/v_{200,\rm crit}| \sim |(R/R_{200,\rm crit})^{-1/2}|$ decreases. We investigated whether the apparent over-density in the outskirts might be due to backsplash galaxies, however, we found no evidence to support this (also see Figure 3.5).

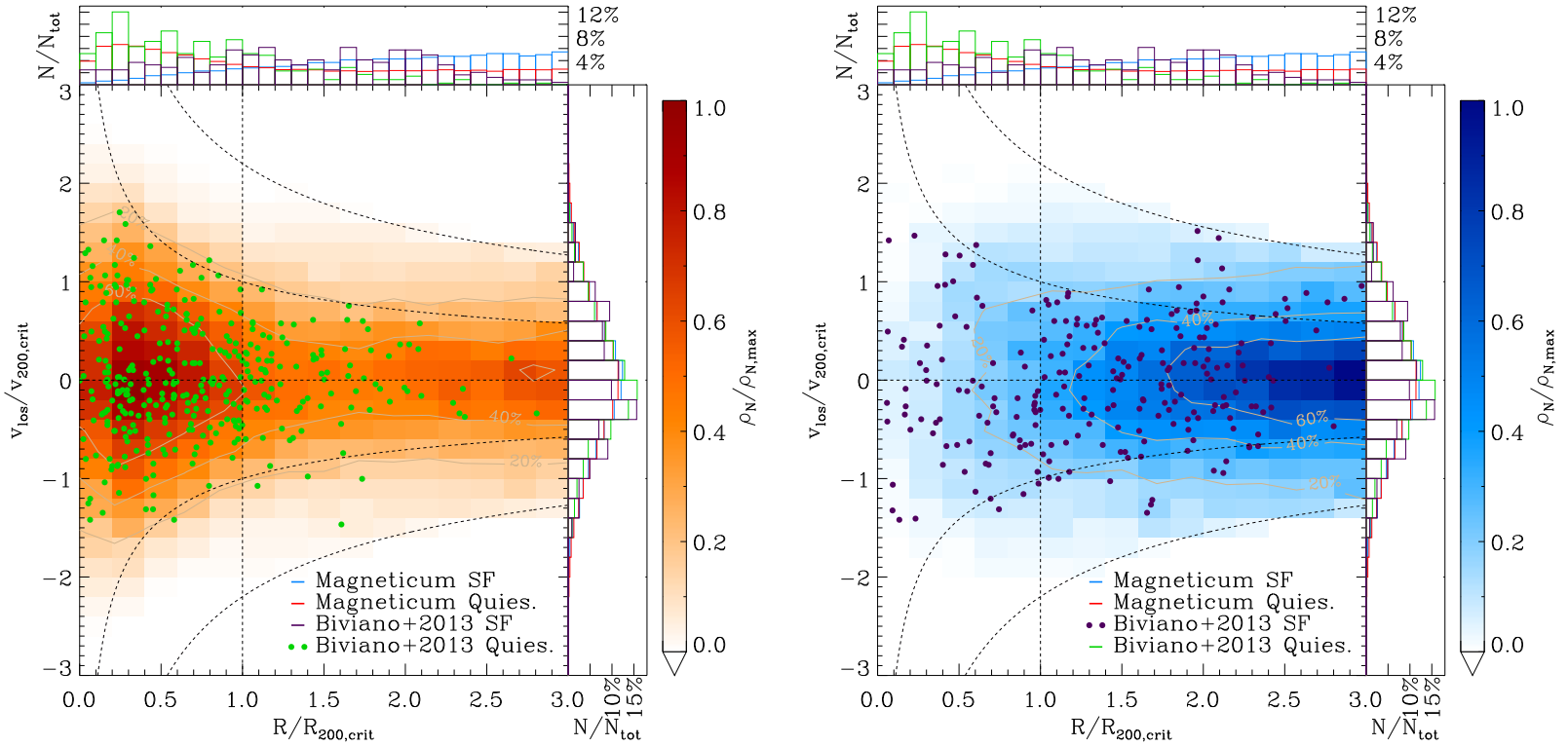

Figure 3.4: Combined Box2 and Box2b quiescent (left) and star-forming (right) line-of-sight (LOS) phase space number density comparison with Biviano et al. (2013) and Magneticum clusters with a mass threshold of $M_{200,\mathrm{crit}} > 5 \cdot 10^{14}\,\mathrm{M}_\odot$ at $z = 0.44$. The figure displays the normalised LOS, i.e. the LOS velocity divided by the $v_{200,\mathrm{crit}}$ velocity ($v_{\mathrm{rad}}/v_{200,\mathrm{crit}}$), in dependence of the projected $R/R_{200,\mathrm{crit}}$ radius. The galaxies obtained through observations are characterised by green and purple indicating quiescent and star-forming galaxies, respectively. In addition, the histograms depict the relative abundance of each population projected onto the respective axes. Contour lines indicate the 20, 40, and 60 per cent regions, with regard to the maximum quiescent LOS phase space density. The two sets of enveloping black lines correspond to $|v_{\mathrm{LOS}}/v_{200,\mathrm{crit}}| \sim |(R/R_{200,\mathrm{crit}})^{-1/2}|$ and $|v_{\mathrm{LOS}}/v_{200,\mathrm{crit}}| \sim 2.2|(R/R_{200,\mathrm{crit}})^{-1/2}|$.

The radial histograms, especially with regard to the star-forming population, also show good agreement between the simulation and the CLASH observations (blue and green lines in Figure 3.4): Both show a decrease below $R < 1\,\mathrm{R}_{200,\mathrm{crit}}$, hinting at a good description of the underlying quenching mechanism by the simulation. In the outskirts of the cluster ($R > 2.2\,\mathrm{R}_{200,\mathrm{crit}}$), the simulation no longer matches the observations. This is likely due to the CLASH cluster not accreting as many galaxies, both star-forming and quiescent, in the outskirts as is the case on average over a wide statistical sample.

Possible other reasons for the different abundances of star-forming and quiescent galaxies at different radii, especially in the outskirts, include shocks. Shocks violently trigger star-formation only to form almost no stars after the initial starburst. Galaxies, which have recently experienced starbursts, thus look blue in colour observations, although technically they have a star-formation rate close to zero. As such, they are classified to be star-forming in Biviano et al. (2013), but are considered quiescent in the simulation which classifies according to the specific star-formation rate rather than the colour. This leads to an underestimation in Magneticum and an overestimation of the number of star-forming galaxies in observations.

To better understand whether the distribution of the galaxies extracted from the simulations within the line-of-sight phase space diagram (as shown in Figure 3.4) is compatible with the distribution of observed galaxies, we computed the normalised distance between the cumulative distributions, as usually done when performing a Kolmogorov-Smirnov (KS) test. As it is not very meaningful to compute the probability from the KS test when comparing a single observed cluster with a large number of stacked clusters from the simulations, we compare this result to what we obtained via cluster by cluster variation from the 86 clusters extracted from the Magneticum simulation, see Figure A.1. Here we compared the radial distribution as well as the line-of-sight distributions for star-forming and quiescent galaxies separately. Interestingly, we find that in the majority of cases the normalised distance of the cumulative distributions between the single cluster observation by Biviano et al. (2013) and the stacked Magneticum clusters is much less than the expected cluster to cluster variation in the simulations. Even the result for the radial distribution of the star-forming galaxies, which shows by far the largest distance, is well within the 2 σ region of the cluster by cluster variation. Within the limits of the observational data, we therefore can quantitatively confirm the impression resulting from Figure 3.4 that the distribution of galaxies within the simulations well represents the observed distribution within the line-of-sight phase space diagram.

3.3.2 Mass and temporal evolution

Figures 3.5 and 3.6 show the temporal and cluster mass evolution of the quiescent and star-forming galaxy population in radial phase space density as a function of the radial profile. At the lowest redshift considered, $z = 0.25$, we calculate the phase space density of $\sim 5 \cdot 10^5$ resolved satellite galaxies within our sample of 6776 clusters with $M_{\mathrm{vir}} > 10^{14}\,\mathrm{M}_{\odot}$. The contour lines correspond to the 20, 40, and 60 per cent thresholds of the maximum density in each panel. Both figures only display satellite galaxies and not BCGs. Each

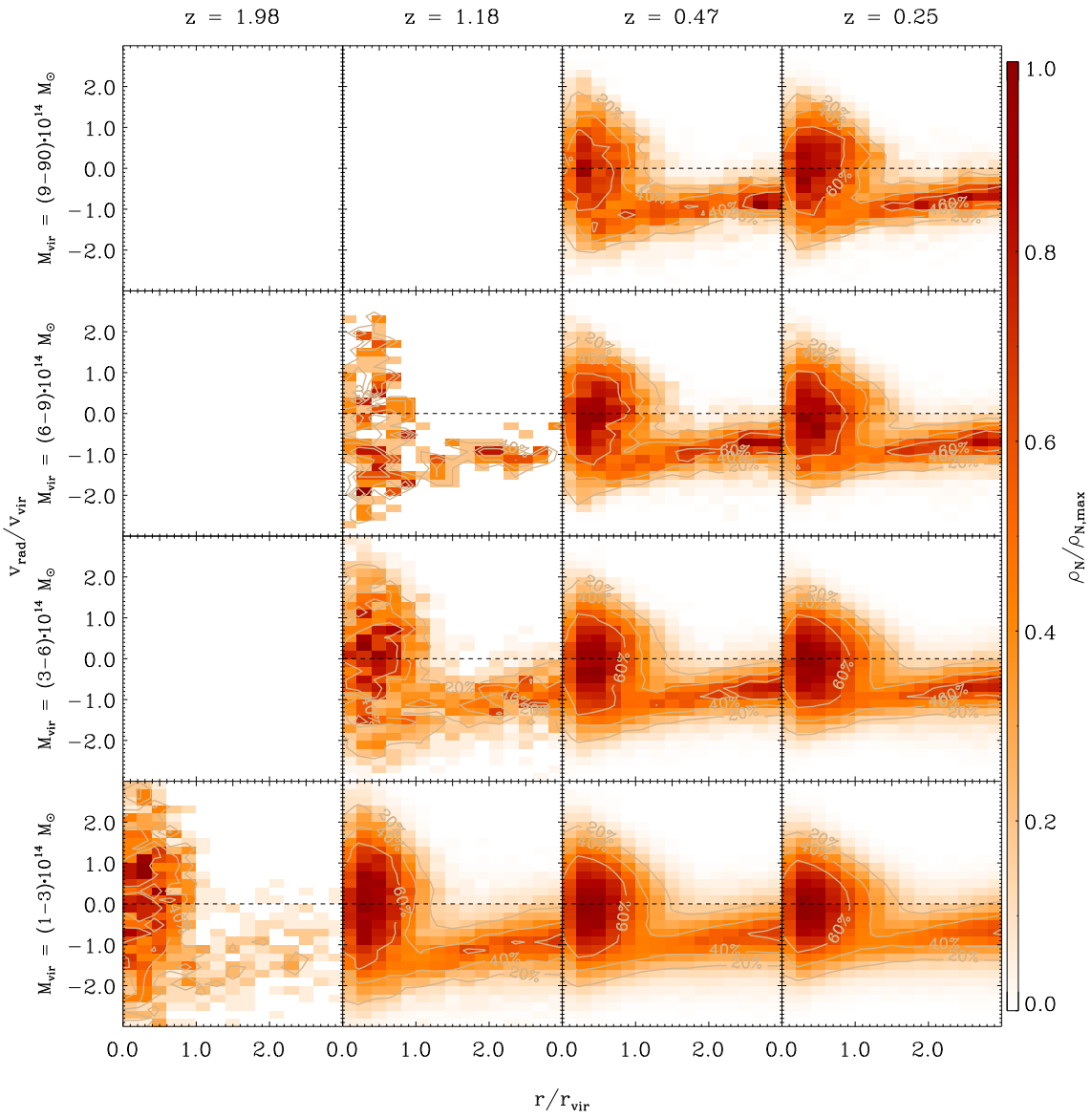

Figure 3.5: Combined Box2 and Box2b normalised relative quiescent radial phase space number density as a function of the 3D radial profile in dependence of redshift and cluster mass. Columns from left to right have the following redshifts: $z = 1.98$, $z = 1.18$, $z = 0.47$ and $z = 0.25$. Rows from top to bottom have the following cluster masses: $M_{\rm vir} = 9 - 90 \cdot 10^{14}\,{\rm M}_\odot$, $M_{\rm vir} = 6 - 9 \cdot 10^{14}\,{\rm M}_\odot$, $M_{\rm vir} = 3 - 6 \cdot 10^{14}\,{\rm M}_\odot$ and $M_{\rm vir} = 1 - 3 \cdot 10^{14}\,{\rm M}_\odot$. The colourbar displays the relative phase space number density normalised to the maximum value of each individual panel. The contour lines correspond to 20, 40, and 60 per cent of the maximum density in each panel. The empty panels are the result of a lack of clusters in the given redshift and cluster mass range.

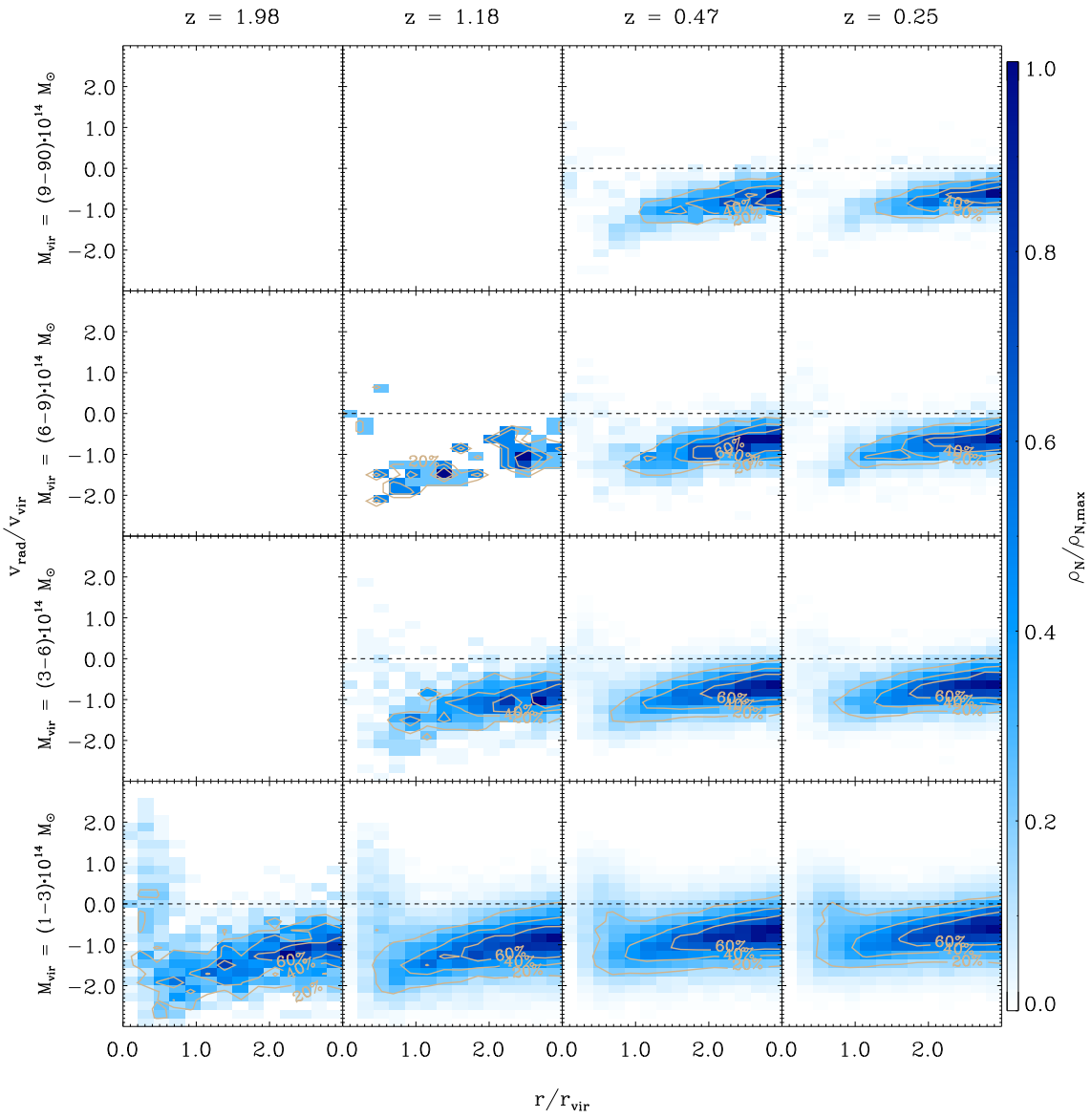

Figure 3.6: Combined Box2 and Box2b normalised relative star-forming radial phase space number density as a function of the 3D radial profile in dependence of redshift and virial cluster mass. Columns from left to right have the following redshifts: $z = 1.98$, $z = 1.18$, $z = 0.47$ and $z = 0.25$. Rows from top to bottom have the following cluster masses: $M_{\rm vir} = 9 - 90 \cdot 10^{14}\,{\rm M}_\odot$, $M_{\rm vir} = 6 - 9 \cdot 10^{14}\,{\rm M}_\odot$, $M_{\rm vir} = 3 - 6 \cdot 10^{14}\,{\rm M}_\odot$ and $M_{\rm vir} = 1 - 3 \cdot 10^{14}\,{\rm M}_\odot$. The colourbar displays the relative phase space number density normalised to the maximum value of each individual panel. The contour lines correspond to 20, 40, and 60 per cent of the maximum density in each panel. The empty panels are the result of a lack of clusters in the given redshift and cluster mass range.

panel in Figures 3.5 and 3.6 is normalised to the maximum value of its individual panel. Consequently, we compare relative densities rather than absolute phase space densities. This relative normalisation is performed to better highlight the effect of quenching, rather than visualising changes in absolute phase space densities. As a result Figures 3.5 and 3.6 disclose no information about the absolute numbers of galaxies.

Considering the quiescent and star-forming population in Figures 3.5 and 3.6, the following details are apparent. First, the star-forming population is overwhelmingly dominated by infall. Specifically, the vast majority of star-forming galaxies are quenched outside $r > 0.5\,\mathrm{r_{vir}}$ during their first passage, independent of redshift. Second, the long term cluster population is almost exclusively made up of quiescent galaxies. This is in agreement with previous hydrodynamic simulations and observations stating that the central cluster region is dominated by quiescent galaxies (Saro et al., 2006). Third, Figure 3.5 suggests that recently accreted satellite galaxies are virialised, i.e. the system has reached virial equilibrium, during the first passage, as they cannot be distinguished from the virialised population. Specifically, there are almost no satellites with positive radial velocity at radii $r \gtrsim 1.5\,\mathrm{r_{vir}}$. This is likely the result of a combination of virialisation and a scaling effect driven by the cluster growth which increases $\mathrm{r_{vir}}$, i.e. decreasing $r/\mathrm{r_{vir}}$ of a given orbit as the cluster accretes more mass.

Figure 3.5 demonstrates that high mass clusters exhibit more extensive accretion than low mass clusters, as implied by the higher relative density in the outskirts ($r > 2.0\,\mathrm{r_{vir}}$). The increased accretion in high mass clusters further strengthens the idea that high mass clusters are located within a surrounding high density environment, i.e. at the cross-section of filaments.

This is in agreement with previous simulations that show that the cluster environment, characterised by increased filamentary thickness, extends out to three to four times the virial radius (Dolag et al., 2006). Along filaments, the radial density profiles decrease less strongly than within the galaxy cluster (Dolag et al., 2006). This physical extension of the cluster environment manifests itself, amongst other things, through the decrease in the percentage of star-forming compared to quiescent galaxies with increasing cluster mass. The percentage of star-forming galaxies compared to their quiescent/passive counterparts in cluster intervals $M_{\mathrm{vir}} = 9 - 90 \cdot 10^{14}\,\mathrm{M_\odot}$, $M_{\mathrm{vir}} = 6 - 9 \cdot 10^{14}\,\mathrm{M_\odot}$, $M_{\mathrm{vir}} = 3 - 6 \cdot 10^{14}\,\mathrm{M_\odot}$ and $M_{\mathrm{vir}} = 1 - 3 \cdot 10^{14}\,\mathrm{M_\odot}$ is $N_{\mathrm{SF}}/N_{\mathrm{PAS}} = 8.9\%$, $N_{\mathrm{SF}}/N_{\mathrm{PAS}} = 10.4\%$, $N_{\mathrm{SF}}/N_{\mathrm{PAS}} = 12.0\%$, and $N_{\mathrm{SF}}/N_{\mathrm{PAS}} = 16.1\%$, respectively. This implies that the overall environment of more massive clusters is more efficient in quenching, despite it extending out further than lower mass clusters. In contrast, Wetzel et al. (2013) find no dependence of host halo mass on quenching timescales. This is likely due to the quenching in the Magneticum simulations being more strongly correlated with infall than is the case in the 'delayed-then-rapid' quenching scenario found in Wetzel et al. (2013). Due to the long time delay, compared to the quenching timescale, in the 'delay-then-rapid' quenching scenario, host halo mass differences do not factor in as strongly when solely considering quenching timescales.

Figure 3.6 offers more insights with regard to different mass bins and their temporal evolution: Lower cluster mass intervals present a lower quenching effectiveness than higher mass clusters. This is in agreement with observations, which find that processes

responsible for the termination of star-formation in galaxy clusters are more effective in denser environments (Raichoor & Andreon, 2012). In the low cluster mass range more star-forming galaxies exist at smaller radii. In contrast to the higher cluster mass intervals, the low mass range also exhibits a star-forming, albeit small, population with positive radial velocity, especially at high redshift, indicating that quenching becomes more effective at lower redshift and higher cluster mass. This is in agreement with a suite of recent cluster resimulations by Arthur et al. (2019), which find ram-pressure stripping of subhalos to be significantly enhanced in more massive halos compared to less massive halos.

3.3.3 Stellar mass comparison

In Figures 3.7 and 3.8, we investigate the effect of splitting the radial phase space of satellite galaxies into high and low stellar mass samples ($M_* > 1.5 \cdot 10^{10}\,\mathrm{M}_\odot$ and $M_* < 1.5 \cdot 10^{10}\,\mathrm{M}_\odot$). As shown in Figure 3.7, we find a relative excess of high stellar mass quiescent satellites outside the virial radius, as indicated by the cyan colour. In contrast, the quiescent population within the clusters is characterised by an excess of low stellar mass satellites.

The excess of low stellar mass quiescent galaxies below the virial radius is likely driven by the dynamical friction timescale. More massive satellite galaxies merge with the BCG on much faster timescales than lower mass satellite galaxies. This is the result of the dynamical friction coefficient being of order of the reciprocal of the time of relaxation of a system, i.e. the dynamical friction timescale is $t_{\mathrm{dynfric}} \sim 1/M$, where M is the sum of the masses of the two objects under consideration (Chandrasekhar, 1943). Consequently, fewer high mass quiescent galaxies are found below the virial radius in Figure 3.7. For a discussion regarding the effect of dynamical friction on orbital decay times see Section 3.4.2.

The apparent lack of high stellar mass quiescent satellites below the virial radius is also driven by the fact that satellite galaxies within clusters no longer experience mass accretion. Instead, after losing their dark matter halo, satellite galaxies in clusters often experience stellar mass loss via tidal stripping (Tollet et al., 2017). As a result, the inner cluster population is biased towards lower stellar mass galaxies.

In contrast to Figure 3.7, Figure 3.8 shows a high stellar mass excess within the cluster, while the outskirts are characterised by a relative excess of low stellar mass star-forming satellites. The overabundance of high stellar mass star-forming satellites within clusters, especially at lower cluster masses, is driven by a selection effect: a higher stellar mass implies a stronger gravitational binding energy and, thus, protects against ram-pressure stripping more effectively. Ultimately, low stellar mass satellite galaxies are less likely to remain star-forming after infall and, hence, are less likely to be found within clusters (see Section 3.4.2). This effect becomes less significant in higher mass clusters as ram-pressure stripping becomes more violent, and stellar mass shielding less effective (see Section 3.4).

We verified that the excess of low stellar mass quiescent satellite galaxies in the inner regions of clusters is not solely driven by a combination of the normalisation and infalling low stellar mass galaxies being preferentially star-forming. The individual panel

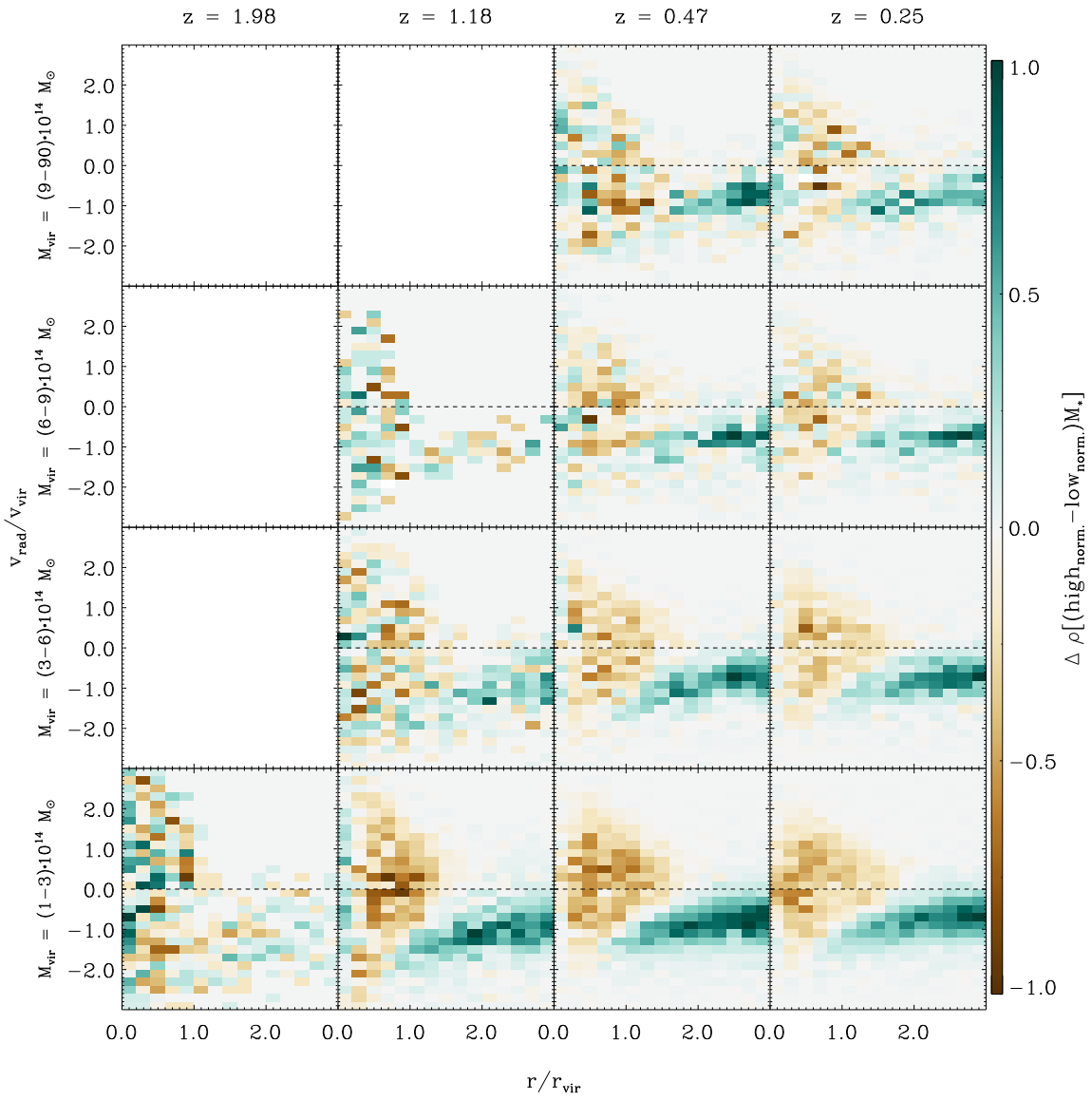

Figure 3.7: Combined Box2 and Box2b comparison of high and low stellar mass of quiescent satellite galaxies. Figure 3.5 was split into a high ($M_* > 1.5 \cdot 10^{10}\,\mathrm{M}_\odot$) and low ($M_* < 1.5 \cdot 10^{10}\,\mathrm{M}_\odot$) stellar mass bin. Thereafter, the two mass bins were normalised to the maximum value of each panel and subsequently subtracted from one another, resulting in maps of relative normalised stellar mass densities, i.e. $\Delta\rho[(\mathrm{high}_{\mathrm{norm.}} - \mathrm{low}_{\mathrm{norm.}})\mathrm{M}_*]$.

normalisation, which implies that any local excess must be compensated by a local deficit within a given panel, contributes to a stronger visual impact in some panels. However, it is not the dominant driver behind the behaviour found in Figures 3.7 and 3.8.

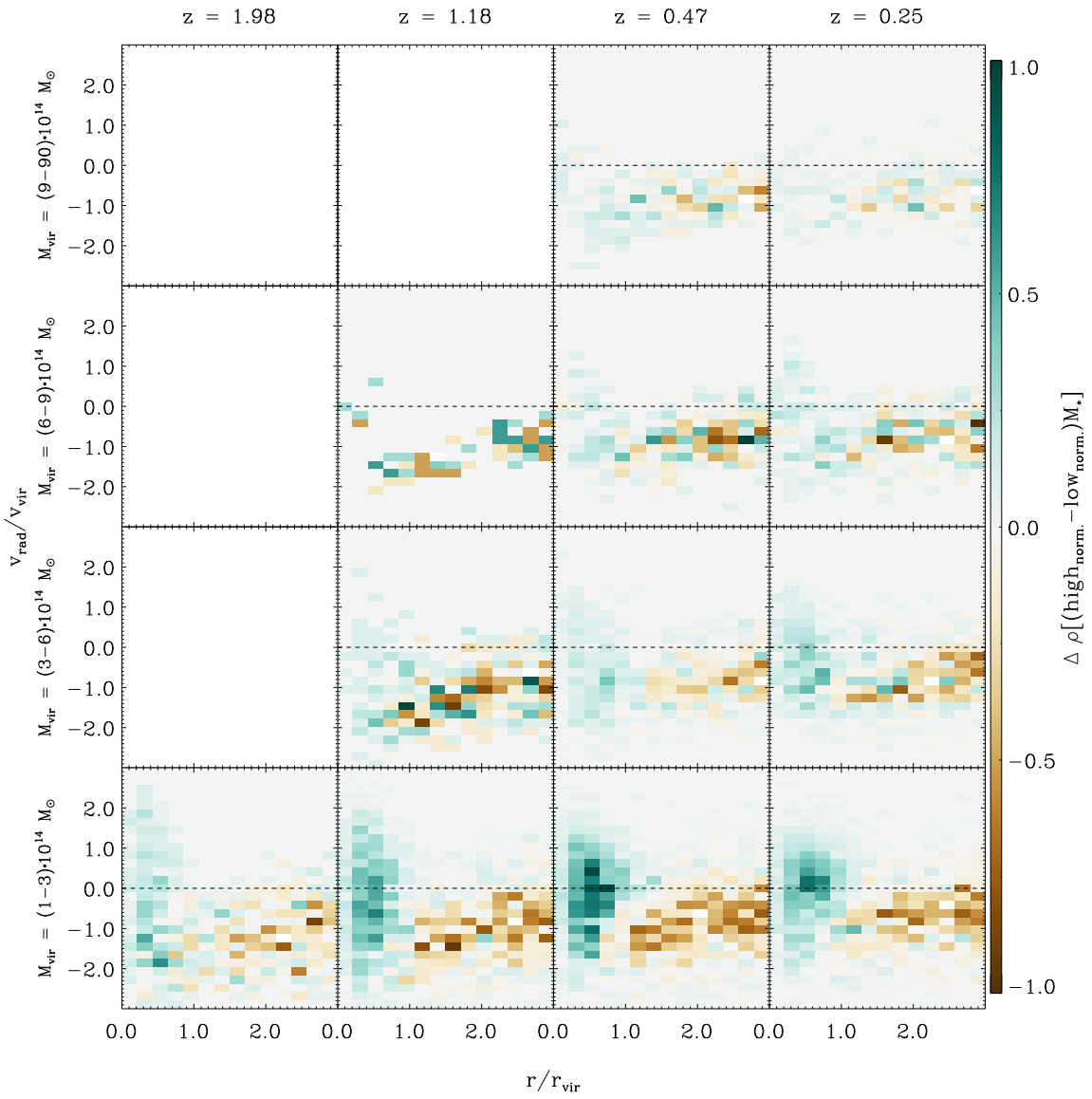

Figure 3.8: Combined Box2 and Box2b comparison of high and low stellar mass of star-forming satellite galaxies. Figure 3.6 was split into a high ($M_* > 1.5 \cdot 10^{10}\,\mathrm{M}_\odot$) and low ($M_* < 1.5 \cdot 10^{10}\,\mathrm{M}_\odot$) stellar mass bin. Thereafter, the two mass bins were normalised to the maximum value of each panel and subsequently subtracted from one another, resulting in maps of relative normalised stellar mass densities, i.e. $\Delta\rho[(\mathrm{high}_{\mathrm{norm.}} - \mathrm{low}_{\mathrm{norm.}})\mathrm{M}_*]$.

3.4 Satellite galaxy quenching prior to infall

3.4.1 Tracking in-falling star-forming satellite galaxies

To better understand the nature of the quenching mechanisms at play, we track individual satellite orbits from the outskirts of clusters to long after they have passed the virial radius.

Figure 3.9 shows the radial distance evolution of two different mass populations of galaxies as they fall into their respective clusters. Figure 3.10 follows the blueness evolution of the same galaxies.

Both figures scale the individual satellite orbits to the point where they cross the virial radius. Specifically, the point in time is identified where the individual galaxies cross the cluster virial radius and the trajectory of the now satellite galaxies is then scaled so that all galaxies cross the virial radius at a deviation to infall time of $\Delta t_{\rm infall} = 0$.

The galaxies are selected according to three criteria: a.) host cluster mass at redshift $z = 1.01$ has to be in the range of $1 \cdot 10^{14} < M_{\rm vir}/{\rm M}_\odot < 3 \cdot 10^{14}$; b.) the satellite galaxies must be located at a radial interval of $1.5 < r/r_{\rm vir} < 4.5$ at $z = 1.01$ before descending into the cluster; c.) satellite galaxies must have at least 100 stellar particles ($M_* > 3.5 \cdot 10^9\, h^{-1}{\rm M}_\odot$) and be considered star-forming, i.e. SSFR $\cdot\, t_{\rm H} > 0.3$.

In order to evaluate the quenching efficiency of different galaxy masses, the tracked satellite galaxies are further subdivided into two populations. The high stellar mass population is characterised by satellite galaxies which consistently, i.e. independent of delta infall time, have a stellar mass above $M_* > 1.5 \cdot 10^{10}\,{\rm M}_\odot$, while, the low mass population in Figures 3.9 and 3.10 consistently has a stellar mass of $M_* < 1.5 \cdot 10^{10}\,{\rm M}_\odot$. It is important to note that if a galaxy crosses the stellar mass threshold $M_* = 1.5 \cdot 10^{10}\,{\rm M}_\odot$, it is no longer considered a member of either group. This is done so as to filter out galaxies that experience significant mass growth and, thus, are likely prone to quenching as a result of internal changes, rather than through the cluster environment, but also filters out satellite galaxies that experience mass loss through tidal stripping.

Figure 3.9 reveals no differences in the behaviour between the high (upper panel) and low (lower panel) stellar mass satellite galaxy populations. Satellite galaxies are accreted onto the cluster and, depending on their initial infall conditions, exhibit different orbital behaviour. The stellar mass, thus, likely has no impact on the radial orbital evolution. This is best exemplified by the wide range of orbital periods in both populations, ranging from shallow tangential orbits, with long orbital timescales and a relatively constant large radial distance, to very radial orbits with short orbital periods that rapidly decrease in amplitude.

However, if we look at the blueness of satellite galaxies (Figure 3.10) it becomes apparent that low stellar mass satellite galaxies generally have a higher average specific star-formation compared to their high mass counterparts prior to infall. At lower stellar mass, i.e. lower stellar particle numbers, increasing resolution effects become non-negligible. As a result, low stellar mass satellite galaxies experience a more bursty SFR than high mass satellite galaxies, for which a more continuous SSFR can be seen. After infall into the cluster's virial radius all satellite galaxies show a strong decline in SSFR, with most galaxies being quenched completely 1 Gyr after infall.

The thick black lines in the middle (dashed line) and bottom (solid line) panel in Figure 3.10 describe the average behaviour of each population in response to quenching. We confirmed that the mean SSFR provides a good proxy for individual galaxy behaviour. To stronger emphasise the difference between the high and low stellar mass populations, the thick black lines are normalised to their respective maximum value and shown in the

top panel.

The high stellar mass satellite galaxies experience a far earlier onset of quenching, characterised by a continuous steady decline in star-formation, rather than a rapid decrease. In contrast, the low stellar mass satellite galaxies are characterised by a constant star-formation until shortly before falling into the cluster ($\Delta t_{infall} \sim 0.3$), only to experience rapid quenching with infall. As the termination of star-formation is effectively instantaneous for many individual low stellar mass galaxies (coloured lines in bottom panel of Figure 3.10), an extended quenching timescale for individual low mass galaxies is not available. Therefore, the average, as shown in the bottom panel of Figure 3.10, reflects the average decline of the entire population rather than individual quenching timescales of low stellar mass galaxies. However, higher resolution simulations likely will extend the quenching timescale of low stellar mass satellite galaxies.

Independent of the stellar mass, almost all satellite galaxies in Figure 3.10 are quenched within 1 Gyr after infall. As a population rather than individually, low stellar mass satellite galaxies are quenched on a timescale of $t_{low} \sim 1\,\mathrm{Gyr}$, while the high stellar mass satellite galaxies are quenched on a timescale roughly twice as long: $t_{high} \sim 2 - 3\,\mathrm{Gyr}$, due to the earlier onset of their quenching. This shows that stellar mass is relevant with regard to the quenching mechanisms at play, as well as the timescales on which they occur. This is discussed further in Section 3.4.3, where the impact of mass quenching and environmental quenching is investigated.

Once commenced, the decrease in specific star-formation for both mass bins appears to be linear. Weinmann et al. (2010) find that the diffuse gas in their model must be stripped linearly, rather than exponentially, in order to reproduce observations. This implies that stripping becomes more efficient the longer a galaxy has been a satellite (Weinmann et al., 2010). This is in agreement with findings from Zinger et al. (2018), which state that, due to the gas depletion times, it is quite plausible for galaxies crossing the cluster's virial radius during infall to be quenched as a result of halo gas removal. Subsequently, this also explains the abundance of quenched galaxies, especially disks, in the outskirts of clusters (Zinger et al., 2018). Wetzel et al. (2012) and Wetzel et al. (2013) find that satellites remain active after infall on timescales longer than the quenching timescale. Once the satellite SFR fading process has begun, it is rapid and likely shorter than $\sim 2.4\,\mathrm{Gyr}$ (Wetzel et al., 2012). In contrast to our findings this 'delayed-then-rapid' quenching scenario finds that satellites evolve unaffected for $2 - 4\,\mathrm{Gyr}$ after infall before being rapidly quenched (Wetzel et al., 2013).

The gradual decline in specific star-formation of the high stellar mass satellite galaxies in Figure 3.10 is characterised by a statistical anomaly. Namely, a bump in specific star-formation is visible around 0.2 Gyr after crossing the virial radius. This is in agreement with numerical studies that have found evidence for an enhancement of star-formation as a result of the additional pressure exerted by the intra-cluster-medium (ICM) on the inter-stellar-medium (ISM) (Bekki & Couch, 2003; Kronberger et al., 2008; Kapferer et al., 2008, 2009; Tonnesen & Bryan, 2009), however Tonnesen & Bryan (2012) find no evidence for a burst in star-formation.

The starburst seen in the high stellar mass, and to a smaller extent in the low stellar

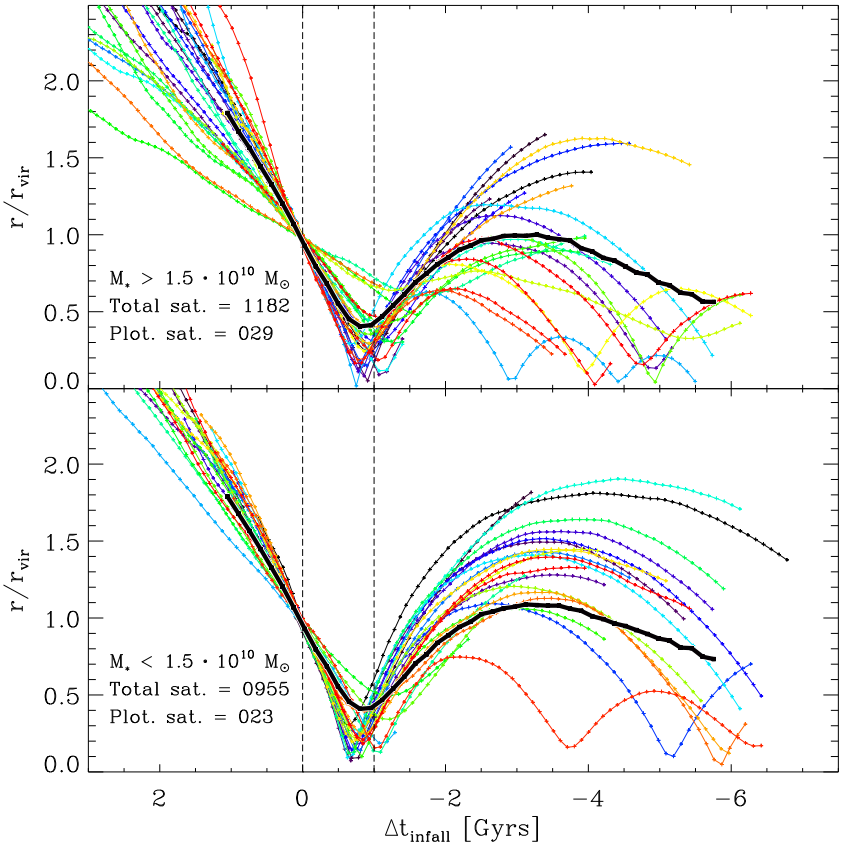

Figure 3.9: Cluster-centric 3D radial distance scaled to the temporal evolution, i.e. deviation to infall time Δt_{infall}, of high and low mass satellite galaxies extracted from Box2. Each line represents an individual satellite galaxy tracked through time from $z = 1.01$ to the present day. Only a selection of satellite galaxy trajectories are plotted for facilitated visualisation. The satellite galaxies are scaled to the point where they pass below $1\,R_{vir}$ and this time is set to $\Delta t_{infall} = 0$. Top panel: satellite galaxies with stellar mass $M_* > 1.5 \cdot 10^{10}\,M_\odot$. Bottom panel: satellite galaxies with stellar mass $M_* < 1.5 \cdot 10^{10}\,M_\odot$. The thick black line depicts the mean value of the entire satellite galaxy population in the given mass range, including the trajectories not plotted. The dashed vertical lines indicate the points in time corresponding to infall and 1 Gyr after infall.

mass, satellite galaxies in Figure 3.10 is probably driven by the onset of ram-pressure stripping. Low stellar mass galaxies cannot shield themselves as effectively as high stellar mass galaxies from ram-pressure. As a result high stellar mass galaxies can retain more gas at the same ram-pressure. Hence, the onset of ram-pressure stripping more likely leads to compression than to expulsion in high stellar mass galaxies; whereas in low stellar mass galaxies the likelihood of quickly losing the cold gas component is higher. To strengthen these assumptions, we study an independent population of satellite galaxies, selected as the discussed sample but in a cluster mass range of $3 \cdot 10^{14} < M_{vir}/M_\odot < 6 \cdot 10^{14}$ at

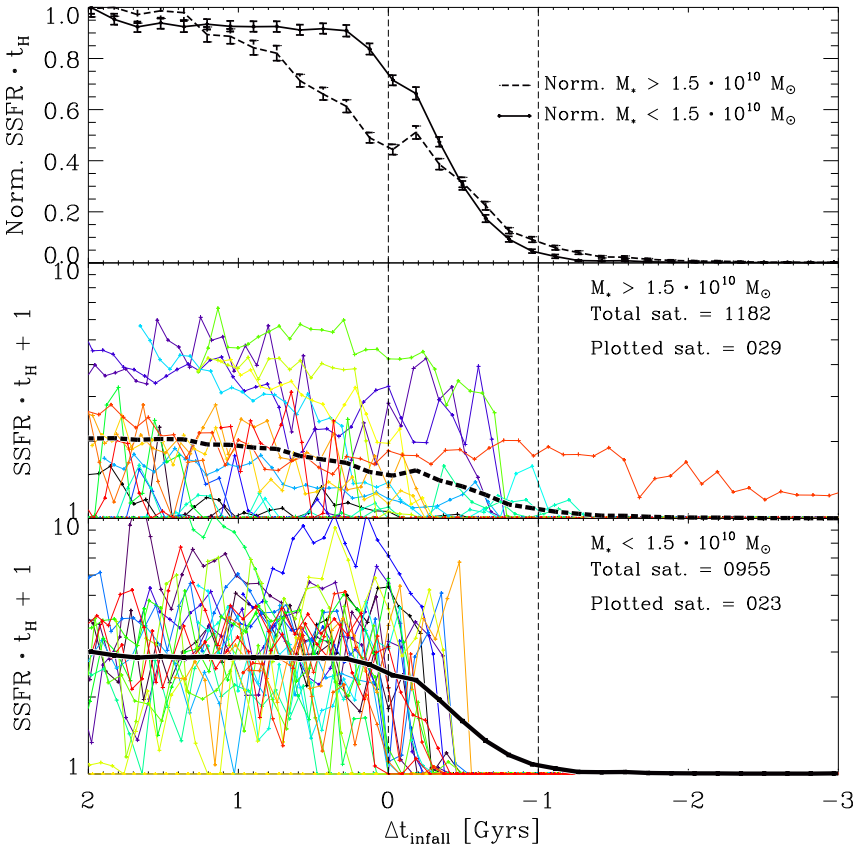

Figure 3.10: Blueness scaled to the temporal evolution, i.e. deviation to infall time Δt_{infall}, of high and low mass satellite galaxies extracted from Box2. Each line represents an individual satellite galaxy tracked through time from $z = 1.01$ to the present day. Only a selection of satellite galaxy trajectories are plotted for facilitated visualisation. The satellite galaxies are scaled to the point where they pass below $1\,R_{vir}$ and this time is set to $\Delta t_{infall} = 0$. The thick black lines depict the mean value of the entire satellite galaxy population in the given mass range, including the trajectories not plotted. Top panel: the two black lines were normalised to their maximum value, as such they are linearly scaled versions of the two thick black lines in the middle and bottom panel. The error bars were obtained through bootstrapping. Middle panel: satellite galaxies with stellar mass $M_* > 1.5 \cdot 10^{10}\,M_\odot$. Bottom panel: satellite galaxies with stellar mass $M_* < 1.5 \cdot 10^{10}\,M_\odot$. The dashed vertical lines indicate the points in time corresponding to infall and 1 Gyr after infall.

$z = 1.01$. We find the same behaviour, i.e. this independent satellite galaxy population is also characterised by a starburst at $\Delta t_{infall} = -0.2$, strongly suggesting a physical origin. Furthermore, we could not find any correlation between pericentre passage and a starburst (see Figure A.2).

3.4.2 Tracking survivors

To better understand the quenching mechanisms at work, we introduce a criterion to identify satellite galaxies that survive, i.e. remain unquenched, much longer than the average of the total population. The surviving satellite population is defined as galaxies that are still considered star-forming 1 Gyr after infall, as indicated by the dashed vertical lines at $\Delta t_{infall} = -1$ in Figures 3.11 and 3.12. Figures 3.11 and 3.12 study the distinguishing attributes of the surviving satellite galaxies, in comparison to the previously discussed total population in Figures 3.9 and 3.10. This allows the study of quenching inhibitors, resulting in a better understanding of the physical quantities responsible for prolonged survival in a galaxy cluster environment.

We find that high stellar mass satellite galaxies ($M_* > 1.5 \cdot 10^{10}\,M_\odot$) preferentially survive if they have a very high stellar mass, compared to the mean stellar mass of the entire high stellar mass population (see Table 3.1). This implies that stellar mass correlates strongly with the ability to remain star-forming, i.e. survival during infall. This is reflected by the significant mass difference (factor ~ 4) between the high stellar mass survivors and the total high stellar mass population. This suggests that a minimum stellar mass threshold needs to be reached to be shielded from ram-pressure stripping.

For low mass satellite galaxies, we find no meaningful correlation between continued star-formation and stellar mass. However, low stellar mass satellite galaxies ($M_* < 1.5 \cdot 10^{10}\,M_\odot$) show a correlation between the infall orbits and their subsequent survival. As the contrast between solid and dashed black lines in Figure 3.11 indicates, surviving low stellar mass satellite galaxies are likely to have shallow orbits, i.e. small radial distance fluctuations and larger pericentres, while their high stellar mass counterparts do not show this behaviour strongly within the first Gyr after infall. However, the comparison between the total (solid line) and surviving (dashed line) high stellar mass populations in the top panel in Figure 3.11 shows that dynamical friction is more effective for higher mass objects. Within the first Gyr after infall the two populations in the top panel are characterised by very similar orbits and pericentres. After the satellite galaxies have been part of the cluster for over a Gyr, their orbits show divergence. As the high stellar mass survivors are on average ~ 4 times more massive than the average total high stellar mass population, they experience dynamical friction to a stronger degree (see Section 3.3.3). Subsequently, the orbits of the high stellar mass survivors are circularised more effectively.

In summary, we conclude that above a certain stellar mass threshold satellite galaxy survival correlates strongly with stellar mass, whereas below this threshold survival is far more dependent on the infall orbit. This implies that stellar mass and shallow orbits shield satellite galaxies from ram-pressure stripping with different efficiencies depending on the satellite galaxies in question. Furthermore, it suggests that stellar mass is more efficient in shielding than the orbital configuration. This is supported by the fact that fewer low stellar mass satellite galaxies survive relative to the total low stellar mass population than is the case for the high stellar mass comparison. Specifically, 4.7 per cent of the high stellar mass population survive, whereas only 3.0 per cent of the low stellar mass satellite galaxies survive up to 1 Gyr after infall.

Considering Equations 1.13 and 1.14, it is also clear that more massive galaxies (with higher M_*) have larger radii, r, at which the ram-pressure, $P_{\rm ram}$, is equivalent to $P_{\rm retain}(r)$. This simple theoretical description implies that high stellar mass galaxies are more efficient at shielding the cold gas component from ram-pressure stripping, as $P_{\rm retain}(r)$ is larger for a given radius for more massive galaxies. As such, Magneticum is in line with simple theoretical predictions.

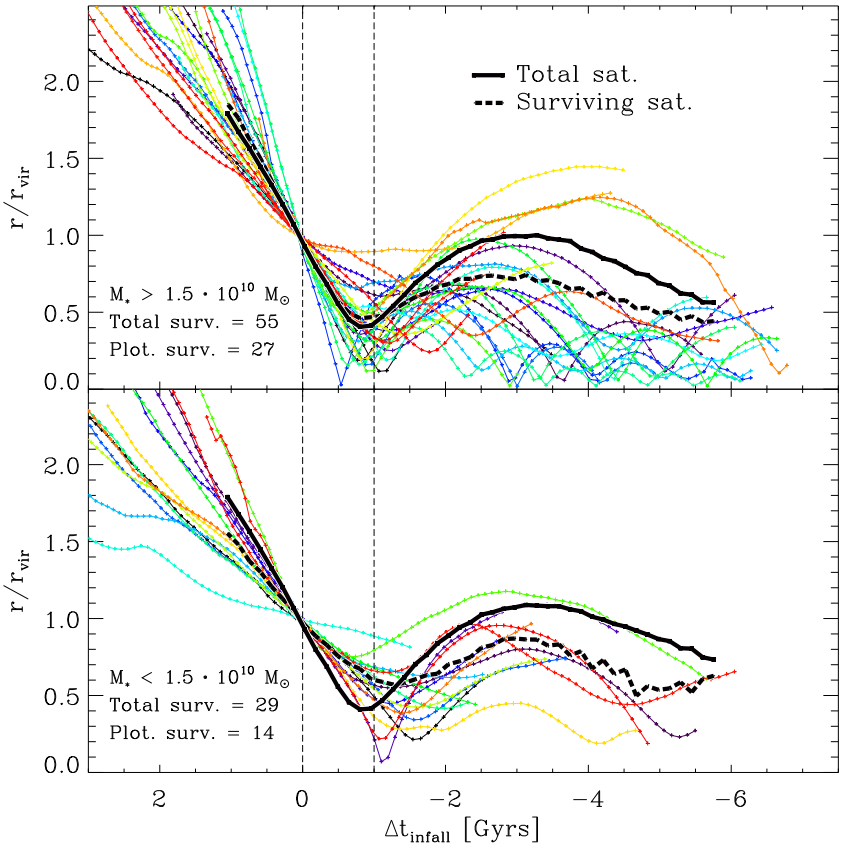

Figure 3.11: Surviving sample's cluster-centric 3D radial distance scaled to the temporal evolution, i.e. deviation to infall time $\Delta t_{\rm infall}$, of high and low mass satellite galaxies extracted from Box2. Each line represents an individual surviving satellite galaxy tracked through time from $z = 1.01$ to the present day. All surviving satellite galaxy trajectories, i.e. all satellite galaxies that are still considered star-forming 1 Gyr after infall are plotted. The satellite galaxies are scaled to the point where they pass below $1\,R_{\rm vir}$ and this time is set to $\Delta t_{\rm infall} = 0$. Top panel: surviving satellite galaxies with stellar mass $M_* > 1.5 \cdot 10^{10}\,M_\odot$. Bottom panel: surviving satellite galaxies with stellar mass $M_* < 1.5 \cdot 10^{10}\,M_\odot$. The dashed vertical lines indicate the points in time corresponding to infall and 1 Gyr after infall.

In contrast to the gradual decline found for the total massive satellite galaxy population, no gradual decline is observed in either population in Figure 3.12. The survival criterion likely filters out any satellite galaxies that experienced quenching in the outskirts of the

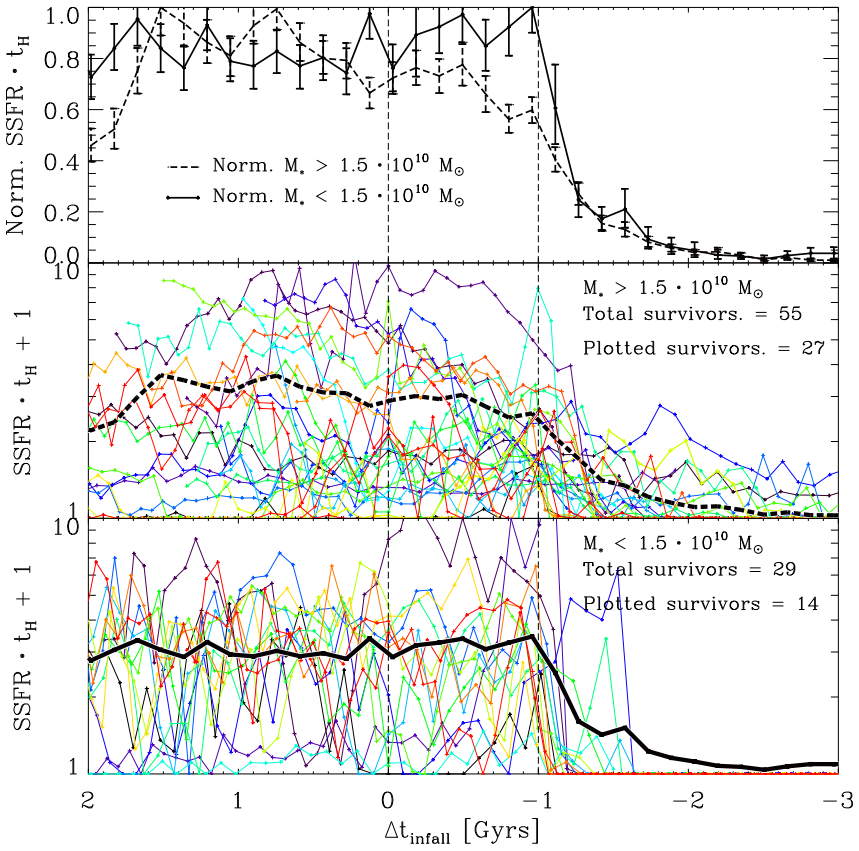

Figure 3.12: Surviving sample's blueness scaled to the temporal evolution, i.e. deviation to infall time Δt_{infall}, of high and low mass satellite galaxies extracted from Box2. Each line represents an individual surviving satellite galaxy tracked through time from $z = 1.01$ to the present day. All surviving satellite galaxy trajectories, i.e. all satellite galaxies that are still considered star-forming 1 Gyr after infall are plotted. The satellite galaxies are scaled to the point where they pass below $1\,R_{vir}$ and this time is set to $\Delta t_{infall} = 0$. The thick black lines depict the mean value of the surviving satellite galaxy population in the given mass range. Top panel: the two black lines were normalised to their maximum value, as such they are linearly scaled versions of the two thick black lines in the middle and bottom panel. The error bars were obtained through bootstrapping. Middle panel: surviving satellite galaxies with stellar mass $M_* > 1.5 \cdot 10^{10}\,M_\odot$. Bottom panel: surviving satellite galaxies with stellar mass $M_* < 1.5 \cdot 10^{10}\,M_\odot$. The dashed vertical lines indicate the points in time corresponding to infall and 1 Gyr after infall.

cluster, as this would inhibit the survival at infall.

In Figure 3.13, we study the impact of galactic orbits on survival. Specifically, Figure 3.13 shows the cluster's virial radius normalised distance (r/r_{vir}) between an individual satellite galaxy's pericentre and the cluster centre as a function of the difference in time between infall and pericentre passage, $\Delta(t_{infall} - t_{pericentre})$. Similarly to previous plots, the

Sample [$M_\odot$]	Mean st. mass [$M_\odot$]	Numb. of sats.
$M_* > 1.5 \cdot 10^{10}$ All	$6.01 \cdot 10^{10}$	1182
$M_* > 1.5 \cdot 10^{10}$ Surv.	$2.38 \cdot 10^{11}$	55
$M_* < 1.5 \cdot 10^{10}$ All	$8.58 \cdot 10^{9}$	955
$M_* < 1.5 \cdot 10^{10}$ Surv.	$9.14 \cdot 10^{9}$	29

Table 3.1: Table listing the relevant information of the samples depicted in Figures 3.9, 3.10, 3.11 and 3.12. The first column references the sample, i.e. the stellar mass range and which population is under consideration. The second column displays the mean stellar satellite galaxy mass of the sample selected in the first column. The third column lists the number of satellite galaxies in a given selected sample. Each satellite galaxy has a stellar mass of at least $M_* > 3.5 \cdot 10^9\, h^{-1}\mathrm{M}_\odot$.

sample is divided into the standard high and low stellar mass bins. In addition to the previously defined 'survivors', we define another category, namely, the 'super survivors'. Super survivors are defined as the subsample of satellite galaxies that are still star-forming 1 Gyr after pericentre passage.

Figure 3.13 shows that orbital characteristic are more important in the low stellar mass bin than they are in the high stellar mass bin. In the high stellar mass bin there we find no evidence for a significant correlation between pericentre height or $\Delta(\mathrm{t_{infall}} - \mathrm{t_{pericentre}})$ and survival (blue triangles). However, super survivors (blue squares) show a preference for high pericentres. The low stellar mass survivors are characterised by a strong preference towards high pericentres and high $\Delta(\mathrm{t_{infall}} - \mathrm{t_{pericentre}})$, supporting our previous findings that orbits are far more relevant in the low stellar mass regime. Low stellar mass super survivors all have pericentres above $0.6\,\mathrm{r/r_{vir}}$, indicating a strong preference towards shallow orbits. To summarise, satellite galaxy orbits are especially important in the low stellar mass regime, as stellar mass shielding against ram-pressure stripping, which is especially violent near the cluster centre, becomes less efficient.

3.4.3 Impact of infall environment

We subdivided galaxies according to their environment at infall into three categories: isolated galaxies, group satellite galaxies and group centrals. This categorisation is useful in determining how the infall environment impacts the evolution of $\mathrm{SSFR} \cdot t_\mathrm{H}$. Similar to Figure 3.10, Figure 3.14 shows the normalisation to the maximum value of $\mathrm{SSFR} \cdot t_\mathrm{H}$ for each case. However, in contrast to previous figures, the infall of galaxies has been normalised to the point where `SUBFIND` identifies galaxies as members of the respective cluster Friends-of-Friends (FoF) halo. Therefore, infall into the cluster FoF halo is given by $\Delta \mathrm{t_{FoF}} = 0$. In this section, galaxies are identified via cluster FoF membership rather than virial radius crossing because this facilitates the identification of the environment prior to infall. The same population as in Section 3.4 was used, albeit only a subsample fulfils our group categorisation criterion, as we only consider groups with at least three

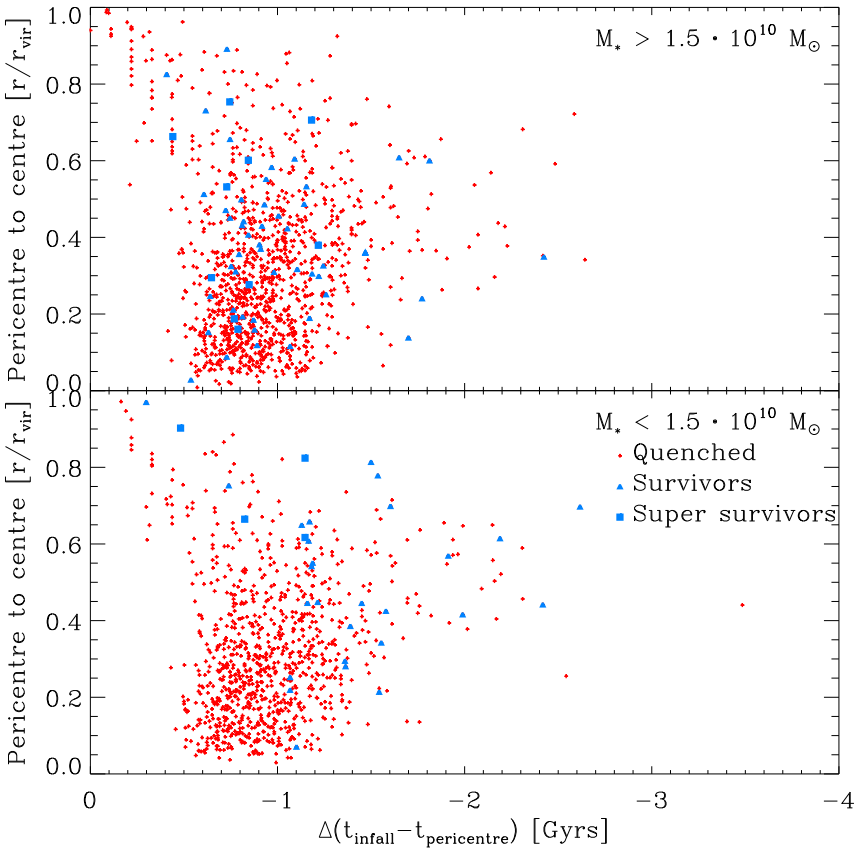

Figure 3.13: Satellite galaxy pericentre to centre of the cluster distance as a function of difference in time between infall and pericentre. Red crosses indicate all satellite galaxies which are quenched within 1 Gyr after infall. Blue triangles indicate all satellite galaxies which remain star-forming for longer than 1 Gyr after infall, while blue squares indicate satellite galaxies which remain star-forming longer than 1 Gyr after passing their pericentre. Top bin shows high stellar mass ($M_* > 1.5 \cdot 10^{10} \mathrm{M}_\odot$) and bottom bin shows low stellar mass ($M_* < 1.5 \cdot 10^{10} \mathrm{M}_\odot$) satellite galaxies.

different galaxies above our standard stellar mass threshold.

As demonstrated by Figure 3.14, the environment at infall has a strong impact on the evolution of star-formation. We find that group centrals (green) and group satellites (cyan) experience stronger quenching prior to cluster infall, while isolated (magenta) galaxies show a weaker decline in star-formation prior to cluster infall. In other words, higher environmental density correlates with stronger quenching prior to cluster infall. This supports the picture established by the morphology-density relation that a higher density environment is more effective in quenching galaxies (Dressler, 1980; Goto et al., 2003).

Similarly to what was shown in Figure 3.10, we also find that low stellar mass galaxies (solid line) are typically less quenched prior to infall compared to their high stellar mass (dashed line) counterparts. The exception to this is the low stellar mass central galaxy

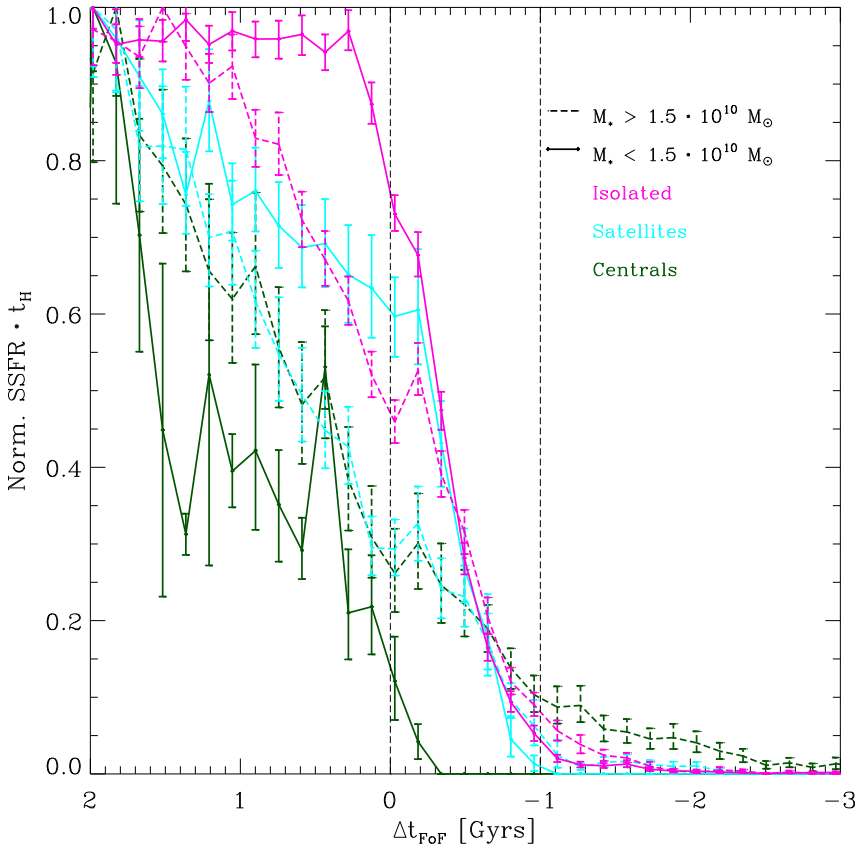

Figure 3.14: Same as Figure 3.10 but displaying different infall categories of satellite galaxies normalised to the point where SUBFIND identifies FoF membership, i.e. $\Delta t_{FoF} = 0$. In-falling satellite galaxies are subdivided into three high (dashed line) and low (solid line) stellar mass groups: isolated galaxies (magenta), group satellite galaxies (cyan) and group centrals (green).

population (green solid line), which only has a sample size of five, and is characterised by the strongest decline in star-formation prior to infall. Excluding the small low stellar mass central galaxy population, this suggests that *mass quenching*, i.e. stellar mass dependent mechanisms which are independent of the environment, play an important role in regulating star-formation in cluster outskirts. This is in agreement with findings from Peng et al. (2010) and Liu et al. (2019), who state that at higher stellar masses quenching is controlled by stellar mass, while at lower stellar masses the halo mass, i.e. environment, is the determining factor in galaxy quenching. Findings based on a smaller Magneticum box with higher resolution further support this notion, stating that environmental quenching is more important for satellite galaxies than for centrals (Teklu et al., 2017).

As shown in Figure 3.9 and 3.10, the original sample is split almost evenly between high (1182) and low (955) stellar mass. When considering the individual sample sizes in Figure 3.14, we find that more dense environments, i.e. groups, are characterised by

a relative overabundance of high stellar mass galaxies, while less dense environments, i.e. isolated galaxies, are characterised by a relative overabundance of low stellar mass galaxies. Specifically, we find 91 high stellar mass group centrals and 167 high stellar mass group satellites, compared to 5 low mass centrals and 99 low mass satellites. In contrast, we find fewer isolated high stellar mass galaxies (506) than isolated low stellar mass galaxies (610). Essentially, this is a reflection of hierarchical galaxy assembly: more dense environments are more likely to host higher stellar mass galaxies (Navarro et al., 1997).

Interestingly, the high stellar mass centrals (green dashed line) remain star-forming the longest after infall. This is likely due to two reasons: First, centrals typically are the most massive galaxy within a group, i.e. they have a higher probability of being able to retain their cold gas during ram-pressure stripping (see Section 3.4). Second, by definition centrals are embedded within a group environment. The group environment further mitigates the violent effects of the onset of ram-pressure stripping. As such, high stellar mass central galaxies belong to the select group of galaxies which do not experience rapid quenching. This is exemplified by the comparably weak gradient of the dashed green line in Figure 3.14.

In agreement with our previous results (see Section 3.4), Figure 3.14 provides evidence for a starburst in several populations at $\Delta t_{FoF} = -0.2$. The starburst is consistently stronger within the high mass populations. In this picture, a minimum stellar mass is needed to retain the cold gas component for a sufficiently long time to trigger a starburst, rather than an immediate continuous quenching.

3.5 Summary & discussion

Magneticum Pathfinder simulations are in fine agreement with a variety of observations, including AGN population properties (Hirschmann et al., 2014; Steinborn et al., 2015) and dynamical properties of galaxies (Remus et al., 2015; Teklu et al., 2015; Remus et al., 2017b). Especially relevant for this chapter are the agreements with Planck Collaboration et al. (2013); McDonald et al. (2014) on the pressure profiles of the intra-cluster medium. Furthermore, both the general shape of the anisotropy profile and its specific values are consistent with the cosmological simulations by Mamon et al. (2013).

The analysis of the anisotropy profiles at $z = 0.44$ in Figure 3.1 and their development in Figure 3.3 clearly shows that throughout varying redshifts and cluster masses the star-forming population is consistently on more radial orbits than the quiescent population. These findings are in good agreement with Biviano et al. (2013), but stand in opposition to other observations, which find that the quiescent population is more radially dominated than the star-forming population (Aguerri et al., 2017). While we find some clusters that behave similarly to the cluster (A85) studied by Aguerri et al. (2017), they are a rare exception.

The interpretation of the anisotropy behaviour found in Magneticum and Biviano et al. (2013) is consolidated by phase space considerations in Section 3.3. We not only find good agreement between observations and our simulation (see Figure 3.4), but also find that the

star-forming population is overwhelmingly comprised of in-falling satellite galaxies. The orbits of the star-forming satellite galaxies are radially dominated because, in contrast to their quiescent counterparts, that are less radially dominated, they are experiencing their first passage into the cluster. We find that the vast majority of star-forming satellite galaxies are quenched during their first passage (see Figures 3.9 and 3.10). This is in agreement with observations, which also find that galaxies experience strong quenching during their first passage through the cluster (Mahajan et al., 2011; Wetzel et al., 2013; Jaffé et al., 2015, 2016; Oman & Hudson, 2016).

The global decrease in anisotropy towards smaller radii is likely driven by an orbital selection mechanism. Of all the galaxies entering a galaxy cluster at a certain time, those that will survive until redshift zero are those characterised by the most tangential orbits at infall (Iannuzzi & Dolag, 2012). More radially dominated satellite galaxies are likely to experience tidal stripping to a stronger degree, resulting in a decrease in satellite galaxy mass and a subsequent drop below our resolution limit. Thus, the destruction of radially dominated orbits leads to a circularisation of the total population. The longer satellite galaxies are members of a given cluster the more likely it is that the more radially dominated subset is selectively destroyed. As older cluster members have a higher likelihood of orbiting at smaller radii, the anisotropy profile decreases towards smaller radii. However, due to smaller sample sizes leading to higher bootstrapping errors, the error scatter towards smaller radii increases and, thus, the ability to make meaningful physical deductions is impeded in the innermost regions.

Annunziatella et al. (2016) finds that passive low-mass ($M_* < 10^{10}\,\mathrm{M}_\odot$) galaxies at radii $R < 0.3\,\mathrm{R}_{200}$ are more likely to be on tangential orbits than their high mass ($M_* > 10^{10}\,\mathrm{M}_\odot$) counterparts. They propose that this may be the result of selective destruction of low mass galaxies on radial orbits through tidal stripping near the cluster centre (Annunziatella et al., 2016). The combination of low mass and small pericentres makes survival near the hostile cluster centre unlikely. As a result, low mass galaxies in the inner regions are only observed on tangential orbits since otherwise they face destruction. When considering passive satellite galaxies at $z \sim 0.2$ in the same cluster mass range as Annunziatella et al. (2016) ($M_{200} = 7.7^{+4.3}_{-2.7} \cdot 10^{14}\,\mathrm{M}_\odot$), we do not replicate the behaviour (Paulin-Henriksson et al., 2007). However, we find a similar behaviour for our star-forming population. Less massive star-forming galaxies are likely to be on more tangential orbits at $r/r_{\mathrm{vir}} \sim 0.5$ than their more massive counterparts.

The orbital selection effect observed by Annunziatella et al. (2016) for passive galaxies and to a lesser extent by our simulation for star-forming galaxies additionally supports the idea that specific orbits selectively influence the morphological transformation of galaxies. It further explains why red discs are identified by Kuchner et al. (2017) to inhabit phase space at projected radii between R_{500} and R_{200}, a region either associated with recent infall or tangential orbits. This would suggest that after blue discs are quenched via ram-pressure stripping during infall, thereby becoming red discs, their orbits fundamentally influence their morphological evolution. Provided they are on sufficiently tangential orbits their morphology remains fairly undisturbed. However, if the red disc galaxies are moving on radially dominated orbits they are likely to be disturbed while moving through their

pericentres, thus experiencing an accelerated evolution pathway towards elliptical galaxies.

Similarly to McCarthy et al. (2008); Bekki (2009); Jaffé et al. (2018), we find that ram-pressure stripping efficiencies depend on the orbital parameters and both the satellite and host halo mass. Specifically, high halo masses, low satellite masses and radially dominated orbits ensure more efficient ram-pressure stripping.

In contrast to Wetzel et al. (2012) and Wetzel et al. (2013), we find no evidence for 'delayed-then-rapid' quenching. Figure 3.2 suggests that if active, our AGN feedback might be more efficient in quenching compared to observations (Wetzel et al., 2012). The combination of stronger AGN feedback and higher quenching efficiencies in Magneticum results in shorter quenching timescales of satellite galaxies.

The higher quenching efficiency in Magneticum can be the result of three effects associated with the simulation. First, we consider the SSFR rather than the colour of galaxies, resulting in a more immediate representation of star-formation or lack thereof. This results in quenching being measured effectively instantaneously rather than delayed via colour changes. Second, the resolution of our simulations do not reproduce morphologies, especially we do not resolve cold thin discs. Consequently, the persistence of cold thin discs against ram-pressure is not properly captured and hence our galaxies are more vulnerable to environmental quenching. Third, stellar mass losses are not modelled to create new gas reservoirs, but rather are distributed to surrounding gas particles. In practice this means that stellar mass loss often is added to already stripped hot gas, further impeding new star-formation.

Similarly to Teklu et al. (2017), we find no meaningful signal dependence on whether we sample a spherical or cylindrical volume. We verified this by evaluating the phase space diagrams for both spherical and cylindrical volumes, where the radii of the sphere and cylinder were kept the same ($R_{\rm sph} = R_{\rm cyl}$), while the cylinder height $H_{\rm cyl}$ was varied, as described in the respective sections.

3.6 Conclusions

In this chapter we studied the velocity-anisotropy, the phase space and tracked the orbital behaviour of satellite galaxies in the cluster environment using the hydrodynamical cosmological *Magneticum Pathfinder* simulations. The evaluation of satellite galaxies in clusters of different mass above the mass threshold of $10^{14}\,\mathrm{M}_\odot$ at varying redshifts between $z \sim 2$ and present-day has provided a wide statistical sample. Furthermore, satellite galaxy behaviour was compared to observations at $z = 0.44$ and $z = 1.18$ (Biviano et al., 2013; Muzzin et al., 2014). The results can be summarised as follows:

- Star-forming satellite galaxies are consistently characterised by more radial orbits than their quiescent counterparts. The velocity-anisotropy profiles show that this behaviour is independent of cluster masses in the studied range $(1-90)\cdot 10^{14}\,\mathrm{M}_\odot$ and in the redshift range $2 > z > 0$. Independent of the population under consideration, the velocity-anisotropy profiles are more radially dominated in the outskirts, while tending towards isotropy at smaller radii.

- The velocity-anisotropy profile calculated based on the Magneticum simulations is in good agreement with the observations from Biviano et al. (2013) at $z = 0.44$. Both the dichotomy between star-forming and quiescent satellite galaxies is reproduced, as is the general decrease towards isotropy at smaller radii. The overwhelming majority of simulated data points lie within the 1σ confidence regions of the observations.

- The line-of-sight phase space comparison shows good agreement between observations and the Magneticum simulations. However, we find a stronger dichotomy between star-forming and quiescent satellite galaxies than the observations conducted by Biviano et al. (2013) at $z = 0.44$. Nonetheless, the overall behaviour is similar: star-forming satellite galaxies are found predominantly outside $R_{200,\mathrm{crit}}$, while quiescent satellite galaxies overwhelmingly lie within $R_{200,\mathrm{crit}}$.

- The radial phase space study in the cluster mass range $(1 - 90) \cdot 10^{14}\,\mathrm{M}_\odot$ and in the redshift range $2 > z > 0$ provided an overview of different quenching efficiencies. We find that high cluster mass and, to a lower extent, low redshift increase quenching of the star-forming satellite galaxies. In addition, we find that the vast majority of star-forming satellite galaxies are quenched during their first passage, independent of cluster mass and redshift.

- The tracking of individual orbits and their specific star-formation over time demonstrates that satellite galaxies experience strong quenching in the vicinity of the virial radius. The overwhelming majority of satellite galaxies are quenched within 1 Gyr after infall, i.e. during their first passage. Further, we find that high stellar mass satellite galaxies ($M_* > 1.5{\cdot}10^{10}\,\mathrm{M}_\odot$) experience an earlier onset of quenching, leading to a longer quenching timescale $t_{\mathrm{high}} \sim 2 - 3\,\mathrm{Gyr}$ than their low stellar mass counterparts ($M_* < 1.5 \cdot 10^{10}\,\mathrm{M}_\odot$), which experience quenching on timescales $t_{\mathrm{low}} \sim 1\,\mathrm{Gyr}$.

- When solely considering satellite galaxies that 'survive', i.e. satellite galaxies that remain star-forming longer than 1 Gyr after infall, we find a difference between high and low stellar mass satellite galaxies. Low stellar mass satellite galaxies are characterised by atypically shallow orbits. Provided a satellite galaxy is able to maintain a relatively large radial distance $\gtrsim 0.5\,\mathrm{R}_{\mathrm{vir}}$ by having a strongly tangentially supported orbit, it will be quenched on a longer timescale, i.e. it will be more likely to be strangled than stripped.

- In contrast, high stellar mass satellite galaxies have an increased probability of survival provided they have a very high stellar mass, i.e. they belong to the highest mass subset of the high mass satellite galaxies. Specifically, the 55 high mass survivors have a mean stellar mass of $M_* = 2.38{\cdot}10^{11}\,\mathrm{M}_\odot$, while the total high mass population of 1182 satellite galaxies has a mean stellar mass of $M_* = 6.01 \cdot 10^{10}\,\mathrm{M}_\odot$, a factor of ~ 4 difference.

- Prior to cluster infall, we find that higher environmental density correlates with a stronger decline in star-formation. Specifically, group centrals experience a stronger

decline in star-formation than group satellites, which in turn experience stronger quenching than isolated galaxies prior to infall. Furthermore, high stellar mass galaxies typically experience stronger quenching prior to infall than low stellar mass galaxies, suggesting that mass quenching plays an important role in regulating star-formation in the outskirts of clusters.

In summary, the results suggest three fundamental conclusions: First, the dominant quenching mechanism in galaxy clusters is ram-pressure stripping. Second, ram-pressure stripping is sufficiently effective to quench the overwhelming majority of star-forming satellite galaxies within $\sim 1\,\mathrm{Gyr}$ during their first passage. Third, ram-pressure stripping preferentially quenches radial star-forming satellite galaxies.

Chapter 4

Rise and fall of post-starburst galaxies

This chapter has been released in Lotz et al. (2020).

Abstract

Context: Post-starburst galaxies (PSBs) belong to a short-lived transition population between star-forming and quiescent galaxies and are found in all environments and at all redshifts. Deciphering their heavily discussed evolutionary pathways is paramount to understanding the processes that drive galaxy evolution in general.

Aim: We aim to determine the dominant mechanisms governing PSB galaxy evolution in both the field and in galaxy clusters.

Method: To understand the different physical processes involved in PSB galaxy evolution, we analyse the cosmological hydrodynamical simulation suite *Magneticum Pathfinder*. At $z \sim 0$, we identify and study a set of 647 PSBs with stellar masses $M_* \geq 4.97 \cdot 10^{10}\,\mathrm{M}_\odot$, in comparison to a quiescent and a star-forming control sample. We track the galactic evolution, merger history, and black holes of PSBs and control samples over a time-span of 3.6 Gyr. Additionally, we study cluster PSBs identified at different redshifts and cluster masses.

Results: Independent of environment and redshift, we find that PSBs, similar to the star-forming control sample, have frequent mergers. At $z = 0$, 89% of PSBs have experienced at least one merger, and 65% even had a major merger event within the last 2.5 Gyr, leading to episodes of strong star formation. In fact, 23% of $z = 0$ PSBs were even rejuvenated before being quenched again after the starburst. After the mergers, field PSBs are generally shutdown via a strong increase in active galactic nucleus (AGN) feedback (the power output is $P_{AGN,PSB} \geq 3 \cdot 10^{56}\,\mathrm{erg/Myr}$). Furthermore, we find agreement with

observations for both stellar mass functions and $z = 0.9$ line-of-sight phase space distributions of galaxy cluster PSBs. Finally, we find that $z \lesssim 0.5$ cluster PSBs are predominantly infalling, especially in high mass clusters and show no signs of enhanced AGN activity. Thus, we conclude that the majority of cluster PSBs are shutdown via an environmental quenching mechanism such as ram-pressure stripping, while field PSBs are mainly quenched by AGN feedback.

4.1 Sample selection

Galaxies are selected to have a minimum stellar mass of $M_* \geq 3.5 \cdot 10^{10}\,h^{-1}\mathrm{M}_\odot$, corresponding to a minimum of ~ 1000 stellar particles for a given galaxy. The only exceptions to this stellar mass threshold is found in Section 4.5, where the threshold is reduced to $M_* \geq 3.5 \cdot 10^{9}\,h^{-1}\mathrm{M}_\odot$ to increase the available sample size in cluster environments. The additional use of Box2b and the lowering of the stellar mass threshold is done to increase the abundance of PSBs within galaxy cluster environments.

We identify post-starburst galaxies (PSBs) in the Magneticum simulations based on the stellar particle age and the 'blueness criterion' (see Section 2.2.2, specifically Equation 2.7): Of all stellar particles of a galaxy, at least 2% need to be younger than 0.5 Gyr. In addition, the galaxy's blueness at identification needs to be smaller than $\mathrm{SSFR} \cdot t_\mathrm{H} < 0.3$. These two parameters describe galaxies that have a sufficiently large young stellar population, while also no longer being star-forming, i.e. galaxies that have experienced a recent starburst. In particular, we choose this criterion as it implies a minimum average SSFR within the past 0.5 Gyr of $\mathrm{SSFR} \geq 4 \cdot 10^{-11}\,\mathrm{yr}^{-1}$, similar to the criterion used by Davis et al. (2019). To verify that our results are robust, we initially varied both the young stellar mass percentage (1, 2, 5 or 10 per cent) and the associated evaluation timescale (0.5, 1 or 2 Gyr). Although the resulting sample size varied, the conclusions and the agreement with observations remained robust.

When considering all Box2 galaxies fulfilling these criteria we obtain a sample of 647 PSBs at $z \sim 0$. This global sample provides the basis of the majority of our analysis and is complemented by additional specific environmental and redshift selections where necessary. To understand how PSBs differ from other galaxies, we introduce two stellar mass matched control (SMMC) samples: quenched (QSMMC) and star-forming (SFSMMC) galaxies, using the above blueness criterion for differentiation. The control samples are constructed by selecting the closest quenched and star-forming stellar mass match for each PSB galaxy at identification redshift. In terms of the star formation at identification redshift the QSMMC sample is indistinguishable from PSBs.

In order to disentangle the details causing the starburst and the following shutdown in star formation, we consider the temporal evolution of PSBs. To this end, we employ two complementary methods to track and trace both PSBs and control galaxies in Box2 of the Magneticum simulations. First, we identify the main galactic black hole particle associated with a galaxy and track this particle and subsequently its host backwards in time. This method provides a temporal resolution of 0.43 Gyr, as only every fourth time step has stored particle data. Second, we analyse the merger trees of the galaxies in question, yielding a complete merger history with a temporal resolution of 0.11 Gyr.

4.2 Environment, distribution, and evolution of post-starburst galaxies

4.2.1 Quenched and PSB fractions

Understanding the abundance of specific galaxy types at different halo masses, i.e. in different environments, is crucial for determining the relevant formation and evolutionary mechanisms of PSBs. Specifically, the environment is key to understanding potential triggers of the starburst phase and, subsequently, the causes of the star formation shutdown. Lotz et al. (2019) already demonstrated agreement between Box2 and observations of quenched fractions at intermediate stellar masses $\log_{10}(M_*/\mathrm{M}_\odot) = [9.7, 11.3]$ (Wetzel et al., 2012). We now extend our investigation to higher stellar mass galaxies $\log_{10}(M_*/\mathrm{M}_\odot) = [10.70, 12.00]$, as well as presenting predictions of the PSB-to-quenched fraction.

Figure 4.1 (top) shows a number of trends and behaviours relating to the quenched fraction: First, at redshifts $z \lesssim 1$ the vast majority ($\geq 80\%$) of galaxies in the stellar mass range $\log_{10}(M_*/\mathrm{M}_\odot) = [10.70, 12.00]$ (black) are quenched, independent of host halo mass. The only exception to this is found in the highest stellar mass bin ($\log_{10}(M_*/\mathrm{M}_\odot) = [11.67, 12.00]$), which shows lower quenched fractions with increasing halo mass, because above halo masses $M_{200,\mathrm{crit}} \geq 10^{14}$ these high mass galaxies are dominated by brightest cluster galaxies (BCGs), which experience episodes of star formation as a result of gas accretion.

Second, Figure 4.1 shows varying agreement with observations: We find broad agreement between our $z = 0.07$ quenched fractions and $0.01 < z < 0.12$ observations by Wang et al. (2018), which are based on NYU-VAGC (Blanton et al., 2005) and SDSS DR7 (Abazajian et al., 2009). Although our Box2 galaxies are characterised by higher quenched fractions and a less distinct split between stellar masses at $z \sim 0$ compared to observations, observations are similarly characterised by high quenched fractions at low redshift, especially towards higher halo mass. When comparing our results at $0.25 < z < 1.04$ to observations of central galaxies in COSMOS groups at median redshift bins $z = [0.36, 0.66, 0.88]$ (George et al., 2011; Tinker et al., 2013), we find the strongest agreement towards higher redshifts, while the lower redshift comparison lacks good agreement. At high redshift, we compare our $z = 1.32$ and $z = 1.71$ results to SPT-SZ cluster galaxies at redshifts $z = [1.38, 1.401, 1.478]$ and $z = [1.520, 1.720]$, respectively (Strazzullo et al., 2019). The cluster galaxies have stellar masses above the common mass completeness limit $\log_{10}(M_*/\mathrm{M}_\odot) > 10.85$, and the quenched fractions are calculated for cluster radii $r < 0.45\, r_{500}$ and $r < 0.7\, r_{500}$ (Strazzullo et al., 2019). To better compare with our results, we convert the halo mass from M_{500} (Strazzullo et al., 2019) to M_{200}, assuming an NFW profile with constant concentration ($c = 5$) (Pierpaoli et al., 2003). The resulting comparison agrees well with our $z = 1.32$ results. Nonetheless, the trend whereby the quenched fraction at constant stellar mass increases towards lower redshift agrees with established models (Hopkins et al., 2008a) and simulations (Behroozi et al., 2019).

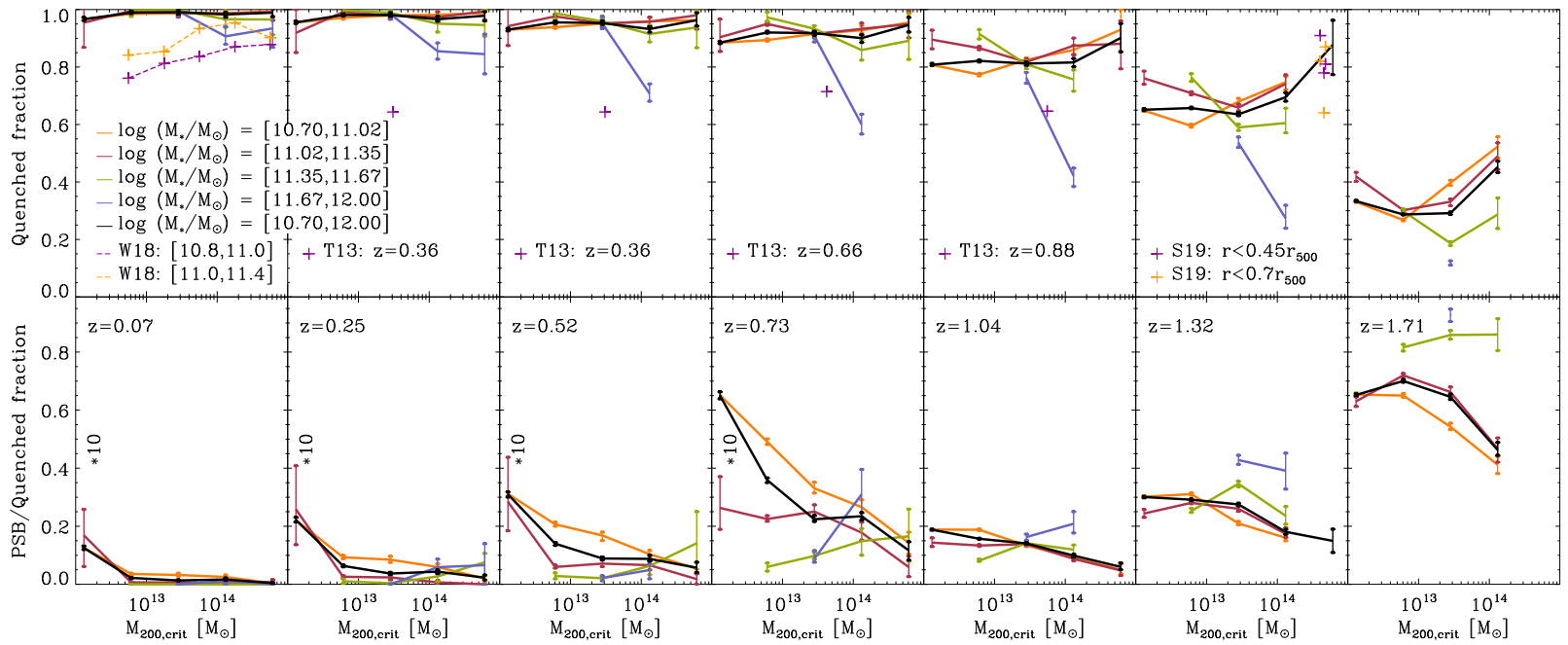

Figure 4.1: Fraction of quenched galaxies (top) and fraction of PSB-to-quenched galaxies (bottom) as a function of $M_{200,\mathrm{crit}}$ halo mass, at different redshifts $0.07 < z < 1.71$ (increasing from left to right) for all Box2 galaxies. Each panel is subdivided into four unique stellar mass bins (colour coded) and one bin showing the behaviour across the entire evaluated stellar mass range $\log_{10}(M_*/\mathrm{M}_\odot) = [10.70, 12.00]$ (black). The quenched and PSB-to-quenched fraction is only shown if the denominator in each case is larger than 100 galaxies. Error bars are calculated via bootstrapping. Note that the PSB-to-quenched fractions at redshifts $z = [0.07, 0.25, 0.52, 0.73]$ is multiplied by a factor of 10, as indicated in the panels, in order to facilitate viewing. At $z = 0.07$, we compare the quenched fraction with low redshift observations in the stellar mass range $\log_{10}(M_*/\mathrm{M}_\odot) = [[10.8, 11.00], [11.0, 11.4]]$ (Wang et al., 2018). At intermediate redshifts, we compare the quenched fractions to central galaxies in COSMOS groups (George et al., 2011; Tinker et al., 2013). In the two highest redshift panels, we compare our results to $1.38 < z < 1.72$ cluster galaxies above the common mass completeness limit $\log_{10}(M_*/\mathrm{M}_\odot) > 10.85$ within $r < 0.45r_{500}$ and $r < 0.7r_{500}$ of SPT-SZ galaxy clusters (Strazzullo et al., 2019).

Third, towards higher redshifts ($z > 1$) our quenched fraction begins to drop and the differences between the stellar mass bins become larger than the bootstrapped errors associated with the individual bins. At $z = 1.71$, we find the highest quenched fraction in the lowest stellar mass bin $\log_{10}(M_*/M_\odot) = [10.70, 11.02]$. This is likely due to higher stellar mass galaxies at this redshift having undergone more recent mass growth, which is typically associated with star formation, thus leading to lower quenched fractions in high stellar mass compared to low stellar mass galaxies. In brief, environmental quenching is more effective than mass quenching at high redshift.

When comparing the PSB-to-quenched fraction in the bottom panels of Figure 4.1, we find that the qualitative behaviour remains broadly similar at redshifts $z \lesssim 1$: The highest abundance of PSBs is consistently found at low stellar and halo masses. We note, that the PSB-to-quenched fractions at redshifts $z \leq 0.73$ are multiplied by a factor of 10 to facilitate viewing. In other words, the PSB-to-quenched fraction is consistently below 7% at redshifts $z \leq 0.73$. Furthermore, the lower the redshift, the lower the PSB-to-quenched fraction. This agrees with observations of PSBs with stellar masses $10.0 < \log_{10}(M_*/\mathrm{M}_\odot) < 12.5$, which find that the fraction of PSBs declines from $\sim 5\%$ of the total population at $z \sim 2$, to $\sim 1\%$ by $z \sim 0.5$ (Wild et al., 2016). Similarly, DEEP2 and SDSS results find that $z \sim 0$ PSBs are found in relatively under-dense environments, while at $z \sim 1$ they are found in relatively over-dense environments (Yan et al., 2009).

At higher redshifts ($z \geq 1.3$) PSBs are no longer most often found at low stellar masses. In particular, the low redshift preference for low stellar masses appears to be inverted at high redshift. High stellar mass galaxies at high redshift belong to the subset of galaxies characterised by the quickest mass assembly. When high stellar mass galaxies become quenched at high redshift, they likely host a significant population of young stars, thus fulfilling our PSB selection criteria. As a result the PSB-to-quenched fraction at high redshift is highest among high stellar mass galaxies.

At low redshifts ($z \leq 0.73$), the PSB-to-quenched fraction exhibits the highest abundances at low halo masses. With increasing redshift ($z \geq 1$), the PSB-to-quenched fraction shows less preference for low halo mass. We conclude, Figure 4.1 (bottom) suggests that both the redshift and environment play an important role in the specific evolution of PSBs.

4.2.2 Stellar mass functions of satellite galaxies

Evaluating the galaxy stellar mass distribution is critical for understanding the relative importance of different evolutionary mechanisms: Figure 4.2 shows the redshift evolution of the stellar mass function and its various components, as well as comparisons to observations. As such, Figure 4.2 provides a useful extension of Figure 4.1 by displaying the stellar mass distribution and an additional component-wise split into various samples. Although we only consider high mass PSBs ($M_* \geq 4.97 \cdot 10^{10}$) for our analysis, we have extended the stellar mass function below our mass threshold, which is indicated by a vertical dashed dotted black line at $\log_{10}(M_*/\mathrm{M}_\odot) \sim 10.7$.

Throughout the studied redshift range ($0.07 < z < 1.71$) displayed in Figure 4.2, the total stellar mass function (1st row) shows little evolution. When comparing the

total stellar mass function with observations based on COSMOS / UltraVISTA (Muzzin et al., 2013), we find agreement at all redshifts, especially towards lower redshifts. In contrast, the star-forming population (2nd row) shows a significant redshift evolution and only matches observations well at high redshift. The kink in the star-forming stellar mass function at $\log_{10}(M_*/\mathrm{M}_\odot) \sim 10.3$, which becomes more evident with decreasing redshift, is the result of our active galactic nucleus (AGN) feedback. Specifically, above these stellar masses the AGN begins to continuously quench galaxies, leading to a relative under-abundance of star-forming galaxies in the stellar mass range $\log_{10}(M_*/\mathrm{M}_\odot) \sim [10.3, 11.5]$ (Steinborn et al., 2015). This difference becomes most evident when comparing our results to observational surveys based on GAMA ($z < 1$) (Rowlands et al., 2018) and on UKIDSS UDS ($0.5 < z < 2$) (Wild et al., 2016). This relative lack of star-forming galaxies, compared to observations, becomes stronger towards lower redshifts, as more galaxies host AGN. This effect also influences the total and quenched stellar mass functions, as evidenced by the perturbation found at $\log_{10}(M_*/\mathrm{M}_\odot) \sim 10.4$ in an otherwise fairly smooth distribution.

When viewing the evolution of the PSB stellar mass function with redshift in Figure 4.2, we find a significant evolution: At low redshifts PSBs are primarily found below our stellar mass cut (vertical dashed dotted black line), while they are typically found above our stellar mass cut at high redshifts. In other words, the abundance of PSBs above our stellar mass threshold increases significantly with increasing redshift. This strong redshift evolution agrees with VVDS observations, which find that the mass density of strong PSB galaxies is 230 times lower at $z \sim 0.07$ than at $z \sim 0.7$ (Wild et al., 2009). When comparing the shape of the PSB galaxy stellar mass function to observations (Wild et al., 2016; Rowlands et al., 2018), we do not find close agreement. However, we note that observations at similar redshifts, as indicated by the legend in the bottom row of Figure 4.2, do not appear to show agreement either. This may be due to different selection mechanisms: While Wild et al. (2016) derive three eigenvectors, termed super-colours, via a principal component analysis (PCA) of the spectral energy distribution (SED) (Wild et al., 2014), Rowlands et al. (2018) use two spectral indices based on a PCA to distinguish different galaxy types. In contrast, we determine the percentage of young stars formed within the last 0.5 Gyr and the current star formation rate (SFR) (see Section 4.1). Evaluating the SED compared to the numerical star formation may lead to discrepancies. In short, the PSB stellar mass function appears quite sensitive to the exact selection criteria, both in our simulation and in observations.

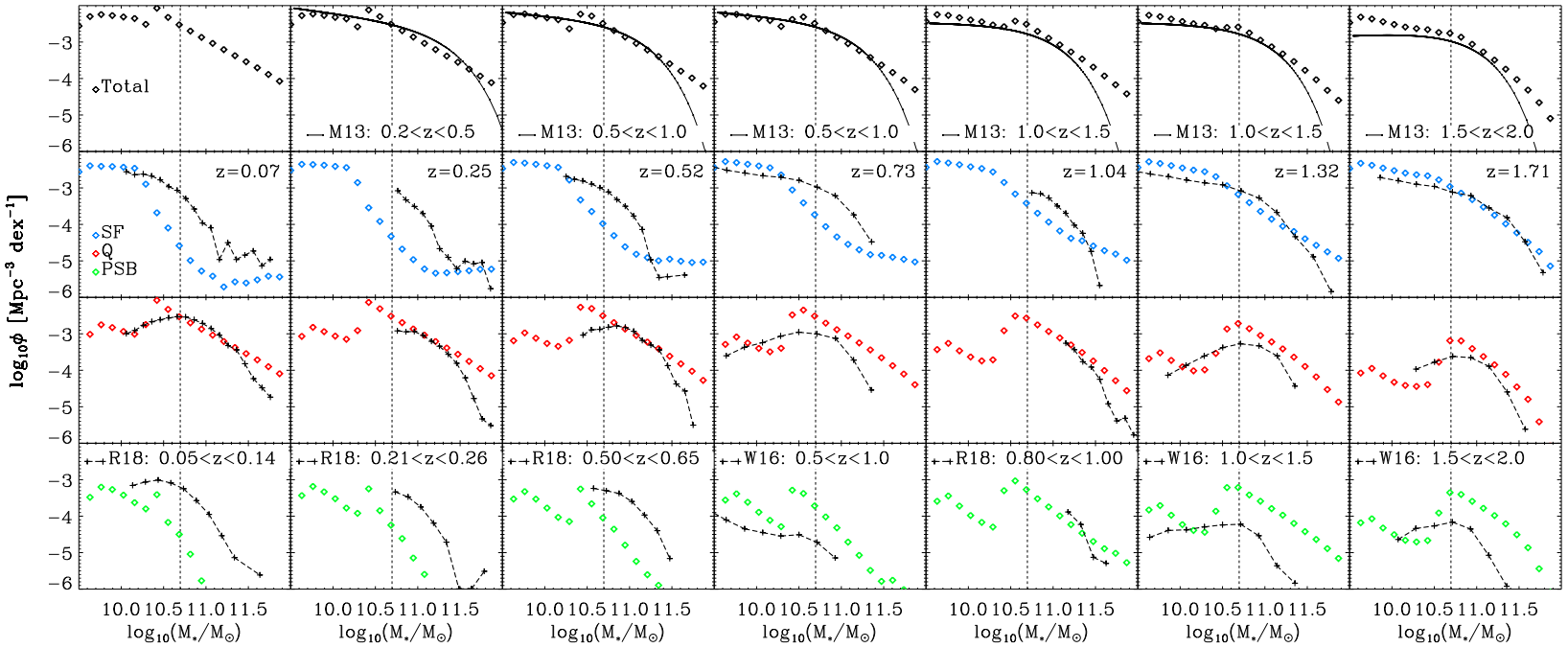

Figure 4.2: Stellar mass functions of all Magneticum Box2 galaxies, split into total (1st row), star-forming (SF: 2nd row), quenched (Q: 3rd row) and PSB galaxies (4th row) at different redshifts in the range $0.07 < z < 1.71$ (increasing from left to right). The vertical dashed dotted black line at $\log_{10}(M_*/\mathrm{M}_\odot) \sim 10.7$ indicates our standard stellar mass threshold. The total stellar mass function (1st row) is compared to $z < 4$ observations based on COSMOS / UltraVISTA, abbreviated with M13 (Muzzin et al., 2013). The SF, Q, and PSB selection is compared to two observational surveys: Rowlands et al. (2018), abbreviated as R18, based on GAMA ($z < 1$), and Wild et al. (2016), abbreviated as W16, based on UKIDSS UDS ($0.5 < z < 2$).

4.2.3 Galaxy distribution within halos

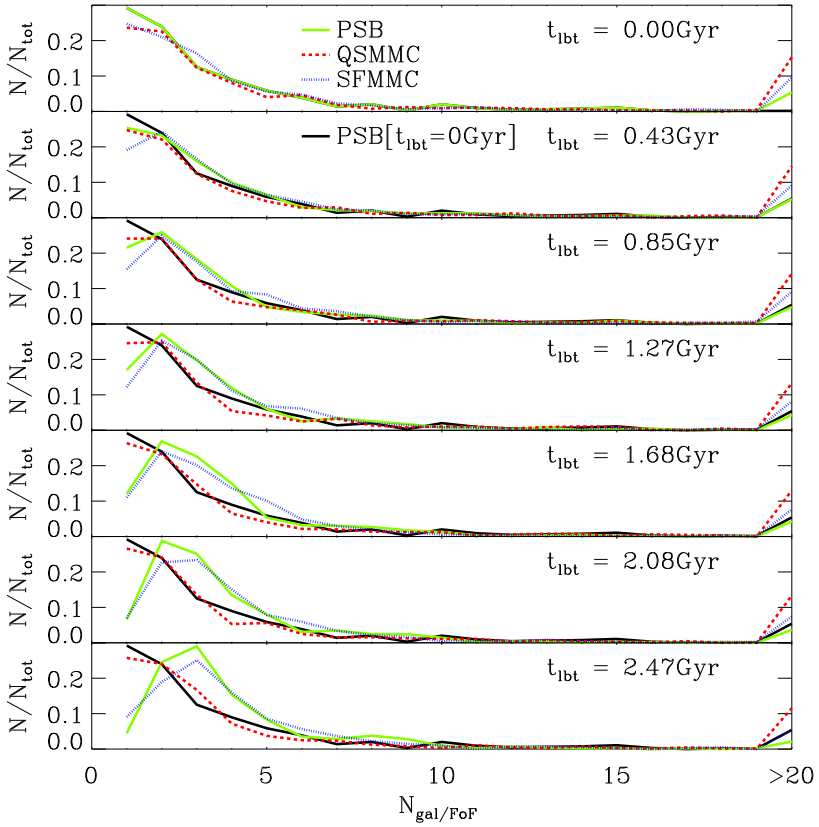

Figure 4.3: Distribution of $N_{gal/FoF}$, the number of galaxies per Friends-of-Friends (FoF) halo, of PSBs (green), quenched (QSMMC, red), and star-forming stellar mass matched control sample (SFSMMC, blue) galaxies as a function of look-back-time $t_{\rm lbt}$. Galaxies are identified at $t_{\rm lbt} = 0\,$Gyr (top panel), thereafter their progenitors are tracked back to $t_{\rm lbt} \sim 2.5\,$Gyr (bottom panel). For a comparison, the PSB $t_{\rm lbt} = 0\,$Gyr distribution is included in each panel as a solid black line. All FoFs with more than 20 galaxies are grouped together in the last bin.

Figure 4.3 shows the distribution of the number of galaxies per Friends-of-Friends (FoF, see Section 2.2.2) halo $N_{\rm gal/FoF}$ of all PSBs identified at $z \sim 0$ in Box2. All PSBs (green solid lines) were tracked from present-day back over the last 2.5 Gyr. To better understand how PSBs differ from other galaxies, quenched (red dashed lines) and star-forming (blue dotted lines) stellar mass matched control samples (QSMMC and SFSMMC, respectively) of galaxies and their evolution are shown in addition.

We find a significantly stronger evolution of $N_{\rm gal/FoF}$ in the PSB (green) and SFSMMC (blue) samples compared to the QSMMC (red) sample. At $t_{\rm lbt} = 0\,$Gyr (top panel), the PSB, QSMMC, and SFSMMC samples initially share a similar distribution. The only meaningful exception being the largest bin, i.e. $N_{\rm gal/FoF} > 20$, which is a factor of ~ 3 larger

for the QSMMC compared to the PSB sample, indicating a preference of quenched galaxies for richer membership FoF halos. In contrast, PSBs are rarely found in rich membership FoF halos. In high membership FoF halos, star-forming galaxies lie in intermediate ranges, centred between the other two samples. The varying galaxy abundances in different halo mass ranges are listed in the bottom row of Table 4.4. As the look-back-time increases, we find that PSBs, and to lesser degree the SFSMMC galaxies, develop a clear peak around $N_{\mathrm{gal/FoF}} \sim 3$, while values of $N_{\mathrm{gal/FoF}} = 1$ experience a strong decrease. In contrast, the QSMMC distribution remains fairly similar over time. This fundamental difference in evolution of PSB and star-forming galaxies compared to quiescent galaxies suggests that the initial environment at $t_{\mathrm{lbt}} = 2.5\,\mathrm{Gyr}$ plays an important role in influencing star formation, and subsequently PSB galaxy evolution.

At $t_{\mathrm{lbt}} = 2.5\,\mathrm{Gyr}$ the overwhelming majority of halos in which PSBs (and SFSMMC galaxies) are found, host $N_{\mathrm{gal/FoF}} \sim 2-4$ galaxies. This differs significantly from QSMMC galaxies, which are most often found in halos hosting one galaxy. In contrast, PSBs are rarely found with $N_{\mathrm{gal/FoF}} = 1$, indicating that they are usually not found in isolation[1]. The similarity between the PSB and SFSMMC distributions at $t_{\mathrm{lbt}} = 2.5\,\mathrm{Gyr}$, shown in the bottom panel of Figure 4.3, suggests that star formation is associated with the relative abundance of galaxies in the direct environment. When connecting the initial abundance of galaxies within the FoF halo with the decrease in the number of galaxies found at lower look-back-times, a mechanism linked to the interaction with other galaxies appears likely. Specifically, Figure 4.3 suggests that galaxy-galaxy processes, such as mergers with nearby galaxies, are important in supporting star formation, as well as possibly being linked to the starburst phase and the following star formation shutdown which characterise PSBs.

4.2.4 A closer look: Evolution of massive post-starburst galaxies

In Table 4.1 we introduce six massive PSBs, which we study in more detail alongside the total population of 647 PSBs. These six massive PSBs are chosen based on their high stellar mass, i.e. higher number of stellar particles, which allows a more detailed (spatial) examination of the involved physical processes. Table 4.1 lists relevant galactic and halo properties of the six PSBs at $t_{\mathrm{lbt}} = 0\,\mathrm{Gyr}$. Similar to the vast majority (89%) of the global 647 PSB sample (see bottom row in Table 4.4), five of our six massive PSBs are found in halos with halo mass $M_{200,\mathrm{crit}} < 10^{13}\,\mathrm{M}_{\odot}$.

Figure 4.4 shows the diverse distributions of the number of stars born at a given look-back-time for the six massive PSBs: The first (last) three galaxies of Table 4.1 are displayed in the top (bottom) row. The star formation histories shown in Figure 4.4 vary: While some massive PSBs are characterised by continuous star formation in recent look-back-times (pink, blue), others show recent strong star formation (black). Both Table 4.1 and Figure 4.4 show that massive PSBs with very different properties and star formation histories are captured by our criteria outlined in Section 4.1 and that the star formation

[1]We note that the number of galaxies found in a given halo is a function of resolution and thus the differences in relative abundance between galaxy types is a more robust quantity.

events of PSBs can be (triggered) rather differently.

ID	M_* $[10^{11}\,\mathrm{M}_\odot]$	SSFR$\cdot t_\mathrm{H}$	M_{gas} $[10^{11}\,\mathrm{M}_\odot]$	M_{cgas} $[10^{11}\,\mathrm{M}_\odot]$	M_{BH} $[10^{7}\,\mathrm{M}_\odot]$	$M_{200,\mathrm{crit}}$ $[10^{12}\,\mathrm{M}_\odot]$	R_{200} [kpc]	$N_{\mathrm{gal,halo}}$
430674	1.55	0.18	6.57	1.42	5.32	6.70	405	13
472029	1.52	0.00	6.42	0.96	22.5	7.67	424	6
625491	1.24	0.21	2.09	0.92	8.02	2.21	280	3
711135	1.20	0.05	1.30	0.34	8.10	1.45	243	1
417642	1.11	0.00	0.90	0.74	17.6	10.9	477	8
659121	1.08	0.00	1.90	0.64	12.0	1.96	269	1

Table 4.1: Overview of properties of six massive PSBs at $z \sim 0$ which are studied in greater detail. From left to right: (1) `SUBFIND` identification (2) Stellar mass, (3) Blueness, (4) Gas mass, (5) Cold gas mass, (6) BH mass, (7) Halo mass, (8) Halo radius, (9) Number of galaxies in halo. All values are given at $t_\mathrm{lbt} = 0\,\mathrm{Gyr}$.

4.2.5 Main sequence tracks

Figure 4.5 shows the positions of post-starburst (PSB: green) and star-forming (SF: blue) galaxies and their progenitors in the stellar mass - star formation rate (SFR) plane from left to right at $z = 0.4$ (1st panel), peak PSB star formation (2nd panel), $z = 0.1$ (3rd panel), and the evolution of the six massive PSBs (4th panel) introduced in Table 4.1. To compare the behaviour with observations, we have added main sequence fits (shaded regions) for redshifts $z = 0.4$ and $z = 0.1$ (Speagle et al., 2014; Pearson et al., 2018). The six massive PSBs in the right panel are identified at $z = 0.07$ (crosses), i.e at $t_\mathrm{lbt} = 0\,\mathrm{Gyr}$. The PSB progenitors are then tracked backwards in intervals of $t_\mathrm{lbt} \sim 0.11\,\mathrm{Gyr}$, yielding additional data points (small diamonds). PSB progenitors are tracked to maximum redshift of $z = 0.42$ (triangle), i.e. to $t_\mathrm{lbt} \sim 3.6\,\mathrm{Gyr}$, depending on how recently their BHs have been seeded (see Section 4.4.2 for more details). Additionally, the relative deviation of galaxies from the observationally based redshift evolving main sequence (MS) fit (Pearson et al., 2018) is plotted in the top panels, i.e. $\Delta MS[z]/MS[z] = (SFR[z] - MS[z])/MS[z]$. In other words $\Delta MS[z]/MS[z] = 0$ galaxies lie on the main sequence, positive (negative) values correspond to the factor they lie above (below) the main sequence.

The $z = 0.4$ display of PSB (green) and SF (blue) galaxies in Figure 4.5 (1st panel) shows no meaningful difference between the two populations. Both populations match the behaviour of the general distribution of the main sequence of Magneticum galaxies at the same redshift, which is shown in the underlying grey density distribution. Furthermore, the general Box2 Magneticum galaxy distribution (grey), as well as the PSB and SF galaxies are well described by observational fits at the $z = 0.4$ (Speagle et al., 2014; Pearson et al., 2018). We note that the least amount of galaxies are found in the first panel, compared to second, and especially the third panel of Figure 4.5, because not all galaxies can be traced

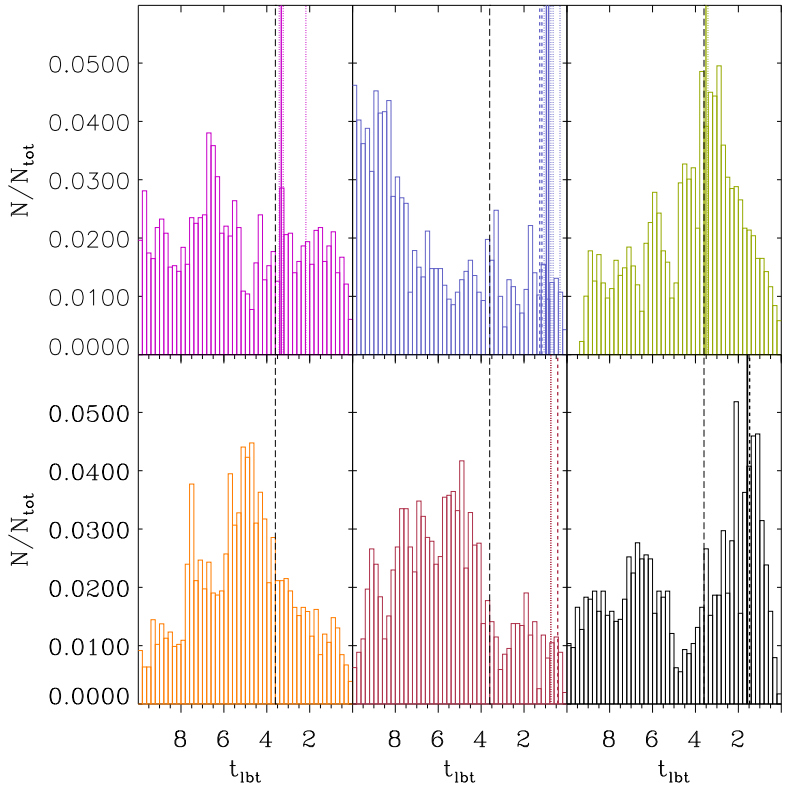

Figure 4.4: Star formation history, i.e. distribution of born stars as a function of look-back-time, of the six massive PSBs introduced in Table 4.1. First row IDs from left to right: 430674, 472029, 625491. Second row IDs from left to right: 711135, 417642, 659121. Coloured vertical lines indicate merger events (more easily visible in Figure 4.9): major (solid), minor (dashed), and mini (dotted). Black dashed line indicates maximum merger tree look-back-time, i.e. only recent mergers with $t_{\rm lbt} \lesssim 3.6\,{\rm Gyr}$ are shown.

back to higher redshifts. Furthermore, at $z = 0.4$ galaxies with $SFR = 0$ are not shown due to the logarithmic scaling.

The second panel in Figure 4.5 displays the distribution of PSB and SF galaxies at the height of PSB star formation within $t_{\rm lbt} < 1.48\,{\rm Gyr}$, i.e. since $z = 0.19$. If available, the corresponding SFSMMC galaxy to a given PSB galaxy is displayed, otherwise a random unique SFSMMC at the same redshift is shown for comparison. The median PSB peak star formation occurs at $z = 0.13$, i.e. at $t_{\rm lbt} = 0.75\,{\rm Gyr}$. When comparing the two populations we find that PSBs are characterised by higher SFRs than SFSMMC galaxies, as illustrated by the dashed horizontal lines indicating the median of each population at different stellar mass intervals. We note that the recent SFR of the most massive progenitors, as shown in Figure 4.5, need not be linked to a young stellar population at $t_{\rm lbt} = 0\,{\rm Gyr}$, as is expected for PSBs. This is evidenced by the fact that within our PSB sample we have

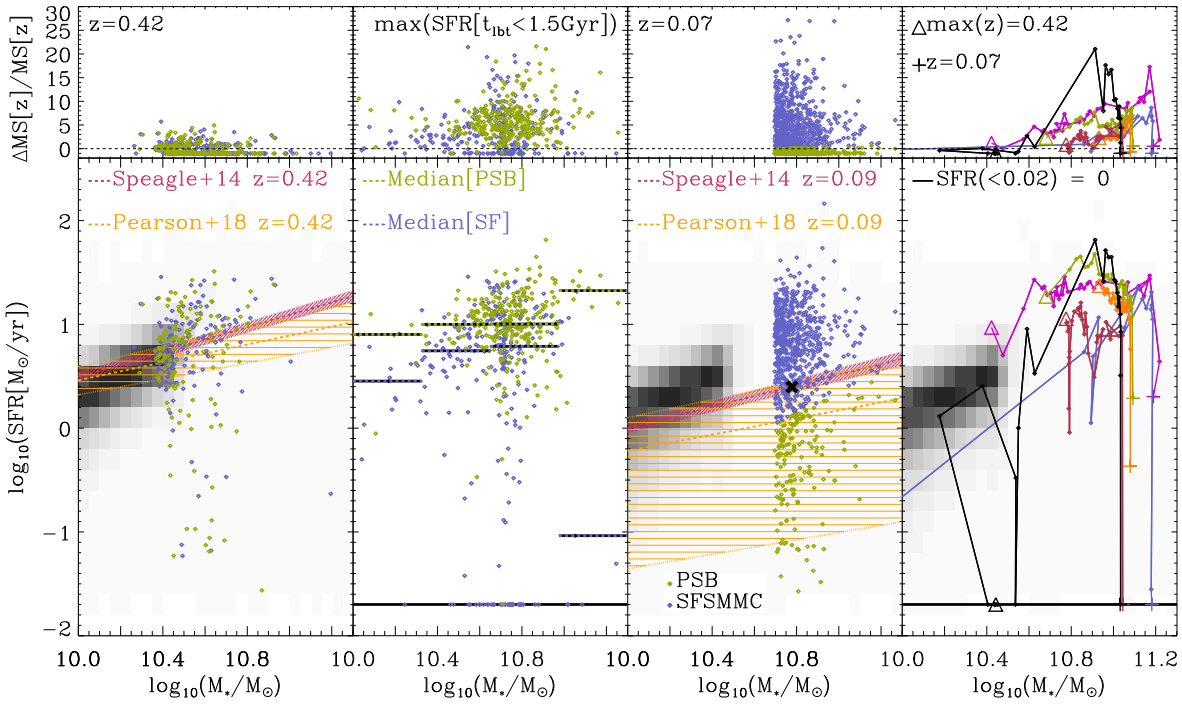

Figure 4.5: PSB progenitor evolution in the stellar mass - star formation rate plane. 1st panel (from left to right): PSB (green) and SFSMMC (blue) progenitors at $z = 0.4$, i.e. at $t_{\mathrm{lbt}} = 3.6\,\mathrm{Gyr}$. 2nd panel: Peak star formation rate (SFR) for each PSB and corresponding SFSMMC. 3rd panel: PSBs and SF galaxies at $z = 0.1$, i.e. $t_{\mathrm{lbt}} = 0\,\mathrm{Gyr}$, and their median SFR values. The shaded regions in the first and third panels provide redshift dependent observational fits to the main sequence (Speagle et al., 2014; Pearson et al., 2018). 4th panel: Evolution of a subset of six massive PSBs (see Table 4.1), which are tracked through time, ending at $t_{\mathrm{lbt}} = 0\,\mathrm{Gyr}$ (crosses). Each step (small diamonds), represents an incremental increase of $t_{\mathrm{lbt}} \sim 0.11\,\mathrm{Gyr}$, ultimately arriving at the furthest tracked progenitors at a maximum $t_{\mathrm{lbt}} = 3.6\,\mathrm{Gyr}$ (triangles). The grey density distribution shows the abundance and location of all Magneticum Box2 galaxies at $z = 0.4$ (1st panel) and $z = 0.4$ (3rd and 4th panel). For plotting purposes, in the 2nd and 4th panel, galaxies with $SFR < 0.02$ are artificially set to zero, i.e. $SFR(< 0.02) = 0$. For reference, a recent Milky Way stellar mass estimate $M_{*,\mathrm{MW}} \sim 6 \cdot 10^{10}\,\mathrm{M}_{\odot}$ has been included (black X) in the 3rd panel (Licquia & Newman, 2015). The top panels show the relative deviation from the redshift evolving main sequence, i.e. $\Delta MS[z]/MS[z] = (SFR[z] - MS[z])/MS[z]$, for each population featured in the main panel below (Pearson et al., 2018).

a galaxy which has no star formation over the evaluated time-span, as illustrated by the green diamond found on the black horizontal line showing galaxies with $SFR(< 0.02) = 0$ (2nd panel). In other words, galaxies need not have formed stars in situ to host a young stellar population, rather, as is the case for the mentioned PSB galaxy, young ex situ stars

can also be accreted during mergers, leading to a young stellar population in the merger remnant at $t_{\rm lbt} = 0\,{\rm Gyr}$.

The distribution of PSB and SF galaxies at $z = 0.07$ is shown in the third panel of Figure 4.5. The dichotomy found at $t_{\rm lbt} = 0\,{\rm Gyr}$, i.e. at our identification time, is the result of our selection criteria (see Section 4.1): By design, PSBs are quenched, while the SFSMMC sample is characterised by star formation. When comparing to observations, we find that this dichotomy is well described by observations (Speagle et al., 2014; Pearson et al., 2018). Furthermore, we see that the SF galaxies appear as an extension of the grey density distribution describing the abundance of all Box2 Magneticum galaxies, while the PSBs scatter below the main sequence. We note that the relative deviation from the evolving main sequence shown above the third panel uses a redshift of $z = 0.09$, as the observational fit is no longer defined at $z = 0.07$ (Pearson et al., 2018), the redshift showing Magneticum results.

The fourth panel of Figure 4.5 shows that massive PSB progenitors are found significantly above the main sequence prior to their quiescent phase at $t_{\rm lbt} = 0\,{\rm Gyr}$ (crosses). PSB progenitors display prolonged strong star formation episodes, with SFRs consistently being significantly larger than the redshift evolving main sequence (Pearson et al., 2018). Generally, independent of the duration, starbursts of massive PSB progenitors are found in the range $5 \lesssim \Delta MS[z]/MS[z] \lesssim 20$ above the redshift evolving main sequence.

In Figure 4.5, we find both galaxies that continuously remain above the main sequence as well as galaxies that experience rejuvenation, i.e. galaxies which were initially below the main sequence but rise above it during their starburst phase. The starburst timescales ($t_{\rm sb}$) differ widely and are within the range $t_{\rm sb} \sim (0.4 - 3)\,{\rm Gyr}$. This spread in timescales is a reflection of the different star formation histories prior to the starburst. As the global 647 PSB sample is tracked backwards, the sample size is reduced, especially if BHs are recently seeded. This results in a sample size of 455 tracked PSB progenitors, which reach a $t_{\rm lbt} \geq 2.5\,{\rm Gyr}$. Of these 455 successfully tracked PSBs, 105 are considered to be rejuvenated galaxies, i.e. 23%. Independent of whether galaxies are rejuvenated or show sustained star formation, they show a sharp decline in star formation at the end of the starburst phase. Typically, this decline to passive levels of star formation happens within $\lesssim 0.4\,{\rm Gyr}$. This conflicts with our understanding of the typical behaviour of field galaxies, which make up the vast majority of our sample (see last row of Table 4.4), as field galaxies generally experience a gradual decline in average SFR (Noeske et al., 2007). In other words, the (massive) PSBs in Figure 4.5 not only show enhanced, often sustained, starbursts, but also experience an abrupt cessation of star formation, the details of which are discussed in Section 4.4.

4.3 The role of mergers

It is well established that galaxy mergers impact the galactic star formation rate (SFR), both directly (Springel et al., 2005a; Johansson et al., 2009b; Ellison et al., 2018; Lagos et al., 2019) and indirectly (Hopkins et al., 2013; Barai et al., 2014; Yesuf et al., 2014).

However, the nature and relevant parameters of the mergers and how they influence the SFR is still debated. For example, while the SIMBA cosmological simulations find an increasing impact (Rodríguez Montero et al., 2019), observations based on SDSS, KiDS, and CANDELS find that mergers do not significantly impact the SFR, compared to non-merging systems (Pearson et al., 2019), and observations based on 32 PSBs from LEGA-C suggest that mergers likely trigger the rapid shutdown of star formation found in PSBs (Wu et al., 2020). To disentangle this complex relationship between mergers and the SFR, we investigate mergers in Box2, both on an individual basis as well as statistically.

4.3.1 Case study: Gas evolution

The case study of one typical PSB (progenitor), selected from Table 4.1 (ID=417642), is shown in Figure 4.6. The goal is to map the (cold) gas evolution as a means of investigating the initial triggering of the starburst and the following starburst phase. To uncover the mechanisms involved, Figure 4.6 shows the evolution of the star formation history (1st column), the gas phase (2nd column), and independent projections of the spatial gas distribution (3rd-5th column) as a function of look-back-time for the selected PSB (progenitor). To better visualise the evolution of the gas involved in the recent starburst phase, all star-forming gas at $t_{\mathrm{lbt}} = 0.43\,\mathrm{Gyr}$, i.e. one time-step before the shutdown, is identified and subsequently coloured green. These identified gas particles maintain their green colouring both prior to and after this look-back-time.

When considering higher look-back-times in Figure 4.6, we find that the onset of star formation at $t_{\mathrm{lbt}} \sim 2\,\mathrm{Gyr}$ coincides with a close galaxy-galaxy interaction, followed by a major merger event at $t_{\mathrm{lbt}} = 0.75\,\mathrm{Gyr}$ (see solid red vertical line in Figure 4.4). The period between $t_{\mathrm{lbt}} \sim (0-2)\,\mathrm{Gyr}$ is characterised by prolonged star formation. This is not an exception, but rather most PSB progenitors experience recent merger events (see Table 4.2). It appears that the initial close galaxy-galaxy interactions and the subsequent mergers provide a mechanism by which gas is transported inwards, increasing the number of gas particles above the density threshold (2nd column) required for star formation. The increase in the supply of cold, dense gas within the PSB progenitor then enables the starburst.

Similarly to the vast majority of PSBs surveyed in this manner, we find a strong diffusion of gas at $t_{\mathrm{lbt}} = 0\,\mathrm{Gyr}$, following the starburst phase. This is displayed in the first row of columns two to five in Figure 4.6. In column two, we find a strong decrease in gas density, accompanied by an overall increase in temperature within a timescale of $t \sim 0.4\,\mathrm{Gyr}$, as evidenced by the distribution of previously star-forming gas (green) over the entire density and temperature regime. This behaviour at low look-back-times is mirrored in the spatial domain (3rd-5th column), which also provides evidence for a strong redistribution of previously star-forming gas (green). Although the spatial distribution widens, large cold gas reservoirs remain within the PSB galaxy at $t_{\mathrm{lbt}} = 0\,\mathrm{Gyr}$, agreeing with recent observations (Yesuf & Ho, 2020). We reviewed the gas evolution of multiple different PSBs and verified that the behaviour shown in Figure 4.6 is not an exception, but rather typical for our (massive) PSB sample.

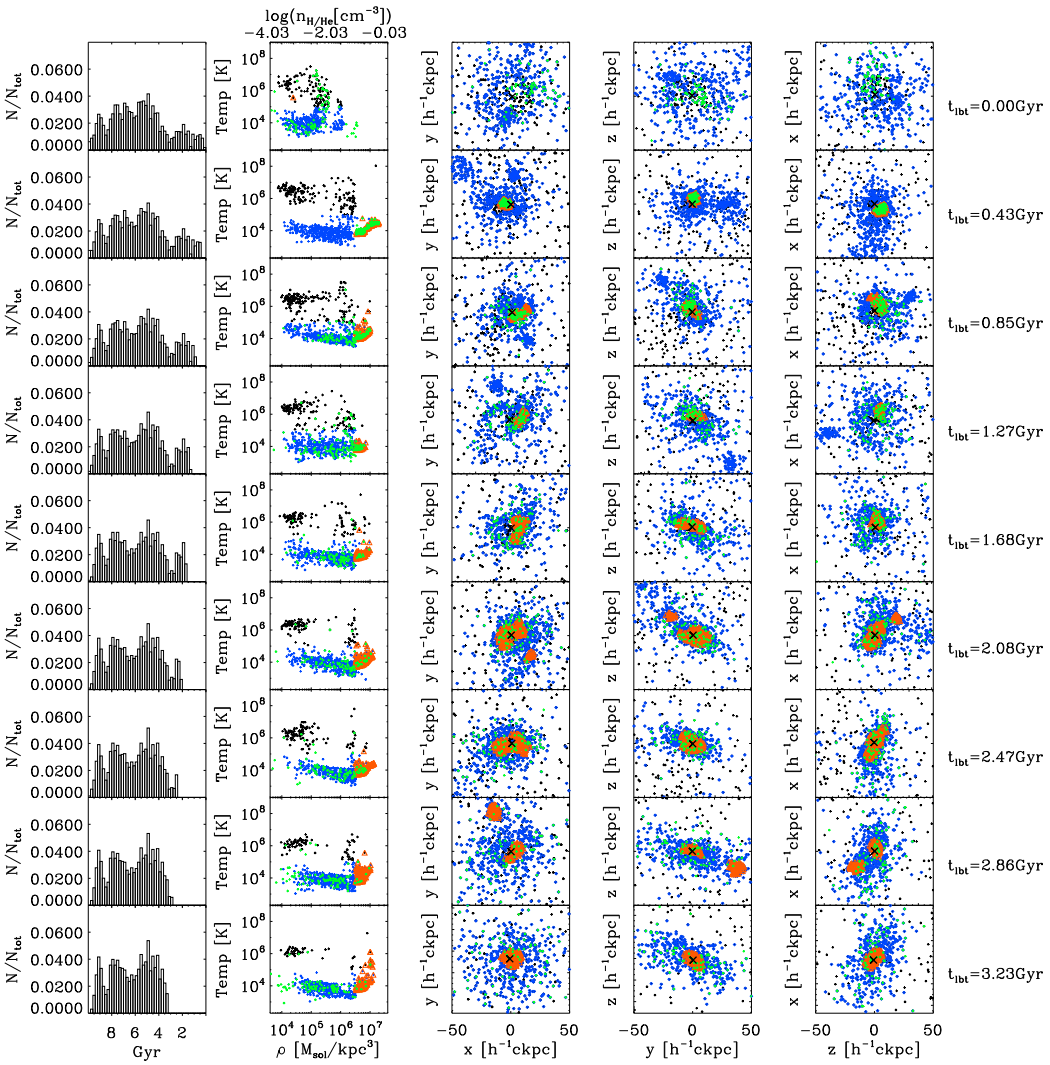

Figure 4.6: Case study of the gas evolution of one of the PSBs (417642), as introduced in Table 4.1. The first column shows the star formation history as a function of look-back-time, while the second column shows the gas phase diagram at different look-back-times. The next three columns display the evolution of the spatial distribution (co-moving side length $100h^{-1}ckpc$) of gas (black), cold gas (blue), i.e. $T < 10^5\,K$, and star-forming gas (orange). To better understand the evolution of the gas involved in star formation, all star-forming gas at $t_{\rm lbt} = 0.43\,{\rm Gyr}$ (green) is identified and tracked through all look-back-times to reveal its origin, as well as its distribution at $t_{\rm lbt} = 0\,{\rm Gyr}$. The tracked gas (green) uses a smaller symbol size, to show the over-plotted star-forming gas (orange) in the background. The 'x' at the centre of the spatial distribution marks the black hole of the PSB (progenitor).

When viewing the evolution of the star formation history in column one of Figure 4.6, the relative weighting of different components appears to change as time progresses. For example, at $t_{\rm lbt} = 1.68\,{\rm Gyr}$ the onset of the starburst appears to be significantly stronger (compared to the older stars) than at lower look-back-times. Investigating this behaviour, we found that a significant population of older stars are accreted onto the PSB progenitor, thus impacting the relative abundance of different components of the star formation history. In other words, during the presented merging process, more ex-situ old stars are accreted than young in-situ stars are formed.

4.3.2 Merger statistics

To extend the case study conducted in Section 4.3.1 by a statistical analysis, we begin by evaluating the merger history of the $z \sim 0$ global 647 PSB sample. In addition, we also analyse the two (quiescent and star-forming, respectively) stellar mass matched control samples QSMMC and SFSMMC. The results of the merger tree evaluation for these samples are listed in Table 4.2.

Mergers are defined by their progenitor stellar mass ratios as follows: mini mergers 1:10 - 1:100, minor mergers 1:3 - 1:10, and major mergers 1:1 - 1:3. The first data row lists the sample size of successfully constructed merger trees. This value is less than the total sample size (647), as merger trees only exist over the entire evaluated time-span of $t_{\rm lbt} = 2.5\,{\rm Gyr}$ if the main progenitor was formed prior to this time-span. The next three rows list the total number of identified mergers (galaxies can have multiple mergers of the same type) for each type. The next three rows in Table 4.2 display the percentage of the analysed merger trees which identify at least one merger event of the respective type. The last row lists the percentage of galaxies with at least one merger event, independent of the type.

Table 4.2 shows that the PSB sample is characterised by an abundance of merger events. This agrees with low redshift observations, which find that PSBs are associated with interactions and/or mergers (Zabludoff et al., 1996; Bekki et al., 2001; Yang et al., 2004; Goto, 2005; Yang et al., 2008; Pracy et al., 2009; Wild et al., 2009; Meusinger et al., 2017; Pawlik et al., 2018). Specifically, 64.7% of PSBs experience a major merger within the last 2.5 Gyr. In contrast, only 9.4% of QSMMC galaxies experience a major merger within the same time-span, while this percentage rises to 58.1% for SFSMMC galaxies. Compared to the QSMMC, the PSB sample experiences a factor of ~ 7 more major merger events. When comparing the samples, we find close similarities between the PSB and SFSMMC sample, i.e. both show an abundance of mergers. In contrast, the QSMMC sample is characterised by a low abundance of mergers and differs significantly from the other two samples. However, it is not clear that this is typical for PSBs identified at higher redshifts.

In Section 4.2, we showed the redshift evolution of both the PSB-to-quenched fraction and the PSB stellar mass function. In this context, we investigate the abundance of mergers at redshift $z = 0.9$, in the same manner as outlined for our global $z \sim 0$ PSB sample. This is motivated by the desire to separate the redshift evolution of identically selected samples from differences resulting from different (later) environmental selections.

Criterion	PSBs	QSMMC	SFSMMC
Evaluated trees	632	646	630
$\Sigma(N_{\mathrm{mini}})$	343	114	285
$\Sigma(N_{\mathrm{minor}})$	295	53	260
$\Sigma(N_{\mathrm{major}})$	465	65	415
$N_{\geq 1\mathrm{mini}}$	40.7%	14.1%	33.7%
$N_{\geq 1\mathrm{minor}}$	37.3%	7.4%	33.8%
$N_{\geq 1\mathrm{major}}$	64.7%	9.4%	58.1%
$N_{\geq 1\mathrm{merger}}$	88.9%	23.4%	79.7%

Table 4.2: Overview of different merger abundances of our global $z \sim 0$ identified PSB sample and its stellar mass matched control (SMMC) samples, subdivided into quiescent (QSMMC) and star-forming (SFSMMC) samples. The first data row displays the number of successfully analysed merger trees out of the 647 galaxies traced for each sample over the time-span $t_{\mathrm{lbt}} = (0.0 - 2.5)\,\mathrm{Gyr}$. The next three rows list the total number of mergers $\Sigma(N)$ encountered over the evaluated time-span, subdivided into the following classes and stellar mass ratios: Mini 1:10 - 1:100, Minor 1:10 - 1:3, Major 1:3 - 1:1. The subsequent three rows list the percentage of galaxies with respect to the analysed merger trees, which encountered at least one merger event of the respective type ($N_{\geq 1}$). The last row shows the percentage of galaxies which encountered at least one merger, independent of type.

We choose redshift $z = 0.9$ because we also study the merger abundance in the cluster environment (see Section 4.5.4) and compare it to observations (see Section 4.5.2) at this redshift.

As established by Figures 4.1 and 4.2, the abundance of PSBs increases with increasing redshift. Table 4.3 reflects this too, as significantly more PSBs are identified at $z = 0.9$ (10624 galaxies), compared to $z \sim 0$ (647 galaxies). Beyond this, we find that: First, the percentage of galaxies which experience more than one merger (last row) increases, especially for the QSMMC sample (factor ~ 2), less so for the SFSMMC sample (increase by $\sim$ 12%), and least for the PSB sample (increase by $\sim$ 3%). Second, the similarity between the PSB and the SFSMMC sample remains, as both continue to show similar (high) merger abundances compared to the QSMMC sample. Third, the overall increase in the abundance of mergers is especially driven by more mini and minor mergers at $z = 0.9$. This behaviour at $z \sim 0.9$ agrees with LEGA-C observations at $z \sim 0.8$, which find that central starbursts are often the result of gas-rich mergers, as evidenced by the high fraction of PSB galaxies with disturbed morphologies and tidal features (40%) (D'Eugenio et al., 2020).

Albeit differences existing between Tables 4.2 ($z \sim 0$) and 4.3 ($z = 0.9$), the link between recent (in relation to the identification redshift) star formation and the abundance of mergers appears strong. To summarise, although PSBs are quiescent at identification redshift, they are characterised by recent (strong) star formation. The similarity with

Criterion	PSBs	QSMMC	SFSMMC
Evaluated trees	10520	10596	10479
$\Sigma(N_{\rm mini})$	8559	4899	8692
$\Sigma(N_{\rm minor})$	6747	2439	6832
$\Sigma(N_{\rm major})$	6014	1638	6822
$N_{\geq 1{\rm mini}}$	50.7%	33.6%	51.3%
$N_{\geq 1{\rm minor}}$	50.5%	20.6%	50.1%
$N_{\geq 1{\rm major}}$	47.3%	14.3%	52.7%
$N_{\geq 1{\rm merger}}$	92.6%	51.9%	92.3%

Table 4.3: Same as Table 4.2 but showing an overview of different merger abundances of $z \sim 0.9$ identified PSBs (also with $M_* \geq 4.97{\cdot}10^{10}\,{\rm M}_\odot$) and their control galaxies (QSMMC and SFSMMC). The first data row displays the number of successfully analysed merger trees out of an initial PSB sample size of 10624. The galaxies were traced for each sample over the time-span $t_{\rm lbt} = (6.5 - 9.0)\,{\rm Gyr}$. The next three rows list the total number of mergers $\Sigma(N)$ encountered over the evaluated time-span, subdivided into the mini, minor, and major mergers. The subsequent three rows list the percentage of galaxies with respect to the analysed merger trees, which encountered at least one merger event of the respective type ($N_{\geq 1}$). The last row shows the percentage of galaxies which encountered at least one merger, independent of type.

respect to merger abundances between star-forming and PSB galaxies is likely driven by the ability of mergers to trigger starbursts on short timescales and to provide cold gas on longer timescales to otherwise exhausted galaxies (Genzel et al., 2010; Hirschmann et al., 2012). In short, we find strong evidence that mergers are linked to increased star formation, while their absence is linked to quiescent levels of star formation. Consequently, the high abundance of mergers appears to be central to the evolution of PSB galaxies, while likely also playing an important role in the subsequent shutdown.

4.3.3 Cold gas fractions

As the timescales of the galaxy-galaxy interactions prior to the detection of a merger event vary widely, depending on the specific geometry of the encounter, we do not individually correlate merger events with the onset of the starburst phase. Rather, to more closely evaluate the properties of the detected mergers and to investigate their differences, we determine the cold gas fractions $f_{\rm cgas} = M_{\rm cold,gas}/M_*$ prior to mergers for the $z \sim 0$ PSB, QSMMC, and SFSMMC samples. The cold gas fraction is calculated within three half-mass radii $r < 3\,R_{1/2}$, where the half-mass radius is defined as the radius of a three dimensional sphere containing half of the total galactic stellar mass. We choose $R_{1/2}$, as its use is well established within our simulations and it is often considered equal to the observationally attained effective radius R_e (Teklu et al., 2015; Remus et al., 2017b; Teklu

et al., 2018; Schulze et al., 2020). We tested the impact of choosing different half-mass radii ($r/R_{1/2} = [0.5, 5]$) on $f_{\rm cgas}$ and found consistent behaviour for varying half-mass radii.

Figure 4.7 shows the distribution of cold gas fractions $f_{\rm cgas}$ within three half-mass radii $r < 3\,R_{1/2}$, split up into main (left) and satellite progenitors (right). We further split the sample into major (top), minor (middle), and mini (bottom) mergers. When a merger event is registered, we determine the cold gas fraction prior to the merger event, i.e. we identify the progenitors peak stellar mass in the $\lesssim 0.4\,$Gyr before the event is registered and determine the cold gas fraction at this time-step. Each progenitor is then assigned to the respective merger type distribution. This is done separately for the PSB (green), QSMMC (red), and SFSMMC (blue) sample. The solid vertical lines indicate the median values of each population, while the shorter dashed vertical lines indicate the percentiles 15.9% and 84.1% respectively, i.e. the equivalent $1\,\sigma$ region of Gaussian distribution.

All panels showing the individual main progenitor distribution (left) in Figure 4.7 display similar distributions for different merger ratios. The reason for this is that independent of the given merger ratio, by definition, the merging main progenitor has the same cold gas fraction. Every time a merger occurs, the population of main progenitors is sampled, resulting in a similar cold gas fraction distribution for all main progenitors, independent of the merger ratio.

In contrast, each sample of satellite progenitors (right) shows an evolving behaviour with merger type. Figure 4.7 (right) displays that the $f_{\rm cgas}$ distribution for each sample migrates towards higher $f_{\rm cgas}$ values as the stellar mass ratio between main and satellite progenitor decreases, i.e. when moving towards smaller mergers. In a nutshell, less massive merging satellite progenitors have higher relative abundances of cold gas.

We find that the behaviour of the cold gas fraction distribution of the PSB and SFSMMC sample is similar with $f_{\rm cgas}(r < 3\,R_{1/2}) \sim (0.8 - 1.0)$ for the main progenitors. The PSB and SFSMMC satellite progenitors have similar cold gas fractions albeit showing an expected (see above) stronger variance between merger types. In contrast to the PSB and SFSMMC galaxies, Figure 4.7 shows that the QSMMC sample consistently has lower $f_{\rm cgas}$ values: The quiescent main progenitors (left) have $f_{\rm cgas}(r < 3\,R_{1/2}) \sim 0$, i.e. compared to their stellar mass almost no cold gas is present in the galaxies. The satellite progenitors (right) also show that satellites which merge via major or minor mergers into the QSMMC sample typically have lower cold gas fractions, compared to the PSB and SFSMMC sample.

Taking all this into account, it appears that Figure 4.7 provides some evidence for *galactic conformity*, i.e. the effect whereby properties, e.g. the star formation rate, of satellite galaxies appear correlated to the properties of the central galaxy (Kawinwanichakij et al., 2016; Teklu et al., 2017; Tinker et al., 2017, 2018). In other words, star-forming and PSB main progenitors appear more likely to merge with satellite progenitors which have similarly high cold gas fractions, while quiescent main progenitors appear more likely to merge with satellite progenitors which exhibit more cold gas depletion, i.e. lower $f_{\rm cgas}$.

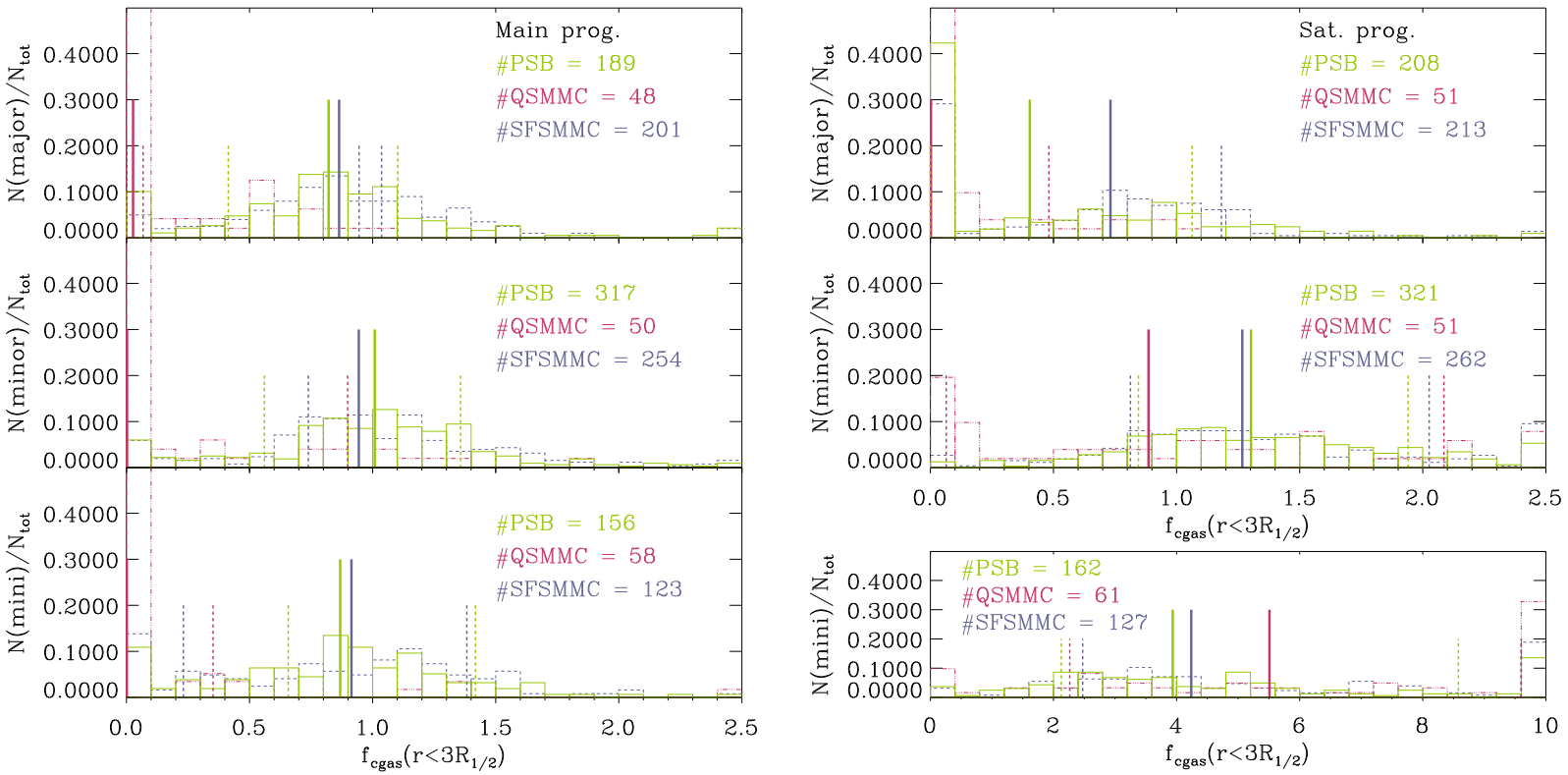

Figure 4.7: Distribution of cold gas fraction $f_{cgas} = M_{cold,gas}/M_*$ within three half-mass radii $r < 3\,R_{1/2}$ for main (left) and satellite progenitors (right). The distributions are further split into major (top), minor (middle), and mini (bottom) mergers and show the behaviour of the PSB (green), QSMMC (red), and SFSMMC (blue) samples. The solid vertical lines indicate the median values of each population, while the shorter dashed vertical lines indicate the percentiles 15.9% and 84.1% respectively, i.e. the $1\,\sigma$ region. In contrast to all other panels, the panel on the bottom right shows a four times larger f_{cgas} domain.

The bottom right panel of Figure 4.7 shows a distinct exception to the previously described behaviours, resulting in a four times larger domain being shown. The mini mergers of satellite progenitors show a significantly flatter distribution of f_{cgas}, while simultaneously having significantly higher f_{cgas} values. This is likely the result of infalling cold gas over-densities being classified as mini mergers or gas-rich satellites merging with their host. Subsequently, the low number of stellar particles compared to the abundant (cold) gas particles, drives high values of f_{cgas}. Due to the low resolution of mini merger satellite progenitors, this panel is less relevant to understanding mergers, while still showing that (cold) gas inflow is relatively similar ($f_{\mathrm{cgas}}(r < 3\,R_{1/2}) \sim 4.0-5.5$) for all analysed samples, with the highest values found in the QSMMC sample.

4.4 Shutdown of star formation

4.4.1 Active galactic nucleus and supernova feedback

We investigate both the active galactic nuclei (AGN) as well as the supernovae (SNe) feedback energy output as a means to better understand the processes involved in shutting down star formation. Specifically, we want to shed light on processes which are linked to the short timescale ($t \sim 0.4\,\mathrm{Gyr}$) redistribution and heating of previously star-forming gas, as discussed in Section 4.3.1. We choose these mechanisms in particular because they are able to deposit large amounts of energy on short timescales (Springel et al., 2005a; Voit et al., 2015; Wild et al., 2020), thereby potentially strongly impacting star formation.

As a precaution, we also investigated the typical depletion timescales of cold gas in PSB progenitors during peak star formation. We find the timescales to be significantly higher ($t_{\mathrm{depl}} \sim (2-5)\,\mathrm{Gyr}$) than the short shutdown timescale ($t_{\mathrm{shutdown}} \lesssim 0.4\,\mathrm{Gyr}$) found throughout our PSB sample. In other words, PSBs progenitors do not appear to run out of gas, rather the reservoir of cold, dense gas is abruptly heated and/or redistributed, leading to a shutdown in star formation, as demonstrated in Figure 4.6.

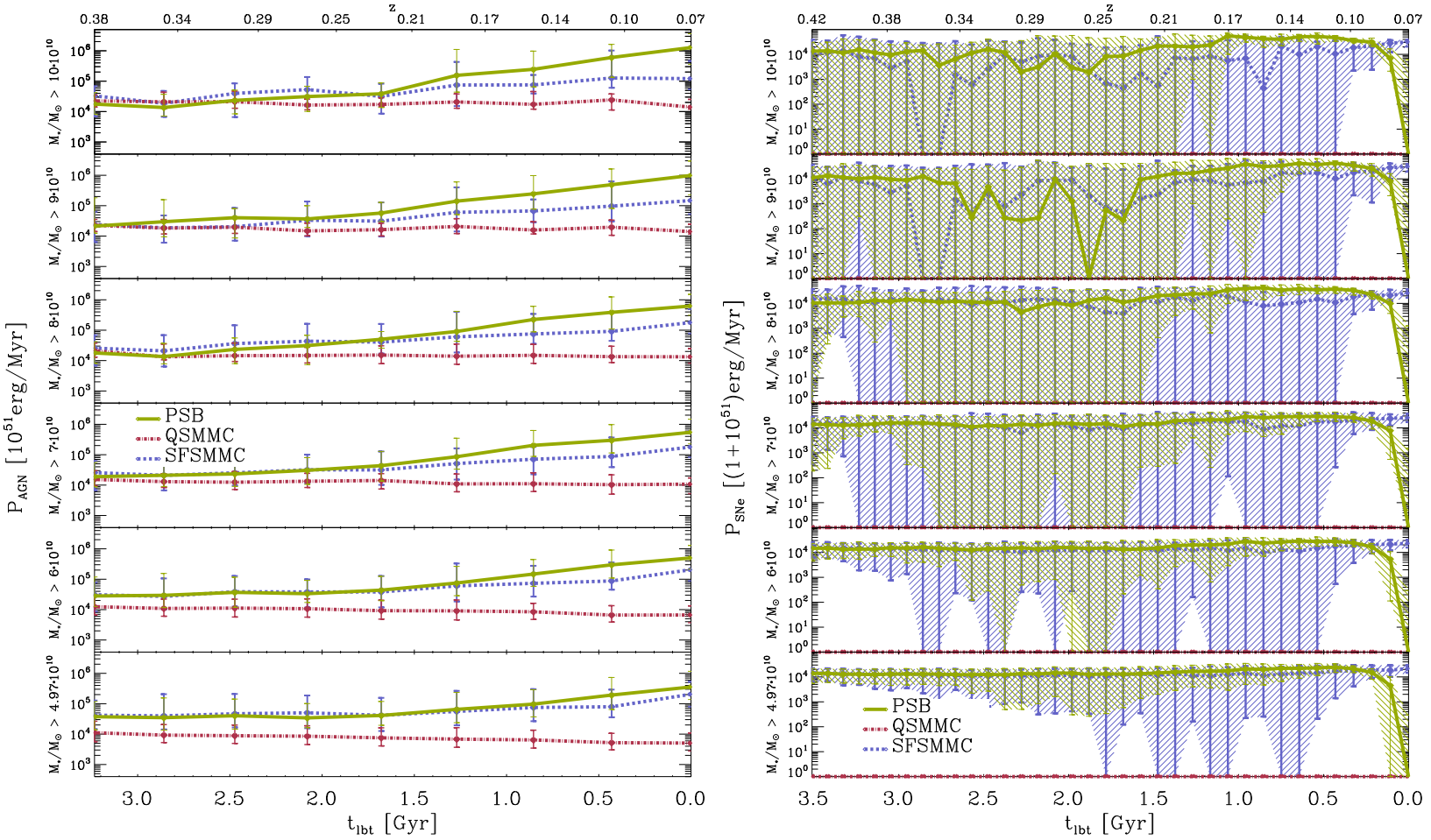

Figure 4.8: Active galactic nuclei (AGN: left figure) and supernovae (SNe: right figure) power output of the global PSB (green), QSMMC (red), and SFSMMC (blue) samples identified at $z \sim 0$ and evaluated over the past $\sim 3.2\,\mathrm{Gyr}$ and $\sim 3.5\,\mathrm{Gyr}$ in units of $10^{51}\,\mathrm{erg/Myr}$ and $1 + 10^{51}\,\mathrm{erg/Myr}$, respectively. The different panels show increasing $t_{\mathrm{lbt}} = 0\,\mathrm{Gyr}$ stellar mass cuts, $M_* > [4.97, 6, 7, 8, 9, 10] \cdot 10^{10}\,\mathrm{M}_\odot$, from the lower to top panel. Both figures show the median, as well as the 30% and 70% percentiles as error bars for each population.

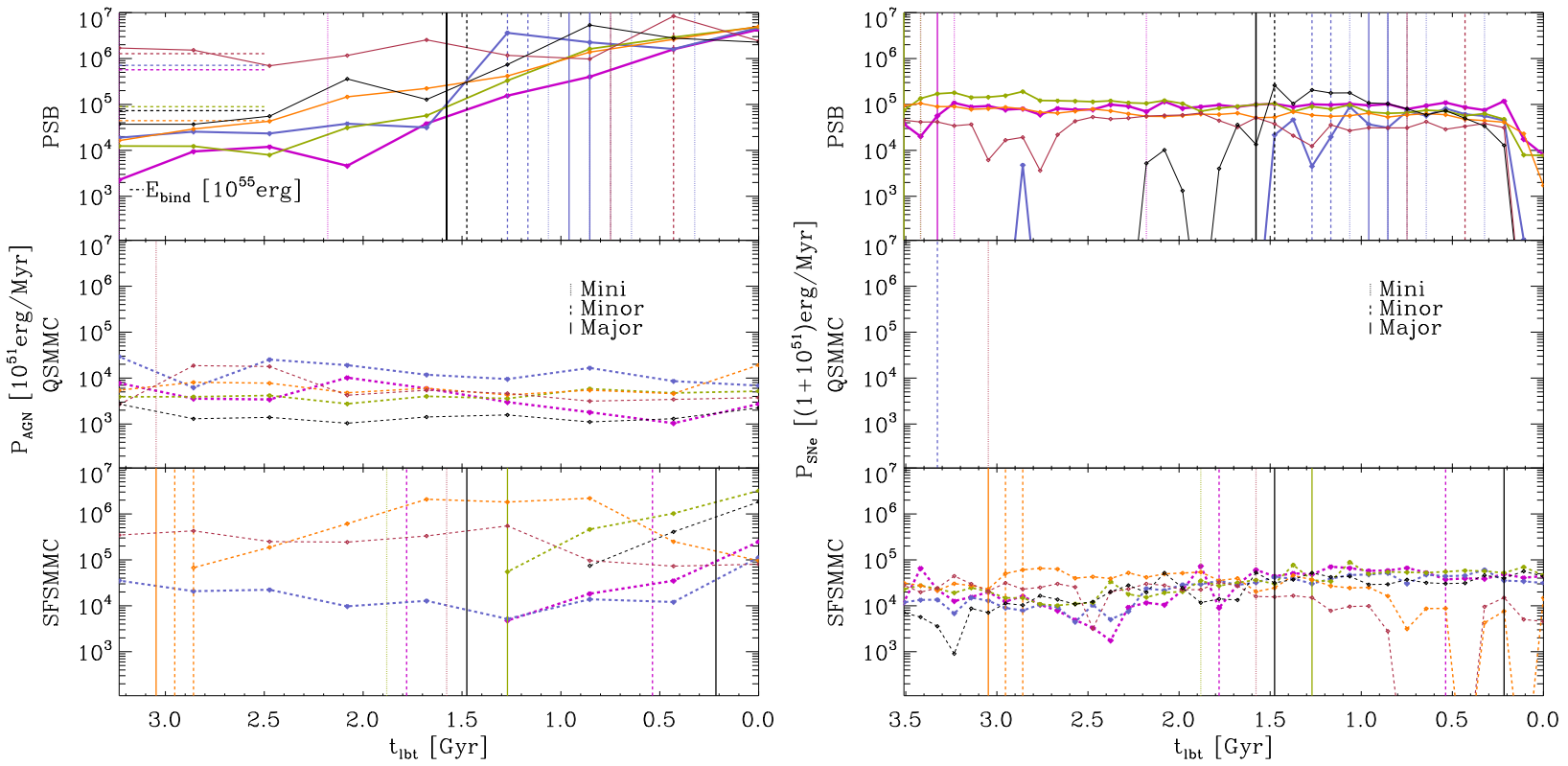

Figure 4.9: Energy deposited by AGN (left figure) and SNe (right figure) in units of 10^{51} erg/Myr and $1 + 10^{51}$ erg/Myr for the six massive PSBs (top panel) introduced in Table 4.1 and their control samples: QSMMC (middle panel), and SFSMMC (bottom panel) over the past ~ 3.2 Gyr (left) and ~ 3.5 Gyr (right), respectively. Vertical lines (following the colour scheme) indicate different merger events: mini (1:10 - 1:100) mergers (dash dotted line), minor (1:3 - 1:10) mergers (dashed line), and major (1:1 - 1:3) mergers (solid lines). Values are only plotted as long as black holes are successfully tracked (left) and if the star formation rate is non-zero, $SFR > 0$ (right). We note, that the temporal resolution differs by a factor of four between the AGN (left) and SNe (right) energy output. As the outputted energy within a given time interval is shown, AGN energies are a factor ~ 4 times larger compared to SNe energies. The horizontal lines in the top left panel at $t_{\rm lbt} \geq 2.5$ Gyr show an estimation of the binding energy of the massive PSBs.

We calculate the AGN power output $P_{\rm AGN}$ based on the change in BH mass $\Delta M_{\rm BH}$ between time steps ($\Delta t = 0.43\,{\rm Gyr}$) (Hirschmann et al., 2014):

$$P_{\rm AGN} = (e_r e_f \Delta M_{\rm BH} \cdot c^2)/\Delta t \tag{4.1}$$

where $e_r = 0.2$ is the fraction of energy which is thermally coupled to the surrounding gas, and e_f is a free parameter usually set to $e_f = 0.15$ (typical for simulations following metal dependent cooling functions (Booth & Schaye, 2009, 2011)).

As we are especially interested in SNe which release their energy on short timescales, our focus is on short lived, i.e. massive, stars. Therefore, supernovae Type II (SNeII), which arise at the end of the lifetime of massive stars, provide the dominant source of supernovae feedback in our analysis (Chevalier, 1976). Following the star formation model by Springel & Hernquist (2003), we expect an average SN energy release per stellar mass of $\epsilon_{\rm SN} = 4 \cdot 10^{48}\,{\rm erg M_\odot}^{-1}$. Combining this with the star formation rate (SFR) at each time step, (temporal resolution $\Delta t = 0.11\,{\rm Gyr}$), we receive the following estimation for the SNe power output $P_{\rm SNe}$:

$$P_{\rm SN} = \epsilon_{\rm SN} \cdot {\rm SFR}. \tag{4.2}$$

The results of these calculations are shown in Figure 4.8 for varying stellar mass cuts: On the left-hand side each data point displays the median AGN power output calculated from the difference in BH mass between time-steps, as indicated in Equation 4.1. Following Equation 4.2, data points in the right figure display the SNe power output estimation based on the current SFR. When the median SFR is zero, which is the case for the entire QSMMC sample, the SNe power output is zero too. Both figures shown in Figure 4.8 show the respective median values, as well as the 30% and 70% percentile as error bars (additionally shaded on the right). The different temporal resolution between the two figures is the result of using the BH particle data on the left, which due to storage constraints is only saved every 0.43 Gyr, and using `SUBFIND` data on the right, which is available every 0.11 Gyr (see Section 2.2.2).

We find the maximum median SNe power output for $M_* > 4.97 \cdot 10^{10}\,{\rm M_\odot}$ (bottom panel right) PSB galaxies to be $P_{\rm SNe,PSB} \leq 2 \cdot 10^{55}\,{\rm erg/Myr}$. In contrast, the maximum median AGN power output is $P_{\rm AGN,PSB} \geq 3 \cdot 10^{56}\,{\rm erg/Myr}$ for the same stellar mass selection (bottom panel left). In other words, Figure 4.8 shows that the AGN outweighs the SNe power output by an order of magnitude, especially at recent look-back-times.

Figure 4.8 (left) shows negligible differences between PSB and SF galaxies at $M_* > 4.97 \cdot 10^{10}\,{\rm M_\odot}$ (bottom panel): Both samples show a recent increase in AGN feedback, which is significantly larger than that of the quenched sample, especially towards more recent look-back-times. However, with increasing stellar mass the difference between PSB and SF galaxies increases. Specifically, at the highest stellar mass, i.e. $M_* > 1 \cdot 10^{11}\,{\rm M_\odot}$ (top panel), the difference at $t_{\rm lbt} = 0\,{\rm Gyr}$ is of order one magnitude between PSBs ($P_{\rm AGN,PSB} \sim 10^{57}\,{\rm erg/Myr}$) and SF ($P_{\rm AGN,SF} \sim 10^{56}\,{\rm erg/Myr}$) galaxies. In contrast to the recent elevation in AGN feedback found in PSB and to a lesser degree in SF galaxies (depending on the stellar mass cut), AGN feedback of quiescent galaxies shows no meaningful temporal evolution and only a weak stellar mass evolution ($P_{\rm AGN,Q} \sim 10^{55}\,{\rm erg/Myr}$ in highest stellar mass bin).

In Figure 4.8 (right) the PSB and SF galaxies show similar median SNe feedback. However, even at $M_* > 4.97 \cdot 10^{10}\,\mathrm{M}_\odot$ (bottom panel), where PSB and SF galaxies show the most similarities, we see a large spread in SNe feedback in the SF sample, while PSBs show a smaller spread in the distribution of SNe feedback. Independent of stellar mass, this is especially the case at recent look-back-times, $t_{\mathrm{lbt}} \sim [0.1, 1]\,\mathrm{Gyr}$: During this period PSBs are typically experiencing their starburst phase. As a result, the SFR is elevated throughout the entire sample, which due to its linear relation to the SNe feedback (see Equation 4.2) results in a tighter and slightly elevated distribution compared to SF galaxies, as evidenced by smaller error bars. Meanwhile, the quiescent galaxy sample is continuously characterised by a lack of SNe feedback, as no meaningful star formation occurs in the sample during the evaluated time span. As dictated by our selection criteria, PSBs show a strong decrease in SNe feedback energy.

In addition to our statistical analysis, we consider the AGN and SNe feedback of the six massive example (see Table 4.1). Figure 4.9 shows the AGN (left) and SNe (right) evolution split into three panels, showing the six massive PSBs (top), as well as the control samples: QSMMC (middle) and SF (bottom). Furthermore, we have added vertical lines indicating specific merger events colour coded to match the associated galaxy: When evaluating the last 3.5 Gyr, we find that the PSB sample is characterised by the most merger events (16), followed by the SFSMMC sample (10) and the QSMMC sample (2). As previously established in Sections 4.3.1 and 4.3.2, this further highlights the significance of mergers for the evolution of (massive) PSBs.

Similarly to the comparison between AGN and SNe feedback shown in Figure 4.8, Figure 4.9 also shows that the AGN feedback significantly outweighs the SNe feedback, especially at recent look-back-times. Specifically, within the last time step ($t_{\mathrm{lbt}} \leq 0.43\,\mathrm{Gyr}$) all six PSBs have an AGN feedback ($P_{\mathrm{AGN,PSB}} \gtrsim 10^{57}\,\mathrm{erg/Myr}$) which outweighs the SNe feedback ($P_{\mathrm{SNe,PSB}} \lesssim 10^{56}\,\mathrm{erg/Myr}$) by more than an order of magnitude. Furthermore, Figure 4.9 shows that most of the mergers (vertical lines) in the PSB sample occur within the last $\sim 1.5\,\mathrm{Gyr}$, i.e. during the same time in which the AGN power output increases by up to ~ 2 orders of magnitude. As a rough comparison, we calculate an estimation of the spherical binding energy ($E_{\mathrm{bind}} = 3GM^2/5R$) of the massive PSBs using the $M_{200,\mathrm{crit}}$ halo mass and R_{200} radius as displayed in Table 4.1 for M and R, respectively. The resulting estimation is shown in the top left panel of Figure 4.9 as horizontal lines above $t_{\mathrm{lbt}} \geq 2.5\,\mathrm{Gyr}$. To compare with the power output, the horizontal binding energy lines use a different scale [10^{55} erg] as indicated by the legend. Five out of the six massive PSBs have binding energies with $E_{\mathrm{bind}} \leq 10^{61}\,\mathrm{erg}$ and the most massive PSB (shown in Figure 4.6) has a binding energy of $E_{\mathrm{bind}} = 1.278 \cdot 10^{61}\,\mathrm{erg}$. Most binding energies are found within an order of magnitude of the AGN energy released within the last time step $t_{\mathrm{lbt}} \lesssim 0.43\,\mathrm{Gyr}$, which further highlights the strong impact the AGN has on (massive) PSBs. Furthermore, we note that the extensive amount of power deposited by the AGN ($P_{\mathrm{AGN,PSB}} \gtrsim 10^{57}\,\mathrm{erg/Myr}$) during $t_{\mathrm{lbt}} \lesssim 0.43\,\mathrm{Gyr}$ is correlated with the gas temperature increase, gas density decrease, and general redistribution of gas seen in Figure 4.6 at $t_{\mathrm{lbt}} = 0\,\mathrm{Gyr}$. Thus, we find strong evidence that the AGN is connected and probably responsible for the shutdown of the star formation in PSBs.

4.4.2 Black hole growth statistics

To complement the analysis in Section 4.4.1, we additionally quantify the black hole (BH) growth for our different samples. We calculated both the relative and absolute BH growth: Indeed, only 7.8% of QSMMC galaxies, compared to 60.2% and 62.7% of the SFSMMC and PSB galaxies respectively, at least double their BH mass over the last 2.5 Gyr. In absolute terms, 80.1% of PSB and 73.7% of the SFSMMC galaxies experience a significant mass growth of $\Delta M_{\rm BH} \geq 10^7\,{\rm M}_\odot$, while this is only the case for 18.7% of the QSMMC galaxies.

To better visualise the scales involved in the BH mass growth over a period of 2.5 Gyr, we introduce $\gamma_{\rm BH}$:

$$\gamma_{\rm BH} = log_{10}\left[\frac{M_{\rm BH}[t_{\rm lbt} = 0\,{\rm Gyr}] - M_{\rm BH}[t_{\rm lbt} = 2.5\,{\rm Gyr}]}{M_{\rm BH}[t_{\rm lbt} = 2.5\,{\rm Gyr}]}\right]. \tag{4.3}$$

Figure 4.10 (left) shows $\gamma_{\rm BH}$ for PSB (colour coded according to the galactic accreted gas mass $M_{\rm gas}$) and QSMMC (black) galaxies as a function of stellar mass. As indicated by the legend, different symbols indicate the host halo mass $M_{\rm 200,crit}$, translating into three types of environment: field galaxies (x), group galaxies (square), and cluster galaxies (triangle).

Figure 4.10 (left) clearly shows that, in contrast to QSMMC galaxies, PSBs are consistently found at higher values of $\gamma_{\rm BH}$. This is in line with previously established behaviour (see Section 4.4.1), where PSBs exhibit a significantly stronger AGN feedback, i.e. BH mass growth, than the QSMMC comparison sample. Interestingly, it appears that the PSB population inhabits distinct regions in the stellar mass - γ_{BH} plane. Most noticeably, there appears to be a bimodality, centred around two PSB populations found at $\gamma_{\rm BH} \sim 2$, i.e. a BH growth by a factor of ~ 100, and $\gamma_{BH} \sim 0$, i.e. a doubling of the BH mass over the last 2.5 Gyr.

After reviewing the merger histories and BH parameters of the PSB galaxies found in these two distinct regions, we find that the $\gamma_{\rm BH} \sim 2$ population is characterised by recently seeded BHs at $t_{\rm lbt} = 2.5\,{\rm Gyr}$. Our BHs are represented by collisionless sink particles, which are seeded with an initial mass of $4.6{\cdot}10^5\,{\rm M}_\odot$ in galaxies with stellar mass $M_* > 2.3{\cdot}10^{10}\,{\rm M}_\odot$ (Steinborn et al., 2015). The BHs are seeded below the Magorrian relation, i.e. the relation between BH and bulge mass (Magorrian et al., 1998). In practice, this means that recently seeded BHs experience an initial rapid BH mass growth at fairly constant stellar masses (Steinborn et al., 2015). In contrast, the $\gamma_{\rm BH} \sim 0$ population is characterised by BHs that have already reached the Magorrian relation at $t_{\rm lbt} = 2.5\,{\rm Gyr}$. Despite the numerical effects associated with seeding BHs, from a physical point of view, the important distinction between PSB and QSMMC galaxies remains: PSBs are characterised by a significantly stronger BH mass growth.

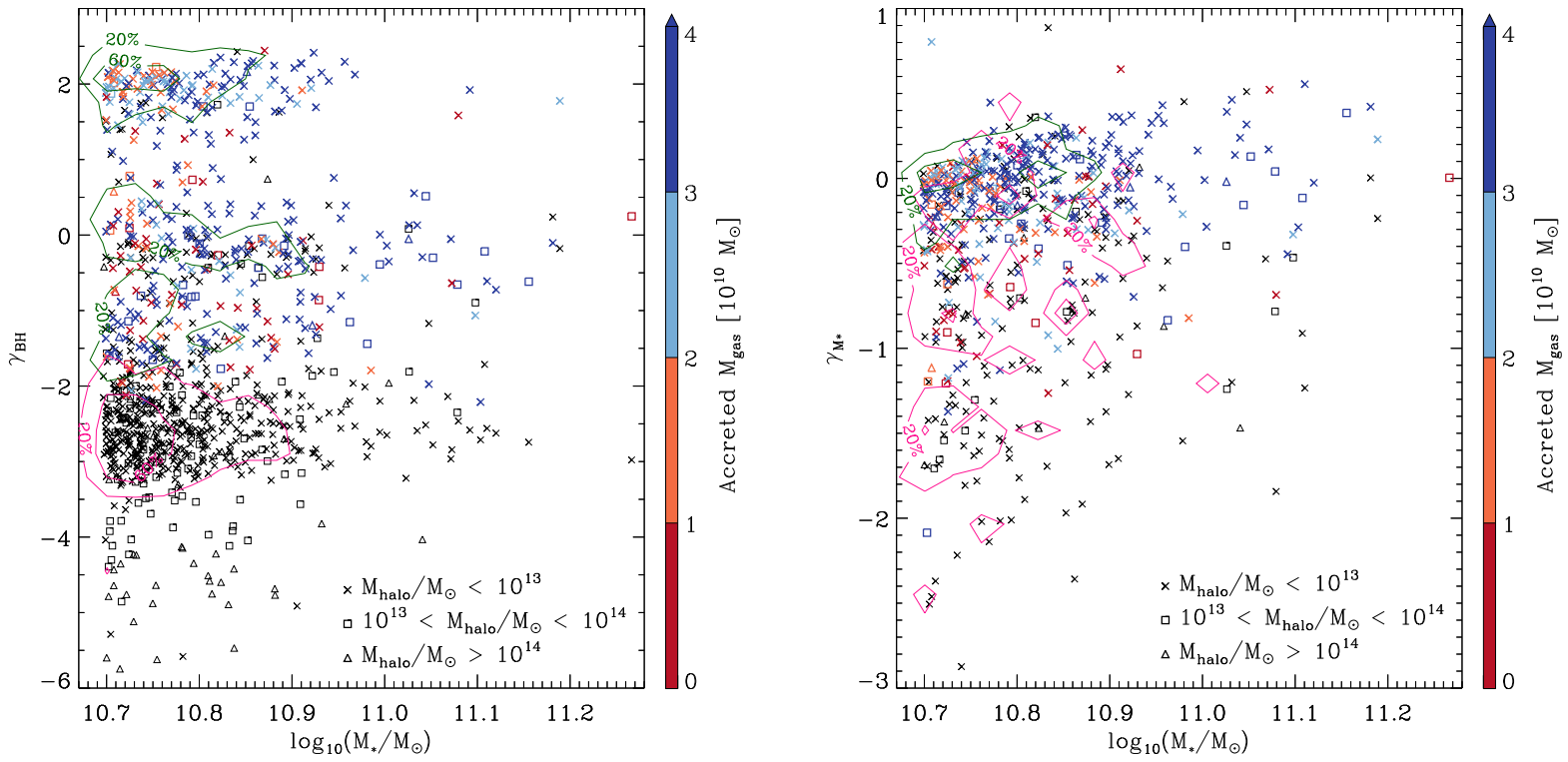

Figure 4.10: Based on Equation 4.3, the left figure shows the black hole mass growth γ_{BH} over a period of 2.5 Gyr, as a function of stellar mass. The colour bar displays the accreted gas mass onto the tracked galaxy due to mergers. The right figure shows the stellar mass growth γ_{M_*}, following the same prescription as Equation 4.3, however using stellar mass rather than BH mass. Both figures show the PSB sample (coloured points, green contours) and the QSMMC sample (black points, pink contours) with contour lines indicating 60% and 20% of the maximum densities. The symbols used encode the halo mass, i.e. the environment: $M_{200,\mathrm{crit}}/\mathrm{M}_\odot < 10^{13}$ (X), $10^{13} < M_{200,\mathrm{crit}}/\mathrm{M}_\odot < 10^{14}$ (squares), and $M_{200,\mathrm{crit}}/\mathrm{M}_\odot > 10^{14}$ (triangles). To avoid cluttering of points due to an increased stellar mass range, one lone high mass galaxy ($log_{10}(M_*/M_\odot) = 11.98$) is excluded from the figures. Only galaxies which experience a BH (left) and stellar mass (right) growth are displayed.

The right panel in Figure 4.10 shows that the γ_{BH} bimodality found in the left panel is not reproduced when evaluating the stellar mass growth γ_{M_*} (using Equation 4.3, but substituting M_{BH} with M_*). Rather, we find that far fewer QSMMC galaxies experience a non-negligible stellar mass growth over the considered time-span, $\Delta t \sim 2.5\,\mathrm{Gyr}$. As a result, Figure 4.10 (right) is underpopulated with QSMMC galaxies. This contrast between PSB and QSMMC galaxies further highlights the statistically rich merger history of PSBs, which are overwhelming located around $\gamma_{\mathrm{M}_*} \sim 0$, i.e. experience a doubling in stellar mass within 2.5 Gyr.

As previously established in Section 4.2, galaxies in Figure 4.10 are overwhelmingly found at lower stellar masses, i.e. close to our mass cut. Furthermore, Figure 4.10 appears to show a weak correlation between stellar mass and gas accretion, as low stellar mass PSBs are more likely to have low gas accretion (red and orange), while gas accretion appears to increase (blue) towards higher stellar masses. We also investigated the correlation between stellar mass and stellar mass accretion via mergers, finding a stronger correlation than in Figure 4.10. This is not surprising, as mergers provide the dominant pathway for stellar mass growth for massive galaxies, while in-situ star formation becomes less relevant (Bournaud & Elmegreen, 2009; van Dokkum et al., 2010; L'Huillier et al., 2012; Lackner et al., 2012; Rodriguez-Gomez et al., 2016; Qu et al., 2017; O'Leary et al., 2020).

Figure 4.11 maintains much of the nomenclature introduced in Figure 4.10 (left). However, the colour bar now displays the BH particle count (BHPC) growth, i.e. the amount of BHs. This provides a comparison between the accretion of BH particles and smooth accretion, i.e. the process whereby (diffuse) gas is continuously accreted (Bournaud & Elmegreen, 2009; L'Huillier et al., 2012). To facilitate the visual analysis, Figure 4.11 also displays the densities (grey) of the control samples, QSMMC (left) and SFSMMC (right), rather than the individual data points.

The comparison between the QSMMC (left) and SFSMMC (right) samples in Figure 4.11 shows the clear distinction between the two control populations (grey). The overlap between the PSB and SFSMMC sample far exceeds that of the PSB and QSMMC sample. In short, both the merger (see Table 4.2) and BH (see Figure 4.11 right) history of PSBs and star-forming galaxies closely match, albeit PSBs being classified as quiescent at $t_{\mathrm{lbt}} = 0\,\mathrm{Gyr}$. This shows that, when no further stellar mass selection is chosen (as is done in the left panel of Figure 4.8) and the major merger progenitor cold gas content is not taken into consideration (see Figure 4.7 top right), PSBs essentially behave like star-forming galaxies until their recent shutdown in star formation.

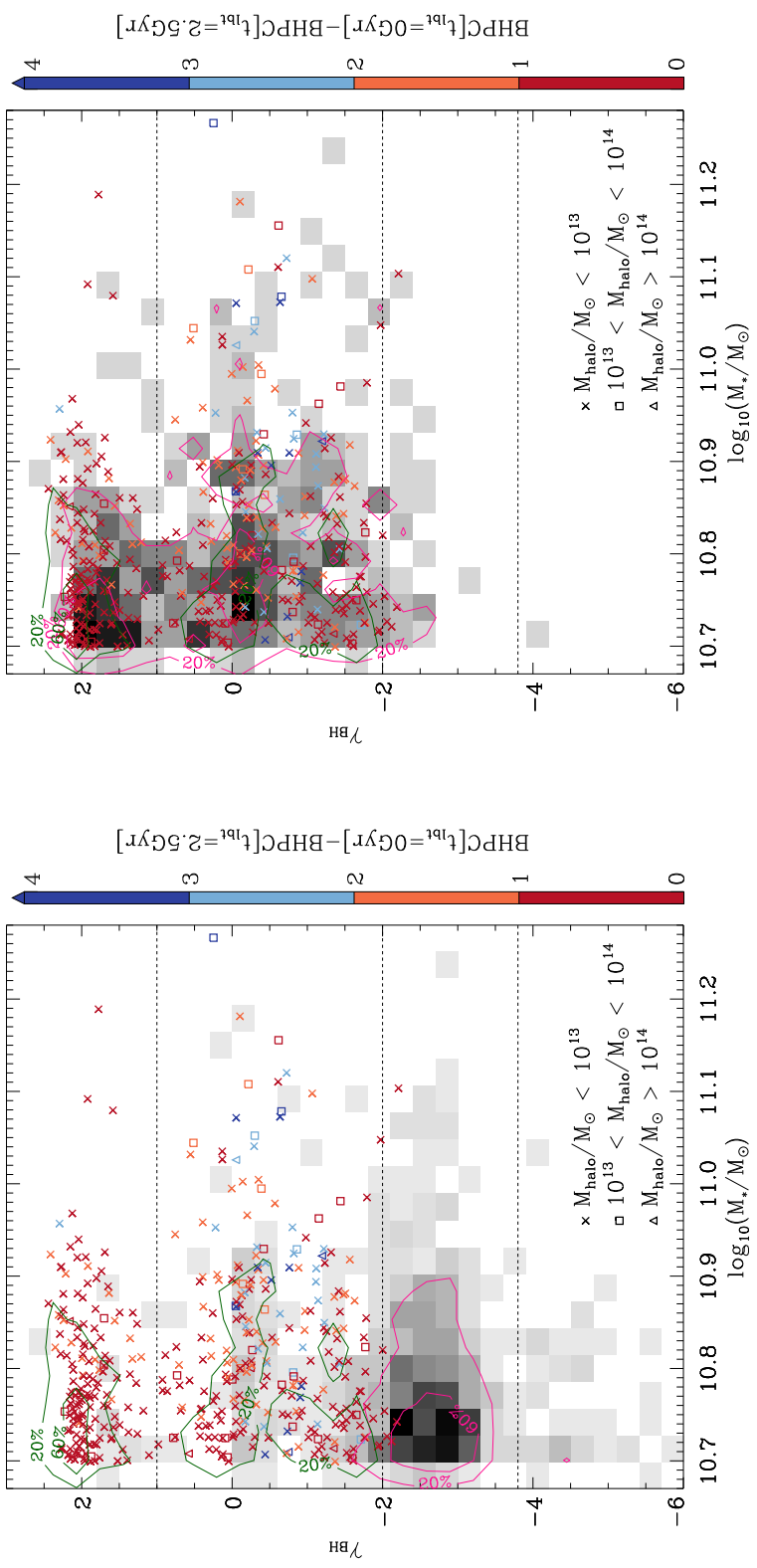

Figure 4.11: Same as the left Figure 4.10, but the colour bar encodes the growth of the BH particle count (BHPC) over the last 2.5 Gyr, i.e. the number of BH particles accreted by the main BH. Additionally, the control samples are shown as grey density distributions: QSMMC (left) and SFSMMC (right).

The majority of BHs in Figure 4.11 do not appear to accrete any other BHs (red), suggesting that BH growth in our simulation typically happens via smooth accretion rather than through the accretion of other BHs. When examining Figure 4.11 more closely, we find a weak correlation between increasing stellar mass and increasing number of accreted BHs. Again, this is not surprising as larger stellar mass galaxies typically grow their stellar mass via mergers (van Dokkum et al., 2010; L'Huillier et al., 2012; Qu et al., 2017). As a result more massive galaxies are more likely to merge with satellites which already host a seeded BH, increasing the likelihood of the main BH accreting a satellite BH. The weak correlation between stellar mass and accreted BHs agrees with our expectations of a hierarchical growth model in a ΛCDM Universe (see Section 1.2.2), in which large halos are formed late via the coalescence of smaller ones (Navarro et al., 1997; Cole et al., 2000; Bower et al., 2006).

	Field			Groups			Clusters		
Selection	PSBs [%]	Q [%]	SF [%]	PSBs [%]	Q [%]	SF [%]	PSBs [%]	Q [%]	SF [%]
$\gamma_{BH} \geq 1.0$	95.6	91.7	87.5	3.8	8.3	10.8	0.6	0	1.7
$1.0 > \gamma_{BH} \geq -2.0$	85.2	82.8	86.2	12.1	12.7	10.8	2.7	4.5	3.1
$-2.0 > \gamma_{BH} > -3.8$	100	84.7	65.4	0	12.4	26.9	0	2.9	7.7
$\gamma_{BH} \leq -3.8$	-	8.9	0	-	28.9	100	-	62.2	0
$3 > \gamma_{BH} > -6$	89.4	79.1	85.0	8.7	13.6	12.0	1.9	7.3	2.9

Table 4.4: Different subdivisions of γ_{BH} (see Equation 4.3), partitioned based on the horizontal lines in Figure 4.11 for the PSB (424), QSMMC (abbreviated Q, 641), and SFSMMC (abbreviated SF, 411) samples. Additionally, the selections are split into three groups according to their environment, i.e. halo mass: The field environment displays all galaxies with $M_{200,\mathrm{crit}}/\mathrm{M}_\odot \leq 10^{13}$, while the group environment shows all galaxies with $10^{13} < M_{200,\mathrm{crit}}/\mathrm{M}_\odot < 10^{14}$. Lastly, the galaxy cluster environment shows all galaxies with $M_{200,\mathrm{crit}}/\mathrm{M}_\odot \geq 10^{14}$.

Table 4.4 displays the BH growth γ_{BH} for the PSB, QSMMC, and SFSMMC samples as a function of halo mass, i.e. local environment. The horizontal lines in Figure 4.11 indicate the different γ_{BH} subdivisions of Table 4.4. As PSB and SFSMMC galaxies typically experience a more rapid evolution, i.e. their BHs have been more recently seeded, the sample size of galaxies evaluated over 2.5 Gyr is smaller for PSBs (424) and SFSMMC (411), compared to the QSMMC sample (641).

The last row of Table 4.4 shows that 89.4% of all PSB, 79.1% of QSMMC, and 85.0% of SFSMMC galaxies are found within a field environment ($M_{200,\mathrm{crit}}/\mathrm{M}_\odot < 10^{13}$) at $t_{\mathrm{lbt}} = 0$ Gyr. In contrast to 7.3% of QSMMC galaxies, only 1.9% of PSB and 2.9% of SFSMMC galaxies are found in clusters ($M_{200,\mathrm{crit}}/\mathrm{M}_\odot > 10^{14}$). This trend reflects the results obtained

in Section 4.2.3, i.e. that PSBs at $t_{\rm lbt} = 0\,\rm Gyr$ are overwhelmingly found in halos with few satellites.

QSMMC galaxies belong to the only sample with a non-negligible population in the $\gamma_{BH} \leq -3.8$ regime (see Figure 4.11). Moreover, galaxies found at these low γ_{BH} values, i.e. BHs with stagnated growth, are more likely to be found in clusters (62.2%) and groups (28.9%). As galaxy clusters are characterised by an abundance of hot gas and cluster galaxies have high relative velocities, inhibiting galaxy mergers, satellite galaxies have very limited opportunities to replenish their (cold) gas reservoir. Consequently, cluster galaxies have a lower likelihood of gas inflow reaching the galactic centre, resulting in low BH growth, and less numbers of PSBs.

4.5 Post-starburst galaxies in galaxy clusters

As observations suggest that the evolution of PSBs differs considerably with environment, we now focus on galaxy clusters (Poggianti et al., 1999; Goto, 2005; Wild et al., 2009; Lemaux et al., 2017; Paccagnella et al., 2019). Particularly, we want to understand how the environment, specifically galaxy clusters, influence PSB galaxy evolution. To increase our sample size, we lower the mass threshold in this section to include galaxies with at least 100 stellar particles, i.e. $M_* \geq 4.97 \cdot 10^9\,\rm M_\odot$. This does not include Table 4.5 and Figure 4.16, where the stellar mass threshold ($M_* \geq 4.97 \cdot 10^{10}\,\rm M_\odot$) is kept the same to allow direct comparisons with Table 4.3 and Figure 4.8.

4.5.1 Galaxy cluster stellar mass function comparison

We extend our study of the global stellar mass functions shown in Figure 4.2 by considering the high density environment and comparing to a catalogue of galaxy cluster candidates detected in the Ultra-Deep-Survey (UDS) (Socolovsky et al., 2018). Socolovsky et al. (2018) study the environment dependent galaxy evolution in the redshift range $0.5 < z < 1.0$ using the UDS. They identify 37 clusters, 11 of which contain more than 45 members. This results in a sample of 2210 galaxies, which provide the basis for the stellar mass function calculation (Socolovsky et al., 2018).

To compare with the observations, we follow a similar, yet not identical, prescription: Due to redshift uncertainties, Socolovsky et al. (2018) sample the volume of cylinders centred on clusters with height $H_{\rm cyl} = 250\,\rm Mpc$. Thereafter, they remove the contaminants by statistically subtracting the field galaxies in each cylinder (Socolovsky et al., 2018). To not unnecessarily introduce statistical contamination, we consider smaller cylinders with height $H_{\rm cyl} = 5\,\rm Mpc$. In both cases, the cylinder has radius $R_{\rm sph} = 1\,\rm Mpc$ and the stellar mass and the number of satellites N is calculated inside the cylinder. Following Socolovsky et al. (2018), we select only those clusters with a member range of $20 \leq N \leq 135$ and stellar mass within 1 Mpc of $10^{11.29} \leq M_*/\rm M_\odot \leq 10^{12.45}$. Subsequently, each cluster is considered along three random yet linearly independent spatial axes, increasing our sampling.

A total of 8406 Magneticum clusters fulfil the above criteria, with a total of 182213

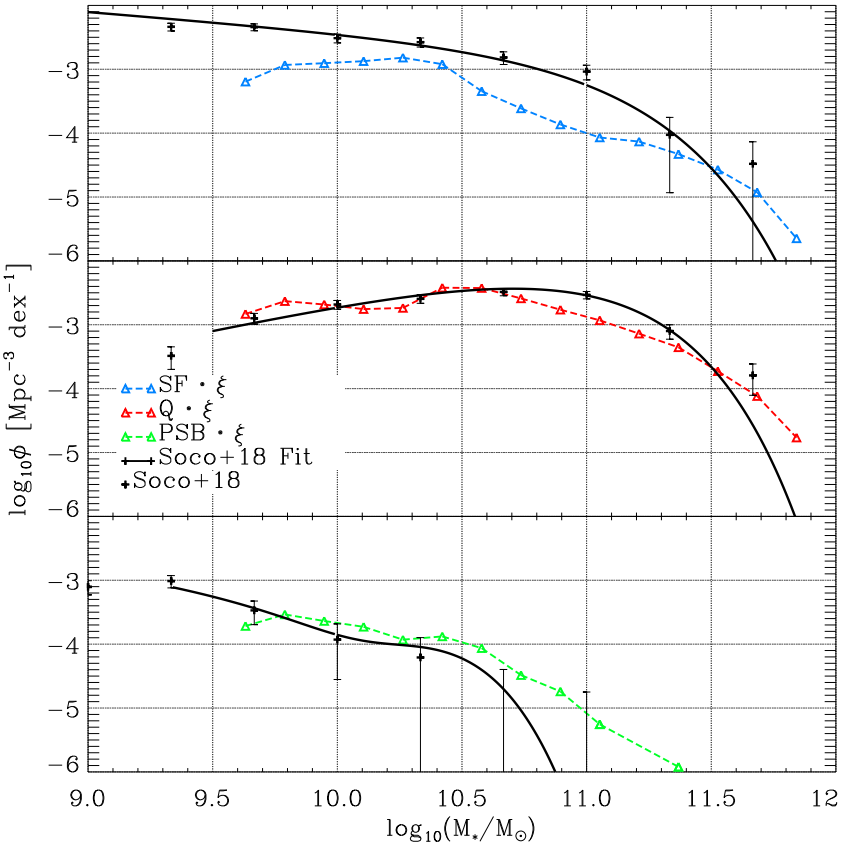

Figure 4.12: Stellar mass functions comparing Magneticum Box2 satellite galaxies to Socolovsky et al. (2018) at $z = 0.7$ in the group and cluster environments. The black solid line indicates the fit to the stellar mass functions by Socolovsky et al. (2018), while the coloured triangles represent the Magneticum results. The black solid fit line extends to the 90% mass completion limit. The different panels show the stellar mass functions of the star-forming (SF: top), the quiescent (Q: middle) and the post-starburst (PSB: bottom) populations. The Magneticum results are normalised by a factor of $\xi = 1/300$ to fit the arbitrarily normalised cluster observations (see Socolovsky et al. (2018)).

member galaxies with stellar mass $M_* \geq 4.97 \cdot 10^9\,\mathrm{M}_\odot$, of which 43084 are star-forming, 139129 are quiescent, and 7704 are identified as PSBs. The cluster and galaxy counts are the total values across all three spatial axes, i.e. are up to a factor of ~ 3 larger than the uniquely identified objects within Box2.

Figure 4.12 shows the $z = 0.7$ galaxy cluster stellar mass function of star-forming (blue), quenched (red) and PSB (green) galaxies. Similarly to the total sample shown in Figure 4.2 at $z = 0.7$, the cluster PSB stellar mass function has two bumps at $\log(M_*/\mathrm{M}_\odot) \sim 9.7$ and $\log(M_*/\mathrm{M}_\odot) \sim 10.4$ and is dominated by the low stellar mass end. However, the amplitude of the PSB bumps differs between the total and cluster sample. Furthermore, we find fewer star-forming and thus more quiescent galaxies in the cluster environment at

low stellar mass compared to the total sample (Figure 4.2).

The observations in Figure 4.12 are fitted by Schechter functions (star-forming and quiescent satellite galaxies) and double Schechter functions (PSBs), respectively (Baldry et al., 2008; Pozzetti et al., 2010). As the stellar mass functions discussed in Socolovsky et al. (2018) are arbitrarily normalised, the Magneticum results were also normalised to fit the observational data. Specifically, the Magneticum results (triangles) were multiplied by a factor of $\xi = 1/300$ to vertically adjust them to the observations. As shown in Figure 4.12, the shape of the cluster galaxy stellar mass functions from Magneticum are in very good agreement with observations (see also Steinborn et al. (2015)).

There are only two discrepancies: First, the star-forming distribution which, similar to Figure 4.2, lacks good agreement for masses between $10.5 < \log(M_*/\mathrm{M}_\odot) < 11.2$. As discussed in Section 4.2.2, this is due to the onset of the AGN feedback. Second, we find evidence for rare massive cluster PSBs which are not found in the significantly smaller observational sample. Further evidence for good agreement is provided by the replication of the PSB plateau in the mass range $10.0 < \log(M_*/\mathrm{M}_\odot) < 10.5$, indicating a preferential intermediate mass range.

4.5.2 Line-of-sight velocity: Observational comparison

In Figure 4.13, we show the normalised line-of-sight phase space velocity $v_{\mathrm{los}}/v_{200,\mathrm{crit}}$ of the PSBs at $z = 0.9$ as a function of the cluster-centric 2D projected radius, $R/r_{200,\mathrm{crit}}$, for both Box2 and Box2b and compare to observations by Muzzin et al. (2014). The left panel shows results using our standard stellar mass threshold $M_* \geq 4.97 \cdot 10^{10}\,\mathrm{M}_\odot$, while the right panel shows all galaxies down to the lower stellar mass threshold ($M_* \geq 4.97 \cdot 10^{9}\,\mathrm{M}_\odot$) previously used in Lotz et al. (2019). We show both stellar mass thresholds in Figure 4.13 to establish the similarity before continuing our analysis including all galaxies down to the lower stellar mass cut, so as to increase our phase space sampling (relevant especially to Figure 4.15).

Magneticum PSBs are shown as density maps and are scaled to the maximum density of the PSB galaxy population. The dashed black lines enveloping the density map in Figure 4.13 are based on the virial theorem and are introduced to provide a relationship between the velocity and the radius via $|v_{\mathrm{los}}/v_{200,\mathrm{crit}}| \sim |(R/r_{200,\mathrm{crit}})^{-1/2}|$. A proportionality factor of 1.6 is introduced to scale the enveloping dashed black lines. The factor is motivated by the strongest outlier of the observational data (Muzzin et al., 2014) and is used to filter out interlopers, i.e. galaxies that are only attributed to a cluster due to the LOS projection.

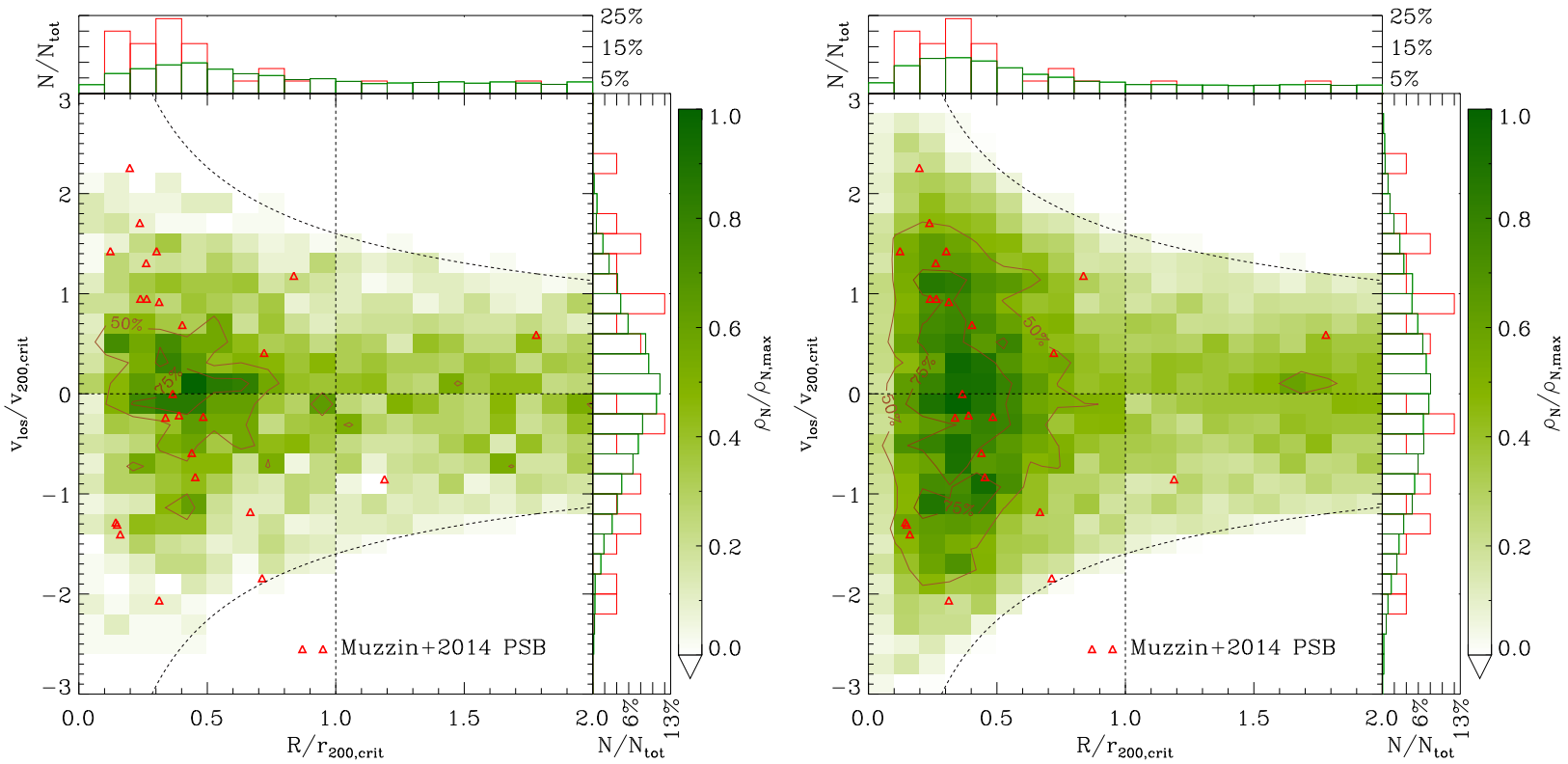

Figure 4.13: Post-starburst (PSB) galaxy normalised line-of-sight (LOS), $v_{\rm los}/v_{\rm 200,crit}$, phase space comparison between Muzzin et al. (2014) (red triangles) and Magneticum Box2 and Box2b (green) at $z = 0.9$ in dependence of the cluster-centric projected radial profile, $R/r_{\rm 200,crit}$. Left: All galaxies above $M_* \geq 4.97 \cdot 10^{10}\,{\rm M}_\odot$. Right: All galaxies above $M_* \geq 4.97 \cdot 10^{9}\,{\rm M}_\odot$. Satellite galaxies hosted by clusters in the mass range $1 \cdot 10^{14} < M_{\rm 200,crit}/{\rm M}_\odot < 20 \cdot 10^{14}$ are shown, following criteria outlined in Muzzin et al. (2014). The contour lines highlight the regions where the density is 50% and 75% of the maximum density. The histograms depict the relative abundance of each population projected onto the respective axes. The enveloping dashed black lines corresponds to $|v_{\rm los}/v_{\rm 200,crit}| \sim 1.6|(R/r_{\rm 200,crit})^{-1/2}|$ and is used to exclude interlopers.

Muzzin et al. (2014) consider data based on the Gemini Cluster Astrophysics Spectroscopic Survey (GCLASS). They investigate the line-of-sight (LOS) phase space of these 424 cluster galaxies at $z \sim 1$, of which 24 are identified as PSBs according to an absence of $O_{\rm II}$ emission while also hosting a young stellar population ($D_n(4000) < 1.45$) (Zahid & Geller, 2017).

To sample a similar volume as the observations, a cylinder of height 179Mpc was used. The cylinder height was calculated by evaluating the scatter around the mean observed redshift, $\sigma_{\rm z}$, resulting in $\sigma_{\rm z} = 0.036$ (van der Burg et al., 2013). The projections were considered along three linearly independent spatial axes. We identified 20371 PSBs in 1239 clusters.

We find that both the PSBs identified by Muzzin et al. (2014) and by Magneticum exhibit a strong preference for the inner region of the clusters independent of the used lower mass cut (see Figure 4.13). The inner over-density of PSBs found between $R \sim (0.15 - 0.5)\, r_{200,\rm crit}$ matches observations well. Of the 20371 identified PSBs, 14790, i.e. 73%, are found inside $r_{200,\rm crit}$. A subset of 9263 satellite galaxies, i.e. 45%, are even found inside $R < 0.5\, r_{200,\rm crit}$. The normalised distributions projected onto each axis further demonstrate the close agreement between observations and our simulation. The PSB galaxy preference for a distinct region of phase space, namely $R \sim (0.15 - 0.5)\, {\rm R}_{200,\rm crit}$, suggests a common cause: Most likely an environmental quenching mechanism leads to the shutdown of previously (strongly) star-forming galaxies on a timescale that brings them about halfway through the cluster until star formation is shutdown. This agrees with previous phase space results concerning the fast quenching of star-forming satellite galaxies in clusters (Lotz et al., 2019).

To better disentangle the underlying mechanisms potentially involved in triggering the starburst and subsequent shutdown in star formation of PSBs in galaxy cluster environments, we extend our investigation beyond the LOS phase space observational comparison. Using much of the same nomenclature as Figure 4.13, Figure 4.14 shows the PSBs within a 3D sphere instead of projections. Thus, Figure 4.14 no longer shows the PSBs inside a cylindrical volume which is the basis of the projected LOS population but a 3D sphere of radius $2r_{200,\rm crit}$, and therefore the sample of PSBs is smaller, i.e. only 5185 PSBs are plotted. Of this population, 3401 PSBs (or 66%) are infalling, i.e. $v_{\rm rad}/v_{200,\rm crit} < 0$. This is similar to the 69% infalling PSBs found in the LOS population. In addition to PSBs typically being characterised by infall, Figure 4.14 shows an abundance of PSBs in the inner cluster region. Furthermore, it appears that the PSB population, when compared to e.g. the older quiescent cluster population in Lotz et al. (2019), is not well mixed within the cluster, clearly indicating a recent infall.

4.5.3 Radial velocity as function of cluster mass and redshift

To better understand the relevant evolutionary pathways of PSBs in galaxy clusters, we analyse the normalised radial velocity of cluster PSBs as a function of the 3D cluster-centric radius at different cluster masses and redshifts. Figure 4.15 shows an overview of four different cluster mass ranges at redshifts $0.06 < z < 1.18$.

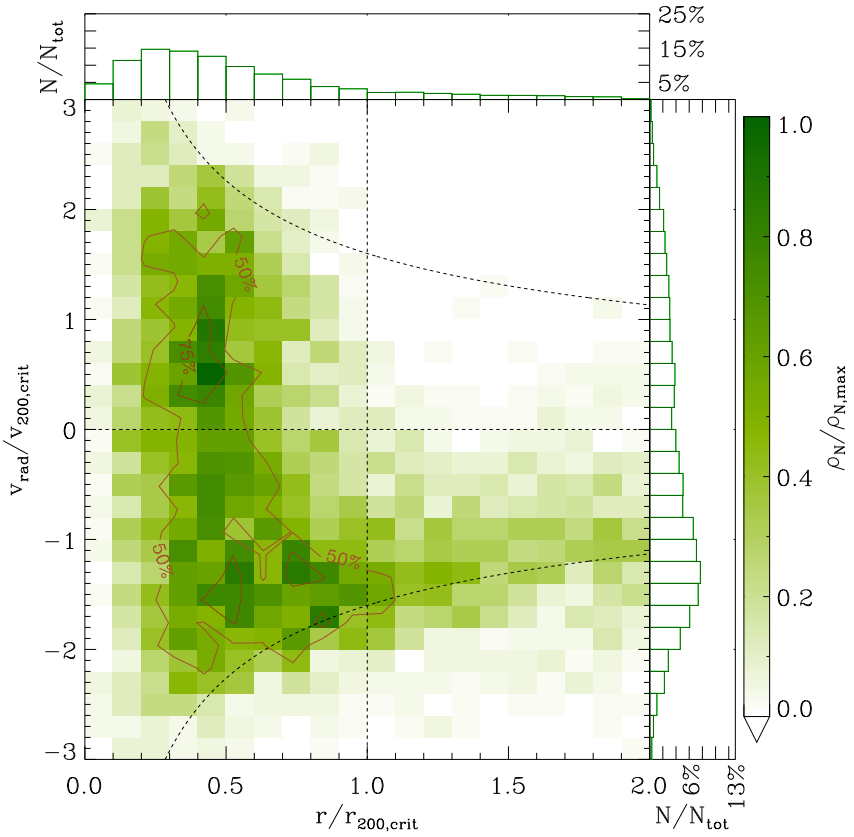

Figure 4.14: Same as Fig 4.13 but showing the normalised radial velocity $v_{\rm rad}/v_{\rm 200,crit}$ as a function of the 3D radius $r/r_{\rm 200,crit}$. The enveloping black line is no longer used to filter out galaxies, it only remains to guide the eye.

We find that cluster PSBs in all halo mass ranges at redshifts $z \lesssim 0.5$ have unusually negative radial velocities, i.e. they are in the process of infall. This means that they are either on their first infall into the cluster or are returning to the cluster after they have left it, typically referred to as backsplash galaxies (Pimbblet, 2011). However, when evaluating cluster PSBs, we find negligible evidence for backsplash orbits, rather the vast majority of cluster PSBs are experiencing their first infall.

In addition to showing that cluster PSBs are overwhelmingly characterised by infall, Figure 4.15 also reveals two important trends: First cluster PSBs become increasingly infall dominated towards higher cluster masses, suggesting a density dependent environmental quenching mechanisms, such as ram-pressure stripping (see Section 1.4.4, specifically Equation 1.13). This agrees with observations, which find that processes linked to the termination of star formation in galaxy clusters are more effective in denser environments (Poggianti et al., 2009; Raichoor & Andreon, 2012). For example, ram-pressure stripping is linearly dependent on the intra-cluster-medium (ICM) density, thus higher mass clusters are more efficient in quenching, i.e. the quenching timescale is shorter (Gunn & Gott,

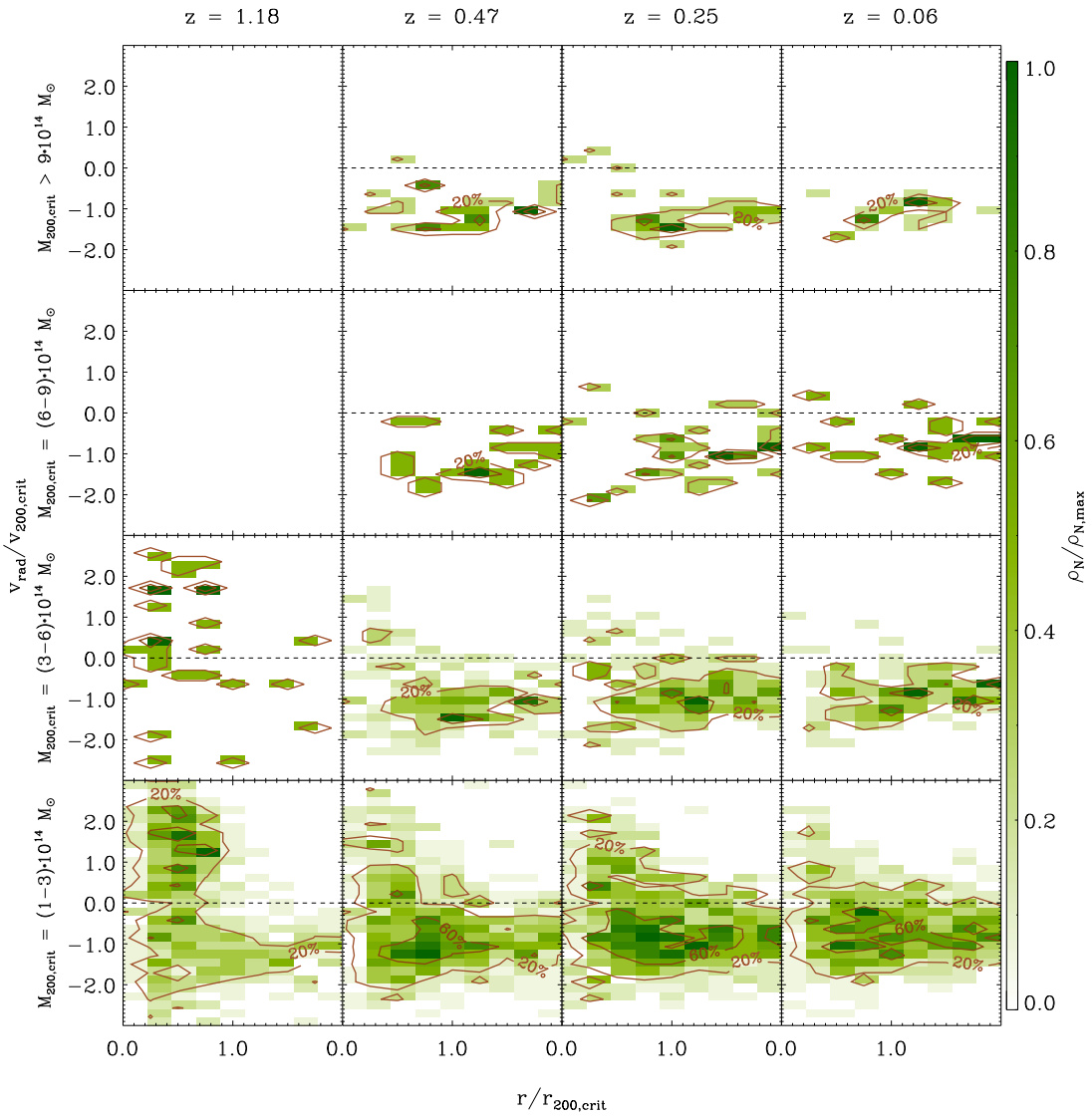

Figure 4.15: Box2 PSB galaxy ($M_* \geq 4.97{\cdot}10^9\,\mathrm{M}_\odot$) normalised radial velocity $v_\mathrm{rad}/v_\mathrm{200,crit}$ as a function of 3D radius $r/r_\mathrm{200,crit}$ for different cluster masses and redshifts. Columns from left to right have the following redshifts: $z = 1.18$, $z = 0.47$, $z = 0.25$, and $z = 0.06$. Rows from top to bottom have the following cluster masses: $M_\mathrm{200,crit} > 9 \cdot 10^{14}\,\mathrm{M}_\odot$, $M_\mathrm{200,crit} = (6-9) \cdot 10^{14}\,\mathrm{M}_\odot$, $M_\mathrm{200,crit} = (3-6) \cdot 10^{14}\,\mathrm{M}_\odot$, and $M_\mathrm{200,crit} = (1-3) \cdot 10^{14}\,\mathrm{M}_\odot$. The colour bar displays the relative phase space number density normalised to the maximum value of each individual panel. The contour lines correspond to regions showing 20% and 60% of the maximum density in each panel. The horizontal dashed line marks $v_\mathrm{rad}/v_\mathrm{200,crit} = 0$: PSBs above this line are moving outwards with respect to the cluster centre, while PSBs below this line are moving into the cluster. The empty panels are the result of a lack of clusters in the given redshift and cluster mass range.

1972; Lotz et al., 2019). In this case, higher mass clusters show an increased likelihood of cluster PSBs being fully quenched before they pass their pericenter.

Second, we find that cluster PSBs become slightly more infall dominated towards lower redshifts, especially visible in the transition from $z \sim 1.2$ to $z \sim 0.5$ in the lowest cluster mass regime in Figure 4.15. This is likely driven by the fact that clusters at $z \sim 1.2$, compared to clusters in the same mass range at $z \sim 0.5$, have an increased likelihood of currently undergoing cluster mergers. In other words, clusters at $z \sim 1.2$ are typically not relaxed, while clusters of similar mass at $z \sim 0.5$ have had enough time to at least centrally relax. Therefore, the same mass clusters at $z \sim 1.2$ are on average more disturbed, which in turn implies a less relaxed and hot ICM. Under these circumstances, the quenching efficiency is inhibited and thus cluster PSBs, on average, are able to penetrate deeper into the galaxy cluster before ram-pressure stripping quenching is efficient.

Considering these findings a picture of cluster PSB galaxy evolution in our simulation emerges, which strongly favours environmental quenching, e.g. ram-pressure stripping, as the responsible shutdown mechanism of cluster PSBs, in contrast to our results found for the field PSBs. Specifically, independent of whether an additional starburst is triggered during cluster infall or the PSB progenitors were previously experiencing significant star formation, the cluster environment appears to shut down the star formation during infall. This rapid shutdown increases the likelihood of previously star-forming/star-bursting galaxies to be classified as PSBs. Consequently, it appears that PSBs in galaxy clusters share a similar shutdown mechanism, rather than necessarily sharing the same SFR increasing mechanism.

4.5.4 Cluster merger statistics

Following the same approach as in Section 4.3.2, we analyse merger abundances in Table 4.5 to understand their statistical relevance to the evolution of cluster PSBs. Of the 411 projection independent PSBs with stellar mass $M_* \geq 4.97 \cdot 10^{10}\,\mathrm{M}_\odot$ identified within galaxy clusters in Box2 at $z = 0.9$, we successfully trace 410 PSBs to $z = 1.7$, i.e. over a time-span of $\sim 2.5\,\mathrm{Gyr}$.

When comparing cluster PSBs (Table 4.5) with non environmentally selected PSBs (Table 4.3) in the redshift range $0.9 < z < 1.7$, we find very similar merger abundances for all samples. For example, 92.9% of cluster PSBs and 92.6% of non environmentally selected PSBs both at $z = 0.9$ have experienced at least one merger event within the last $\sim 2.5\,\mathrm{Gyr}$. Additionally the similarity between the PSB and SFSMMC sample appears independent of the environment surveyed, further providing evidence for the importance of mergers for (recently) star-forming galaxies in our simulation. The only difference we find between Tables 4.5 and 4.3 is a slightly higher abundance of mini (57.1%) and minor (55.6%) mergers and a slightly lower abundance of major mergers (43.2%) in cluster PSBs, compared to mini (50.7%), minor (50.5%), and major (47.3%) mergers of non environmentally selected PSBs. Beyond these small differences the abundances found in Table 4.5 agree with the analysis presented in Section 4.3.2.

Criterion	PSBs	QSMMC	SFSMMC
Evaluated trees	410	409	405
$\Sigma(N_{\mathrm{mini}})$	370	197	400
$\Sigma(N_{\mathrm{minor}})$	290	98	293
$\Sigma(N_{\mathrm{major}})$	216	94	238
$N_{\geq 1\mathrm{mini}}$	57.1%	32.8%	53.6%
$N_{\geq 1\mathrm{minor}}$	55.6%	20.3%	51.4%
$N_{\geq 1\mathrm{major}}$	43.2%	20.8%	49.9%
$N_{\geq 1\mathrm{merger}}$	92.9%	53.1%	91.9%

Table 4.5: Following the nomenclature as introduced in Table 4.2, but showing results for cluster galaxies in the redshift range $0.9 < z < 1.7$ (compare to Table 4.3 in the same redshift range without an environmental selection). Of the 411 uniquely identified cluster PSBs with stellar mass $M_* \geq 4.97 \cdot 10^{10}\,\mathrm{M}_\odot$ in Box2 at $z = 0.9$, 410 progenitors were successfully traced over a time-span of 2.5 Gyr. PSB, QSMMC, and SFSMMC galaxies are selected so as to reproduce the cluster criteria outlined in Muzzin et al. (2014) (see Section 4.5.2).

4.5.5 Active galactic nuclei and supernovae

As observations suggest that ram-pressure stripping may trigger AGN activity (Poggianti et al., 2017; George et al., 2019; Poggianti et al., 2020), we investigate the AGN and SNe feedback of cluster PSBs at $z = 0.9$. We follow the method presented in Section 4.4.1 closely, with the exception that, instead of using the global $z \sim 0$ PSB sample, we use the cluster PSB sample presented in Table 4.5. Following the same nomenclature as Figure 4.8, Figure 4.16 shows the AGN (left) and SNe (right) power output for the PSB (green), SFSMMC (blue), and QSMMC (red) samples. We note that $t_{\mathrm{lbt}} = 0\,\mathrm{Gyr}$ corresponds to the identification redshift $z = 0.9$. Furthermore, we note that at $z \sim 1$ the time-steps in our simulation become larger, which leads the change in abundance of data points in Figure 4.16 at $t_{\mathrm{lbt}} \sim 0.5\,\mathrm{Gyr}$. As the feedback energy is normalised per unit time, this does not impact our results.

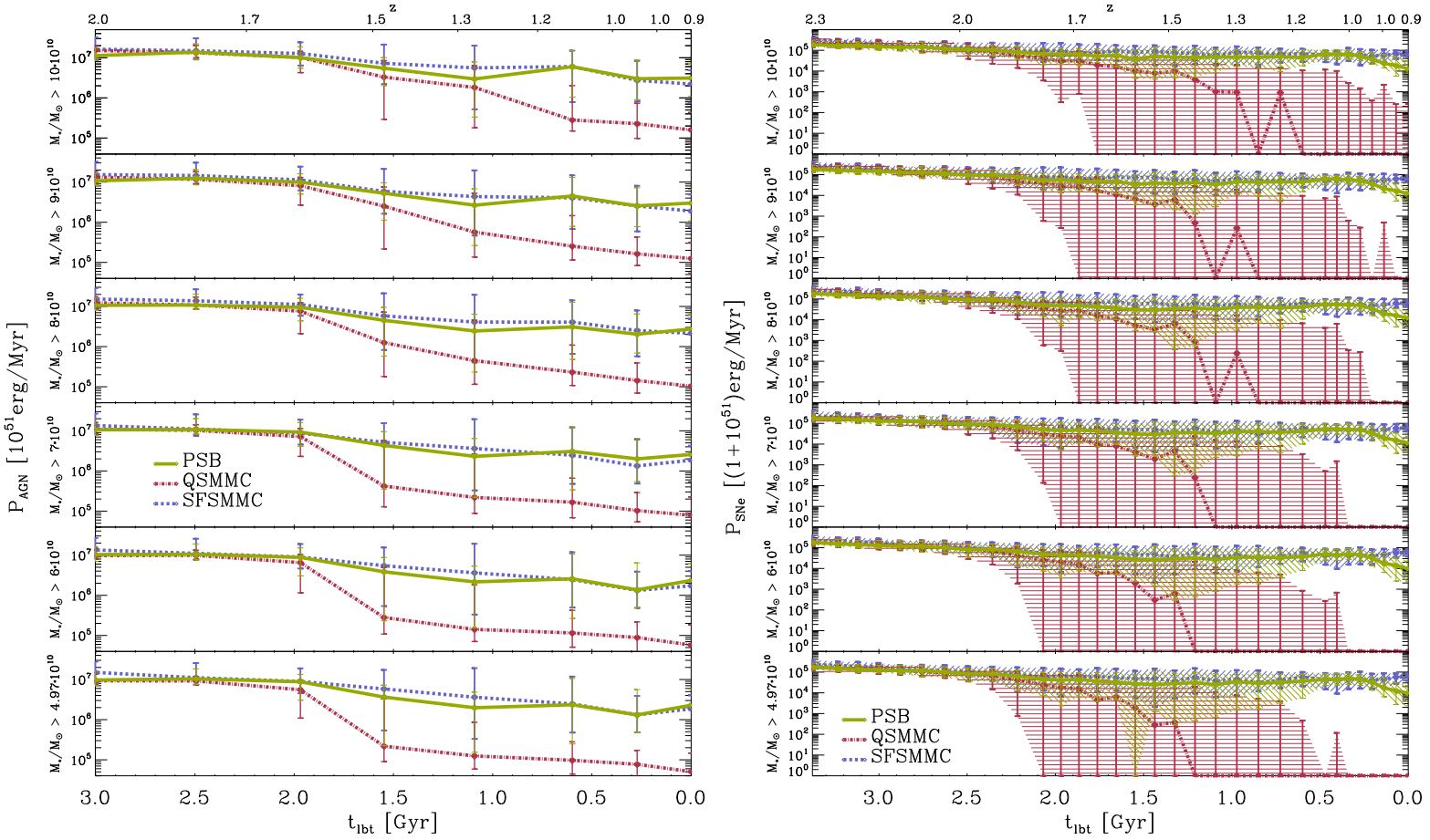

Figure 4.16: Active galactic nuclei (AGN: left figure) and supernovae (SNe: right figure) power output of cluster PSB (green), QSMMC (red), and SFSMMC (blue) samples identified at $z = 0.9$ and evaluated over the past $\sim 3.2\,\mathrm{Gyr}$ and $\sim 3.5\,\mathrm{Gyr}$ in units of $10^{51}\,\mathrm{erg/Myr}$ and $1 + 10^{51}\,\mathrm{erg/Myr}$, respectively. The cluster samples shown are based on the results displayed in Table 4.3. The different panels show increasing $z = 0.9$ stellar mass cuts, $M_* > [4.97, 6, 7, 8, 9, 10] \cdot 10^{10}\,\mathrm{M}_\odot$, from the lower to top panel. Both figures show the median, as well as the 30% and 70% percentiles as error bars for each population.

Figure 4.16 (left) shows no clear signs of an increase in recent AGN activity. As established in Section 4.5.3, cluster PSBs belong to a population of recently in-fallen galaxies. Consequently, if ram-pressure stripping would trigger AGN feedback, we would expect a signal within the last $\sim 1\,\mathrm{Gyr}$ (Lotz et al., 2019). However, we find no evidence for enhanced AGN activity. In fact, it appears that the AGN activity for all samples has been (gradually) declining since $t_{\mathrm{lbt}} \sim 2\,\mathrm{Gyr}$. Furthermore, there appears to be no strong stellar mass evolution for the PSB and SFSMMC samples. Only the QSMMC sample shows signs of a stellar mass evolution: As the stellar mass increases, the onset of the decline in AGN activity at $t_{\mathrm{lbt}} \sim 2\,\mathrm{Gyr}$ begins earlier, while the QSMMC AGN power output at $t_{\mathrm{lbt}} \sim 0\,\mathrm{Gyr}$ increases by a factor ~ 2 between the lowest and highest stellar mass selection.

In contrast, the SNe power output, i.e. the SFR, shows signs of small increase in activity starting at $t_{\mathrm{lbt}} \sim 0.5\,\mathrm{Gyr}$ for both the PSB and SFSMMC sample. However, as Figure 4.16 (right) shows, at $t_{\mathrm{lbt}} \sim 0.2\,\mathrm{Gyr}$ the PSB and SFSMMC samples diverge: The PSBs experience a short timescale decrease in star formation, reaching quiescent levels of star formation according to our blueness criterion, while the SFSMMC galaxies continue to experience an elevated star formation with signs of a small increase. The fact that SFSMMC galaxies are able to sustain star formation despite being located in a high density environment is likely due to their tangential infall orbits, ideally at large cluster-centric radii (Lotz et al., 2019). Figure 4.16 (right) also appears to show no indication of a stellar mass evolution: The only exception being the QSMMC sample, which appears to be characterised by more recent quenching with increasing stellar mass.

Generally, integrated over the evaluated time-span, both the AGN and SNe feedback shown in Figure 4.16 is significantly stronger than at $z \sim 0$ in Figure 4.8. As discussed in Section 4.4.2, recent BH seeding leads to an over-estimation of BH growth. Given the same stellar mass threshold, this becomes more relevant towards higher redshift, as galaxies need to assemble their mass in a shorter time period, i.e. more rapidly. As such, it appears likely that recent BH seeding impacts our $z = 0.9$ cluster sample. This likely explains the strong median AGN feedback at high look-back-times. Nonetheless, the fact that the AGN feedback does not increase towards recent look-back-times holds and suggests that AGN feedback is not relevant to shutting down star formation in cluster PSBs. This is further supported by the similarity in AGN feedback between the PSB and SFSMMC sample: While the former population is quenched at $t_{\mathrm{lbt}} = 0\,\mathrm{Gyr}$, the latter is not. Compared to low redshift, we also find a higher median SNe feedback at $z = 0.9$. This, however, appears purely physical as the star formation, and thus the SNe feedback, was significantly stronger at higher redshift compared to low redshift (Heavens et al., 2004). To conclude, we find that cluster PSBs are shutdown via environmental quenching with no evidence that additional galactic feedback is triggered.

4.6 Discussion

4.6.1 Environment and redshift evolution

We find that PSBs at low redshift are more frequently found in low halo mass environments and that the PSB-to-quenched fraction increases with redshift (Figure 4.1). The preference for low halo masses is further strengthened by the fact that 89.4% of $z \sim 0$ PSBs are found in halos with $M_{200,\mathrm{crit}}/\mathrm{M}_{\odot} < 10^{13}$ (Table 4.4). This agrees with DEEP2 and SDSS results which find low redshift PSBs in relatively under-dense environments (Goto, 2005) compared to high redshift PSBs (Yan et al., 2009). Similarly to the decline of the PSB-to-quenched fraction with decreasing redshift found in our simulation (Figure 4.1), observations also show that the fraction of PSBs declines from $\sim 5\%$ of the total population at $z \sim 2$, to $\sim 1\%$ by $z \sim 0.5$ (Wild et al., 2016). We note that MOSFIRE observations at $z \sim 1$ find a higher number of PSBs, relative to star-forming galaxies, in clusters than in groups or the field (Lemaux et al., 2017). Considering that we determine the abundance of PSBs with respect to quiescent galaxies, a comparison is difficult, however, as fewer star-forming than quiescent galaxies are found in high density environments (Dressler, 1980; Goto et al., 2003), and our PSB-to-quenched fraction does not show a strong preference for low halo mass at $z \sim 1$ (Figure 4.1), agreement seems plausible. Given these points, it appears that PSB galaxy evolution is strongly redshift dependent, favouring decreasing environmental densities towards lower redshifts, supporting the idea that the formation mechanism of PSBs is affected by redshift and environment.

Similarly, we also find a strong stellar mass function evolution (Figure 4.2): The abundance of PSBs above our stellar mass threshold increases significantly with increasing redshift, matching VVDS observations which find that the stellar mass density ($\log_{10}(M_*/\mathrm{M}_{\odot}) > 9.75$) of strong PSB galaxies is 230 times higher at $z \sim 0.7$ than at $z \sim 0.07$ (Wild et al., 2009). In contrast, when comparing the PSB galaxy stellar mass function shape to observations at redshifts $0.07 < z < 1.71$ (Wild et al., 2016; Rowlands et al., 2018) and the observations with each other, we do not find close agreement. These discrepancies are likely due to the stellar mass function sensitivity to the exact selection criteria of PSBs. Interestingly, when comparing the PSB stellar mass function at $z = 0.7$ to observations in the group and cluster environment (Figure 4.12), we find close agreement, including the double Schechter behaviour.

4.6.2 The impact of mergers

Evaluating PSBs in relation to the star-forming main sequence (Figure 4.5) shows that during their starburst phase, which is often correlated with recent mergers (Figure 4.9 and Table 4.2), massive PSBs are found significantly above the normalised redshift evolving main sequence (Speagle et al., 2014). Considering our global low redshift PSB sample, of which 89% have experienced a merger in the last 2.5 Gyr, we find that during peak star formation PSBs have SFRs which are a few times higher than on the main sequence, with a wide spread in their distribution. This behaviour matches observations by Pearson et al.

(2019), which, on the one hand, find that mergers have little effect on the SFR for the majority of merging galaxies, but, on the other hand, also find that an increasing merger fraction correlates with the distance above the main sequence, i.e. at sometimes mergers may induce starbursts. Furthermore, simulations by Di Matteo et al. (2008) suggest that strong starbursts, where the SFR is increased by a factor ≥ 5, are rare and only found in 15% of major galaxy interactions and mergers. Hani et al. (2020) highlights the impact of mergers on the SFR: Star-forming post-merger galaxies, which make up 67% of their post-merger galaxies identified in the IllustrisTNG simulation experience on average a SFR increase by a factor of ~ 2. This behaviour is in qualitative agreement with the correlation between mergers and the SFR increase found in our star-forming and, to a stronger extent, PSB galaxies (Figure 4.5). Additionally, when studying adjacent galaxies in IllustrisTNG, Patton et al. (2020) find that the presence of closest companions boost the average specific SFR of massive galaxies by 14.5%. This agrees with our study of an individual PSB in Figure 4.6, where we find an increase in star formation prior to identifying a merger event while another galaxy is in close proximity.

Figure 4.5 also shows that 23% of the tracked PSBs were previously quiescent, i.e. have undergone rejuvenation. When comparing quiescently star-forming, quenching, and rejuvenating galaxies in the EAGLE simulation, Trayford et al. (2016) find that $\sim 1.6\%$ and $\sim 10\%$ of all galaxies can be characterised as fast and slow rejuvenating galaxies, respectively. In other words, although (fast) rejuvenation is generally rare, rejuvenation may well be a relevant pathway for the evolution of PSBs. Consistent with the high merger abundances throughout our PSB sample, observations find quiescent galaxies may undergo rejuvenation events, e.g. via (gas rich) minor mergers, triggering the required starburst phase found in PSBs (Fang et al., 2012; Young et al., 2014; Belli et al., 2017; Rowlands et al., 2018; Yesuf & Ho, 2020).

Even when solely considering isolated merger simulations, much of the ambiguity concerning the quenching impact of mergers remains: Different types of mergers have been associated with varying quenching impacts, both directly, e.g. by introducing turbulence (Ellison et al., 2018), and indirectly, e.g. by facilitating BH growth (Hopkins et al., 2013; Barai et al., 2014). For example, binary galaxy merger simulations find that the termination of star formation by BH feedback in disc galaxies is significantly less important for higher progenitor mass ratios (Johansson et al., 2008, 2009a). Similar studies find that galaxies, which are dominated by minor merging and smooth accretion in their late formation history ($z \lesssim 2$), experience an energy release via gravitational heating which is sufficient to form red and dead elliptical galaxies by $z \sim 1$, even in the absence of SNe and AGN feedback (Johansson et al., 2009b). Meanwhile, SPH simulations of major mergers demonstrate that consistency with observations does not require BH feedback to terminate star formation in massive galaxies or unbind large quantities of cold gas (Debuhr et al., 2011). When linking the BH accretion rate with the galaxy-wide SFR, the disc galaxy mergers in the hydrodynamical simulations by Volonteri et al. (2015), typically find no temporal correlation and different variability timescales. However, when averaging over time during $\sim (0.2 - 0.3)$ Gyr long merger events, they find a typical increase of a factor of a few in the ratio of BH accretion rate to SFR (Volonteri et al., 2015). This qualita-

tively agrees with our results shown in Figures 4.8 and 4.9, that the recent AGN feedback increase in PSB and star-forming galaxies correlates with high merger abundances. Note, however, that not all simulations agree in that mergers and AGN feedback are correlated (e.g. Hayward et al. (2014)).

The ambiguous nature of merger impacts is also reflected in our results: Using a statistical approach, i.e. comparing merger abundances at $z \sim 0$ (Table 4.2), we find that 88.9% of PSBs, 23.4% of quenched (QSMMC), and 79.7% of star-forming stellar mass matched control (SFSMMC) galaxies experience at least one merger within the last 2.5 Gyr. The high merger abundance found in both our PSB and our SFSMMC sample highlights the varying merger impact: While our PSB sample is considered quiescent at $z \sim 0$, the reverse is true for SFSMMC galaxies with similarly rich merger histories, especially compared to the QSMMC sample. A similar behaviour is found when considering merger abundances at $z = 0.9$ (Table 4.3). Our high merger abundance broadly agrees with observations of local PSBs in SDSS, which, in their youngest age bin (< 0.5 Gyr), classify at least 73% of PSBs, far more than their control sample, as distorted or merging galaxies Meusinger et al. (2017). Generally, observations of PSBs in the local low density Universe are associated with galaxy-galaxy interactions and galaxy mergers (Zabludoff et al., 1996; Bekki et al., 2001; Yang et al., 2004; Goto, 2005; Yang et al., 2008; Pracy et al., 2009; Wild et al., 2009; Pawlik et al., 2018), in excellent agreement with our results.

When evaluating the cold gas fractions of PSB, QSMMC, and SFSMMC galaxies within three half-mass radii (Figure 4.7), we find wide agreement between PSB and SFSMMC galaxies, which show a preference for higher cold gas fractions, especially at higher merger mass ratios, i.e. towards minor and mini mergers. This is in line with observations, which find evidence for gas-rich mergers triggering central starbursts (Pawlik et al., 2018; D'Eugenio et al., 2020), fast quenching (Belli et al., 2019), and that recently merged galaxies typically are a factor of ~ 3 more atomic hydrogen rich than control galaxies at the same stellar mass (Ellison et al., 2018). The only difference between PSB and SFSMMC galaxies is found for the satellite progenitor populations in major mergers (Figure 4.7): The merging satellite progenitors of PSBs are characterised by a lower cold gas fraction compared to the SFSMMC sample. The subsequent lower cold gas content of post merger PSBs, compared to SFSMMC galaxies, may be linked to a higher likelihood of a subsequent shutdown in star formation. The implication being that less cold gas is available to maintain star formation, in addition to heating and/or redistribution of the available cold gas being supported at constant feedback. We note that the main progenitors of PSB and SFSMMC galaxies are typically already characterised by an abundance of cold gas prior to the merger. Meanwhile, the QSMMC sample is consistently found at lower cold gas fractions.

4.6.3 Shutting down star formation

As shown for our global $z \sim 0$ PSB sample (Figure 4.8) and the subset of six massive PSBs (Figure 4.9), we find a significant increase in AGN feedback at recent look-back-times and towards higher stellar masses. The importance of AGN feedback in shutting down PSBs is also evidenced by the decreasing agreement between the otherwise often

similarly behaving PSB and SFSMMC sample with increasing stellar mass. As the fraction of galaxies hosting an AGN is a strong function of stellar mass (Best et al., 2005), the apparent lack of strong AGN activity in the SFSMMC sample, compared to the PSB sample at high stellar masses, is a strong indicator of the AGN quenching effectiveness. In addition, the short shutdown timescale (Figure 4.5), the redistribution and heating of gas (Figure 4.6), the correlated BH growth (Figures 4.10 and 4.11), and the comparatively weak SNe energy (Figure 4.8) all suggest that merger triggered AGN feedback generally is the dominant shutdown mechanism of PSBs at low redshift. However, we can neither fully exclude other causes, nor do all PSBs necessarily experience the same shutdown sequence. Nonetheless, it appears likely that merger facilitated BH growth, which triggers AGN feedback, plays an important, albeit not necessarily exclusive, role in mediating between the starburst and post-starburst phase within our simulation at low redshifts. This agrees with previous Magneticum results, which found that merger events are not statistically dominant in fuelling mechanisms for nuclear activity, while still finding elevated merger fractions in AGN hosting galaxies compared to inactive galaxies, pointing towards an intrinsic connection between AGN and mergers (Steinborn et al., 2018). Generally, the importance of AGN feedback in explaining the sharp decline in the SFR found in (PSB) galaxies is also supported by several other works (Springel et al., 2005a; Yuan et al., 2010; Hopkins et al., 2013; Baron et al., 2018; Calabrò et al., 2019; Baron et al., 2020; Lanz et al., 2020; Wild et al., 2020).

We find evidence for the simultaneous mechanical expulsion and heating of previously star-forming cold gas (Figure 4.6). The rapid shutdown in this and similar examples (Figure 4.5) happens on timescales of $t_{\mathrm{shutdown}} \lesssim 0.4\,\mathrm{Gyr}$, which, due to the short timescale, generally favours AGN feedback as the expected quenching mechanism (Wild et al., 2020). Although much of the dense cold gas is heated, some cold gas remains in the recently quenched galaxy (Figure 4.6). The fact that significant amounts of cold gas are redistributed on short timescales rather than only being directly heated may provide an explanation to observations which find significant non star-forming (molecular) gas reservoirs in PSBs (Zwaan et al., 2013; French et al., 2015). This also agrees with other simulations, suggesting that the SFR is quenched with feedback via gas removal, with little effect on the SFR via gas heating (Barai et al., 2014). Furthermore, the large amounts of molecular gas found in PSBs rules out processes such as gas depletion, expulsion, and/or starvation as the dominant shutdown mechanisms (French et al., 2015), which is supported by the results presented in this thesis.

4.6.4 Post-starburst galaxies in galaxy clusters

Cluster PSBs are typically infalling, especially towards lower redshift and higher cluster masses (Figure 4.15). This matches previous results concerning the quenching of satellite galaxies in clusters (Lotz et al., 2019), showing that star-forming galaxies are more likely to be on their first infall, especially for higher mass clusters, indicating that ram-pressure stripping typically quickly shuts down star formation already during the first infall of satellite galaxies. This higher quenching effectiveness matches other simulations which find a

similar significant enhancement of ram-pressure stripping in massive halos compared to less massive halos (Arthur et al., 2019). In fact, several observations suggest that environmental quenching mechanisms, such as interactions with the ICM (Poggianti et al., 2009; Pracy et al., 2010) or specifically ram-pressure stripping (Gavazzi et al., 2013; Gullieuszik et al., 2017; Paccagnella et al., 2017; Owers et al., 2019; Paccagnella et al., 2019; Vulcani et al., 2020a), are responsible for the abundance of PSBs in galaxy clusters.

Generally, different populations of satellite galaxies, e.g. infalling, backsplash and virialised, occupy distinct regions of phase space (Oman et al., 2013). Hence, the clear preference of cluster PSBs for infall (Figure 4.15) provides a strong indication for environmental quenching such as ram-pressure stripping. This is also reflected in the PSB galaxy preference for distinct cluster-centric radii ($R \sim (0.15-0.5)\, r_{200,\mathrm{crit}}$) found in projections (Figure 4.13), showing excellent agreement with observations (Muzzin et al., 2014). It also agrees with SAMI observations of recently quenched cluster galaxies, which are exclusively found within $R \leq 0.6\, R_{200}$ and show a significantly higher velocity dispersion relative to the cluster population (Owers et al., 2019). Similarly, GASP observations find that PSB galaxies avoid cluster cores and are characterised by a large range in relative velocities (Vulcani et al., 2020a). Furthermore, both the SAMI and GASP phase space behaviour is consistent with recent infall, suggesting that PSBs could be descendants of galaxies which were quenched during first infall via ram-pressure stripping (Owers et al., 2019; Vulcani et al., 2020a). Providing multiple lines of evidence, Vulcani et al. (2020a) conclude that the outside-in quenching (Owers et al., 2019; Matharu et al., 2020), the morphology, and kinematics of the stellar component, along with the position of GASP PSBs within massive clusters point to a scenario in which ram-pressure stripping has shutdown star formation via gas removal. This is in excellent agreement with our findings.

When comparing merger abundances at $z = 0.9$ between non environmentally selected PSBs (Table 4.3) and cluster PSBs in (Table 4.5), we find broad agreement: Both samples are characterised by high merger abundances, i.e. in both samples $\sim 93\%$ of PSBs experience at least one merger event in the past 2.5 Gyr. In contrast to the non environmentally selected sample, cluster galaxies have slightly fewer major mergers (47.3% vs. 43.2% for PSBs). It appears that mergers are important in enabling the conditions necessary for (strong) star formation in cluster PSB progenitors, while it remains unclear what impact they have on shutting down star formation in cluster PSBs. In contrast to the majority of cluster PSB galaxy observations, observations of the Cl J1604 supercluster at $z \sim 0.9$ indicate that galaxy mergers are the principal mechanism for producing PSBs in clusters, while both interactions between galaxies and with the ICM also appear effective (Wu et al., 2014). As found by observations (Owers et al., 2019; Vulcani et al., 2020a) and our results (Figure 4.15), cluster PSBs belong to a population of recently in-fallen galaxies. Hence, it appears likely that PSB progenitors have had ample opportunity to experience mergers in the outskirts of clusters prior to infall, likely positively impacting recent star formation, thereby building a young stellar population necessary for their later identification as PSBs. As discussed in Section 4.6.2, the impact of mergers is varied and need not lead to a subsequent shutdown in star formation, e.g. via triggering AGN feedback. It seems plausible that ram-pressure stripping is more efficient in shutting down star formation than merger

triggered mechanisms, and hence is the dominant shutdown mechanism in cluster PSBs.

In Section 3.4, we found evidence for a starburst 0.2 Gyr after satellite galaxies first fall into their respective clusters, i.e. after crossing the cluster virial radius for the first time (Lotz et al., 2019). Specifically, we found that the average normalised blueness, i.e. $\mathrm{SSFR} \cdot t_{\mathrm{H}}$, of satellite galaxies with stellar masses $M_* > 1.5 \cdot 10^{10}\,\mathrm{M}_\odot$ shows a significant starburst lasting $\sim 0.2\,\mathrm{Gyr}$. As discussed by Lotz et al. (2019), this is likely driven by the onset of ram-pressure stripping which triggers a short starburst, followed by a complete shutdown in star formation within $< 1\,\mathrm{Gyr}$, often on shorter timescales. Observations of local cluster galaxies undergoing ram-pressure stripping come to similar conclusions: Ram-pressure likely drives an enhancement in star formation prior to quenching (Vulcani et al., 2018; Roberts & Parker, 2020). Similarly, cluster galaxies undergoing ram-pressure stripping in the GASP sample show a systematic enhancement of the star formation rate: As the excess is found at all galacto-centric distances within the discs and is independent of both the degree of stripping and star formation in the tails, Vulcani et al. (2020b) suggest that the star formation is most likely induced by compression waves triggered by ram-pressure stripping. Furthermore, HST observations have found strong evidence of ram-pressure stripping first shock compressing and subsequently expelling large quantities of gas from infalling cluster galaxies, which experience violent starbursts during this intense period (Ebeling et al., 2014). When evaluating the median SNe feedback, i.e. the SFR, at $z = 0.9$ for cluster PSBs (Figure 4.16), we find on average no evidence for a strong starburst at recent look-back-times. However, this signal likely correlates more strongly with cluster-centric radius (e.g. Lotz et al. (2019)). Hence it does not seem surprising that we find no signal. To better understand cluster PSB galaxy evolution, we also investigated whether cluster PSBs are found in the vicinity or crossing of cluster shock fronts: We found no evidence for an increased abundance of cluster PSBs near shocks.

Observations of GASP jellyfish galaxies undergoing strong ram-pressure stripping find that the majority host an AGN (Poggianti et al., 2017; George et al., 2019; Poggianti et al., 2020) and that the suppression of star formation in the central region is driven by AGN feedback (Radovich et al., 2019). Similarly, the Romulus C simulation finds evidence for ram-pressure stripping triggering AGN feedback, which may aid in the quenching process (Ricarte et al., 2020). When comparing these results to our study of median AGN feedback in cluster PSBs at $z = 0.9$ (Figure 4.16), we find no evidence for a recent increase in AGN feedback. However, we note that such an increase would likely correlate more strongly when evaluating the AGN feedback as a function of cluster-centric radius, which goes beyond the scope of this chapter. While observations based on the UKIDSS UDS conclude that a combination of environmental and secular processes are most likely to explain the appearance of PSBs in galaxy clusters (Socolovsky et al., 2019), all our evidence (Figures 4.15 and 4.16) suggests that environmental quenching in the form of ram-pressure stripping leads to the shutdown in star formation found in our cluster PSBs.

4.6.5 Numerical considerations

In addition to the ambiguous involvement of various physical mechanisms, the implementation and approximation of known physical mechanisms in simulations comes with its own set of challenges. For example, many simulations underestimate the effectiveness of feedback due to excessive radiative losses (Dalla Vecchia & Schaye, 2012), which, in turn, are the result of a lack of resolution and insufficiently realistic modelling of the interstellar medium (Schaye et al., 2015). Zheng et al. (2020) highlights the difficulty of reproducing very young PSBs in simulations, potentially indicating that new sub-resolution star formation recipes are required to properly model the process of star formation quenching.

Generally, we note that the identification and comparison of Magneticum PSBs to observations may be influenced by a number of effects: As discussed in Lotz et al. (2019), we measure the star formation rate rather than the colour of galaxies. In other words, we determine the star formation directly and instantaneously, rather than via the indirect, at times delayed, observation of local and/or global galactic properties. However, the galaxies selected in Box2 do not reproduce the detailed morphologies, especially concerning the cold thin discs, found in observations. Hence, we cannot capture the details of mechanisms which act on scales similar to our gas softening ($\epsilon_{\mathrm{gas}} = 3.75\,\mathrm{h}^{-1}\mathrm{kpc}$). This, for example, becomes relevant during ram-pressure stripping, where cold thin discs, dependent on infall geometry, provide additional shielding compared to more diffuse galactic configurations, thereby impacting quenching efficiencies and timescales. These limitations need to be addressed with the next generation of cosmological simulations.

4.7 Conclusions

In order to understand the physical mechanisms leading to the formation of post-starburst galaxies (PSBs), i.e. the reasons for both the onset of the initial starburst and the abrupt shutdown in star formation, we studied the environment and temporal evolution of PSBs with stellar mass $M_* > 4.97 \cdot 10^{10}\,\mathrm{M}_\odot$. To this end, we used Box2 of the hydrodynamical cosmological *Magneticum Pathfinder* simulations to resolve the behaviour of PSBs at varying redshifts $0.07 < z < 1.71$ both throughout our whole box volume as well as in specific environments such as galaxy clusters. The principal sample studied consists of 647 PSBs, identified at $z \sim 0$, i.e. a global sample spanning the whole box volume. Throughout our analysis the behaviour and evolution of PSBs is compared to star-forming (SF) and quiescent (Q) stellar mass matched control (SMMC) galaxy samples at different look-back-times (lbt). Furthermore, Magneticum PSBs are compared with observed quenched fractions (George et al., 2011; Tinker et al., 2013; Wang et al., 2018; Strazzullo et al., 2019), stellar mass functions (Muzzin et al., 2013; Wild et al., 2016; Rowlands et al., 2018), and the star formation main sequence (Speagle et al., 2014; Pearson et al., 2018) at different redshifts. Especially, we compare Magneticum galaxy cluster PSBs to observed high environmental density stellar mass functions (Socolovsky et al., 2018) and the cluster phase space behaviour at high redshift (Muzzin et al., 2014). Our results are summarised

as follows:

- At $z \sim 0$ PSBs and SF galaxies both are characterised by an abundance of mergers: 89% of PSB and 80% of SF galaxies experience at least one merger event within the last 2.5 Gyr, compared to 23% of quiescent galaxies. Over the same time-span, 65% of PSB, 58% of SF, and 9% of quiescent galaxies experience at least one major merger (M_* ratio: ¿ 1:3) event. This established similarity in merger abundances between PSB and SF galaxies is also found at redshift $z \sim 0.9$, both when evaluating the entire box volume as well as when specifically selecting galaxy cluster environments.

- Inspecting $z \sim 0$ PSB, quiescent, and SF galaxies with $M_* > 4.97 \cdot 10^{10}\,\mathrm{M}_\odot$, we find that the AGN feedback, which is associated with recent mergers, consistently outweighs the supernova (SNe) feedback. Within the last 0.5 Gyr, the difference between AGN and SNe feedback increases significantly: While the maximum median SNe power output for PSBs is $P_{\mathrm{SNe,PSB}} \leq 2 \cdot 10^{55}\,\mathrm{erg/Myr}$, the maximum median AGN power output is $P_{\mathrm{AGN,PSB}} \geq 3 \cdot 10^{56}\,\mathrm{erg/Myr}$. In contrast to the SF galaxies, PSBs are characterised by increasing AGN feedback with increasing stellar mass: At stellar masses $M_* > 1 \cdot 10^{11}\,\mathrm{M}_\odot$, the AGN feedback at $z = 0$ of PSBs ($P_{\mathrm{AGN,PSB}} \sim 10^{57}\,\mathrm{erg/Myr}$) is an order of magnitude larger than that of SF galaxies ($P_{\mathrm{AGN,SF}} \sim 10^{56}\,\mathrm{erg/Myr}$), which is similarly larger than that of quenched galaxies ($P_{\mathrm{AGN,Q}} \sim 10^{55}\,\mathrm{erg/Myr}$). This strongly indicates that the star formation in PSBs generally is shut down by AGN feedback.

- In our global $z \sim 0$ PSB sample we find that during the star formation shutdown, typically at $t_{\mathrm{lbt}} \lesssim 0.4\,\mathrm{Gyr}$, galactic gas, especially previously star-forming gas, is often abruptly heated, while simultaneously being redistributed. This results in a sharp decrease in the (cold) gas density. This is often correlated with a recent strong increase in black hole mass, triggering significant AGN feedback.

- In contrast to SF galaxies, PSBs in our global sample, especially at $t_{\mathrm{lbt}} = [0.1, 1]\,\mathrm{Gyr}$, show less spread, i.e. are more continuous in the distribution of SNe feedback energy. As the star formation rate (SFR) linearly impacts the SNe feedback, the smaller spread in the distribution of PSB SNe feedback in combination with slightly elevated median SFRs during recent times, compared to SF galaxies, is a reflection of the recent starburst phase. As the stellar mass increases, the median PSB SNe feedback increases slightly and the difference to SF galaxies, which continue to be associated with a wider distribution in feedback, becomes stronger.

- When evaluating the cold gas content prior to mergers in our global sample, PSB and SF progenitors show similar cold gas fractions ($f_{\mathrm{cgas}} \sim 0.9$) for the main progenitors. However, when considering cold gas abundances of satellite progenitors, i.e. not the most massive progenitors prior to major merger events, PSBs are characterised by lower cold gas fractions ($f_{\mathrm{cgas}} \sim 0.4$) compared to SF satellite progenitors ($f_{\mathrm{cgas}} \sim 0.7$). This is also reflected in the different abundance of satellite major

merger progenitors which have low cold gas fractions: $\sim 40\%$ of PSBs compared to $\sim 30\%$ of SF galaxies have $f_{\rm cgas} \lesssim 0.1$. This indicates that, statistically, PSBs have less cold gas available following major mergers than SF galaxies, leading to a higher likelihood of a subsequent shutdown in star formation.

- Prior to the star formation shutdown, PSB progenitors exhibit both sustained long term star formation ($t \sim 3\,\mathrm{Gyr}$), as well as short starbursts ($t \sim 0.4\,\mathrm{Gyr}$). During the starbursts, independent of the duration, massive PSB progenitors are found at least a factor of $\Delta MS[z]/MS[z] \gtrsim 5$ above the redshift evolving main sequence. Of the tracked PSBs in our global sample, 23% are rejuvenated galaxies, i.e. were considered quiescent before their starburst. At $z \sim 0.4$, Magneticum Box2 main sequence galaxies agree well with observations, while at $z \sim 0.1$ our galaxies lie slightly above observations (Speagle et al., 2014; Pearson et al., 2018).

- At $t_{\rm lbt} \sim 2.5\,\mathrm{Gyr}$, PSB and SF progenitors from our global sample are rarely found in isolated halos, whereas quenched progenitors are most often found in isolated halos. This initial difference between the PSB and SF versus quenched distribution of galaxies within a given halo, becomes indistinguishable at $t_{\rm lbt} \sim 2.5\,\mathrm{Gyr}$. This indicates that common initial conditions, i.e. an abundance, albeit not saturation, of galaxies in the immediate vicinity, are shared among SF and PSB galaxies, enabling the rich merger history found in these populations.

- We compared the Box2 total, SF, quenched, and PSB stellar mass functions (SMF) at multiple redshifts $0.07 < z < 1.71$ to observations, finding broad agreement (Muzzin et al., 2013; Wild et al., 2016; Rowlands et al., 2018): While the total and quenched SMF agree well with observations over the evaluated redshift range, the agreement for SF galaxies improves with increasing redshift. Meanwhile, PSB SMFs show that both the agreement between simulation and observations, as well as between observations, is subject to variation. When comparing stellar mass functions in group and cluster environments at $z = 0.7$, we are able to closely reproduce the observations (Socolovsky et al., 2018). In particular, similarly to observations, we also find evidence for a PSB plateau in the stellar mass range $10.0 < \log(M_*/\mathrm{M}_\odot) < 10.5$ in group and cluster environments.

- At redshifts $z \lesssim 1$, PSBs are consistently found close to our stellar mass threshold ($M_* > 4.97 \cdot 10^{10}\,\mathrm{M}_\odot$) and at low halo masses. Towards higher redshift the abundance of PSBs increases significantly, especially at higher stellar masses. Overall, the PSB-to-quenched fraction increases with redshift, most significantly between $z \sim 1.3$ and $z \sim 1.7$.

- To compare with line-of-sight (LOS) phase space observations of cluster PSBs at $z \sim 1$ (Muzzin et al., 2014), we environmentally selected PSBs in the same halo mass range ($10^{14} < M_{200,\rm crit}/\mathrm{M}_\odot < 2 \cdot 10^{15}$) and found close agreement with observations. In particular, cluster PSBs are preferentially located in a narrow region of phase

space with projected cluster-centric radii $R \sim (0.15 - 0.5)\,\mathrm{R}_{200,\mathrm{crit}}$. The fact that both simulated and observed cluster PSBs are found in the same preferential region of phase space suggests a shared environmentally driven mechanism relevant to the formation of PSBs, which is specific to galaxy clusters, such as ram-pressure stripping. When evaluating cluster PSBs at different redshifts and cluster masses, we find that cluster PSBs at $z \lesssim 0.5$ are overwhelmingly infall dominated, especially towards higher cluster masses. This further supports the idea that, different to the PSBs in the field, ram-pressure stripping shuts down star formation of previously active galaxies, thus leading to the identification of cluster PSBs within a distinct region of phase space.

- Cluster PSBs further show no signs of significantly increased AGN or SNe feedback at recent look-back-times. In other words, we find no evidence suggesting that AGN feedback is triggered via ram-pressure stripping during cluster infall for PSBs. We also find no evidence that the AGN is responsible for quenching cluster PSBs. This is further supported by the similarity in AGN feedback between the PSB and SF sample: While the former population is quenched at $t_{\mathrm{lbt}} = 0\,\mathrm{Gyr}$, the latter is not. Hence, we conclude that cluster PSBs are primarily shut down via environmental quenching, likely ram-pressure stripping.

To summarise, PSBs with stellar mass $M_* > 4.97 \cdot 10^{10}\,\mathrm{M}_\odot$ at $z \sim 0$ typically evolved as follows: First, PSB progenitors, which at $t_{\mathrm{lbt}} = 2.5\,\mathrm{Gyr}$ are predominantly found in halos with more than one galaxy, experience a merger event. Specifically, 89% of PSBs experience at least one merger within the last $t_{\mathrm{lbt}} = 2.5\,\mathrm{Gyr}$, with 65% undergoing at least one major merger. Second, the merger provides additional gas and/or facilitates the inflow of gas onto the PSB progenitor, often triggering a starburst phase. After the merger, the BH accretion, and thereby the AGN power output ($P_{\mathrm{AGN,PSB}} \geq 3 \cdot 10^{56}\,\mathrm{erg/Myr}$), typically increases significantly, leading to a quick shutdown in star formation often accompanied by a dispersal and heating of (previously star-forming) gas. Lastly, a PSB galaxy remains, i.e. a galaxy with a young stellar population and quiescent levels of star formation.

Strikingly, this evolution is different for PSBs found in galaxy clusters: While cluster PSBs also experience an abundance of mergers, leading to star formation enhancement, they are found in a distinct region of phase space, implying a shared environmentally driven quenching mechanisms. Moreover, cluster PSBs are usually just at first infall, especially in higher mass clusters, favouring a density dependent quenching mechanism such as ram-pressure stripping. In other words, although the merger abundance, associated with an increased SFR in cluster PSB progenitors prior to their infall, is similar to our global sample, the reason for the shutdown in star formation is not.

To conclude, we find that PSBs experience starbursts due to merger events, independent of their environment, but the quenching mechanisms strongly depend on environment: While AGN feedback is the dominant quenching mechanism for field PSBs, PSBs in galaxy clusters are quenched by ram-pressure stripping due to the hot cluster environment. Thus, for field galaxies their cold gas fraction prior to quenching from the AGN is important to

whether they stay star-forming or become PSBs, while for cluster PSBs their infall orbit is the most important factor for quenching, as discussed already by (Lotz et al., 2019). This likely leads to very different fundamental properties of PSBs in the field and clusters, but to study this in detail remains to be done in a future study.

Chapter 5

Summary and conclusion

This thesis was dedicated to studying the galactic star formation of rapidly evolving galaxies. To resolve both the evolution of individual galaxies and to provide a large statistical sample, we used the cosmological hydrodynamical simulation suite *Magneticum Pathfinder*. The astrophysical processes modelled by *Magneticum Pathfinder* include stellar winds, detailed star formation and stellar populations, chemical enrichment, black holes, active galactic nuclei (AGN), supernovae, thermal conduction, and cooling. These simulations enable the analysis of galaxies at different redshifts and in all cosmological environments, ranging from the low density field to high density galaxy clusters.

To study the quick evolution of transition galaxies, we focused on two galaxy populations: First, we studied star-forming satellite galaxies within, and in the vicinity of galaxy clusters in Chapter 3. The aim of this study was to determine the dominant quenching mechanism in galaxy clusters and to analyse the effect on galactic star formation. Second, we analysed post-starburst galaxies (PSBs) in different environments to determine the reasons for the starburst and the following shutdown of star formation. These results were presented in Chapter 4. We explored these key galactic transformations to identify the mechanisms driving rapid galaxy evolution and to determine their dependence on redshift, mass, and environment.

Regarding the first focus, we find that star-forming satellite galaxies in clusters are dominated by radial orbits compared to quiescent galaxies. As the velocity-anisotropy profiles show, this is the case at all cluster masses and throughout the studied redshift range $0 < z < 2$. However, the orbits of star-forming satellite galaxies are most strongly radially dominated at high cluster mass and low redshift. When comparing the profiles with observations we find good agreement at $z = 0.44$ (Biviano et al., 2013): Both the behaviour of star-forming (more radial orbits) and quiescent (more circular orbits) satellite galaxies, and the general increase of radially dominated orbits at larger cluster-centric radii are reproduced. The distinct correlation between radial orbits and star formation indicates that a connection exists between the details of cluster accretion and the internal galactic evolution.

We explore this connection further, by considering the line-of-sight and radial phase space behaviour: We find a strong dichotomy between star-forming and quiescent satellite

galaxies, in agreement with line-of-sight phase space observations (Biviano et al., 2013). Indeed, star-forming galaxies are predominantly found outside the virial radius, while quiescent galaxies are generally found within the central cluster region. Moreover, star-forming galaxies are dominated by negative radial velocities, i.e. are in the process of falling into the cluster. Therefore, we conclude that star-forming galaxies are quenched during their first infall into the galaxy cluster, thereby building the inner quiescent galaxy population. In particular, the phase space analysis shows that at high cluster mass and, to a lesser extent, low redshift star-forming galaxies are more likely to be quenched at the same cluster-centric radii, suggesting a quenching mechanism which scales with environmental density such as ram-pressure stripping.

To determine the details by which star-forming galaxies are quenched, we track individual orbits during cluster infall. We find that the quenching of star-forming satellite galaxies depends on stellar mass: In general, the star formation of high stellar mass galaxies begins to decrease long before crossing the cluster virial radius, leading to a longer overall quenching timescale ($\sim 2-3\,\mathrm{Gyr}$). In contrast, low stellar mass galaxies typically have a constant star formation rate until they approach the cluster virial radius, at which point the star formation rate declines sharply. As a result, low stellar mass galaxies have a shorter quenching timescale ($\sim 1\,\mathrm{Gyr}$). Notably, the overwhelming majority of star-forming satellite galaxies are completely quenched within 1 Gyr after crossing the cluster virial radius, independent of stellar mass. Indeed, the rapid quenching which is correlated with cluster infall strongly indicates that ram-pressure stripping is the dominant quenching mechanism in galaxy clusters.

The analysis of the small subset ($< 5\%$) of the so-called 'surviving' galaxies, classified as the galaxies which remain star-forming longer than 1 Gyr after infall, yields additional insights: First, survival among high stellar mass galaxies is strongly correlated with stellar mass. In other words, the probability of survival is highest among the highest stellar mass subset within the high stellar mass sample. Specifically, the subset of high mass survivors has a mean stellar mass ~ 4 times greater than the mean stellar mass of the total high mass sample. This indicates that the higher stellar mass, i.e. stronger gravitational binding, provides additional shielding during infall against ram-pressure stripping, which otherwise rapidly removes a galaxy's star-forming gas. Second, low stellar mass survivors have atypically shallow and tangential orbits. In particular, they have increased pericentres and maintain larger radial distance during their orbits. To summarise, low stellar mass survivors belong to the subset of galaxies which spend the least time in the high density, i.e. high quenching efficiency, regions of galaxy clusters, while high stellar mass survivors strongly favour the highest stellar masses within the high stellar mass sample. Ultimately, surviving galaxies are characterised by the properties which best mitigate the effects of ram-pressure stripping.

To differentiate between the impact of the cluster region and the environment prior to cluster infall, we divide infalling galaxies according to their previous environment. We find that a higher environmental density prior to infall, correlates with a faster decline in star-formation prior to cluster infall. Specifically, prior to infall the central galaxies of galaxy groups experience a quicker decline in star-formation compared to group satellites,

which in turn experience quicker quenching compared to isolated galaxies. Furthermore, high stellar mass galaxies typically experience stronger quenching prior to infall than low stellar mass galaxies, suggesting that mass quenching plays an important role in regulating star-formation in the outskirts of clusters.

Concerning the second focus of this thesis, we find that PSBs and star-forming galaxies share a high abundance of mergers, which is associated with a short timescale increase of star formation. In particular, 89% of PSB and 80% of star-forming galaxies at $z \sim 0$ experience at least one merger event within the last 2.5 Gyr, compared to only 23% of quiescent galaxies. On a related note, we find that, ~ 2.5 Gyr prior to identification, PSB and star-forming progenitors are rarely found in isolated halos, whereas quiescent progenitors are most often found in isolated halos, indicating that the initial environment strongly impacts the subsequent merger abundance, and thus the galactic evolution. The merger abundance of PSBs and star-forming galaxies remains similar across different environments, redshifts, and when divided according to merger fraction. However, a notable difference between the properties of the major merger progenitors exists. Namely, galaxies that merge with the main PSB progenitors have a significantly lower cold gas fraction prior to major merger events compared to star-forming main progenitors. This indicates that, statistically, PSBs have less cold gas available following major mergers than star-forming galaxies, thereby increasing the susceptibility to subsequent quenching.

Generally, we find evidence for both extended star formation and short starbursts prior to the decline of star formation. However, compared to star-forming galaxies, low redshift PSBs show a smaller spread in star formation, i.e. their star formation rates are more continuously distributed at recent look-back-times. Strikingly, 23% of the PSB progenitors are rejuvenated during their starburst, i.e. the star formation rate prior to the starburst is elevated from quiescent levels to rates greater equal that of the star-forming main sequence. This high rejuvenation rate further demonstrates the positive impact mergers can have on the short timescale star formation.

The analysis of the rapid star formation shutdown shows that the AGN feedback consistently outweighs the supernova feedback, especially towards recent look-back-times. In contrast to star-forming galaxies, the AGN feedback of PSBs at $z \sim 0$ increases with stellar mass. In particular, at the highest stellar masses, the PSB galaxy AGN feedback is an order of magnitude greater compared to star forming galaxies, which in turn is an order of magnitude greater than that of quiescent galaxies. The onset of AGN feedback is associated with the abrupt heating and redistribution of previously star-forming gas on timescales $\lesssim 0.4$ Gyr. The aforementioned statistical lack of cold gas in PSBs compared to star-forming galaxies implies that at constant AGN feedback PSBs are shutdown faster, as less cold gas needs to be heated or redistributed to suppress star formation. In other words, the cold gas fraction prior to mergers has a determining effect on the subsequent shutdown efficiency. To summarise, following the starburst, the star formation of $z \sim 0$ PSBs is generally shut down by AGN feedback.

Over time the abundance and distribution of PSBs evolves: At redshifts $z \lesssim 1$, PSBs are consistently found close to the stellar mass threshold and at low halo masses. Towards higher redshift the abundance of PSBs increases significantly, especially at high stellar

mass. Overall, the PSB-to-quenched fraction increases with redshift, most significantly between $z \sim 1.3$ and $z \sim 1.7$. In other words, both the absolute and relative abundance of PSBs increases with redshift. Furthermore, we find general agreement with observations when comparing the total, star-forming, quiescent and PSB stellar mass functions in the redshift range $0.07 < z < 1.71$ (Muzzin et al., 2013; Wild et al., 2016; Rowlands et al., 2018; Socolovsky et al., 2018). However, both the PSB stellar mass function agreement between different observations, and between observations and our results is subject to variation, depending on the exact observational classification used. Compared to observations, our results appear more robust to changes of the selection criteria.

As consistently indicated by observations, the evolution of PSBs differs significantly within galaxy clusters. We find that cluster PSBs are preferentially located within distinct regions of both line-of-sight and radial phase space, suggesting a shared environmentally driven formation mechanism. Moreover, similar to results discussed in the first part, cluster PSBs at $z \lesssim 0.5$ are overwhelmingly infall dominated, especially at high cluster mass. Thus, we conclude that ram-pressure stripping leads to the abrupt cessation of star formation in previously actively star-forming cluster PSBs. This conclusion is further strengthened by the fact that cluster PSBs show no significant signs of increased AGN or supernovae feedback at recent look-back-times. In contrast to field PSBs, we find no evidence that the AGN is relevant to the quenching of cluster PSBs, or for that matter, previously star-forming cluster galaxies. However, as the interplay between ram-pressure stripping and AGN triggering is rather complex, this may change with higher resolution and should be subject of future research.

In summary, this thesis has led to five key results. First, ram-pressure stripping is the dominant quenching mechanisms in galaxy clusters and leads to the quenching of most star-forming satellite galaxies during their first passage. Second, the satellite galaxies that remain star-forming the longest after infall have either shallow, tangential orbits or very high stellar mass, i.e. the properties that mitigate the effects of ram-pressure stripping. Third, PSB progenitors experience starbursts, and to a lesser extent rejuvenation, due to merger events, independent of environment. Fourth, field PSBs are primarily quenched by AGN feedback, which is especially effective in PSBs as the cold gas fraction of PSB progenitors is statistically lower compared to star-forming galaxies. Fifth, cluster PSBs are quenched by ram-pressure stripping, likely explaining the different properties observed between field and cluster PSBs. To study the evolution of galactic star formation with similar sample sizes and in greater detail, higher resolution simulations are needed. These would, for example, allow the in-depth study of merger geometry and its impact, and shed light on the details associated with the onset of AGN feedback.

Appendix A

Gone after one orbit: How cluster environments quench galaxies

Further tests were conducted to distinguish whether: a.) simulated line-of-sight galaxy distributions are compatible with the observations (Figure A.1) and b.) a correlation exists between pericentre passage and a star-burst (Figure A.2).

To compute the KS statistic shown in Figure A.1 each satellite galaxy distribution (both star-forming and quiescent and along each axis) of each cluster was compared with every other Magneticum cluster. The compared satellite galaxy sample is based on the same 86 clusters as shown in Figure 3.4 and provides a statistical metric to access the similarity between individual Magneticum clusters. As described in Section 3.3.1, we find that the differences between the single cluster observation by Biviano et al. (2013) and the stacked Magneticum clusters is typically much less than the expected cluster to cluster variation within the simulation. The only exception to this is the radial distribution of star-forming galaxies, which, however, still lie well within the 2 σ region of the cluster by cluster variation.

In Figure A.2, we investigated whether a correlation between pericentre passage of cluster satellite galaxies and a star-burst exists. We found no evidence for a star-burst. As we find a star-burst when normalising to cluster infall rather than pericentre passage (see Figure 3.10), this suggests that the star-burst is linked to infall rather than the pericentre passage, likely indicating the onset of ram-pressure stripping.

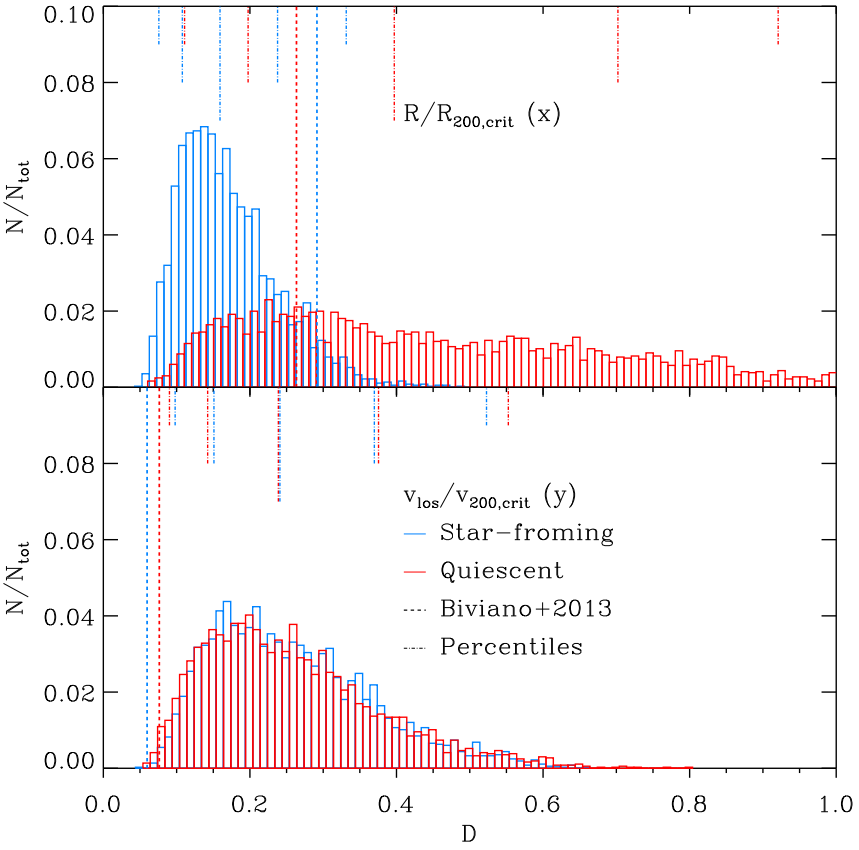

Figure A.1: Histograms of the normalised frequency of the Kolmogorov-Smirnov (KS) statistic, quantifying the distance between cluster-cluster distribution functions in Magneticum. The top panel shows the Magneticum cluster-cluster histograms of the radial distribution of both star-forming (blue) and quiescent (red) cluster satellite galaxies as presented in Figure 3.4. The bottom panel shows the same populations as the top panel, but along the line-of-sight velocity distribution. In each panel the dashed long vertical lines indicate the KS statistic from the comparison between Biviano et al. (2013) and the entire 86 cluster Magneticum sample. The dash-dotted lines at the top of the panels show the percentiles of the Magneticum cluster-cluster histograms. Short lines correspond to the 2σ region, medium lines correspond to the 1σ region, and the longest line indicates the median of the distribution.

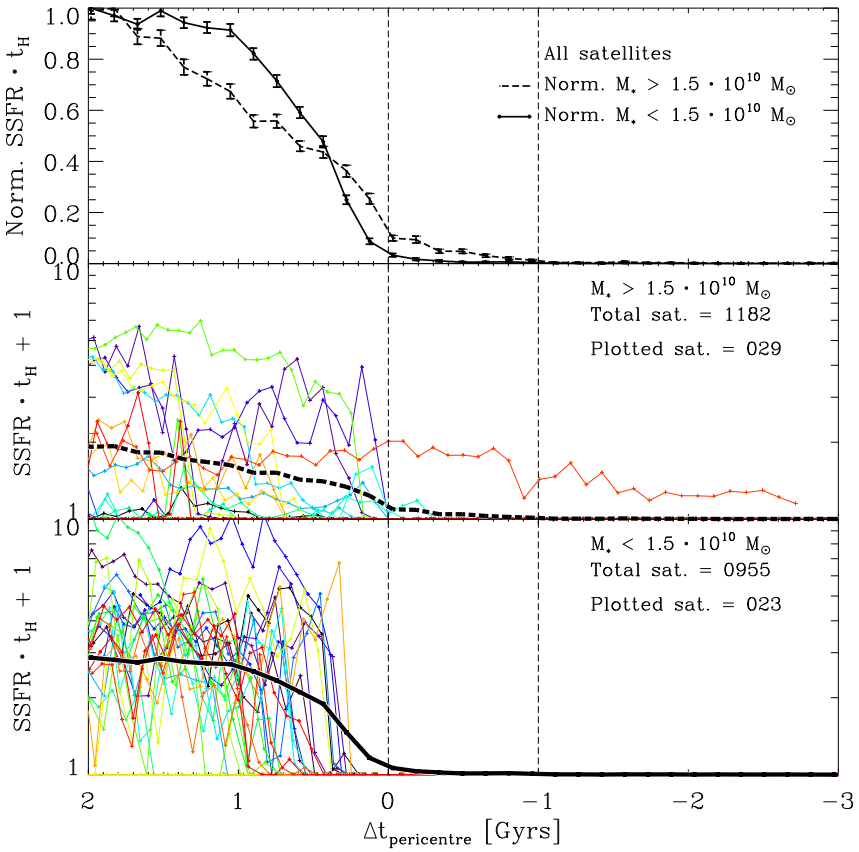

Figure A.2: Same as 3.10 but normalised to pericentre passage rather than cluster virial radius crossing, i.e. $\Delta t_{pericentre} = 0$ marks the pericentre passage of each satellite galaxy.

Bibliography

G. Aad, et al. (2012). 'Observation of a new particle in the search for the Standard Model Higgs boson with the ATLAS detector at the LHC'. *Physics Letters B* **716**(1):1–29.

K. N. Abazajian, et al. (2009). 'The Seventh Data Release of the Sloan Digital Sky Survey'. *ApJS* **182**(2):543–558.

B. P. Abbott, et al. (2016). 'GW151226: Observation of Gravitational Waves from a 22-Solar-Mass Binary Black Hole Coalescence'. *Phys. Rev. Lett.* **116**(24):241103.

B. P. Abbott, et al. (2017). 'GW170817: Observation of Gravitational Waves from a Binary Neutron Star Inspiral'. *Phys. Rev. Lett.* **119**(16):161101.

R. G. Abraham & S. van den Bergh (2001). 'The Morphological Evolution of Galaxies'. *Science* **293**(5533):1273–1278.

O. Agertz, et al. (2007). 'Fundamental differences between SPH and grid methods'. *MNRAS* **380**(3):963–978.

J. A. L. Aguerri, et al. (2017). 'Deep spectroscopy in nearby galaxy clusters - III. Orbital structure of galaxies in Abell 85'. *MNRAS* **468**:364–377.

J. A. L. Aguerri, et al. (2018). 'Deep spectroscopy of nearby galaxy clusters - IV. The quench of the star formation in galaxies in the infall region of Abell 85'. *MNRAS* **477**(2):1921–1934.

J. A. L. Aguerri, et al. (2009). 'The population of barred galaxies in the local universe. I. Detection and characterisation of bars'. *A&A* **495**(2):491–504.

S. W. Allen, et al. (2011). 'Cosmological Parameters from Observations of Galaxy Clusters'. *ARA&A* **49**(1):409–470.

O. Almaini, et al. (2017). 'Massive post-starburst galaxies at z 1 are compact proto-spheroids'. *MNRAS* **472**:1401–1412.

M. Annunziatella, et al. (2016). 'CLASH-VLT: Environment-driven evolution of galaxies in the z = 0.209 cluster Abell 209'. *A&A* **585**:A160.

E. Aprile, et al. (2012). 'Dark Matter Results from 225 Live Days of XENON100 Data'. *Phys. Rev. Lett.* **109**(18):181301.

M. Arnaud, et al. (2005). 'The structural and scaling properties of nearby galaxy clusters. II. The M-T relation'. *A&A* **441**(3):893–903.

M. Arnaud, et al. (2010). 'The universal galaxy cluster pressure profile from a representative sample of nearby systems (REXCESS) and the Y_{SZ} - M_{500} relation'. *A&A* **517**:A92.

A. Arth, et al. (2014). 'Anisotropic thermal conduction in galaxy clusters with MHD in Gadget'. *arXiv e-prints* p. arXiv:1412.6533.

J. Arthur, et al. (2019). 'THETHREEHUNDRED Project: ram pressure and gas content of haloes and subhaloes in the phase-space plane'. *MNRAS* **484**:3968–3983.

P. Aughton (2013). *The Story of Astronomy*. Quercus.

W. Baade & F. Zwicky (1934). 'On Super-novae'. *Proceedings of the National Academy of Science* **20**(5):254–259.

H. W. Babcock (1939). 'The rotation of the Andromeda Nebula'. *Lick Observatory Bulletin* **498**:41–51.

D. J. Bacon, et al. (2000). 'Detection of weak gravitational lensing by large-scale structure'. *MNRAS* **318**(2):625–640.

H. Baer, et al. (2015). 'Dark matter production in the early Universe: Beyond the thermal WIMP paradigm'. *Phys. Rep.* **555**:1–60.

Y. M. Bahé, et al. (2013). 'Why does the environmental influence on group and cluster galaxies extend beyond the virial radius?'. *MNRAS* **430**:3017–3031.

Y. M. Bahé, et al. (2012). 'The competition between confinement and ram pressure and its implications for galaxies in groups and clusters'. *MNRAS* **424**:1179–1186.

I. K. Baldry, et al. (2008). 'On the galaxy stellar mass function, the mass-metallicity relation and the implied baryonic mass function'. *MNRAS* **388**:945–959.

M. L. Balogh, et al. (1997). 'Star Formation in Cluster Galaxies at 0.2 Z 0.55'. *ApJ* **488**:L75–L78.

M. L. Balogh, et al. (1999). 'Differential Galaxy Evolution in Cluster and Field Galaxies at z˜0.3'. *ApJ* **527**(1):54–79.

M. L. Balogh, et al. (2000). 'The Origin of Star Formation Gradients in Rich Galaxy Clusters'. *ApJ* **540**:113–121.

C. Bambi & A. Dolgov (2015). *Introduction to Particle Cosmology: The Standard Model of Cosmology and its Open Problems*. UNITEXT for Physics. Springer Berlin Heidelberg.

P. Barai, et al. (2014). 'Kinetic or thermal AGN feedback in simulations of isolated and merging disc galaxies calibrated by the M-σ relation'. *MNRAS* **437**(2):1456–1475.

D. J. Barnes, et al. (2017). 'The Cluster-EAGLE project: global properties of simulated clusters with resolved galaxies'. *MNRAS* **471**:1088–1106.

J. Barnes & P. Hut (1986). 'A hierarchical O(N log N) force-calculation algorithm'. *Nature* **324**(6096):446–449.

J. E. Barnes & L. Hernquist (1992). 'Dynamics of interacting galaxies.'. *ARA&A* **30**:705–742.

D. Baron, et al. (2020). 'Multiphase outflows in post-starburst E+A galaxies - II. A direct connection between the neutral and ionized outflow phases'. *MNRAS* **494**(4):5396–5420.

D. Baron, et al. (2018). 'Direct evidence of AGN feedback: a post-starburst galaxy stripped of its gas by AGN-driven winds'. *MNRAS* **480**(3):3993–4016.

G. Battaglia, et al. (2005). 'The radial velocity dispersion profile of the Galactic halo: constraining the density profile of the dark halo of the Milky Way'. *MNRAS* **364**:433–442.

A. Bauer & V. Springel (2012). 'Subsonic turbulence in smoothed particle hydrodynamics and moving-mesh simulations'. *MNRAS* **423**(3):2558–2578.

A. M. Beck, et al. (2016). 'An improved SPH scheme for cosmological simulations'. *MNRAS* **455**:2110–2130.

P. Behroozi, et al. (2019). 'UNIVERSEMACHINE: The correlation between galaxy growth and dark matter halo assembly from z = 0-10'. *MNRAS* **488**(3):3143–3194.

K. Bekki (2009). 'Ram-pressure stripping of halo gas in disc galaxies: implications for galactic star formation in different environments'. *MNRAS* **399**:2221–2230.

K. Bekki & W. J. Couch (2003). 'Starbursts from the Strong Compression of Galactic Molecular Clouds due to the High Pressure of the Intracluster Medium'. *ApJ* **596**:L13–L16.

K. Bekki, et al. (2005). 'Origin of E+A galaxies - I. Physical properties of E+A galaxies formed from galaxy merging and interaction'. *MNRAS* **359**(3):949–965.

K. Bekki, et al. (2001). 'Formation and Evolution of E+A Galaxies in Dusty Starburst Galaxies'. *ApJ* **547**(1):L17–L20.

E. F. Bell, et al. (2003). 'The Optical and Near-Infrared Properties of Galaxies. I. Luminosity and Stellar Mass Functions'. *ApJS* **149**(2):289–312.

E. F. Bell, et al. (2004). 'Nearly 5000 Distant Early-Type Galaxies in COMBO-17: A Red Sequence and Its Evolution since z˜1'. *ApJ* **608**(2):752–767.

S. Belli, et al. (2017). 'KMOS^{3D} Reveals Low-level Star Formation Activity in Massive Quiescent Galaxies at 0.7 ¡ z ¡ 2.7'. *ApJ* **841**(1):L6.

S. Belli, et al. (2019). 'MOSFIRE Spectroscopy of Quiescent Galaxies at 1.5 ¡ z ¡ 2.5. II. Star Formation Histories and Galaxy Quenching'. *ApJ* **874**(1):17.

P. Belloni, et al. (1995). 'Detectability and incidence of E+A galaxies in the distant cluster Cl0939+472 (z=0.41).'. *A&A* **297**:61–76.

R. Bender, et al. (1992). 'Dynamically Hot Galaxies. I. Structural Properties'. *ApJ* **399**:462.

A. J. Benson, et al. (2002). 'The effects of photoionization on galaxy formation - I. Model and results at z=0'. *MNRAS* **333**(1):156–176.

L. Bergström (2000). 'Non-baryonic dark matter: observational evidence and detection methods'. *Reports on Progress in Physics* **63**(5):793–841.

J. Beringer, et al. (2012). 'Review of Particle Physics'. *Phys. Rev. D* **86**(1):010001.

P. N. Best, et al. (2005). 'The host galaxies of radio-loud active galactic nuclei: mass dependences, gas cooling and active galactic nuclei feedback'. *MNRAS* **362**(1):25–40.

P. N. Best, et al. (2007). 'On the prevalence of radio-loud active galactic nuclei in brightest cluster galaxies: implications for AGN heating of cooling flows'. *MNRAS* **379**(3):894–908.

H. A. Bethe (1939). 'Energy Production in Stars'. *Physical Review* **55**(5):434–456.

H. A. Bethe (1940). 'Recent Evidence on the Nuclear Reactions in the Carbon Cycle.'. *ApJ* **92**:118.

V. Biffi, et al. (2018). 'AGN contamination of galaxy-cluster thermal X-ray emission: predictions for eRosita from cosmological simulations'. *MNRAS* **481**(2):2213–2227.

J. Binney & S. Tremaine (1987). *Galactic dynamics*.

J. Binney & S. Tremaine (2011). *Galactic Dynamics: Second Edition*. Princeton Series in Astrophysics. Princeton University Press.

Y. Birnboim & A. Dekel (2003). 'Virial shocks in galactic haloes?'. *MNRAS* **345**(1):349–364.

A. Biviano, et al. (2017). 'The concentration-mass relation of clusters of galaxies from the OmegaWINGS survey'. *A&A* **607**:A81.

A. Biviano & B. M. Poggianti (2009). 'The orbital velocity anisotropy of cluster galaxies: evolution'. *A&A* **501**:419–427.

A. Biviano, et al. (2013). 'CLASH-VLT: The mass, velocity-anisotropy, and pseudo-phase-space density profiles of the z = 0.44 galaxy cluster MACS J1206.2-0847'. *A&A* **558**:A1.

A. Biviano & P. Salucci (2006). 'The radial profiles of the different mass components in galaxy clusters'. *A&A* **452**(1):75–81.

A. Biviano, et al. (2016). 'The dynamics of z ˜ 1 clusters of galaxies from the GCLASS survey'. *A&A* **594**:A51.

M. R. Blanton, et al. (2005). 'New York University Value-Added Galaxy Catalog: A Galaxy Catalog Based on New Public Surveys'. *AJ* **129**(6):2562–2578.

G. R. Blumenthal, et al. (1984). 'Formation of galaxies and large-scale structure with cold dark matter.'. *Nature* **311**:517–525.

S. Bocquet, et al. (2016). 'Halo mass function: baryon impact, fitting formulae, and implications for cluster cosmology'. *MNRAS* **456**:2361–2373.

P. Bodenheimer, et al. (2006). *Numerical Methods in Astrophysics: An Introduction*. Series in Astronomy and Astrophysics. Taylor & Francis.

M. Bolt, et al. (2007). *Biographical Encyclopedia of Astronomers*. Biographical Encyclopedia of Astronomers. Springer New York.

C. M. Booth & J. Schaye (2009). 'Cosmological simulations of the growth of supermassive black holes and feedback from active galactic nuclei: method and tests'. *MNRAS* **398**(1):53–74.

C. M. Booth & J. Schaye (2011). 'Towards an understanding of the evolution of the scaling relations for supermassive black holes'. *MNRAS* **413**(2):1158–1164.

T. Boroson (1981). 'The distribution of luminosity in spiral galaxies.'. *ApJS* **46**:177–209.

A. Boselli & G. Gavazzi (2006). 'Environmental Effects on Late-Type Galaxies in Nearby Clusters'. *PASP* **118**(842):517–559.

A. Boselli & G. Gavazzi (2014). 'On the origin of the faint-end of the red sequence in high-density environments'. *A&ARv* **22**:74.

F. Bournaud & B. G. Elmegreen (2009). 'Unstable Disks at High Redshift: Evidence for Smooth Accretion in Galaxy Formation'. *ApJ* **694**(2):L158–L161.

R. G. Bower, et al. (2006). 'Breaking the hierarchy of galaxy formation'. *MNRAS* **370**(2):645–655.

M. Boylan-Kolchin, et al. (2008). 'Dynamical friction and galaxy merging time-scales'. *MNRAS* **383**(1):93–101.

F. G. Braglia, et al. (2009). 'Multi-wavelength study of X-ray luminous clusters at z ˜ 0.3. I. Star-formation activity of cluster galaxies'. *A&A* **500**:947–963.

G. B. Brammer, et al. (2009). 'The Dead Sequence: A Clear Bimodality in Galaxy Colors from z = 0 to z = 2.5'. *ApJ* **706**(1):L173–L177.

J. P. Britton (2010). 'Studies in Babylonian lunar theory: part III. The introduction of the uniform zodiac'. *Archive for History of Exact Sciences* **64**(6):617–663.

P. Bull, et al. (2016). 'Beyond Λ CDM: Problems, solutions, and the road ahead'. *Physics of the Dark Universe* **12**:56–99.

A. Burkert (1995). 'The Structure of Dark Matter Halos in Dwarf Galaxies'. *ApJ* **447**:L25–L28.

R. Buta & F. Combes (1996). 'Galactic Rings'. *Fundamentals Cosmic Phys.* **17**:95–281.

H. Butcher & A. Oemler, Jr. (1978). 'The evolution of galaxies in clusters. I - ISIT photometry of C1 0024+1654 and 3C 295'. *ApJ* **219**:18–30.

A. Calabrò, et al. (2019). 'Deciphering an evolutionary sequence of merger stages in infrared-luminous starburst galaxies at z ∼ 0.7'. *A&A* **623**:A64.

N. Caldwell & J. A. Rose (1997). 'The Butcher-Oemler Effect at Low Redshift: Spectroscopy of Five Nearby Clusters of Galaxies'. *AJ* **113**:492.

N. Caldwell, et al. (1999). 'On the Origins of Starburst and Poststarburst Galaxies in Nearby Clusters'. *AJ* **117**:140–156.

N. Caldwell, et al. (1996). 'Spatial Distribution of the Starbursts in Post-Starburst Coma Cluster Galaxies'. *AJ* **111**:78.

R. R. Caldwell, et al. (1998). 'Cosmological Imprint of an Energy Component with General Equation of State'. *Phys. Rev. Lett.* **80**(8):1582–1585.

L. Canetti, et al. (2012). 'Matter and antimatter in the universe'. *New Journal of Physics* **14**(9):095012.

M. Cappellari, et al. (2006). 'The SAURON project - IV. The mass-to-light ratio, the virial mass estimator and the Fundamental Plane of elliptical and lenticular galaxies'. *MNRAS* **366**(4):1126–1150.

S. M. Carroll (2001). 'The Cosmological Constant'. *Living Reviews in Relativity* **4**(1):1.

S. M. Carroll, et al. (1992). 'The cosmological constant.'. *ARA&A* **30**:499–542.

T. Castro, et al. (2018). 'The effect of baryons in the cosmological lensing PDFs'. *MNRAS* **478**:1305–1325.

A. Cava, et al. (2017). 'Structural and dynamical modeling of WINGS clusters. I. The distribution of cluster galaxies of different morphological classes within regular and irregular clusters'. *A&A* **606**:A108.

R. Y. Cen, et al. (1990). 'The Universe in a Box: Thermal Effects in the Standard Cold Dark Matter Scenario'. *ApJ* **362**:L41.

D. Ceverino & A. Klypin (2009). 'The Role of Stellar Feedback in the Formation of Galaxies'. *ApJ* **695**(1):292–309.

E. Chaisson (1988). *Universe: An Evolutionary Approach to Astronomy*. Prentice-Hall.

T. K. Chan, et al. (2018). 'The origin of ultra diffuse galaxies: stellar feedback and quenching'. *MNRAS* **478**:906–925.

S. Chandrasekhar (1931a). 'The highly collapsed configurations of a stellar mass'. *MNRAS* **91**:456–466.

S. Chandrasekhar (1931b). 'The Maximum Mass of Ideal White Dwarfs'. *ApJ* **74**:81.

S. Chandrasekhar (1939). *An introduction to the study of stellar structure*.

S. Chandrasekhar (1943). 'Dynamical Friction. I. General Considerations: the Coefficient of Dynamical Friction.'. *ApJ* **97**:255.

S. Chatrchyan, et al. (2012). 'Observation of a new boson at a mass of 125 GeV with the CMS experiment at the LHC'. *Physics Letters B* **716**(1):30–61.

E. Cheung, et al. (2013). 'Galaxy Zoo: Observing Secular Evolution through Bars'. *ApJ* **779**(2):162.

R. A. Chevalier (1976). 'The hydrodynamics of type II supernovae.'. *ApJ* **207**:872–887.

Y. Chi & J. You (1995). *Molecular Clouds And Star Formation - Proceedings Of The 7th Guo Shoujing Summer School On Astrophysics*. World Scientific Publishing Company.

C. Chun (2006). *Thunder Over the Horizon: From V-2 Rockets to Ballistic Missiles*. War, technology, and history. Praeger Security International.

C. Cicone, et al. (2014). 'Massive molecular outflows and evidence for AGN feedback from CO observations'. *A&A* **562**:A21.

C. Clarkson (2012). 'Establishing homogeneity of the universe in the shadow of dark energy'. *Comptes Rendus Physique* **13**:682–718.

D. Clowe, et al. (2006). 'A Direct Empirical Proof of the Existence of Dark Matter'. *ApJ* **648**(2):L109–L113.

D. Clowe, et al. (2004). 'Weak-Lensing Mass Reconstruction of the Interacting Cluster 1E 0657-558: Direct Evidence for the Existence of Dark Matter'. *ApJ* **604**(2):596–603.

S. Cole, et al. (2000). 'Hierarchical galaxy formation'. *MNRAS* **319**(1):168–204.

H. Colebrooke, et al. (1817). *Algebra, with Arithmetic and Mensuration, from the Sanscrit of Brahmegupta and Bhascara. Translated by Henry Thomas Colebrooke ...* John Murray, Albemarle Street.

C. B. Collins & S. W. Hawking (1973). 'Why is the Universe Isotropic?'. *ApJ* **180**:317–334.

C. J. Conselice, et al. (2016). 'The Evolution of Galaxy Number Density at z 8 and Its Implications'. *ApJ* **830**:83.

W. J. Couch & R. M. Sharples (1987). 'A spectroscopic study of three rich galaxy clusters at zeta=0.31.'. *MNRAS* **229**:423–456.

A. Crelle, et al. (1908). *Journal für die reine und angewandte Mathematik*. No. Bd. 134-135. W. de Gruyter.

D. J. Croton (2013). 'Damn You, Little h! (Or, Real-World Applications of the Hubble Constant Using Observed and Simulated Data)'. *Publ. Astron. Soc. Australia* **30**:e052.

D. J. Croton, et al. (2006). 'The many lives of active galactic nuclei: cooling flows, black holes and the luminosities and colours of galaxies'. *MNRAS* **365**(1):11–28.

H. H. Crowl, et al. (2005). 'Dense Cloud Ablation and Ram Pressure Stripping of the Virgo Spiral NGC 4402'. *AJ* **130**(1):65–72.

L. Cullen & W. Dehnen (2010). 'Inviscid smoothed particle hydrodynamics'. *MNRAS* **408**(2):669–683.

C. Cunningham (2017). *The Scientific Legacy of William Herschel*. Historical & Cultural Astronomy. Springer International Publishing.

H. D. Curtis (1917). 'Novae in the Spiral Nebulae and the Island Universe Theory'. *PASP* **29**(171):206–207.

J. J. Dalcanton, et al. (1997). 'The Formation of Disk Galaxies'. *ApJ* **482**(2):659–676.

J. E. Dale (2015). 'The modelling of feedback in star formation simulations'. *New Astron. Rev.* **68**:1–33.

C. Dalla Vecchia & J. Schaye (2008). 'Simulating galactic outflows with kinetic supernova feedback'. *MNRAS* **387**(4):1431–1444.

C. Dalla Vecchia & J. Schaye (2012). 'Simulating galactic outflows with thermal supernova feedback'. *MNRAS* **426**(1):140–158.

T. J. Davidge (2008). 'The Stellar Content of the Post-Starburst s0 Galaxy NGC 5102'. *AJ* **135**(4):1636–1648.

M. Davis, et al. (1985). 'The evolution of large-scale structure in a universe dominated by cold dark matter'. *ApJ* **292**:371–394.

T. A. Davis, et al. (2019). 'Evolution of the cold gas properties of simulated post-starburst galaxies'. *MNRAS* **484**(2):2447–2461.

P. Dayal & A. Ferrara (2018). 'Early galaxy formation and its large-scale effects'. *Phys. Rep.* **780**:1–64.

P. de Bernardis, et al. (2000). 'A flat Universe from high-resolution maps of the cosmic microwave background radiation'. *Nature* **404**(6781):955–959.

W. J. G. de Blok (2010). 'The Core-Cusp Problem'. *Advances in Astronomy* **2010**:789293.

W. J. G. de Blok, et al. (2001). 'Mass Density Profiles of Low Surface Brightness Galaxies'. *ApJ* **552**(1):L23–L26.

G. de Vaucouleurs (1948). 'Recherches sur les Nebuleuses Extragalactiques'. *Annales d'Astrophysique* **11**:247.

G. de Vaucouleurs (1953). 'On the distribution of mass and luminosity in elliptical galaxies'. *MNRAS* **113**:134.

G. de Vaucouleurs (1956). 'Luminosity Functions and Population Subtypes in the Magellanic Clouds'. *Irish Astronomical Journal* **4**:13.

G. de Vaucouleurs (1958). 'Photoelectric photometry of the Andromeda Nebula in the UBV system.'. *ApJ* **128**:465.

G. de Vaucouleurs (1959a). 'Classification and Morphology of External Galaxies.'. *Handbuch der Physik* **53**:275.

G. de Vaucouleurs (1959b). 'General Physical Properties of External Galaxies.'. *Handbuch der Physik* **53**:311.

G. de Vaucouleurs (1959c). 'Photoelectric Photometry of Messier 33 IN the u, b, v, System.'. *ApJ* **130**:728.

H. De Vega, et al. (2012). *Phase Transitions in the Early Universe: Theory and Observations*. Nato Science Series II:. Springer Netherlands.

J. Debuhr, et al. (2011). 'The growth of massive black holes in galaxy merger simulations with feedback by radiation pressure'. *MNRAS* **412**(2):1341–1360.

W. Dehnen (2001). 'Towards optimal softening in three-dimensional N-body codes - I. Minimizing the force error'. *MNRAS* **324**(2):273–291.

W. Dehnen & H. Aly (2012). 'Improving convergence in smoothed particle hydrodynamics simulations without pairing instability'. *MNRAS* **425**:1068–1082.

A. Dekel & Y. Birnboim (2008). 'Gravitational quenching in massive galaxies and clusters by clumpy accretion'. *MNRAS* **383**(1):119–138.

A. Dekel, et al. (2009). 'Cold streams in early massive hot haloes as the main mode of galaxy formation'. *Nature* **457**(7228):451–454.

A. Dekel & J. Ostriker (1999). *Formation of Structure in the Universe*. Formation of Structure in the Universe. Cambridge University Press.

A. Dekel & J. Silk (1986). 'The Origin of Dwarf Galaxies, Cold Dark Matter, and Biased Galaxy Formation'. *ApJ* **303**:39.

W. Demtröder (2017). *Mechanics and Thermodynamics*. Undergraduate Lecture Notes in Physics. Springer International Publishing.

F. D'Eugenio, et al. (2020). 'Inverse stellar population age gradients of post-starburst galaxies at z = 0.8 with LEGA-C'. *MNRAS* **497**(1):389–404.

P. Di Matteo, et al. (2008). 'On the frequency, intensity, and duration of starburst episodes triggered by galaxy interactions and mergers'. *A&A* **492**(1):31–49.

M. Dickinson, et al. (2003). 'The Evolution of the Global Stellar Mass Density at 0z3'. *ApJ* **587**:25–40.

G. A. Dilts (1999). 'Moving-least-squares-particle hydrodynamics?I. Consistency and stability'. *International Journal for Numerical Methods in Engineering* **44**(8):1115–1155.

S. Dodelson & L. Knox (2000). 'Dark Energy and the Cosmic Microwave Background Radiation'. *Phys. Rev. Lett.* **84**(16):3523–3526.

K. Dolag, et al. (2009). 'Substructures in hydrodynamical cluster simulations'. *MNRAS* **399**:497–514.

K. Dolag, et al. (2015). 'Constraints on the distribution and energetics of fast radio bursts using cosmological hydrodynamic simulations'. *MNRAS* **451**:4277–4289.

K. Dolag, et al. (2004). 'Thermal Conduction in Simulated Galaxy Clusters'. *ApJ* **606**:L97–L100.

K. Dolag, et al. (2006). 'Simulating the physical properties of dark matter and gas inside the cosmic web'. *MNRAS* **370**:656–672.

K. Dolag, et al. (2017). 'Distribution and Evolution of Metals in the Magneticum Simulations'. *Galaxies* **5**:35.

K. Dolag & F. Stasyszyn (2009). 'An MHD GADGET for cosmological simulations'. *MNRAS* **398**:1678–1697.

K. Dolag, et al. (2005). 'Turbulent gas motions in galaxy cluster simulations: the role of smoothed particle hydrodynamics viscosity'. *MNRAS* **364**:753–772.

A. Dressler (1980). 'Galaxy morphology in rich clusters - Implications for the formation and evolution of galaxies'. *ApJ* **236**:351–365.

A. Dressler (1984). 'The Evolution of Galaxies in Clusters'. *ARA&A* **22**:185–222.

A. Dressler & J. E. Gunn (1983). 'Spectroscopy of galaxies in distant clusters. II - The population of the 3C 295 cluster'. *ApJ* **270**:7–19.

A. Dressler, et al. (2013). 'The IMACS Cluster Building Survey. II. Spectral Evolution of Galaxies in the Epoch of Cluster Assembly'. *ApJ* **770**(1):62.

A. Dressler, et al. (1999). 'A Spectroscopic Catalog of 10 Distant Rich Clusters of Galaxies'. *ApJS* **122**(1):51–80.

Y. Dubois, et al. (2016). 'The HORIZON-AGN simulation: morphological diversity of galaxies promoted by AGN feedback'. *MNRAS* **463**(4):3948–3964.

P. C. Duffell & A. I. MacFadyen (2011). 'TESS: A Relativistic Hydrodynamics Code on a Moving Voronoi Mesh'. *ApJS* **197**(2):15.

S. A. Eales, et al. (2018). 'The causes of the red sequence, the blue cloud, the green valley, and the green mountain'. *MNRAS* **481**(1):1183–1194.

H. Ebeling, et al. (2014). 'Jellyfish: Evidence of Extreme Ram-pressure Stripping in Massive Galaxy Clusters'. *ApJ* **781**(2):L40.

O. J. Eggen, et al. (1962). 'Evidence from the motions of old stars that the Galaxy collapsed.'. *ApJ* **136**:748.

J. Einasto (1965). 'On the Construction of a Composite Model for the Galaxy and on the Determination of the System of Galactic Parameters'. *Trudy Astrofizicheskogo Instituta Alma-Ata* **5**:87–100.

A. Einstein (1915). 'Die Feldgleichungen der Gravitation'. *Sitzungsberichte der Königlich Preußischen Akademie der Wissenschaften (Berlin* pp. 844–847.

A. Einstein (1917). *Kosmologische Betrachtungen zur allgemeinen Relativitätstheorie*. Verlag d. Akad. d. Wiss.

A. Einstein & W. de Sitter (1932). 'On the Relation between the Expansion and the Mean Density of the Universe'. *Proceedings of the National Academy of Science* **18**(3):213–214.

A. Einstein & K. P. A. der Wissenschaften (1915). *Die Feldgleichungen der Gravitation*. Sitzungsberichte der Königlich Preussischen Akademie der Wissenschaften zu Berlin. Vlg. der Königlichen Akademie der Wissenschaften.

D. J. Eisenstein, et al. (2011). 'SDSS-III: Massive Spectroscopic Surveys of the Distant Universe, the Milky Way, and Extra-Solar Planetary Systems'. *AJ* **142**(3):72.

D. J. Eisenstein, et al. (2005). 'Detection of the Baryon Acoustic Peak in the Large-Scale Correlation Function of SDSS Luminous Red Galaxies'. *ApJ* **633**(2):560–574.

V. R. Eke, et al. (1996). 'Cluster evolution as a diagnostic for Omega'. *MNRAS* **282**:263–280.

S. L. Ellison, et al. (2018). 'Enhanced atomic gas fractions in recently merged galaxies: quenching is not a result of post-merger gas exhaustion'. *MNRAS* **478**(3):3447–3466.

B. G. Elmegreen, et al. (2004). 'A Constant Bar Fraction out to Redshift z ~1 in the Advanced Camera for Surveys Field of the Tadpole Galaxy'. *ApJ* **612**(1):191–201.

B. G. Elmegreen & J. Scalo (2004). 'Interstellar Turbulence I: Observations and Processes'. *ARA&A* **42**(1):211–273.

E. Emsellem, et al. (2011). 'The ATLAS^{3D} project - III. A census of the stellar angular momentum within the effective radius of early-type galaxies: unveiling the distribution of fast and slow rotators'. *MNRAS* **414**(2):888–912.

D. K. Erb, et al. (2006). 'The Mass-Metallicity Relation at z¿~2'. *ApJ* **644**(2):813–828.

A. C. Fabian (2012). 'Observational Evidence of Active Galactic Nuclei Feedback'. *ARA&A* **50**:455–489.

X. Fan, et al. (2006). 'Observational Constraints on Cosmic Reionization'. *ARA&A* **44**(1):415–462.

J. J. Fang, et al. (2012). 'The Slow Death (Or Rebirth?) of Extended Star Formation in z ~0.1 Green Valley Early-type Galaxies'. *ApJ* **761**(1):23.

D. J. Fixsen (2009). 'The Temperature of the Cosmic Microwave Background'. *ApJ* **707**:916–920.

C. Flammarion (1888). *L'atmosphère*. Librairie Hachette et cie.

D. A. Forbes & R.-S. Remus (2018). 'Metallicity gradients in the globular cluster systems of early-type galaxies: in situ and accreted components?'. *MNRAS* **479**(4):4760–4769.

J. Franco, et al. (1994). *Numerical simulations in astrophysics*.

M. Franx, et al. (2008). 'Structure and Star Formation in Galaxies out to z = 3: Evidence for Surface Density Dependent Evolution and Upsizing'. *ApJ* **688**:770–788.

K. Freeman & G. McNamara (2006). *In Search of Dark Matter*. Springer Praxis Books. Springer New York.

K. C. Freeman (1970). 'On the Disks of Spiral and S0 Galaxies'. *ApJ* **160**:811.

K. D. French, et al. (2015). 'Discovery of Large Molecular Gas Reservoirs in Post-starburst Galaxies'. *ApJ* **801**(1):1.

A. Friedmann (1922). 'Über die Krümmung des Raumes'. *Zeitschrift fur Physik* **10**:377–386.

E. Gaburov & K. Nitadori (2011). 'Astrophysical weighted particle magnetohydrodynamics'. *MNRAS* **414**(1):129–154.

G. Galilei & H. Blumenberg (1965). *Sidereus Nuncius: Nachricht Von Neuen Sternen. Dialog Über Die Weltsysteme (Auswahl) Vermessung Der Hölle Dantes. Marginalien Zu Tasso*. Sammlung Insel. Insel-Verlag.

G. Galilei, et al. (2009). *Galileo's Sidereus Nuncius, Or, A Sidereal Message*. Science History Publications.

G. Gavazzi, et al. (2013). 'Hα3: an Hα imaging survey of HI selected galaxies from ALFALFA. III. Nurture builds up the Hubble sequence in the Great Wall'. *A&A* **553**:A90.

R. Genzel, et al. (2008). 'From Rings to Bulges: Evidence for Rapid Secular Galaxy Evolution at z ~2 from Integral Field Spectroscopy in the SINS Survey'. *ApJ* **687**(1):59–77.

R. Genzel, et al. (2010). 'A study of the gas-star formation relation over cosmic time'. *MNRAS* **407**(4):2091–2108.

K. George, et al. (2019). 'GASP XVIII: star formation quenching due to AGN feedback in the central region of a jellyfish galaxy'. *MNRAS* **487**(3):3102–3111.

M. R. George, et al. (2011). 'Galaxies in X-Ray Groups. I. Robust Membership Assignment and the Impact of Group Environments on Quenching'. *ApJ* **742**(2):125.

R. A. Gingold & J. J. Monaghan (1977). 'Smoothed particle hydrodynamics: theory and application to non-spherical stars.'. *MNRAS* **181**:375–389.

R. A. Gingold & J. J. Monaghan (1982). 'Kernel estimates as a basis for general particle methods in hydrodynamics'. *Journal of Computational Physics* **46**:429–453.

S. L. Glashow (1959). 'The renormalizability of vector meson interactions'. *Nuclear Physics* **10**:107–117.

N. Y. Gnedin (2000). 'Effect of Reionization on Structure Formation in the Universe'. *ApJ* **542**(2):535–541.

O. Y. Gnedin (2003). 'Tidal Effects in Clusters of Galaxies'. *ApJ* **582**(1):141–161.

D. Goldsmith (1997). *Einstein's Greatest Blunder?: The Cosmological Constant and Other Fudge Factors in the Physics of the Universe*. Questions of Science (HUP) Series. Harvard University Press.

B. R. Goldstein (1997). 'Saving the Phenomena: The Background to Ptolemy's Planetary Theory'. *Journal for the History of Astronomy* **28**:1.

T. Goto (2005). '266 E+A galaxies selected from the Sloan Digital Sky Survey Data Release 2: the origin of E+A galaxies'. *MNRAS* **357**(3):937–944.

T. Goto, et al. (2008). 'Integrated field spectroscopy of E+A (post-starburst) galaxies with the Kyoto tridimensional spectrograph II'. *MNRAS* **386**(3):1355–1365.

T. Goto, et al. (2003). 'The morphology-density relation in the Sloan Digital Sky Survey'. *MNRAS* **346**:601–614.

S. T. Gottesman, et al. (1966). 'A neutral hydrogen survey of the southern regions of the Andromeda nebula'. *MNRAS* **133**:359.

F. Governato, et al. (2010). 'Bulgeless dwarf galaxies and dark matter cores from supernova-driven outflows'. *Nature* **463**(7278):203–206.

R. J. J. Grand, et al. (2017). 'The Auriga Project: the properties and formation mechanisms of disc galaxies across cosmic time'. *MNRAS* **467**(1):179–207.

M. Gullieuszik, et al. (2017). 'GASP. IV. A Muse View of Extreme Ram-pressure-stripping in the Plane of the Sky: The Case of Jellyfish Galaxy JO204'. *ApJ* **846**(1):27.

J. E. Gunn & J. R. Gott, III (1972). 'On the Infall of Matter Into Clusters of Galaxies and Some Effects on Their Evolution'. *ApJ* **176**:1.

A. Guth (1998). *The Inflationary Universe*. Basic Books.

L. Haemmerlé, et al. (2018). 'The evolution of supermassive Population III stars'. *MNRAS* **474**(2):2757–2773.

A. Hall & D. Knight (1996). *Isaac Newton: Adventurer in Thought*. Cambridge Science Biographies. Cambridge University Press.

D. C. Hambrick, et al. (2011). 'The effects of X-ray and UV background radiation on the low-mass slope of the galaxy mass function'. *MNRAS* **413**(4):2421–2428.

M. H. Hani, et al. (2020). 'Interacting galaxies in the IllustrisTNG simulations - II: star formation in the post-merger stage'. *MNRAS* **493**(3):3716–3731.

S. M. Hansen, et al. (2009). 'The Galaxy Content of SDSS Clusters and Groups'. *ApJ* **699**:1333–1353.

N. Häring & H.-W. Rix (2004). 'On the Black Hole Mass-Bulge Mass Relation'. *ApJ* **604**(2):L89–L92.

W. E. Harris, et al. (2020). 'Measuring Dark Matter in Galaxies: The Mass Fraction Within 5 Effective Radii'. *arXiv e-prints* p. arXiv:2010.14372.

J. Hawley & K. Holcomb (2005). *Foundations of Modern Cosmology*. OUP Oxford.

C. C. Hayward, et al. (2014). 'Galaxy mergers on a moving mesh: a comparison with smoothed particle hydrodynamics'. *MNRAS* **442**(3):1992–2016.

W. Heacox (2015). *The Expanding Universe: A Primer on Relativistic Cosmology*. Cambridge University Press.

A. Heavens, et al. (2004). 'The star-formation history of the Universe from the stellar populations of nearby galaxies'. *Nature* **428**(6983):625–627.

L. Hernquist (1992). 'Structure of Merger Remnants. I. Bulgeless Progenitors'. *ApJ* **400**:460.

L. Hernquist (1993). 'Structure of Merger Remnants. II. Progenitors with Rotating Bulges'. *ApJ* **409**:548.

E. Hertzsprung (1909). 'Über die Sterne der Unterabteilungen c und ac nach der Spektralklassifikation von Antonia C. Maury'. *Astronomische Nachrichten* **179**(24):373.

E. Hertzsprung (1911). *Uber die verwendung photographischer effektiver wellenlängen zur bestimmung von farbenäquivalenten*. Publikationen des Astrophysikalischen Observatoriums zu Potsdam.

E. Hertzsprung (1913). 'Über die räumliche Verteilung der Veränderlichen vom δ Cephei-Typus'. *Astronomische Nachrichten* **196**:201.

M. Hirschmann, et al. (2014). 'Cosmological simulations of black hole growth: AGN luminosities and downsizing'. *MNRAS* **442**:2304–2324.

M. Hirschmann, et al. (2012). 'Galaxy formation in semi-analytic models and cosmological hydrodynamic zoom simulations'. *MNRAS* **419**:3200–3222.

R. Hockney & J. Eastwood (1988). *Computer Simulation Using Particles*. CRC Press.

H. Hoekstra, et al. (2005). 'Virial Masses and the Baryon Fraction in Galaxies'. *ApJ* **635**(1):73–85.

D. W. Hogg, et al. (2006). 'What Triggers Galaxy Transformations? The Environments of Poststarburst Galaxies'. *ApJ* **650**(2):763–769.

P. F. Hopkins (2015). 'A new class of accurate, mesh-free hydrodynamic simulation methods'. *MNRAS* **450**(1):53–110.

P. F. Hopkins, et al. (2013). 'Star formation in galaxy mergers with realistic models of stellar feedback and the interstellar medium'. *MNRAS* **430**(3):1901–1927.

P. F. Hopkins, et al. (2008a). 'A Cosmological Framework for the Co-Evolution of Quasars, Supermassive Black Holes, and Elliptical Galaxies. II. Formation of Red Ellipticals'. *ApJS* **175**(2):390–422.

P. F. Hopkins, et al. (2008b). 'A Cosmological Framework for the Co-Evolution of Quasars, Supermassive Black Holes, and Elliptical Galaxies. I. Galaxy Mergers and Quasar Activity'. *ApJS* **175**(2):356–389.

P. F. Hopkins, et al. (2014). 'Galaxies on FIRE (Feedback In Realistic Environments): stellar feedback explains cosmologically inefficient star formation'. *MNRAS* **445**:581–603.

P. F. Hopkins & E. Quataert (2010). 'How do massive black holes get their gas?'. *MNRAS* **407**(3):1529–1564.

P. F. Hopkins, et al. (2012). 'Stellar feedback in galaxies and the origin of galaxy-scale winds'. *MNRAS* **421**(4):3522–3537.

R. C. W. Houghton (2015). 'Revisiting the original morphology-density relation'. *MNRAS* **451**:3427–3436.

E. Hubble (1926a). 'No. 324. Extra-galactic nebulae.'. *Contributions from the Mount Wilson Observatory / Carnegie Institution of Washington* **324**:1–49.

E. Hubble (1929). 'A Relation between Distance and Radial Velocity among Extra-Galactic Nebulae'. *Proceedings of the National Academy of Science* **15**(3):168–173.

E. Hubble & M. L. Humason (1931). 'The Velocity-Distance Relation among Extra-Galactic Nebulae'. *ApJ* **74**:43.

E. P. Hubble (1925). 'Cepheids in Spiral Nebulae'. *Popular Astronomy* **33**:252–255.

E. P. Hubble (1926b). 'Extragalactic nebulae.'. *ApJ* **64**.

E. P. Hubble (1927). 'The classification of spiral nebulae'. *The Observatory* **50**:276–281.

E. P. Hubble (1936). *Realm of the Nebulae*.

S. Hughes (2012). *Catchers of the Light: The Forgotten Lives of the Men and Women Who First Photographed the Heavens*. Stefan Hughes.

D. Huterer & M. S. Turner (1999). 'Prospects for probing the dark energy via supernova distance measurements'. *Phys. Rev. D* **60**(8):081301.

C. Huygens (1654). *De circuli magnitudine inventa*. J & D Elzevier.

C. Huygens & J. Clarke (2014). *The Celestial Worlds Discovered: Or Conjectures Concerning the Inhabitants, Plants and Productions of the Worlds in the Planets (1722)*. Literary Licensing, LLC.

F. Iannuzzi & K. Dolag (2012). 'On the orbital and internal evolution of cluster galaxies'. *MNRAS* **427**:1024–1033.

Y. L. Jaffé, et al. (2018). 'GASP. IX. Jellyfish galaxies in phase-space: an orbital study of intense ram-pressure stripping in clusters'. *MNRAS* **476**:4753–4764.

Y. L. Jaffé, et al. (2015). 'BUDHIES II: a phase-space view of H I gas stripping and star formation quenching in cluster galaxies'. *MNRAS* **448**:1715–1728.

Y. L. Jaffé, et al. (2016). 'BUDHIES - III: the fate of H I and the quenching of galaxies in evolving environments'. *MNRAS* **461**:1202–1221.

J. H. Jeans (1902). 'The Stability of a Spherical Nebula'. *Philosophical Transactions of the Royal Society of London Series A* **199**:1–53.

H. Joglekar, et al. (2011). 'Oldest sky-chart with Supernova record'. *Puratattva-Bulletin of the Indian Archaeological Society* **41**:207–211.

P. H. Johansson, et al. (2008). 'Termination of star formation by BH feedback in equal- and unequal-mass mergers of disk and elliptical galaxies'. *Astronomische Nachrichten* **329**:956.

P. H. Johansson, et al. (2009a). 'Equal- and Unequal-Mass Mergers of Disk and Elliptical Galaxies with Black Holes'. *ApJ* **690**(1):802–821.

P. H. Johansson, et al. (2009b). 'Gravitational Heating Helps Make Massive Galaxies Red and Dead'. *ApJ* **697**(1):L38–L43.

H. L. Johnson & W. W. Morgan (1953). 'Fundamental stellar photometry for standards of spectral type on the Revised System of the Yerkes Spectral Atlas.'. *ApJ* **117**:313.

G. Joseph (2011). *The Crest of the Peacock: Non-European Roots of Mathematics (Third Edition)*. Princeton University Press.

M. Jubelgas, et al. (2008). 'Cosmic ray feedback in hydrodynamical simulations of galaxy formation'. *A&A* **481**(1):33–63.

N. Kaiser & G. Squires (1993). 'Mapping the Dark Matter with Weak Gravitational Lensing'. *ApJ* **404**:441.

I. Kant (1755). *Allgemeine Naturgeschichte und Theorie des Himmels*. Kant im Original. Fischer.

W. Kapferer, et al. (2008). 'On the influence of ram-pressure stripping on interacting galaxies in clusters'. *MNRAS* **389**:1405–1413.

W. Kapferer, et al. (2009). 'The effect of ram pressure on the star formation, mass distribution and morphology of galaxies'. *A&A* **499**:87–102.

J. C. Kapteyn (1922). 'First Attempt at a Theory of the Arrangement and Motion of the Sidereal System'. *ApJ* **55**:302.

N. Katz & J. E. Gunn (1991). 'Dissipational Galaxy Formation. I. Effects of Gasdynamics'. *ApJ* **377**:365.

S. Kaviraj, et al. (2017). 'The Horizon-AGN simulation: evolution of galaxy properties over cosmic time'. *MNRAS* **467**(4):4739–4752.

M. Kawaharada, et al. (2010). 'Suzaku Observation of A1689: Anisotropic Temperature and Entropy Distributions Associated with the Large-scale Structure'. *ApJ* **714**(1):423–441.

D. Kawata & J. S. Mulchaey (2008). 'Strangulation in Galaxy Groups'. *ApJ* **672**:L103.

L. Kawinwanichakij, et al. (2016). 'Satellite Quenching and Galactic Conformity at 0.3 ¡ z ¡ 2.5'. *ApJ* **817**(1):9.

W. Kelvin (1904). *Baltimore Lectures on Molecular Dynamics and the Wave Theory of Light*. Cambridge University Press.

E. Kennedy (1956). *A Survey of Islamic Astronomical Tables*. American Philosophical Society: Transactions of the ... . New series. American Philosophical Society.

J. Kennicutt, Robert C. (1989). 'The Star Formation Law in Galactic Disks'. *ApJ* **344**:685.

J. Kepler & W. Donahue (2004). *Selections from Kepler's Astronomia Nova*. Science classics for humanities studies. Green Lion Press.

D. Kereš, et al. (2005). 'How do galaxies get their gas?'. *MNRAS* **363**(1):2–28.

S. Khochfar & J. P. Ostriker (2008). 'Adding Environmental Gas Physics to the Semianalytic Method for Galaxy Formation: Gravitational Heating'. *ApJ* **680**(1):54–69.

H. King (2003). *The History of the Telescope*. Dover Books on Astronomy Series. Dover Publications.

S. Kitsionas, et al. (2009). 'Algorithmic comparisons of decaying, isothermal, supersonic turbulence'. *A&A* **508**(1):541–560.

R. K. Kochhar (1991). 'French astronomers in India during the 17th - 19th centuries'. *Journal of the British Astronomical Association* **101**:95–100.

S. Kohler (2020). 'New Discoveries from Old Spacecraft'. AAS Nova Highlights.

E. Kolb (2018). *The Early Universe*. CRC Press.

E. Komatsu, et al. (2009). 'Five-Year Wilkinson Microwave Anisotropy Probe Observations: Cosmological Interpretation'. *ApJS* **180**(2):330–376.

E. Komatsu, et al. (2011). 'Seven-year Wilkinson Microwave Anisotropy Probe (WMAP) Observations: Cosmological Interpretation'. *ApJS* **192**(2):18.

J. Kormendy, et al. (2009). 'Structure and Formation of Elliptical and Spheroidal Galaxies'. *ApJS* **182**:216–309.

J. Kormendy & L. C. Ho (2013). 'Coevolution (Or Not) of Supermassive Black Holes and Host Galaxies'. *ARA&A* **51**(1):511–653.

J. Kormendy & D. Richstone (1995). 'Inward Bound—The Search For Supermassive Black Holes In Galactic Nuclei'. *ARA&A* **33**:581.

J. M. Kovac, et al. (2002). 'Detection of polarization in the cosmic microwave background using DASI'. *Nature* **420**(6917):772–787.

D. Krajnović, et al. (2011). 'The ATLAS^{3D} project - II. Morphologies, kinemetric features and alignment between photometric and kinematic axes of early-type galaxies'. *MNRAS* **414**(4):2923–2949.

A. V. Kravtsov & S. Borgani (2012). 'Formation of Galaxy Clusters'. *ARA&A* **50**:353–409.

A. V. Kravtsov, et al. (1997). 'Adaptive Refinement Tree: A New High-Resolution N-Body Code for Cosmological Simulations'. *ApJS* **111**(1):73–94.

T. Kronberger, et al. (2008). 'On the influence of ram-pressure stripping on the star formation of simulated spiral galaxies'. *A&A* **481**:337–343.

M. R. Krumholz & C. D. Matzner (2009). 'The Dynamics of Radiation-pressure-dominated H II Regions'. *ApJ* **703**(2):1352–1362.

E. Krupp (2003). *Echoes of the Ancient Skies: The Astronomy of Lost Civilizations*. Astronomy Series. Dover Publications.

J. M. Kubo, et al. (2007). 'The Mass of the Coma Cluster from Weak Lensing in the Sloan Digital Sky Survey'. *ApJ* **671**(2):1466–1470.

U. Kuchner, et al. (2017). 'The effects of the cluster environment on the galaxy mass-size relation in MACS J1206.2-0847'. *A&A* **604**:A54.

G. P. Kuiper (1938). 'The Empirical Mass-Luminosity Relation.'. *ApJ* **88**:472.

A. V. Kuznetsov, et al. (2014). 'Creation of electron-positron pairs at excited Landau levels by neutrino in a strong magnetic field'. *International Journal of Modern Physics A* **29**(26):1450136.

C. N. Lackner, et al. (2012). 'Building galaxies by accretion and in situ star formation'. *MNRAS* **425**(1):641–656.

C. D. P. Lagos, et al. (2008). 'Effects of AGN feedback on ΛCDM galaxies'. *MNRAS* **388**(2):587–602.

C. d. P. Lagos, et al. (2019). 'From the far-ultraviolet to the far-infrared - galaxy emission at $0 \leq z \leq 10$ in the SHARK semi-analytic model'. *MNRAS* **489**(3):4196–4216.

L. Landau & E. Lifshitz (2013). *Fluid Mechanics: Volume 6*. No. Bd. 6. Elsevier Science.

L. Lanz, et al. (2020). 'The Puzzling Nuclei of Local Post-Starburst Galaxies'. In *American Astronomical Society Meeting Abstracts*, American Astronomical Society Meeting Abstracts, p. 207.19.

R. B. Larson (1974). 'Effects of supernovae on the early evolution of galaxies'. *MNRAS* **169**:229–246.

R. B. Larson (1981). 'Turbulence and star formation in molecular clouds.'. *MNRAS* **194**:809–826.

R. B. Larson, et al. (1980). 'The evolution of disk galaxies and the origin of S0 galaxies'. *ApJ* **237**:692–707.

H. S. Leavitt (1908). '1777 variables in the Magellanic Clouds'. *Annals of Harvard College Observatory* **60**:87–108.3.

H. S. Leavitt & E. C. Pickering (1912). 'Periods of 25 Variable Stars in the Small Magellanic Cloud.'. *Harvard College Observatory Circular* **173**:1–3.

G. Lemaître (1927). 'Un Univers homogène de masse constante et de rayon croissant rendant compte de la vitesse radiale des nébuleuses extra-galactiques'. *Annales de la Société Scientifique de Bruxelles* **47**:49–59.

G. Lemaître (1933). 'L'Univers en expansion'. *Annales de la Société Scientifique de Bruxelles* **53**:51.

B. C. Lemaux, et al. (2017). 'Chronos and KAIROS: MOSFIRE observations of post-starburst galaxies in z $\sim$ 1 clusters and groups'. *MNRAS* **472**(1):419–438.

J. Lesgourgues, et al. (2013). *Neutrino Cosmology*. Cambridge University Press.

R. LeVeque, et al. (2002). *Finite Volume Methods for Hyperbolic Problems*. Cambridge Texts in Applied Mathematics. Cambridge University Press.

B. L'Huillier, et al. (2012). 'Mass assembly of galaxies. Smooth accretion versus mergers'. *A&A* **544**:A68.

T. C. Licquia & J. A. Newman (2015). 'Improved Estimates of the Milky Way's Stellar Mass and Star Formation Rate from Hierarchical Bayesian Meta-Analysis'. *ApJ* **806**:96.

E. M. Lifshitz (1946). 'On the gravitational stability of the expanding universe'. *Zhurnal Eksperimentalnoi i Teoreticheskoi Fiziki* **16**:587–602.

S. J. Lilly, et al. (1996). 'The Canada-France Redshift Survey: The Luminosity Density and Star Formation History of the Universe to Z approximately 1'. *ApJ* **460**:L1.

C. Lintott, et al. (2011). 'Galaxy Zoo 1: data release of morphological classifications for nearly 900 000 galaxies'. *MNRAS* **410**(1):166–178.

C. J. Lintott, et al. (2008). 'Galaxy Zoo: morphologies derived from visual inspection of galaxies from the Sloan Digital Sky Survey'. *MNRAS* **389**(3):1179–1189.

C. Liu, et al. (2019). 'The Morphological Transformation and the Quenching of Galaxies'. *ApJ* **878**(1):69.

J. N. Lockyer (1868). 'Notice of an Observation of the Spectrum of a Solar Prominence, by J. N. Lockyer, Esq'. *Proceedings of the Royal Society of London Series I* **17**:91–92.

Y.-S. Loh, et al. (2010). 'The UV-optical colour dependence of galaxy clustering in the local universe'. *MNRAS* **407**(1):55–70.

M. Lotz, et al. (2020). 'Rise and fall of post-starburst galaxies in Magneticum Pathfinder'. *arXiv e-prints* p. arXiv:2011.06602.

M. Lotz, et al. (2019). 'Gone after one orbit: How cluster environments quench galaxies'. *MNRAS* **488**(4):5370–5389.

B. Lowry & I. Lowry (2000). *The Silver Canvas: Daguerreotype Masterpieces from the J. Paul Getty Museum*. Getty Publications virtual library. The Museum.

L. B. Lucy (1977). 'A numerical approach to the testing of the fission hypothesis.'. *AJ* **82**:1013–1024.

M.-M. Mac Low & R. S. Klessen (2004). 'Control of star formation by supersonic turbulence'. *Reviews of Modern Physics* **76**(1):125–194.

P. Madau, et al. (1996). 'High-redshift galaxies in the Hubble Deep Field: colour selection and star formation history to z˜4'. *MNRAS* **283**:1388–1404.

P. Madau, et al. (1998). 'The Star Formation History of Field Galaxies'. *ApJ* **498**:106–116.

J. Magorrian, et al. (1998). 'The Demography of Massive Dark Objects in Galaxy Centers'. *AJ* **115**(6):2285–2305.

S. Mahajan, et al. (2011). 'The velocity modulation of galaxy properties in and near clusters: quantifying the decrease in star formation in backsplash galaxies'. *MNRAS* **416**:2882–2902.

D. T. Maltby, et al. (2018). 'The structure of post-starburst galaxies at 0.5 z 2: evidence for two distinct quenching routes at different epochs'. *MNRAS* **480**:381–401.

G. A. Mamon, et al. (2013). 'MAMPOSSt: Modelling Anisotropy and Mass Profiles of Observed Spherical Systems - I. Gaussian 3D velocities'. *MNRAS* **429**:3079–3098.

A. Marconi & L. K. Hunt (2003). 'The Relation between Black Hole Mass, Bulge Mass, and Near-Infrared Luminosity'. *ApJ* **589**(1):L21–L24.

S. Marri & S. D. M. White (2003). 'Smoothed particle hydrodynamics for galaxy-formation simulations: improved treatments of multiphase gas, of star formation and of supernovae feedback'. *MNRAS* **345**(2):561–574.

M. Martig, et al. (2009). 'Morphological Quenching of Star Formation: Making Early-Type Galaxies Red'. *ApJ* **707**(1):250–267.

D. C. Martin, et al. (2005). 'The Galaxy Evolution Explorer: A Space Ultraviolet Survey Mission'. *ApJ* **619**(1):L1–L6.

K. L. Masters, et al. (2011). 'Galaxy Zoo: bars in disc galaxies'. *MNRAS* **411**(3):2026–2034.

J. Matharu, et al. (2020). 'HST/WFC3 grism observations of z $\sim$ 1 clusters: evidence for evolution in the mass-size relation of quiescent galaxies from post-starburst galaxies'. *MNRAS* **493**(4):6011–6032.

F. Matteucci & L. Greggio (1986). 'Relative roles of type I and II supernovae in the chemical enrichment of the interstellar gas'. *A&A* **154**(1-2):279–287.

C. D. Matzner (2002). 'On the Role of Massive Stars in the Support and Destruction of Giant Molecular Clouds'. *ApJ* **566**(1):302–314.

I. G. McCarthy, et al. (2008). 'Ram pressure stripping the hot gaseous haloes of galaxies in groups and clusters'. *MNRAS* **383**:593–605.

M. McDonald, et al. (2014). 'The Redshift Evolution of the Mean Temperature, Pressure, and Entropy Profiles in 80 SPT-Selected Galaxy Clusters'. *ApJ* **794**:67.

C. F. McKee & J. C. Tan (2003). 'The Formation of Massive Stars from Turbulent Cores'. *ApJ* **585**(2):850–871.

P. J. McMillan (2017). 'The mass distribution and gravitational potential of the Milky Way'. *MNRAS* **465**(1):76–94.

A. J. Meadows (1972). *Science and controversy; a biography of Sir Norman Lockyer.*

J. Melnick & I. F. Mirabel (1990). 'NTT images of ultraluminous infrared galaxies.'. *A&A* **231**:L19–L22.

N. Menci & R. Fusco-Femiano (1996). 'Galaxy Velocity Dispersion Profiles from Merging in Clusters'. *ApJ* **472**:46.

A. Mercurio, et al. (2014). 'Galaxy population as a function of the environment: a study in MACSJ1206 at z˜0.44'. In *The evolution of galaxy clusters and cluster galaxies in the epoch of large optical/IR surveys, proceedings of a conference held 13-17 January, 2014 at the Sexten Center for Astrophysics*, p. 12.

C. Messier (1781). 'Catalogue des Nébuleuses et des Amas d'Étoiles (Catalog of Nebulae and Star Clusters)'. Connoissance des Temps ou des Mouvements Célestes.

H. Meusinger, et al. (2017). 'A large sample of Kohonen selected E+A (post-starburst) galaxies from the Sloan Digital Sky Survey'. *A&A* **597**:A134.

D. M. Meyer, et al. (1989). 'Element Abundances at High Redshift'. *ApJ* **343**:L37.

M. Milgrom (1983a). 'A modification of the Newtonian dynamics - Implications for galaxies.'. *ApJ* **270**:371–383.

M. Milgrom (1983b). 'A modification of the newtonian dynamics : implications for galaxy systems.'. *ApJ* **270**:384–389.

M. Milgrom (1983c). 'A modification of the Newtonian dynamics as a possible alternative to the hidden mass hypothesis.'. *ApJ* **270**:365–370.

H. Mo, et al. (2010). *Galaxy Formation and Evolution*. Galaxy Formation and Evolution. Cambridge University Press.

H. J. Mo, et al. (1998). 'The formation of galactic discs'. *MNRAS* **295**(2):319–336.

J. J. Mohr, et al. (1999). 'Properties of the Intracluster Medium in an Ensemble of Nearby Galaxy Clusters'. *ApJ* **517**(2):627–649.

J. J. Monaghan (1992). 'Smoothed particle hydrodynamics.'. *ARA&A* **30**:543–574.

J. J. Monaghan (2002). 'SPH compressible turbulence'. *MNRAS* **335**(3):843–852.

J. J. Monaghan & J. C. Lattanzio (1985). 'A refined particle method for astrophysical problems'. *A&A* **149**(1):135–143.

S. Montgomery & A. Kumar (2015). *A History of Science in World Cultures: Voices of Knowledge*. Taylor & Francis.

B. Moore, et al. (1996). 'Galaxy harassment and the evolution of clusters of galaxies'. *Nature* **379**:613–616.

B. Moore, et al. (1998). 'Morphological Transformation from Galaxy Harassment'. *ApJ* **495**:139–151.

J. P. Morris (1996). 'A study of the stability properties of smooth particle hydrodynamics'. *Publ. Astron. Soc. Australia* **13**(1):97–102.

V. Mukhanov (2005). *Physical Foundations of Cosmology*.

E. Munari, et al. (2014). 'Mass, velocity anisotropy, and pseudo phase-space density profiles of Abell 2142'. *A&A* **566**:A68.

N. Murray, et al. (2010). 'The Disruption of Giant Molecular Clouds by Radiation Pressure & the Efficiency of Star Formation in Galaxies'. *ApJ* **709**(1):191–209.

A. Muzzin, et al. (2013). 'The Evolution of the Stellar Mass Functions of Star-forming and Quiescent Galaxies to z = 4 from the COSMOS/UltraVISTA Survey'. *ApJ* **777**(1):18.

A. Muzzin, et al. (2014). 'The Phase Space and Stellar Populations of Cluster Galaxies at z ˜ 1: Simultaneous Constraints on the Location and Timescale of Satellite Quenching'. *ApJ* **796**:65.

P. B. Nair & R. G. Abraham (2010). 'On the Fraction of Barred Spiral Galaxies'. *ApJ* **714**(2):L260–L264.

S. Narison (2015). *Particles And The Universe: From The Ionian School To The Higgs Boson And Beyond*. World Scientific Publishing Company.

J. F. Navarro, et al. (1996). 'The Structure of Cold Dark Matter Halos'. *ApJ* **462**:563.

J. F. Navarro, et al. (1997). 'A Universal Density Profile from Hierarchical Clustering'. *ApJ* **490**(2):493–508.

J. F. Navarro & M. Steinmetz (1997). 'The Effects of a Photoionizing Ultraviolet Background on the Formation of Disk Galaxies'. *ApJ* **478**(1):13–28.

D. Nelson, et al. (2018). 'First results from the IllustrisTNG simulations: the galaxy colour bimodality'. *MNRAS* **475**(1):624–647.

W. Neuber, et al. (2014). *The Making of Copernicus: Early Modern Transformations of a Scientist and his Science*. Intersections. Brill.

I. Newton (1999). *The Principia : mathematical principles of natural philosophy*.

K. Niazi (2014). *Qub al-Dīn Shīrāzī and the Configuration of the Heavens*. Springer Netherlands.

K. G. Noeske, et al. (2007). 'Star Formation in AEGIS Field Galaxies since z=1.1: The Dominance of Gradually Declining Star Formation, and the Main Sequence of Star-forming Galaxies'. *ApJ* **660**(1):L43–L46.

K. Nomoto, et al. (2013). 'Nucleosynthesis in Stars and the Chemical Enrichment of Galaxies'. *ARA&A* **51**(1):457–509.

C. A. Norman & A. Ferrara (1996). 'The Turbulent Interstellar Medium: Generalizing to a Scale-dependent Phase Continuum'. *ApJ* **467**:280.

P. Ocvirk, et al. (2008). 'Bimodal gas accretion in the Horizon-MareNostrum galaxy formation simulation'. *MNRAS* **390**(4):1326–1338.

S. C. Odewahn (1996). 'Properties of the Magellanic Type Galaxies'. In R. Buta, D. A. Crocker, & B. G. Elmegreen (eds.), *IAU Colloq. 157: Barred Galaxies*, vol. 91 of *Astronomical Society of the Pacific Conference Series*, p. 30.

A. Oemler, Jr. (1974). 'The Systematic Properties of Clusters of Galaxies. Photometry of 15 Clusters'. *ApJ* **194**:1–20.

P. A. Oesch, et al. (2016). 'A Remarkably Luminous Galaxy at z=11.1 Measured with Hubble Space Telescope Grism Spectroscopy'. *ApJ* **819**(2):129.

T. Okamoto, et al. (2003). 'Momentum transfer across shear flows in smoothed particle hydrodynamic simulations of galaxy formation'. *MNRAS* **345**(2):429–446.

J. A. O'Leary, et al. (2020). 'EMERGE: Empirical predictions of galaxy merger rates since $z \sim 6$'. *arXiv e-prints* p. arXiv:2001.02687.

K. A. Olive & Particle Data Group (2014). 'Review of Particle Physics'. *Chinese Physics C* **38**(9):090001.

K. A. Olive, et al. (2000). 'Primordial nucleosynthesis: theory and observations'. *Phys. Rep.* **333**:389–407.

K. A. Oman & M. J. Hudson (2016). 'Satellite quenching time-scales in clusters from projected phase space measurements matched to simulated orbits'. *MNRAS* **463**:3083–3095.

K. A. Oman, et al. (2013). 'Disentangling satellite galaxy populations using orbit tracking in simulations'. *MNRAS* **431**(3):2307–2316.

J. H. Oort (1932). 'The force exerted by the stellar system in the direction perpendicular to the galactic plane and some related problems'. *Bull. Astron. Inst. Netherlands* **6**:249.

J. H. Oort (1940). 'Some Problems Concerning the Structure and Dynamics of the Galactic System and the Elliptical Nebulae NGC 3115 and 4494.'. *ApJ* **91**:273.

B. D. Oppenheimer & R. Davé (2008). 'Mass, metal, and energy feedback in cosmological simulations'. *MNRAS* **387**(2):577–600.

E. C. Ostriker, et al. (2010). 'Regulation of Star Formation Rates in Multiphase Galactic Disks: A Thermal/Dynamical Equilibrium Model'. *ApJ* **721**(2):975–994.

E. C. Ostriker & R. Shetty (2011). 'Maximally Star-forming Galactic Disks. I. Starburst Regulation Via Feedback-driven Turbulence'. *ApJ* **731**(1):41.

M. S. Owers, et al. (2019). 'The SAMI Galaxy Survey: Quenching of Star Formation in Clusters I. Transition Galaxies'. *ApJ* **873**(1):52.

A. Paccagnella, et al. (2017). 'OmegaWINGS: The First Complete Census of Post-starburst Galaxies in Clusters in the Local Universe'. *ApJ* **838**:148.

A. Paccagnella, et al. (2019). 'The strong correlation between post-starburst fraction and environment'. *MNRAS* **482**(1):881–894.

E. Papastergis, et al. (2012). 'A Direct Measurement of the Baryonic Mass Function of Galaxies and Implications for the Galactic Baryon Fraction'. *ApJ* **759**(2):138.

R. B. Partridge & D. T. Wilkinson (1967). 'Isotropy and Homogeneity of the Universe from Measurements of the Cosmic Microwave Background'. *Phys. Rev. Lett.* **18**(14):557–559.

F. S. Patterson (1940). 'The Luminosity Gradient of Messier 33'. *Harvard College Observatory Bulletin* **914**:9–10.

D. R. Patton, et al. (2020). 'Interacting galaxies in the IllustrisTNG simulations - I: Triggered star formation in a cosmological context'. *MNRAS* **494**(4):4969–4985.

S. Paulin-Henriksson, et al. (2007). 'Weak lensing mass reconstruction of the galaxy cluster Abell 209'. *A&A* **467**:427–436.

M. M. Pawlik, et al. (2019). 'The diverse evolutionary pathways of post-starburst galaxies'. *Nature Astronomy* **3**:440–446.

M. M. Pawlik, et al. (2018). 'The origins of post-starburst galaxies at z ¡ 0.05'. *MNRAS* **477**(2):1708–1743.

M. M. Pawlik, et al. (2016). 'Shape asymmetry: a morphological indicator for automatic detection of galaxies in the post-coalescence merger stages'. *MNRAS* **456**:3032–3052.

C. H. Payne (1925). *Stellar Atmospheres; a Contribution to the Observational Study of High Temperature in the Reversing Layers of Stars.* Ph.D. thesis, RADCLIFFE COLLEGE.

J. Peñarrubia, et al. (2014). 'A dynamical model of the local cosmic expansion'. *MNRAS* **443**(3):2204–2222.

J. Peacock (1999). *Cosmological Physics*. Cambridge Astrophysics. Cambridge University Press.

R. Pearson (????). *The History of Astronomy*. Lulu.com.

W. J. Pearson, et al. (2019). 'Effect of galaxy mergers on star-formation rates'. *A&A* **631**:A51.

W. J. Pearson, et al. (2018). 'Main sequence of star forming galaxies beyond the Herschel confusion limit'. *A&A* **615**:A146.

R. D. Peccei & H. R. Quinn (1977a). 'Constraints imposed by CP conservation in the presence of pseudoparticles'. *Phys. Rev. D* **16**(6):1791–1797.

R. D. Peccei & H. R. Quinn (1977b). 'CP conservation in the presence of pseudoparticles'. *Phys. Rev. Lett.* **38**(25):1440–1443.

P. J. Peebles & B. Ratra (2003). 'The cosmological constant and dark energy'. *Reviews of Modern Physics* **75**(2):559–606.

P. J. E. Peebles (1980). *The large-scale structure of the universe*.

P. J. E. Peebles (1993). *Principles of Physical Cosmology*.

P. J. E. Peebles & J. T. Yu (1970). 'Primeval Adiabatic Perturbation in an Expanding Universe'. *ApJ* **162**:815.

C. Y. Peng, et al. (2002). 'Detailed Structural Decomposition of Galaxy Images'. *AJ* **124**(1):266–293.

Y.-j. Peng, et al. (2010). 'Mass and Environment as Drivers of Galaxy Evolution in SDSS and zCOSMOS and the Origin of the Schechter Function'. *ApJ* **721**:193–221.

Y.-j. Peng, et al. (2012). 'Mass and Environment as Drivers of Galaxy Evolution. II. The Quenching of Satellite Galaxies as the Origin of Environmental Effects'. *ApJ* **757**(1):4.

A. A. Penzias & R. W. Wilson (1965). 'A Measurement of Excess Antenna Temperature at 4080 Mc/s.'. *ApJ* **142**:419–421.

S. Perlmutter, et al. (1998). 'Discovery of a supernova explosion at half the age of the Universe'. *Nature* **391**(6662):51–54.

S. Perlmutter, et al. (1999a). 'Measurements of Ω and Λ from 42 High-Redshift Supernovae'. *ApJ* **517**(2):565–586.

S. Perlmutter, et al. (1999b). 'Constraining Dark Energy with Type Ia Supernovae and Large-Scale Structure'. *Phys. Rev. Lett.* **83**(4):670–673.

E. Pierpaoli, et al. (2003). 'On determining the cluster abundance normalization'. *MNRAS* **342**(1):163–175.

A. Pillepich, et al. (2018). 'Simulating galaxy formation with the IllustrisTNG model'. *MNRAS* **473**(3):4077–4106.

K. A. Pimbblet (2011). 'Backsplash galaxies in isolated clusters'. *MNRAS* **411**(4):2637–2643.

Planck Collaboration, et al. (2014a). 'Planck 2013 results. XXIII. Isotropy and statistics of the CMB'. *A&A* **571**:A23.

Planck Collaboration, et al. (2014b). 'Planck 2013 results. XVI. Cosmological parameters'. *A&A* **571**:A16.

Planck Collaboration, et al. (2016a). 'Planck 2015 results. XX. Constraints on inflation'. *A&A* **594**:A20.

Planck Collaboration, et al. (2013). 'Planck intermediate results. V. Pressure profiles of galaxy clusters from the Sunyaev-Zeldovich effect'. *A&A* **550**:A131.

Planck Collaboration, et al. (2016b). 'Planck 2015 results. XIII. Cosmological parameters'. *A&A* **594**:A13.

Planck Collaboration, et al. (2020). 'Planck 2018 results. VI. Cosmological parameters'. *A&A* **641**:A6.

K. Plofker (2009). *Mathematics in India*. Princeton University Press.

H. C. Plummer (1911). 'On the problem of distribution in globular star clusters'. *MNRAS* **71**:460–470.

Plutarch (2006). *The Complete Works Volume 3: Essays and Miscellanies*. Echo Library.

B. M. Poggianti, et al. (2009). 'The Environments of Starburst and Post-Starburst Galaxies at z = 0.4-0.8'. *ApJ* **693**:112–131.

B. M. Poggianti, et al. (2020). 'The role of environment on quenching, star formation and AGN activity'. *arXiv e-prints* p. arXiv:2005.03735.

B. M. Poggianti, et al. (2016). 'Jellyfish Galaxy Candidates at Low Redshift'. *AJ* **151**(3):78.

B. M. Poggianti, et al. (2017). 'Ram-pressure feeding of supermassive black holes'. *Nature* **548**(7667):304–309.

B. M. Poggianti, et al. (1999). 'The Star Formation Histories of Galaxies in Distant Clusters'. *ApJ* **518**(2):576–593.

M. Pohlen & I. Trujillo (2006). 'The structure of galactic disks. Studying late-type spiral galaxies using SDSS'. *A&A* **454**(3):759–772.

M. Postman, et al. (2012). 'The Cluster Lensing and Supernova Survey with Hubble: An Overview'. *ApJS* **199**:25.

L. Pozzetti, et al. (2010). 'zCOSMOS - 10k-bright spectroscopic sample. The bimodality in the galaxy stellar mass function: exploring its evolution with redshift'. *A&A* **523**:A13.

M. B. Pracy, et al. (2010). 'Spatially Resolved Spectroscopy of Starburst and Post-Starburst Galaxies in the Rich z~0.55 Cluster CL 0016+16 [1]'. *Publ. Astron. Soc. Australia* **27**(3):360–373.

M. B. Pracy, et al. (2013). 'Stellar population gradients and spatially resolved kinematics in luminous post-starburst galaxies'. *MNRAS* **432**(4):3131–3140.

M. B. Pracy, et al. (2009). 'The kinematics and spatial distribution of stellar populations in E+A galaxies'. *MNRAS* **396**(3):1349–1369.

G. W. Pratt, et al. (2009). 'Galaxy cluster X-ray luminosity scaling relations from a representative local sample (REXCESS)'. *A&A* **498**(2):361–378.

D. J. Price (2012). 'Smoothed particle hydrodynamics and magnetohydrodynamics'. *Journal of Computational Physics* **231**(3):759–794.

D. J. Price & C. Federrath (2010). 'A comparison between grid and particle methods on the statistics of driven, supersonic, isothermal turbulence'. *MNRAS* **406**(3):1659–1674.

D. J. Price & J. J. Monaghan (2007). 'An energy-conserving formalism for adaptive gravitational force softening in smoothed particle hydrodynamics and N-body codes'. *MNRAS* **374**(4):1347–1358.

E. Puchwein & V. Springel (2013). 'Shaping the galaxy stellar mass function with supernova- and AGN-driven winds'. *MNRAS* **428**(4):2966–2979.

Y. Qu, et al. (2017). 'A chronicle of galaxy mass assembly in the EAGLE simulation'. *MNRAS* **464**(2):1659–1675.

V. Quilis, et al. (2000). 'Gone with the Wind: The Origin of S0 Galaxies in Clusters'. *Science* **288**(5471):1617–1620.

M. Radovich, et al. (2019). 'GASP - XIX. AGN and their outflows at the centre of jellyfish galaxies'. *MNRAS* **486**(1):486–503.

A. Raichoor & S. Andreon (2012). 'Galaxy mass, cluster-centric distance and secular evolution: their role in the evolution of galaxies in clusters in the last 10 Gyr'. *A&A* **543**:A19.

S. W. Randall, et al. (2008). 'Constraints on the Self-Interaction Cross Section of Dark Matter from Numerical Simulations of the Merging Galaxy Cluster 1E 0657-56'. *ApJ* **679**(2):1173–1180.

M. Rappenglück (2010). 'Earlier prehistory'. In *Heritage Sites of Astronomy and Archaeoastronomy in the Context of the UNESCO World Heritage Convention: A Thematic Study, edited by CLN Ruggles and M. Cotte. Paris: ICOMOS and the International Astronomical Union.*

B. Ratra & P. J. E. Peebles (1988). 'Cosmological consequences of a rolling homogeneous scalar field'. *Phys. Rev. D* **37**(12):3406–3427.

B. Ray, et al. (2009). *Different Types of History.* History of science, philosophy and culture in Indian civilization. Pearson Longman.

R.-S. Remus, et al. (2015). 'Disk Galaxies in the Magneticum Pathfinder Simulations'. In B. L. Ziegler, F. Combes, H. Dannerbauer, & M. Verdugo (eds.), *Galaxies in 3D across the Universe*, vol. 309 of *IAU Symposium*, pp. 145–148.

R.-S. Remus, et al. (2017a). 'The Outer Halos of Very Massive Galaxies: BCGs and their DSC in the Magneticum Simulations'. *Galaxies* **5**:49.

R.-S. Remus, et al. (2017b). 'The co-evolution of total density profiles and central dark matter fractions in simulated early-type galaxies'. *MNRAS* **464**:3742–3756.

A. Ricarte, et al. (2020). 'A Link between Ram Pressure Stripping and Active Galactic Nuclei'. *ApJ* **895**(1):L8.

A. G. Riess, et al. (1998). 'Observational Evidence from Supernovae for an Accelerating Universe and a Cosmological Constant'. *AJ* **116**(3):1009–1038.

B. W. Ritchie & P. A. Thomas (2001). 'Multiphase smoothed-particle hydrodynamics'. *MNRAS* **323**(3):743–756.

I. D. Roberts & L. C. Parker (2020). 'Ram pressure stripping candidates in the coma cluster: evidence for enhanced star formation'. *MNRAS* **495**(1):554–569.

M. S. Roberts (1966). 'A High-Resolution 21-CM Hydrogen-Line Survey of the Andromeda Nebula'. *ApJ* **144**:639.

M. S. Roberts & R. N. Whitehurst (1975). 'The rotation curve and geometry of M31 at large galactocentric distances.'. *ApJ* **201**:327–346.

H. P. Robertson (1935). 'Kinematics and World-Structure'. *ApJ* **82**:284.

V. Rodriguez-Gomez, et al. (2016). 'The stellar mass assembly of galaxies in the Illustris simulation: growth by mergers and the spatial distribution of accreted stars'. *MNRAS* **458**(3):2371–2390.

F. Rodríguez Montero, et al. (2019). 'Mergers, starbursts, and quenching in the SIMBA simulation'. *MNRAS* **490**(2):2139–2154.

P. Rosati, et al. (2014). 'CLASH-VLT: A VIMOS Large Programme to Map the Dark Matter Mass Distribution in Galaxy Clusters and Probe Distant Lensed Galaxies'. *The Messenger* **158**:48–53.

G. Roth (1976). *Joseph von Fraunhofer: Handwerker, Forscher, Akad.-Mitglied : 1787-1826*. Grosse Naturforscher. Wissenschaftliche Verlagsgesellschaft.

G. W. Rougoor & J. H. Oort (1960). 'Distribution and Motion of Interstellar Hydrogen in the Galactic System with Particular Reference to the Region Within 3 Kiloparsecs of the Center'. *Proceedings of the National Academy of Science* **46**(1):1–13.

K. Rowlands, et al. (2018). 'Galaxy And Mass Assembly (GAMA): The mechanisms for quiescent galaxy formation at z ¡ 1'. *MNRAS* **473**(1):1168–1185.

V. Rubakov & D. Gorbunov (2011). *Introduction To The Theory Of The Early Universe: Cosmological Perturbations And Inflationary Theory*. World Scientific Publishing Company.

V. C. Rubin & J. Ford, W. Kent (1970). 'Rotation of the Andromeda Nebula from a Spectroscopic Survey of Emission Regions'. *ApJ* **159**:379.

B. Russell (2008). *History of Western Philosophy*. Touchstone.

H. N. Russell (1914). 'Relations Between the Spectra and Other Characteristics of the Stars'. *Popular Astronomy* **22**:275–294.

A. Salam & J. C. Ward (1959). 'Weak and electromagnetic interactions'. *Il Nuovo Cimento* **11**(4):568–577.

G. Saliba (1995). *A History of Arabic Astronomy: Planetary Theories During the Golden Age of Islam*. NYU Press.

G. Saliba (2011). *Islamic Science and the Making of the European Renaissance*. Transformations (Cambridge, Mass.). MIT Press.

P. Salucci & A. Burkert (2000). 'Dark Matter Scaling Relations'. *ApJ* **537**(1):L9–L12.

A. Sandage (1961). *The Hubble Atlas of Galaxies*.

A. Sandage & G. A. Tammann (1981). *A Revised Shapley-Ames Catalog of Bright Galaxies*.

B. C. Sanders, et al. (2008). 'EDITORIAL: Focus on Visualization in Physics FOCUS ON VISUALIZATION IN PHYSICS'. *New Journal of Physics* **10**(12):125001.

D. B. Sanders, et al. (1988). 'Ultraluminous Infrared Galaxies and the Origin of Quasars'. *ApJ* **325**:74.

C. L. Sarazin (1988). *X-ray emission from clusters of galaxies*.

A. Saro, et al. (2006). 'Properties of the galaxy population in hydrodynamical simulations of clusters'. *MNRAS* **373**:397–410.

C. Scannapieco, et al. (2008). 'Effects of supernova feedback on the formation of galaxy discs'. *MNRAS* **389**(3):1137–1149.

G. Schaller, et al. (1992). 'New grids of stellar models from 0.8 to 120 M_solar at Z=0.020 and Z=0.001'. *A&AS* **96**:269.

K. Schawinski, et al. (2007). 'Observational evidence for AGN feedback in early-type galaxies'. *MNRAS* **382**(4):1415–1431.

K. Schawinski, et al. (2014). 'The green valley is a red herring: Galaxy Zoo reveals two evolutionary pathways towards quenching of star formation in early- and late-type galaxies'. *MNRAS* **440**(1):889–907.

J. Schaye, et al. (2015). 'The EAGLE project: simulating the evolution and assembly of galaxies and their environments'. *MNRAS* **446**(1):521–554.

B. P. Schmidt, et al. (1998). 'The High-Z Supernova Search: Measuring Cosmic Deceleration and Global Curvature of the Universe Using Type IA Supernovae'. *ApJ* **507**(1):46–63.

M. Schmidt (1965). *Rotation Parameters and Distribution of Mass in the Galaxy*, p. 513.

J. Schneider, et al. (2011). 'Defining and cataloging exoplanets: the exoplanet.eu database'. *A&A* **532**:A79.

F. Schulze, et al. (2020). 'Kinematics of simulated galaxies II: Probing the stellar kinematics of galaxies out to large radii'. *MNRAS* **493**(3):3778–3799.

K. Schwarzschild (1916). 'On the Gravitational Field of a Mass Point According to Einstein's Theory'. *Abh. Konigl. Preuss. Akad. Wissenschaften Jahre 1906,92, Berlin,1907* **1916**:189–196.

F. Schweizer (1996). 'Colliding and Merging Galaxies. III. The Dynamically Young Merger Remnant NGC 3921'. *AJ* **111**:109.

N. Scoville, et al. (2007). 'The Cosmic Evolution Survey (COSMOS): Overview'. *ApJS* **172**(1):1–8.

L. Searle & R. Zinn (1978). 'Composition of halo clusters and the formation of the galactic halo.'. *ApJ* **225**:357–379.

J. A. Sellwood & A. Wilkinson (1993). 'Dynamics of barred galaxies'. *Reports on Progress in Physics* **56**(2):173–256.

J. L. Sérsic (1963). 'Influence of the atmospheric and instrumental dispersion on the brightness distribution in a galaxy'. *Boletin de la Asociacion Argentina de Astronomia La Plata Argentina* **6**:41–43.

H. Shapley (1918). 'Studies based on the colors and magnitudes in stellar clusters. VII. The distances, distribution in space, and dimensions of 69 globular clusters.'. *ApJ* **48**:154–181.

H. Shapley & H. D. Curtis (1921). 'The Scale of the Universe'. *Bulletin of the National Research Council* **2**(11):171–217.

Y.-K. Sheen, et al. (2017). 'Discovery of Ram-pressure Stripped Gas around an Elliptical Galaxy in Abell 2670'. *ApJ* **840**:L7.

D. Sijacki, et al. (2012). 'Moving mesh cosmology: the hydrodynamics of galaxy formation'. *MNRAS* **424**(4):2999–3027.

F. Simien & G. de Vaucouleurs (1986). 'Systematics of Bulge-to-Disk Ratios'. *ApJ* **302**:564.

V. M. Slipher (1917). 'Radial velocity observations of spiral nebulae'. *The Observatory* **40**:304–306.

M. Socolovsky, et al. (2018). 'The enhancement of rapidly quenched galaxies in distant clusters at 0.5 z 1.0'. *MNRAS* **476**:1242–1257.

M. Socolovsky, et al. (2019). 'Compact star-forming galaxies preferentially quenched to become PSBs in z < 1 clusters'. *MNRAS* **482**(2):1640–1650.

J. M. Solanes, et al. (2002). 'The Three-dimensional Structure of the Virgo Cluster Region from Tully-Fisher and H I Data'. *AJ* **124**:2440–2452.

R. S. Somerville, et al. (2008). 'A semi-analytic model for the co-evolution of galaxies, black holes and active galactic nuclei'. *MNRAS* **391**(2):481–506.

M. Souli & D. Benson (2013). *Arbitrary Lagrangian Eulerian and Fluid-Structure Interaction: Numerical Simulation*. ISTE. Wiley.

L. Sparke & J. Gallagher (2000). *Galaxies in the Universe: An Introduction*. Galaxies in the Universe: An Introduction. Cambridge University Press.

J. S. Speagle, et al. (2014). 'A Highly Consistent Framework for the Evolution of the Star-Forming "Main Sequence" from z ~0-6'. *ApJS* **214**(2):15.

D. N. Spergel & P. J. Steinhardt (2000). 'Observational Evidence for Self-Interacting Cold Dark Matter'. *Phys. Rev. Lett.* **84**(17):3760–3763.

D. N. Spergel, et al. (2003). 'First-Year Wilkinson Microwave Anisotropy Probe (WMAP) Observations: Determination of Cosmological Parameters'. *ApJS* **148**(1):175–194.

V. Springel (2005). 'The cosmological simulation code GADGET-2'. *MNRAS* **364**(4):1105–1134.

V. Springel (2010a). 'E pur si muove: Galilean-invariant cosmological hydrodynamical simulations on a moving mesh'. *MNRAS* **401**(2):791–851.

V. Springel (2010b). 'Smoothed Particle Hydrodynamics in Astrophysics'. *ARA&A* **48**:391–430.

V. Springel, et al. (2005a). 'Modelling feedback from stars and black holes in galaxy mergers'. *MNRAS* **361**(3):776–794.

V. Springel & L. Hernquist (2002). 'Cosmological smoothed particle hydrodynamics simulations: the entropy equation'. *MNRAS* **333**(3):649–664.

V. Springel & L. Hernquist (2003). 'Cosmological smoothed particle hydrodynamics simulations: a hybrid multiphase model for star formation'. *MNRAS* **339**:289–311.

V. Springel, et al. (2018). 'First results from the IllustrisTNG simulations: matter and galaxy clustering'. *MNRAS* **475**(1):676–698.

V. Springel, et al. (2005b). 'Simulations of the formation, evolution and clustering of galaxies and quasars'. *Nature* **435**:629–636.

V. Springel, et al. (2001). 'GADGET: a code for collisionless and gasdynamical cosmological simulations'. *New Astron.* **6**:79–117.

L. K. Steinborn, et al. (2016). 'Origin and properties of dual and offset active galactic nuclei in a cosmological simulation at z=2'. *MNRAS* **458**(1):1013–1028.

L. K. Steinborn, et al. (2015). 'A refined sub-grid model for black hole accretion and AGN feedback in large cosmological simulations'. *MNRAS* **448**:1504–1525.

L. K. Steinborn, et al. (2018). 'Cosmological simulations of black hole growth II: how (in)significant are merger events for fuelling nuclear activity?'. *MNRAS* **481**:341–360.

M. Steinmetz & E. Mueller (1993). 'On the capabilities and limits of smoothed particle hydrodynamics'. *A&A* **268**(1):391–410.

I. Strateva, et al. (2001). 'Color Separation of Galaxy Types in the Sloan Digital Sky Survey Imaging Data'. *AJ* **122**(4):1861–1874.

V. Strazzullo, et al. (2019). 'Galaxy populations in the most distant SPT-SZ clusters. I. Environmental quenching in massive clusters at $1.4 \lesssim z \lesssim 1.7$'. *A&A* **622**:A117.

B. Strömgren (1939). 'The Physical State of Interstellar Hydrogen.'. *ApJ* **89**:526.

R. S. Sutherland & M. A. Dopita (1993). 'Cooling Functions for Low-Density Astrophysical Plasmas'. *ApJS* **88**:253.

M. Tanabashi, et al. (2018). 'Review of Particle Physics*'. *Phys. Rev. D* **98**(3):030001.

H. Tanimura, et al. (2020). 'Direct detection of the kinetic Sunyaev-Zel'dovich effect in galaxy clusters'. *arXiv e-prints* p. arXiv:2007.02952.

M. Tegmark, et al. (2006). 'Cosmological constraints from the SDSS luminous red galaxies'. *Phys. Rev. D* **74**(12):123507.

A. F. Teklu, et al. (2018). 'Declining Rotation Curves at $z = 2$ in ΛCDM Galaxy Formation Simulations'. *ApJ* **854**(2):L28.

A. F. Teklu, et al. (2015). 'Connecting Angular Momentum and Galactic Dynamics: The Complex Interplay between Spin, Mass, and Morphology'. *ApJ* **812**:29.

A. F. Teklu, et al. (2017). 'The morphology-density relation: impact on the satellite fraction'. *MNRAS* **472**:4769–4785.

R. Teyssier (2002). 'Cosmological hydrodynamics with adaptive mesh refinement. A new high resolution code called RAMSES'. *A&A* **385**:337–364.

R. Teyssier, et al. (2011). 'Mass distribution in galaxy clusters: the role of Active Galactic Nuclei feedback'. *MNRAS* **414**(1):195–208.

J. L. Tinker, et al. (2018). 'Halo histories versus galaxy properties at z = 0 II: large-scale galactic conformity'. *MNRAS* **477**(1):935–945.

J. L. Tinker, et al. (2013). 'Evolution of the Stellar-to-dark Matter Relation: Separating Star-forming and Passive Galaxies from z = 1 to 0'. *ApJ* **778**(2):93.

J. L. Tinker, et al. (2017). 'Halo histories versus Galaxy properties at z = 0 - I. The quenching of star formation'. *MNRAS* **472**(2):2504–2516.

P. Tisserand, et al. (2007). 'Limits on the Macho content of the Galactic Halo from the EROS-2 Survey of the Magellanic Clouds'. *A&A* **469**(2):387–404.

É. Tollet, et al. (2017). 'On stellar mass loss from galaxies in groups and clusters'. *MNRAS* **471**(4):4170–4193.

N. Tominaga, et al. (2007). 'Supernova Nucleosynthesis in Population III 13-50 M_{solar} Stars and Abundance Patterns of Extremely Metal-poor Stars'. *ApJ* **660**(1):516–540.

S. Tonnesen & G. L. Bryan (2009). 'Gas Stripping in Simulated Galaxies with a Multiphase Interstellar Medium'. *ApJ* **694**:789–804.

S. Tonnesen & G. L. Bryan (2012). 'Star formation in ram pressure stripped galactic tails'. *MNRAS* **422**:1609–1624.

A. Toomre (1977). 'Mergers and Some Consequences'. In B. M. Tinsley & D. C. Larson, Richard B. Gehret (eds.), *Evolution of Galaxies and Stellar Populations*, p. 401.

A. Toomre & J. Toomre (1972). 'Galactic Bridges and Tails'. *ApJ* **178**:623–666.

L. Tornatore, et al. (2003). 'Cooling and heating the intracluster medium in hydrodynamical simulations'. *MNRAS* **342**:1025–1040.

M. Tornatore, et al. (2006). 'Capacity versus availability trade-offs for availability-based routing'. *Journal of Optical Networking* **5**:858–869.

K.-V. H. Tran, et al. (2003). 'The Nature of E+A Galaxies in Intermediate-Redshift Clusters'. *ApJ* **599**:865–885.

J. W. Trayford, et al. (2016). 'It is not easy being green: the evolution of galaxy colour in the EAGLE simulation'. *MNRAS* **460**(4):3925–3939.

M. Tremmel, et al. (2019). 'Introducing ROMULUSC: a cosmological simulation of a galaxy cluster with an unprecedented resolution'. *MNRAS* **483**(3):3336–3362.

V. Trimble (1995). 'The 1920 Shapley-Curtis Discussion: Background, Issues, and Aftermath'. *PASP* **107**:1133.

S. Tucker (2020). *The Cold War: The Definitive Encyclopedia and Document Collection [5 volumes]*. ABC-CLIO.

M. S. Turner & A. G. Riess (2002). 'Do Type Ia Supernovae Provide Direct Evidence for Past Deceleration of the Universe?'. *ApJ* **569**(1):18–22.

M. S. Turner & M. White (1997). 'CDM models with a smooth component'. *Phys. Rev. D* **56**(8):R4439–R4443.

J. A. Tyson, et al. (1998). 'Detailed Mass Map of CL 0024+1654 from Strong Lensing'. *ApJ* **498**(2):L107–L110.

K. Umetsu, et al. (2012). 'CLASH: Mass Distribution in and around MACS J1206.2-0847 from a Full Cluster Lensing Analysis'. *ApJ* **755**:56.

J. Valle & J. Romao (2015). *Neutrinos in High Energy and Astroparticle Physics*. Wiley.

G. Van Brummelen (2009). *The Mathematics of the Heavens and the Earth: The Early History of Trigonometry*. Princeton University Press.

J. van de Sande, et al. (2019). 'The SAMI Galaxy Survey: comparing 3D spectroscopic observations with galaxies from cosmological hydrodynamical simulations'. *MNRAS* **484**(1):869–891.

F. C. van den Bosch, et al. (2008). 'The importance of satellite quenching for the build-up of the red sequence of present-day galaxies'. *MNRAS* **387**:79–91.

R. F. J. van der Burg, et al. (2013). 'The environmental dependence of the stellar mass function at z ˜ 1. Comparing cluster and field between the GCLASS and UltraVISTA surveys'. *A&A* **557**:A15.

R. P. van der Marel (1994). 'Velocity Profiles of Galaxies with Claimed Black-Holes - Part Three - Observations and Models for M87'. *MNRAS* **270**:271.

P. G. van Dokkum, et al. (1998). 'The Color-Magnitude Relation in CL 1358+62 at Z = 0.33: Evidence for Significant Evolution in the S0 Population'. *ApJ* **500**(2):714–737.

P. G. van Dokkum, et al. (2010). 'The Growth of Massive Galaxies Since z = 2'. *ApJ* **709**(2):1018–1041.

L. Van Waerbeke, et al. (2000). 'Detection of correlated galaxy ellipticities from CFHT data: first evidence for gravitational lensing by large-scale structures'. *A&A* **358**:30–44.

M. Verdugo, et al. (2008). 'The galaxy populations from the centers to the infall regions in z 0.25 clusters'. *A&A* **486**:9–24.

D. Vergani, et al. (2010). 'K+a galaxies in the zCOSMOS survey . Physical properties of systems in their post-starburst phase'. *A&A* **509**:A42.

J. Voelkel (2001). *The Composition of Kepler's Astronomia Nova*. Princeton University Press.

M. Vogelsberger, et al. (2014). 'Introducing the Illustris Project: simulating the coevolution of dark and visible matter in the Universe'. *MNRAS* **444**:1518–1547.

G. M. Voit, et al. (2015). 'Supernova Sweeping and Black Hole Feedback in Elliptical Galaxies'. *ApJ* **803**(2):L21.

B. Vollmer, et al. (2001). 'Ram Pressure Stripping and Galaxy Orbits: The Case of the Virgo Cluster'. *ApJ* **561**(2):708–726.

M. Volonteri, et al. (2015). 'Growing black holes and galaxies: black hole accretion versus star formation rate'. *MNRAS* **449**(2):1470–1485.

A. von der Linden, et al. (2010). 'Star formation and AGN activity in SDSS cluster galaxies'. *MNRAS* **404**:1231–1246.

B. Vulcani, et al. (2020a). 'GASP XXIV. The History of Abruptly Quenched Galaxies in Clusters'. *ApJ* **892**(2):146.

B. Vulcani, et al. (2018). 'Enhanced Star Formation in Both Disks and Ram-pressure-stripped Tails of GASP Jellyfish Galaxies'. *ApJ* **866**(2):L25.

B. Vulcani, et al. (2020b). 'GASP XXX. The Spatially Resolved SFRMass Relation in Stripping Galaxies in the Local Universe'. *ApJ* **899**(2):98.

M. Wadepuhl & V. Springel (2011). 'Satellite galaxies in hydrodynamical simulations of Milky Way sized galaxies'. *MNRAS* **410**(3):1975–1992.

A. G. Walker (1935). 'On Riemannian spaces with spherical symmetry about a line, and the conditions for isotropy in general relativity'. *The Quarterly Journal of Mathematics* **6**:81–93.

H. Wang, et al. (2018). 'ELUCID. IV. Galaxy Quenching and its Relation to Halo Mass, Environment, and Assembly Bias'. *ApJ* **852**(1):31.

L. Wang, et al. (2015). 'NIHAO project - I. Reproducing the inefficiency of galaxy formation across cosmic time with a large sample of cosmological hydrodynamical simulations'. *MNRAS* **454**:83–94.

P. A. Wayman (2002). 'C H Payne-Gaposchkin: Cecilia Payne-Gaposchkin: astronomer extraordinaire'. *Astronomy and Geophysics* **43**(1):1.27–1.29.

S. Weinberg (1967). 'A Model of Leptons'. *Phys. Rev. Lett.* **19**(21):1264–1266.

S. Weinberg (1989). 'The cosmological constant problem'. *Reviews of Modern Physics* **61**(1):1–23.

S. M. Weinmann, et al. (2009). 'Environmental effects on satellite galaxies: the link between concentration, size and colour profile'. *MNRAS* **394**:1213–1228.

S. M. Weinmann, et al. (2010). 'Cluster galaxies die hard'. *MNRAS* **406**:2249–2266.

S. M. Weinmann, et al. (2006). 'Properties of galaxy groups in the Sloan Digital Sky Survey - I. The dependence of colour, star formation and morphology on halo mass'. *MNRAS* **366**:2–28.

A. R. Wetzel (2011). 'On the orbits of infalling satellite haloes'. *MNRAS* **412**:49–58.

A. R. Wetzel, et al. (2012). 'Galaxy evolution in groups and clusters: star formation rates, red sequence fractions and the persistent bimodality'. *MNRAS* **424**:232–243.

A. R. Wetzel, et al. (2013). 'Galaxy evolution in groups and clusters: satellite star formation histories and quenching time-scales in a hierarchical Universe'. *MNRAS* **432**:336–358.

K. E. Whitaker, et al. (2012). 'A Large Population of Massive Compact Post-starburst Galaxies at z ¿ 1: Implications for the Size Evolution and Quenching Mechanism of Quiescent Galaxies'. *ApJ* **745**(2):179.

V. Wild, et al. (2014). 'A new method for classifying galaxy SEDs from multiwavelength photometry'. *MNRAS* **440**(2):1880–1898.

V. Wild, et al. (2016). 'The evolution of post-starburst galaxies from z=2 to 0.5'. *MNRAS* **463**(1):832–844.

V. Wild, et al. (2020). 'The star formation histories of z $\sim$ 1 post-starburst galaxies'. *MNRAS* **494**(1):529–548.

V. Wild, et al. (2009). 'Post-starburst galaxies: more than just an interesting curiosity'. *MNRAS* **395**:144–159.

C. L. Wilkinson, et al. (2017). 'The evolutionary sequence of post-starburst galaxies'. *MNRAS* **472**(2):1447–1457.

C. L. Wilkinson, et al. (2018). 'Evolution of starburst galaxies in the Illustris simulation'. *MNRAS* **479**(1):758–767.

J. Wolf, et al. (2010). 'Accurate masses for dispersion-supported galaxies'. *MNRAS* **406**(2):1220–1237.

M. Wolf (1901). 'Ein merkwürdiger Haufen von Nebelflecken'. *Astronomische Nachrichten* **155**:127.

A. Wolszczan & D. A. Frail (1992). 'A planetary system around the millisecond pulsar PSR1257 + 12'. *Nature* **355**(6356):145–147.

P.-F. Wu, et al. (2014). 'Star Formation Quenching in High-redshift Large-scale Structure: Post-starburst Galaxies in the Cl 1604 Supercluster at z ~0.9'. *ApJ* **792**(1):16.

P.-F. Wu, et al. (2020). 'The Colors and Sizes of Recently Quenched Galaxies: A Result of Compact Starburst before Quenching'. *ApJ* **888**(2):77.

T. K. Wyder, et al. (2007). 'The UV-Optical Galaxy Color-Magnitude Diagram. I. Basic Properties'. *ApJS* **173**(2):293–314.

L. Wyrzykowski, et al. (2011). 'The OGLE view of microlensing towards the Magellanic Clouds - IV. OGLE-III SMC data and final conclusions on MACHOs'. *MNRAS* **416**(4):2949–2961.

B. Yadav & M. Mohan (2011). *Ancient Indian Leaps into Mathematics*. Birkhäuser Boston.

A. Yahil & G. Beaudet (1976). 'Big-Bang Nucleosynthesis with Nonzero Lepton Numbers'. *ApJ* **206**:26–29.

R. Yan, et al. (2009). 'The DEEP2 Galaxy Redshift Survey: environments of post-starburst galaxies at z ~0.1 and ~0.8'. *MNRAS* **398**(2):735–753.

Y. Yang, et al. (2004). 'E+A Galaxies and the Formation of Early-Type Galaxies at z~0'. *ApJ* **607**(1):258–273.

Y. Yang, et al. (2008). 'The Detailed Evolution of E+A Galaxies into Early Types'. *ApJ* **688**(2):945–971.

H. M. Yesuf, et al. (2014). 'From Starburst to Quiescence: Testing Active Galactic Nucleus feedback in Rapidly Quenching Post-starburst Galaxies'. *ApJ* **792**(2):84.

H. M. Yesuf & L. C. Ho (2020). 'Some Die Filthy Rich: The Diverse Molecular Gas Contents of Post-starbust Galaxies Probed by Dust Absorption'. *arXiv e-prints* p. arXiv:2007.14004.

P. Yoachim & J. J. Dalcanton (2006). 'Structural Parameters of Thin and Thick Disks in Edge-on Disk Galaxies'. *AJ* **131**(1):226–249.

D. G. York, et al. (2000). 'The Sloan Digital Sky Survey: Technical Summary'. *AJ* **120**:1579–1587.

M. Yoshizawa & K. Wakamatsu (1975). 'On the Relative Importance of the Bulge to the Disk of Spiral and SO Galaxies'. *A&A* **44**:363.

L. M. Young, et al. (2014). 'The ATLAS^{3D} project - XXVII. Cold gas and the colours and ages of early-type galaxies'. *MNRAS* **444**(4):3408–3426.

T. T. Yuan, et al. (2010). 'The Role of Starburst-Active Galactic Nucleus Composites in Luminous Infrared Galaxy Mergers: Insights from the New Optical Classification Scheme'. *ApJ* **709**(2):884–911.

A. I. Zabludoff, et al. (1996). 'The Environment of "E+A" Galaxies'. *ApJ* **466**:104.

H. J. Zahid, et al. (2014). 'The Universal Relation of Galactic Chemical Evolution: The Origin of the Mass-Metallicity Relation'. *ApJ* **791**(2):130.

H. J. Zahid & M. J. Geller (2017). 'Velocity Dispersion, Size, Sérsic Index, and D $_n$4000: The Scaling of Stellar Mass with Dynamical Mass for Quiescent Galaxies'. *ApJ* **841**:32.

I. Zehavi, et al. (2011). 'Galaxy Clustering in the Completed SDSS Redshift Survey: The Dependence on Color and Luminosity'. *ApJ* **736**(1):59.

Y. Zheng, et al. (2020). 'Comparison of stellar populations in simulated and real post-starburst galaxies in MaNGA'. *MNRAS* **498**(1):1259–1277.

E. Zinger, et al. (2018). 'Quenching of satellite galaxies at the outskirts of galaxy clusters'. *MNRAS* **475**:3654–3681.

M. A. Zwaan, et al. (2013). 'The cold gas content of post-starburst galaxies'. *MNRAS* **432**(1):492–499.

F. Zwicky (1933). 'Die Rotverschiebung von extragalaktischen Nebeln'. *Helvetica Physica Acta* **6**:110–127.

F. Zwicky (1937). 'On the Masses of Nebulae and of Clusters of Nebulae'. *ApJ* **86**:217.

List of Figures

List of Tables

Danksagung

I thank Prof. Andreas Burkert for sharing insights and providing ample opportunities both in- and outside of astrophysics, from Santa Cruz to the exploration of the emergent properties of life. I thank Dr. Klaus Dolag for always answering my questions and for connecting the details with the broader context. Furthermore, I thank Dr. Rhea-Silvia Remus for energetic discussions and delivering a valuable lesson. In addition, I would like to thank Felix Schulze, Dr. Ulrich Steinwandel, Dr. Alex Arth, Dr. Adelheid Teklu, Ludwig Böss, Joseph O'Leary, Raphael Franz, Dr. Stefan Heigl, Dr. Manuel Behrendt, Dr. Tadziu Hoffmann, Matías Blaña, Prof. Harald Lesch, Marco Smolla, Jana Steuer and Dr. Matthias Kluge. Generally, I want to express my thanks to the people at the USM, as well as the current and former members of the CAST group for countless interesting discussions.